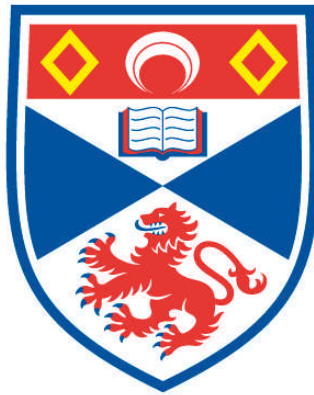


# **MINERAL DISSOLUTION IN SILICATE MELTS**

**Richard M. Curry**

**A Thesis Submitted for the Degree of PhD  
at the  
University of St Andrews**



**1990**

**Full metadata for this item is available in  
Research@StAndrews:FullText  
at:**

**<http://research-repository.st-andrews.ac.uk/>**

**Please use this identifier to cite or link to this item:**

**<http://hdl.handle.net/10023/7278>**

**This item is protected by original copyright**

**This item is licensed under a  
Creative Commons Licence**

**Mineral dissolution in silicate melts**

**Richard M. Curry**

Thesis presented in partial fulfilment for the degree

Doctor of Philosophy

August 1989.



Declaration

I, Richard Michael Curry, hereby certify that this thesis has been composed by myself, that it is a record of my own work, and that it has not been accepted in partial or complete fulfilment of any other degree or professional qualification.

 11 August 1989.

I was admitted to the Faculty of Science of the University of St. Andrews under Ordinance General No. 12 on 1st October 1985 and as a candidate for the degree of Ph.D. on 9th October 1986.

 11 August 1989.

I hereby certify that the candidate has fulfilled the conditions of the Resolution and Regulations appropriate to the Degree of Ph.D.

 11 August 1989

Copyright

In submitting this thesis to the University of St. Andrews I understand that I am giving permission for it to be made available for use in accordance with the regulations of the University Library for the time being in force, subject to any copyright vested in the work not being affected thereby. I also understand that the title and abstract will be published, and that a copy of the work may be made and supplied to any *bona fide* library or research worker.

## Abstract

Quartz and orthopyroxene in mafic rocks are commonly observed to be surrounded by fringes of granular pyroxene, and of olivine and clinopyroxene, respectively. This study reproduces the conditions of formation of these textures, and investigates their origins, kinetics and phase relations.

Pieces of silica glass or crystals of orthopyroxene were dissolved into tholeiitic and slightly alkaline basalts, suspended from wire loops in an atmospheric pressure quenching furnace, and run for 10 minutes to 32 days at subliquidus temperatures between 1120° and 1190°C and oxygen fugacities close to the QFM buffer. Polished sections of charges were examined primarily by backscattered electron imagery and by microprobe analysis.

The textures developed in silica dissolution experiments consist of fringes of elongate skeletal pyroxenes radially arranged around the silica. The pyroxenes first nucleate on the surface of the silica. As dissolution continues, growth continues mostly on existing crystals, rather than by the nucleation of additional crystals.

Dissolution rates for silica range from  $2.8 \cdot 10^{-11}$  to  $4.4 \cdot 10^{-10} \text{ms}^{-1}$ , and are time-independent until growth of the pyroxene fringe hinders transport processes in the melt. This causes dissolution to slow down, until it ceases altogether after 3 to 8 days. A silica-rich layer of melt forms around the surface of charges run at higher temperatures, suggesting that convection driven by variations in surface tension may operate in the charges.

The textures developed in orthopyroxene dissolution experiments consist of granular olivines, some of which nucleate on the pyroxene surface, whereas others nucleate within the pyroxene as a result of the decomposition of included phases. With time, olivine crystals become connected and form complex grain shapes.

Dissolution rates for orthopyroxene range from  $1.7 \cdot 10^{-11}$  to  $1.2 \cdot 10^{-9} \text{ms}^{-1}$ . At higher temperatures dissolution rates are constant, but at lower temperatures dissolution is time-dependent. Unlike silica dissolution, orthopyroxene dissolution does not cease as a result of continued neocryst growth hindering melt transport, indicating that the fringe remains permeable.

For both systems, the neocryst compositions are strongly dependent on the chemistry of the melt formed at the interface between the dissolving crystal and the bulk melt, and the neocrysts may be metastable with respect to the bulk melt. Chemical equilibration of olivine neocrysts with time is observed for longer experiments. Textural equilibration of olivine grains occurs by the processes of liquid-phase sintering in runs longer than 12 hours.

Subliquidus dissolution data are applied to textures from natural samples collected from dykes, lava flows and lava lakes, to estimate the residence time of reacted crystals; values range from 0.6 to 208 days for reacted quartz, and from 0.7 to 462 days for reacted orthopyroxenes. The rates of cooling of the magma and the size of the magma body in which the reaction occurred are also estimated.

## Acknowledgements

As for all research theses, there are many people without whom this volume would not have come into being. First I must thank my supervisor Colin Donaldson, for expert guidance, stimulating discussion and generally trying to keep me on the rails. Extensive technical support for the microprobe, as well as probing questioning ("why are you doing this? why don't you do that"), staunch drinking and excellent darts playing was provided by Donald Herd. Technical assistance and instruction in the manufacture of thin sections was provided by Andy Mackie, and photographs were expertly created by Jim Allen. My brother Alex must be thanked for excellent work in creating programs for the Atari computer that could easily be adapted by a comparative novice (eg me) for the manipulation of 'probe data' (for projections, thermometers, quality control etc).

Although computers are not yet able to think for themselves, I would like to thank Freddie, my Atari computer, for being an excellent data handler, word processor and musician. I couldn't have done it without you. (This is in case he finally becomes conscious and takes exception to the fact that I might not have acknowledged him).

Thanks are also due to my fellow research workers, for stimulating discussion on matters geological, as well as golf, outings to the puuuuuub, holidays and generally sociable behaviour. Especial thanks are due to Martin (the Goat) and Bruce (the Moose) for cooking, washing-up and occasionally cleaning the house in which we all take refuge from the research environment.

I would also like to thank all those people who have done their best to distract me from academic research during my time here, especially the Boat Club (Martin and Adrian), the Musical Society, the Music Department (what's left of it), the Gilbert and Sullivan Society, the Mermaids and everybody involved with Offbeat (ie Andy and Adrian). These (and others) have conspired to prolong my delightful sojourn in St. Andrews, and allowed me to pursue my favourite hobbies.

Finally, I would like to thank my parents, Katie and all those of my family and friends who kept asking me "Haven't you finished yet?". This is for you.

"It is testimony to the marvellous adaptability of geological observations that well exposed and thoroughly studied localities can provide competent petrologists with evidence for diametrically opposed conclusions. Whatever the popularly accepted theory of the moment maybe, one can usually find evidence to support it."

Alexander McBirney, in "The evolution of the igneous rocks; fiftieth anniversary perspectives" (ed. Yoder, 1979).

## Contents

Abstract

Acknowledgements

Contents

<b>1 Introduction, previous work, aims and terminology</b>	<b>1</b>
1.1 Introduction	1
1.2 Review of previous work	2
1.2.1 Dissolution in simple systems	3
1.2.2 Dissolution in complex systems	3
1.2.3 Dissolution rate controls	4
1.2.4 Textures developed during dissolution	5
1.2.4a Quartz	6
1.2.4b Orthopyroxene	6
1.2.4c Olivine	7
1.2.4d Garnet	8
1.2.4e Plagioclase	8
1.2.5 Summary	8
1.3 Aims	8
1.4 Terminology	9
1.4.1 Simple melting	9
1.4.2 Partial melting	10
1.4.3 Incongruent melting	10
1.4.4 Dissolution	10
1.4.5 Partial dissolution	10
1.4.6 Incongruent dissolution	11
1.4.6a Down temperature	12
1.4.6b Up temperature	13
1.4.7 Distinguishing partial and incongruent dissolution	14
<b>2 Experimental techniques and analytical methods</b>	<b>16</b>
2.1 Experimental techniques	17
2.1.1 Silica dissolution	19
2.1.2 Cooling-rate experiments	20
2.1.3 Orthopyroxene dissolution	21
2.2 Thin section preparation	25
2.3 Measurements of crystal sizes	25
2.3.1 Silica dissolution experiments	27
2.3.2 Pyroxene dissolution experiments	29
2.4 Electron microscopy and microprobe investigations	30
2.4.1 Electron microscopy	31
2.4.2 Chemical analysis	31
2.4.2a Qualitative scans	31
2.4.2b Quantitative analysis	32
2.4.3 Quality control of microprobe analysis	33

2.5	Calculation of melt properties . . . . .	34
2.5.1	Density calculations . . . . .	34
2.5.2	Viscosity calculations . . . . .	35
2.6	Projection of melt and crystal compositions . . . . .	36
2.7	Pyroxene thermometry . . . . .	37
<b>3</b>	<b>The experimental dissolution of silica . . . . .</b>	<b>39</b>
3.1	Petrography . . . . .	39
3.1.1	General features of experimental charges . . . . .	39
3.1.2	Vesicles . . . . .	44
3.1.3	Development of the glass-rich zone . . . . .	45
3.1.4	Dissolution shape of the silica rod . . . . .	47
3.1.5	Crystallization of silica . . . . .	49
3.1.6	Cooling-rate experiments . . . . .	50
3.2	Kinetics of silica dissolution and fringe growth . . . . .	52
3.2.1	Rates of silica dissolution . . . . .	53
3.2.2	Fringe growth . . . . .	54
3.2.3	Activation energy of dissolution . . . . .	56
3.2.4	Growth of the glass-rich zone . . . . .	57
3.2.5	Silica-rich boundary layers . . . . .	59
3.2.5a	Around the rod . . . . .	60
3.2.5b	Around the charge . . . . .	62
3.2.6	Summary of kinetic data . . . . .	64
3.2.7	Convection in the charges . . . . .	64
3.2.7a	Compositional convection . . . . .	66
3.2.7b	Surface tension-driven phenomena . . . . .	68
3.2.7c	Cessation of convection . . . . .	69
3.2.7d	Summary . . . . .	70
3.3	Pyroxenes and coexisting melts . . . . .	71
3.3.1	Pyroxene compositions . . . . .	71
3.3.1a	Variation in individual experiments . . . . .	72
3.3.1b	Pyroxenes from cooling-rate experiments . . . . .	73
3.3.2	The nature of the pyroxene phase . . . . .	73
3.3.2a	Metastable crystallization? . . . . .	76
3.3.2b	Pigeonite stability . . . . .	77
3.3.2c	Other factors . . . . .	78
3.3.3	Melt compositions . . . . .	80
3.3.3a	Why does augite crystallize? . . . . .	81
3.3.3b	Melt chemistry . . . . .	82
3.3.3c	Theoretical considerations regarding the composition of interfacial melts . . . . .	85
3.3.4	Summary . . . . .	86
3.4	Summary of experimental quartz dissolution . . . . .	87

<b>4 Quartz-melt reaction textures in mafic and intermediate rocks . . . . .</b>	<b>88</b>
4.1 Documented examples . . . . .	88
4.2 Origin of the quartz . . . . .	90
4.3 Petrography of reacted quartz . . . . .	93
4.3.1 General features . . . . .	94
4.3.2 Regrowth features . . . . .	96
4.3.3 Comparison with experimental textures . . . . .	98
4.4 Shapes of quartz . . . . .	98
4.4.1 Mechanisms of rounding . . . . .	99
4.4.2 Mechanisms of fracture . . . . .	100
4.4.3 Mechanisms of embayment . . . . .	101
4.4.4 Summary . . . . .	102
4.5 Chemistry of pyroxenes and coexisting phases . . . . .	102
4.5.1 Chemistry of pyroxenes . . . . .	102
4.5.2 Pyroxene-melt relationships . . . . .	110
4.5.3 Pyroxene thermometry . . . . .	111
4.6 Summary . . . . .	113
<b>5 The experimental dissolution of orthopyroxene . . . . .</b>	<b>114</b>
5.1 Petrography of enstatite experiments . . . . .	114
5.1.1 Heating in the absence of basalt . . . . .	114
5.1.2 Heating in the presence of basalt . . . . .	115
5.2 Petrography of bronzite experiments . . . . .	118
5.2.1 Heating in the absence of basalt . . . . .	118
5.2.2 Heating in the presence of basalt . . . . .	119
5.3 Kinetics . . . . .	121
5.3.1 Dissolution rates of orthopyroxene . . . . .	121
5.3.2 Activation energies of dissolution . . . . .	123
5.4 Chemical relationships . . . . .	126
5.4.1 Fe-Mg contents of olivine . . . . .	126
5.4.2 Olivine-melt thermometry . . . . .	127
5.4.3 Mechanisms of equilibration . . . . .	129
5.5 Non-primary textures . . . . .	130
5.5.1 Olivines in enstatite charges . . . . .	130
5.5.2 Olivines in bronzite charges . . . . .	131
5.5.3 Textural equilibration . . . . .	132
5.5.4 Summary of textural equilibration . . . . .	138
5.6 Summary . . . . .	139

<b>6 Orthopyroxene-melt reaction textures in mafic rocks . . . . .</b>	<b>140</b>
6.1 Documented examples . . . . .	140
6.2 Petrography of reacted orthopyroxene . . . . .	142
6.2.1 Reactions crystallizing olivine . . . . .	142
6.2.2 Reactions crystallizing clinopyroxene . . . . .	143
6.3 Textural equilibration . . . . .	143
6.4 Chemistry . . . . .	144
6.4.1 Mg-Fe exchange between minerals and melt . . . . .	144
6.4.2 Olivine thermometry . . . . .	147
6.4.3 Pyroxene thermometry . . . . .	148
6.5 Summary . . . . .	148
<b>7 Reaction textures around other minerals . . . . .</b>	<b>150</b>
<b>A: Anhydrous minerals . . . . .</b>	<b>150</b>
7.1 Olivine . . . . .	150
7.1.1 Examples of rimmed olivine . . . . .	153
7.1.2 Chemistry of olivine and rim phases . . . . .	154
7.2 Clinopyroxene . . . . .	154
7.3 Spinel . . . . .	156
<b>B: Hydrous minerals . . . . .</b>	<b>156</b>
7.4 Amphibole . . . . .	157
7.4.1 Chemistry of amphibole and rim phases . . . . .	158
7.5 Biotite . . . . .	159
7.5.1 Examples of rimmed biotite . . . . .	160
7.5.2 Chemistry of biotite and rim phases . . . . .	160
7.6 Summary . . . . .	161
<b>8 Applications . . . . .</b>	<b>162</b>
8.1 Xenocryst digestion in a crystallizing magma . . . . .	164
8.2 Residence times . . . . .	165
8.2.1 Reacted quartz . . . . .	165
8.2.2 Reacted orthopyroxene . . . . .	172
8.3 Estimation of cooling rates . . . . .	174
8.3.1 Size estimates of cooling magma bodies . . . . .	177
8.4 Magma ascent velocities . . . . .	181
8.5 Summary . . . . .	185

<b>9 Recapitulation and suggestions for further work . . .</b>	<b>187</b>
Suggestions for further work . . . . .	191
<b>Appendix 1: Sample descriptions . . . . .</b>	<b>193</b>
Area one: Lassen . . . . .	194
Area two: Yellowstone . . . . .	193
Area three: Labrador . . . . .	196
Area four: Great Britain . . . . .	197
Area five: France . . . . .	197
Area six: Japan . . . . .	200
Area seven: New Zealand . . . . .	203
<b>Appendix 2: Microprobe data . . . . .</b>	<b>204</b>
Silica dissolution experiments . . . . .	204
Enstatite dissolution experiments . . . . .	208
Bronzite dissolution experiments . . . . .	211
Natural samples . . . . .	214
<b>References cited . . . . .</b>	<b>224</b>

**Frontispiece one.**

Summit crater of Lassen Peak. The 1915 dacite flow can be seen at the right (black).



## Chapter one

### Introduction, previous work, aims and terminology

#### 1.1 Introduction

In the last fifteen years there has been considerable interest in the processes associated with the cooling and crystallization of magma bodies, that is, the nucleation and growth of crystalline phases, the mechanisms of heat loss, and the effect these may have on the development of compositional stratification of a body. Some studies have developed the theory of nucleation and crystallization (eg Kirkpatrick, 1975, 1983; Dowty, 1980; Lasaga, 1982) and allow empirical studies to distinguish between various rate-controlling processes of nucleation and growth. However, such theoretical studies suffer large discrepancies with reality, mostly due to heterogeneous nucleation and the inability of experimentalists to produce impurity-free starting materials (Marsh, 1988).

Other experimental studies (eg Lofgren, 1974, 1980; Donaldson, 1976) have enabled textural information from natural samples (eg crystal shapes) to be related to cooling rates, or to the degree of supersaturation (eg by undercooling) of the melt from which they crystallized.

With improvements in electron microscopy, microprobe analysis, and isotope and trace element analysis, petrologists are discovering that the evolution of magmatic systems is not dominated purely by crystallization and heat loss, but frequently also involves magma contamination. Recent petrologic studies of orogenic volcanoes have revealed that many of the mineralogical and chemical features of calc-alkaline rocks cannot be explained by magmatic evolution in closed systems; petrogenetic models have

been forced to invoke open system behaviour, in which crystallization in evolving magmatic systems is accompanied by wall-rock assimilation and/or magma mixing (eg Eichelberger, 1975; Anderson, 1976; Sakuyama, 1978, 1979, 1981; Heiken and Eichelberger, 1980; Gerlach and Grove, 1982; Koyaguchi, 1986b).

Contamination of a magma must occur by one of two mechanisms: by mixing with another magma (ie liquid  $\pm$  crystals  $\pm$  gas), by reaction with, and possibly solution of, solid material, or by some combination of these two. Solids in a (hybrid) magma with which they are not in thermal equilibrium may undergo melting, or, if they are in thermal but not chemical equilibrium, they may undergo dissolution. Since the temperatures at which dissolution reactions occur in magmas are often lower than the solidus of the minerals concerned (eg Lofgren and Norris, 1981) simple or partial *melting* of a crystal is rare, and since a crystal will never find itself in a liquid of identical composition, dissolution reactions are more relevant than melting ones to the study of assimilation processes. An exception is the melting of crustal material following intrusion of basalt.

## 1.2 Review of previous work

In order to understand the mechanisms of assimilation, experiments, which are scarce in the geological literature, have been undertaken by workers to investigate the dissolution of various minerals species in different magmas. The majority of studies have been conducted at superliquidus temperatures where dissolution reactions are most rapid, enabling some assessment of contamination rates to be made.

### 1.2.1 Dissolution in simple systems

Melting and dissolution experiments in synthetic systems are often reported in the chemistry, glass-making and ceramics literatures (eg Löffler, 1958; Schwerdtfeger, 1966), but are scarce in the geological literature. Kuo and Kirkpatrick (1985a) showed that quartz, enstatite, diopside and forsterite dissolve into superheated iron-free melts at constant rates, and suggested that the rate-controlling process is diffusion across a boundary layer maintained at a constant thickness under conditions of natural convection. Quartz was observed to dissolve more rapidly at quartz-melt-air contacts, in experimental runs where the quartz had floated to the top of a charge. The increased dissolution is due to enhanced natural convection driven by differences in the surface energy between bulk and boundary layer melts (see also Jebesen-Marwedel, 1956; Brückner, 1961).

### 1.2.2 Dissolution in complex systems

Experimental work in natural systems is more prevalent in the geological literature, with petrologists addressing specific problems rather than the general principles investigated by scientists working in specific systems. Natural systems are chemically more complex and individual effects are less easily isolated.

At atmospheric pressure, dissolution experiments in superheated basalt involving magnesian olivine, have been conducted by Thornber and Huebner (1985) and Donaldson (1985b), and the kinetics of quartz and feldspar dissolution into superheated basalt have been investigated by Donaldson (1985b) and Watson (1982). Dissolution rates (stated in terms of length/time) are independent of time and crystallographic

direction, except for alkali feldspars which melt below typical basalt magma temperatures, and the resultant viscous liquid blends with the basalt by diffusion. This is one of the few examples of a melting reaction taking precedence over dissolution. The other minerals dissolve at constant rates.

Experiments at higher pressures (0.5 - 3GPa) with a alkali basalt melt have been conducted by Scarfe *et al.* (1980) and Brearley and Scarfe (1986), determining the relative superliquidus dissolution rates of olivine, orthopyroxene, clinopyroxene, spinel and garnet.

### 1.2.3 Dissolution rate controls

The rate of dissolution in any particular crystallographic direction is governed by a combination of (a) reaction kinetics at the crystal-melt interface, and (b) the rate of transport of melt components to and from the interface. The transport of melt components has been shown to determine dissolution rates, both by numerical calculation and by experiments (Zhang *et al.*, 1989). Convection of melt around a dissolving crystal may supplement diffusion as a mechanism for transporting melt components.

In dissolution experiments designed to suppress melt convection, concentration profiles of all components propagate into the melt according to the square root of run duration (Zhang *et al.*, 1989); the length of the concentration profiles is frequently referred to as a **boundary layer**. In dissolution experiments not designed to suppress convection, for all run durations concentration profiles in melt adjacent to dissolving crystals are identical, implying that dissolution is time-independent and a steady state process (Watson, 1982; Kuo and Kirkpatrick, 1985a; Donaldson, 1985b; Brearley and Scarfe, 1986).

In experiments where dissolution is time-independent, dissolution is controlled by a combination of (a) the diffusion of components across the compositional boundary layer, and (b) convection in the melt maintaining this boundary layer at a constant thickness (Watson, 1982; Kuo and Kirkpatrick, 1985a; Donaldson, 1985b).

As confirmation, Watson (1982) found that rates of quartz dissolution under conditions of forced convection were constant with time; the rate only varying with stirring rate. This is consistent with the rate of dissolution being controlled by the thickness of a boundary layer, which is, in turn, controlled by the rate of (forced) convection.

At lower temperatures typical of rhyolitic liquids, the dissolution of silica (Blake and Hamilton, 1988) or of the accessory minerals zircon and apatite (Harrison and Watson, 1983, 1984) is controlled by the diffusion rates of Si, Zr or P (respectively) in the melt, which, in turn, are highly dependent on the water content of the system.

#### **1.2.4 Textures developed during dissolution**

In systems where convection and/or diffusion in the melt (rather than interface kinetics) govern the dissolution rate of a crystal, dissolution at corners and edges will be more rapid than in the middle of faces because of better bulk melt access, and the crystal will develop a rounded form. On the other hand, if melt transport is rapid compared to interface kinetics during dissolution, and the interface kinetics are anisotropic in different crystallographic directions, a faceted morphology may result (Donaldson, 1985a).

In all dissolution experiments involving a silicate melt, the dominant textural modification is the rounding of the

dissolving phase, regardless of the degree of superheating, and the primary textures developed in superliquidus experiments are related to mineral stability in melt (Brearley and Scarfe, 1986). Mineral phases stable on or near the liquidus may exhibit simple dissolution (rounding of the crystal), whereas complex reaction textures and crystallization are characteristic of the dissolution of minerals that are not stable near the liquidus.

The following subsections document specific examples of other textures reproduced in dissolution experiments. Terms such as partial and incongruent dissolution will be explained in §1.4.

#### 1.2.4a Quartz

Quartz does not invert to tridymite and may persist metastably to temperatures in excess of 300°C above the inversion temperature during melting (eg Ainslie *et al.*, 1961) or dissolution (eg Donaldson, 1985b).

Donaldson (1985b) reproduced the conditions, in subliquidus experiments, under which a dissolving quartz may develop a reaction rim of radial pyroxene prisms. The rates of dissolution under these conditions were determined to be almost two orders of magnitude lower than extrapolation from superliquidus experiments would suggest.

Dissolution of quartz in a water-saturated rhyolitic melt leads to the formation of hemispherical embayments on the quartz surface by the action of bubbles (Donaldson and Henderson, 1988).

#### 1.2.4b Orthopyroxene

Brearley and Scarfe (1986) reproduced a natural reaction texture involving orthopyroxene (1300°C, 0.5MPa), where a thin band of equant chromite crystals formed at the original crystal-

melt interface and further dissolution of the orthopyroxene caused olivine ( $f_{O_{90}}$ , the liquidus phase) to crystallize from the melt. In this example, crystallization of olivine occurred at temperatures above the olivine liquidus of the basalt, because dissolution changed the chemistry, and thus the phase relations, of the melt immediately adjacent to the dissolving phase.

#### 1.2.4c Olivine

Tschiyama (1986b) investigated the reactions between three olivines and two silica-rich melts at atmospheric pressure, to determine the conditions for the formation of pyroxene reaction rims on olivine. Pyroxene rims form on all olivines in andesite, except at temperatures greater than the pyroxene liquidus, when olivine simply becomes rounded. Forsteritic olivine dissolves simply, whereas fayalitic olivine dissolves either partially, leading to a vermicular olivine texture, or incongruently<sup>1</sup>, leading to the formation of opaque zones of magnetite, orthopyroxene, melt and sometimes olivine. Pyroxene reaction rims were not observed for reaction with boninite melt, even though orthopyroxene was present in the groundmass.

Olivine dissolution into a siliceous basalt at temperatures just above the orthopyroxene liquidus resulted in the crystallization of a rim of granular orthopyroxene (Thornber and Huebner, 1985).

---

<sup>1</sup> Tschiyama (1986b) describes this as partial dissolution (see discussion on partial and incongruent reactions, §1.4).

#### 1.2.4d Garnet

Dissolution of garnet into an alkali basalt (1300°C at 1.2GPa) initially produces olivine crystals ( $fo_{90}$ ), before the formation of an aggregate of aluminous orthopyroxene and spinel (Brearley and Scarfe, 1986). At atmospheric pressure, pyrope-rich garnet decomposes very rapidly to elongate, skeletal olivine and melt before dissolution can occur (Donaldson, 1984).

#### 1.2.4e Plagioclase

Tsuchiyama (1985) investigated plagioclase dissolution kinetics and the formation of sponge-textured plagioclase crystals in andesites. Calcic plagioclase dissolving in a melt saturated with a more sodic plagioclase either remain euhedral or become rounded, and dissolution of a more sodic plagioclase in a melt saturated with a more calcic composition leads to the formation of a mantle of more calcic plagioclase and melt (sponge-texture).

#### 1.2.5 Summary

Dissolution of minerals into superliquidus silicate liquids has been fairly well covered for the major minerals. Apart from one or two brief forays below the liquidus, little work on the dissolution of crystalline phases into a subliquidus melt has been attempted, and there has been no detailed investigation of the textures, processes and mechanisms of such dissolution.

#### 1.3 Aims

This project aims to investigate the reactions of minerals with partially molten silicate magmas. Specifically, the aims are:

- a) to investigate (and hopefully reproduce) textures formed around reacted quartz and orthopyroxene in basalt;
- b) to investigate the kinetics of formation of these textures;
- c) to investigate chemical relationships between dissolving crystals, reacting liquid and new crystalline phases;
- d) to use the comparison with natural textures to estimate the duration of the texture-forming reaction in some natural examples, which may then provide insight into the time interval between mixing and eruption in volcanoes (eg Sparks *et al.*, 1977b; Eichelberger, 1980);
- e) to estimate cooling rates in magma chambers or the ascent rates of xenolith- and xenocryst-bearing magmas (Kuo and Kirkpatrick, 1985b);
- f) to examine visually similar textures around minerals (not experimentally investigated) to assess whether they might have formed in similar manner.

## **1.4 Terminology**

There is need for distinctions to be made between the various types of melting and dissolution processes in terms of their reaction products.

### **1.4.1 Simple melting**

A crystalline phase melts at temperatures in excess of its melting point to form a liquid of the same composition. The solid-liquid transition occurs as the thermal stability limits of the weakest bonds in the crystal are exceeded. Theoretically, the

rate of melting is controlled by a combination of (a) heat transfer to the crystal and (b) the rearrangement of atoms at the crystal-liquid interface. In practice, melting occurs as fast as heat can diffuse into the crystal if sufficient energy is present (Tsuchiyama, 1986a).

#### **1.4.2 Partial melting**

An isolated crystal of a solid-solution series partially melts when diffusion in the crystal causes it to dissociate into a melt and another crystal whose composition is richer in the higher temperature component of the solid-solution series (Tsuchiyama and Takahashi, 1983).

#### **1.4.3 Incongruent melting**

An isolated crystal incongruently decomposes to form a crystal and a liquid, both of which are chemically and structurally distinct from the original crystal.

#### **1.4.4 Dissolution**

At temperatures above its stability in a melt, a crystal dissolves by loss of components from its surface to the melt. Control of the process is by the transfer of both heat and mass, as well as by the kinetics of reactions at the crystal-melt interface.

#### **1.4.5 Partial dissolution**

Crystals of a solid-solution series react readily with melt saturated in a higher temperature member of that series. By reaction along crystal defects, they are disintegrated into a crystal-melt mixture from the surface inwards, in which the

residual crystals are enriched in the high-temperature component. The composition of the crystal must become more refractory by diffusion in the crystal, which controls the rate of partial dissolution (Tsuchiyama, 1985). In the case of plagioclase, this leads to the development of the well-known sponge texture, where the crystallographic orientation is maintained.

In contrast, a higher temperature member reacts with melt, and is made over to the equilibrium (lower temperature member) composition, with a decrease in liquid volume and with evolution of heat. However, in the case of experiments with plagioclase, diffusion is too slow to advance the reaction on a laboratory timescale and evidence of reaction is not detectable (Tsuchiyama, 1985).

#### 1.4.6 Incongruent dissolution

If the melt formed at the interface of a dissolving crystal is saturated with another solid, or if the composition path between interface and bulk melts intersects the primary phase field of another solid (or even the metastable extension of a primary phase field), this second phase may crystallize. Oishi *et al.*, (1965) applied the term "incongruent dissolution" to this process. Solution chemists use a similar term ("incongruent hydrolysis") for similar processes in aqueous fluid (eg Helgeson *et al.*, 1984).

Within the bounds of this definition, two varieties of this process may be distinguished:

#### 1.4.6a Down-temperature

A higher temperature mineral may react with a melt saturated in a lower temperature mineral (eg olivine in orthopyroxene-saturated andesite). The higher temperature mineral dissolves, resulting on precipitation of the lower temperature mineral along with a net release of heat and decrease in liquid volume (Bowen, 1928).

a1) A variety of this reaction occurs at peritectic conditions, where, during the course of normal cooling and crystallization, a magma becomes saturated with a lower temperature phase that crystallizes at the expense of the higher temperature mineral. For non-solid solution systems under equilibrium conditions, the peritectic temperature is maintained until the higher temperature phase has completely reacted out. In systems with solid solution (eg forsterite-fayalite-quartz; Bowen and Schairer, 1935) the temperature of the peritectic condition decreases with increasing Fe content, so that both the reactant and product materials will be zoned. If equilibrium is not achieved, cooling of the magma might occur before resorption is complete, confusing this reaction with that described in (a2).

a2) The more general variety is reaction at other than peritectic conditions, which may follow xenocryst incorporation (either by assimilation or by magma mixing).

Both of these situations were covered by the term

"discontinuous reaction" as applied to igneous rocks by Bowen (1928). If the reaction does not go to completion, this may lead to the formation of reaction rims of the lower temperature phase about the more refractory crystal. Recognition of (a1) and (a2) in rocks and distinction between them is difficult because the effects of assimilation are largely governed by the same phase relations that operate during spontaneous crystallization. However, the compositions of the crystallizing phases may be different for examples where the refractory crystal dissolves at the peritectic condition (a1) and below it (a2). At the peritectic, the whole magma will be saturated with the less refractory phase, which may crystallize throughout the liquid and not just as coronas around the higher temperature phase, and so the composition of crystals of the less refractory phase should be the same throughout the magma. If, however, the more refractory phase is introduced into the magma at temperatures *below* the peritectic and starts to dissolve (case a2), the composition of the lower temperature phase growing in the boundary layer around the dissolving phase will, in general, be different from crystals of the same phase growing in the bulk of the magma. Unfortunately, any distinction in major element compositions (especially Mg-Fe) will probably be obscured by the continuous zoning of phases during normal cooling. Only in rapidly quenched (glassy) samples may such chemical distinction be unambiguously preserved.

#### **1.4.6b Up-temperature**

Reaction of a lower temperature mineral with a liquid saturated with a higher temperature phase or phases (eg quartz in basalt) leads to the solution of the crystals and precipitation

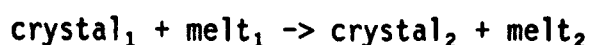
of the phase with which the magma is saturated. This reaction is endothermic and results in a net increase in liquid volume. As with (a), this too can be separated into two varieties:

- b1) Heating of a magma (eg as a consequence of magma mixing) to a peritectic condition will simply lead to a reverse of (a1). At the peritectic temperature the higher temperature mineral will crystallize at the expense of the less refractory phase. For solid-solution situations the peritectic reaction will occur over a range of temperatures.
- b2) Similar reactions will occur at temperatures other than peritectics, following xenocryst incorporation into the magma.

Since magmas tend to cool rather than heat up, a distinction between the products of (b1) and (b2), based on their chemistry, may be possible in situations involving minerals with solid solutions (eg orthopyroxene dissolving in olivine-saturated basalt). Reactions of type (b1) would lead to reverse-zoned olivines, as the peritectic becomes Mg-rich with increasing temperature, whereas reaction above the peritectic (at constant temperature) should lead to unzoned crystals. Reaction in a cooling magma will lead to normally zoned crystals, which may themselves react at a peritectic condition.

#### **1.4.7 Distinguishing partial and incongruent dissolution**

It is important to make a clear distinction between partial and incongruent dissolution. While they are both of the general type



there is a significant difference between examples where  $crystal_1$  and  $crystal_2$  are both members of the same solid-solution series (partial dissolution), and those where  $crystal_1$  and  $crystal_2$  are different mineral species (incongruent dissolution). The same distinction should be made for partial and incongruent melting

$crystal_1 \rightarrow crystal_2 + melt.$

## Chapter two

### Experimental techniques and analytical methods

One hundred and seventeen experiments were conducted as part of this project, and these divide into two roughly equal parts. One investigates the incongruent dissolution of quartz in basalt, and the other the incongruent dissolution of two compositions of orthopyroxene in basalt. Forty nine experiments were repeated, twenty eight to establish reproducibility and twenty one as repeats if the furnace failed or if a thin section proved to be unusable.

To elucidate the kinetics of these reactions, charges containing measured pieces of quartz (or a silica-glass substitute) or orthopyroxene were run at temperatures between 1123°C and 1194°C with durations ranging from 3 to 774 hours. After quenching, a thin section of each charge was made, and the final size of the dissolving phase and the width of the reaction rim measured, enabling rates of dissolution and rim growth to be calculated.

Analyses of the starting materials are given in table 2.1. Early quartz dissolution experiments (table 2.2) used the ferrodiorite exposed in Harker's Gully on Marsco, Isle of Skye, in an attempt to reproduce reaction textures found in samples from Marsco (Wager *et al.*, 1965). Approximate phase relations were determined, and some quartz dissolution runs were attempted (§3.3.3). However, it became apparent that the high viscosity of the melt meant that these experiments would be extremely long to run (several weeks each). The ferrodiorite was therefore abandoned and replaced by a tholeiitic basalt from the Taos Plateau, New Mexico, allowing quartz reactions to be studied at higher temperatures and thus faster rates. The orthopyroxene

Table 2.1  
Compositions of basalts used.

	<u>7M-5X</u>	<u>SK918</u>	<u>RC342</u>
SiO <sub>2</sub>	51.91	46.51	54.18
TiO <sub>2</sub>	1.16	2.23	1.97
Al <sub>2</sub> O <sub>3</sub>	15.85	14.60	13.74
Cr <sub>2</sub> O <sub>3</sub>	0.06	nr	nr
Fe <sub>2</sub> O <sub>3</sub>	1.65	1.55	1.88
FeO	8.27	11.33	10.79
MnO	0.15	0.19	0.30
MgO	7.01	10.66	2.42
CaO	8.66	8.85	6.34
Na <sub>2</sub> O	3.03	3.27	3.46
K <sub>2</sub> O	0.75	0.54	1.85
P <sub>2</sub> O <sub>5</sub>	0.17	0.27	1.30
H <sub>2</sub> O <sup>tot</sup>	0.86	-	1.66
	99.53	100.00	99.89
qz	0.43	-	7.77
or	4.43	3.07	10.91
ab	25.64	22.02	29.26
an	27.43	22.86	16.52
ne	-	2.56	-
di	11.88	14.51	5.58
hy	23.83	-	18.72
ol	-	24.89	-
mt	2.39	2.18	2.73
ilm	2.20	4.08	3.74
ap	0.37	0.57	3.02
T <sub>LIQ</sub> (°C)	1198±1	1222	1130±10
T <sub>PLAG</sub> (°C)	1187±3	1189	1130±10
T <sub>CPX</sub> (°C)	1133±5	1164±4	1090±10
T <sub>ILM,MT</sub> (°C)	1090±10		1130±10

nr - not reported

- 7M-5X: Servilleta basalt (olivine tholeiite), Lofgren (1983).  
 SK918: Alkali olivine basalt, recalculated water-free. (Thompson *et al.*, 1972).  
 RC342: Ferrodiorite from Shelter Stone, Harker's Gully, Marsco, Isle of Skye (Wager and Vincent, 1962; analysis #344). Approximate phase relations were determined prior to quartz dissolution experiments.

Table 2.2  
Experimental conditions imposed on ferrodiorite charges.

Run	Final conditions			Run duration		Quartz present?
	temp(°C)	-logfO <sub>2</sub>	δQFM	(hours)	(days)	
19	1070	9.89	-0.11	6.75	0.25	no
26	1069	9.73	-0.27	17.83	0.75	no
25	1071	9.98	-0.02	64.00	2.67	no
27	1069	9.64	-0.36	230.20	9.60	yes

δQFM is defined in table 2.3

dissolution experiments were run in a slightly alkaline olivine basalt from the Isle of Skye. Few grains in any of the rock powders exceed 50µm in length, rare crystals are up to 100µm.

### 2.1 Experimental techniques

Cylindrical pressed pellets (2mm long and 3mm in diameter) were made from powdered rock and contained a piece of the material to be dissolved. The pellet was attached to a 2mm diameter loop of 0.125mm gauge Pt-wire by passing a current through the wire until the rock powder in contact with the wire fused (Donaldson *et al.*, 1975a).

The pellets were suspended one at a time from a ceramic rod at the hotspot of a one-atmosphere vertical quenching furnace. The hotspot was measured to be 10mm long, and since the charges are only about 4mm in diameter, there is unlikely to be an externally imposed thermal gradient across the charge. Soret diffusion and thermal migration should therefore be negligible (Walker *et al.*, 1988, and references therein). The temperature at the furnace hotspot was continuously monitored with a Pt<sub>100</sub>-Pt<sub>87</sub>Rh<sub>13</sub> thermocouple and a digital thermometer, with 1°C resolution and ±1°C accuracy, calibrated periodically against the melting point of gold. The partial pressure of oxygen in the furnace was controlled by a downward flow of a mixture of CO and CO<sub>2</sub> gases (at a flow rate of 60cm<sup>3</sup>min<sup>-1</sup>). The partial

pressure of oxygen was measured with a  $ZrO_2$ -CaO electrolytic cell (Williams and Mullins, 1976) and calibrated by bracketing reversals across the Ni-NiO buffer at typical run temperatures. The bracket could only be constrained to  $\pm 0.1$  log unit. During experiments, the partial pressure of oxygen was controlled to within  $\pm 1$  log unit<sup>1</sup> of the QFM buffer, giving values typical of terrestrial basalts (Sack *et al.*, 1980), by adjusting the ratio of the gases entering the work tube. It should be noted that use of hydrogen-free gases will make the basalt nominally anhydrous, resulting in higher melt viscosity and thus slower dissolution rates than under natural conditions.

The charges were quenched either by removing them rapidly from the furnace to room temperature (quench rate  $\approx 200^\circ\text{Cs}^{-1}$ ), or by dropping them into cold water (quench rate  $> 1000^\circ\text{Cs}^{-1}$ ). The latter was achieved by suspending the Pt wire loop from a 2mm diameter ceramic ring, which in turn was suspended from another piece of Pt wire which could be fused by passing an electric current through it. When this wire fused, the charge would (hopefully) drop straight out of the bottom of the furnace into a waiting jar of water. Some orthopyroxene dissolution charges were quenched in this manner to try to prevent olivine crystallization during cooling, which had been observed in some preliminary runs. Unfortunately, the thermal shock of such rapid quenching severely weakened the charges, often causing them to fragment during sectioning, and necessitating vacuum impregnation with epoxy resin prior to section preparation. With practice, though, charges could be removed from the furnace into air with

---

<sup>1</sup> The partial pressure of oxygen during a run would vary by less than 0.2 log units.

Table 2.3  
Silica glass runs

Run	Final conditions			Run duration		
	temp (°C)	-logfO <sub>2</sub>	δQFM	(hours)	(days)	
72	1126	9.00	-0.20	24.03	1	
69	1127	9.12	-0.08	23.70	1	
71	1127	8.61	-0.59	24.47	1	
70	1127	8.71	-0.49	48.53	2	
61	1123	9.39	0.19	98.78	4	
68	1127	8.89	-0.31	139.43	6	
62	1123	9.14	-0.06	572.23	24	
33	1141	9.09	0.09	5.98	0.25	
34	1142	9.10	0.10	13.20	0.5	
35	1142	9.09	0.09	13.03	0.5	
52	1146	8.62	-0.38	23.67	1	
30	1142	8.99	-0.01	42.43	2	
31	1141	9.00	0.00	70.65	3	
103	1144	8.66	-0.34	95.85	4	
36	1143	9.03	0.03	95.88	4	
102	1144	8.69	-0.31	140.25	6	
63	1145	8.73	-0.27	140.72	6	
104	1142	8.25	-0.75	146.98	6	
38	1143	8.90	-0.10	192.12	8	
67	1144	8.84	-0.16	194.32	8	
105	1142	8.53	-0.47	196.82	8	
37	1143	9.03	0.03	382.08	16	
49	1143	8.49	-0.51	773.70	32	
56	1165	8.20	-0.50	24.70	1	
146	1163	7.83	-0.87	45.90	2	
66	1166	8.60	-0.10	47.92	2	
64	1166	8.74	0.04	49.12	2	
58	1165	8.67	-0.03	69.88	3	
43	1167	8.65	-0.05	69.92	3	
65	1167	8.70	0.00	70.28	3	
55	1166	8.18	-0.52	94.58	4	
44	1167	8.64	-0.06	140.85	6	
57	1164	8.67	-0.03	190.17	8	
42	1175	8.98	0.38	18.52	0.75	no pyroxene rim

Notes:

- 1) Conditions in the furnace immediately prior to the removal of the charge are assumed to be the steady state conditions prevailing during the run.
- 2) δQFM is the difference between log(oxygen fugacity) measured in the furnace and log(oxygen fugacity) of the QFM buffer at that temperature, calculated by the method of Eugster and Wones (1962).

sufficient rapidity to prevent detectable quench olivine growth occurring.

### 2.1.1 Silica dissolution

Experimental details are given in table 2.3.

Initial experiments used spheres of vein quartz<sup>2</sup> tumbled in a grinding apparatus. Subsequently, quartz was replaced by cylinders of silica glass<sup>3</sup> of a standard size, to simplify the preparation of thin sections, and with the following advantages:

- (a) Mechanically rounded quartz grains are not spherical and each exhibits a range of diameters, varying by up to 5% (Donaldson, 1985b).
- (b) The rod has a constant diameter along its length, with the advantage that it does not matter where along the length of the rod the section is made. In contrast, the technique of grinding and periodically measuring the diameter of a quartz sphere during thin section preparation is critically dependent on measuring the exposed section at exactly the widest point.
- (c) As the thin sections are being prepared, the shape of the section through the cylinder will signify when a diameter of the rod has been exposed (§2.3; plate 2a).

---

<sup>2</sup> San Jose Main Vein, Llallagua, Bolivia (Donaldson 1985b).

<sup>3</sup> The pieces of industrially fabricated silica glass rod are 1mm diameter and about 2mm long, broken from a longer piece.

Plate 2

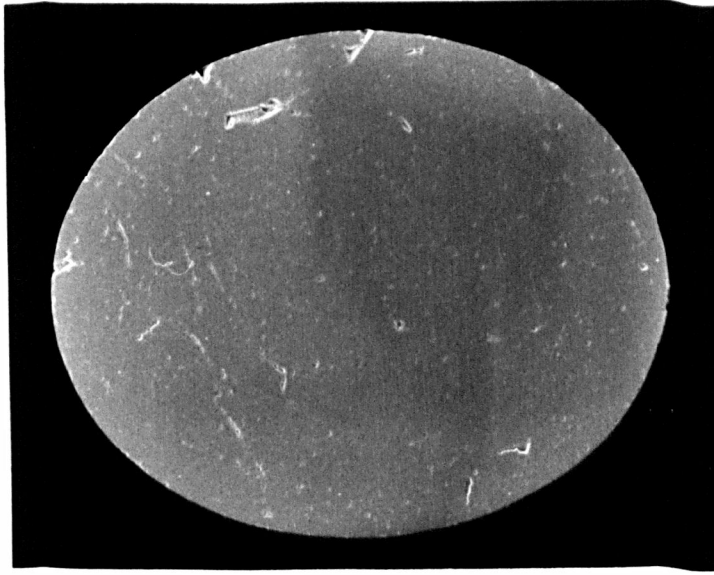
**Backscattered electron images of starting materials.**  
Scale bars are 100 $\mu$ m.

- (a) Typical elliptical section through silica rod mounted in epoxy.
- (b) Enstatite fragment with straight cleavage. Grains of chromite (white), narrow lamellae of chrome diopside (medium grey) and trails of granular chrome pyrope (medium grey) have exsolved along planes which were later bent.
- (c) Bronzite: three different phases have exsolved parallel to the cleavage trace (bottom left - top right). The thin elongate blades of high backscatter coefficient material (white) are spinel. The larger rounded inclusions are striped, and now consist of clinopyroxene (grey) and amphibole (black).

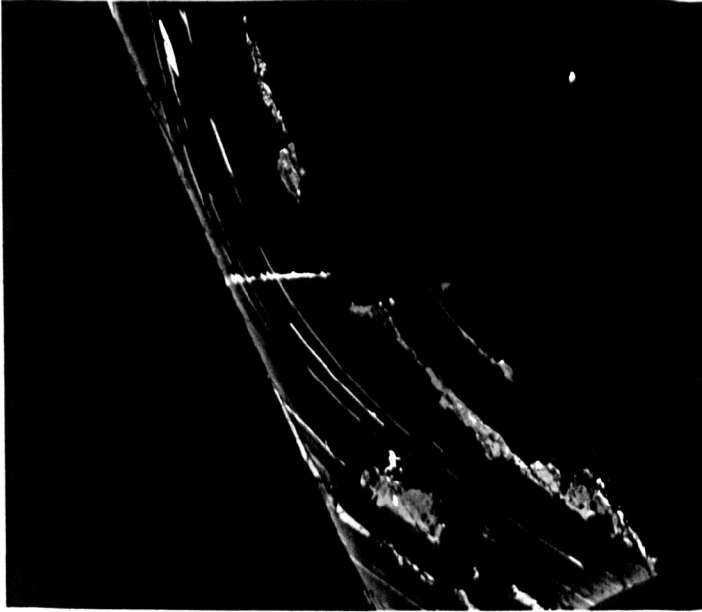
# Plate 2

Backscattered electron images of starting materials.

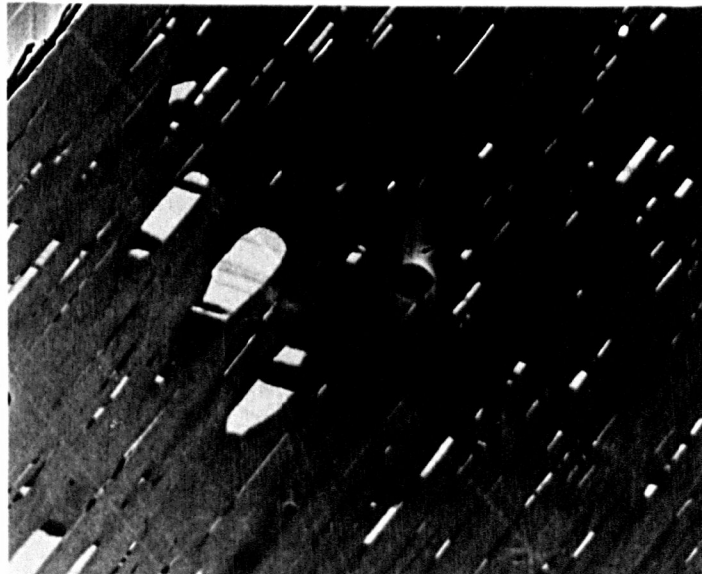
a



b



c



In a superheated basaltic melt, the dissolution of quartz is controlled mainly by transport processes operating in the melt and not by interface reactions, (Kuo and Kirkpatrick, 1985a; Donaldson, 1985b). Under these conditions, the physical state of the silica appears immaterial and the use of silica glass rather than crystalline quartz is believed to be satisfactory.

However, a melt in equilibrium with solid phases (in this case olivine and plagioclase) will be more polymerised than a superheated melt of the same composition. As a result its rheological properties may be quite different, affecting the mechanism of dissolution. If reaction at the interface was the rate-controlling step under these conditions, the nature of the dissolving phase might be important. Here it is assumed that under these conditions silica glass does not behave differently from crystalline quartz. This is supported in §3.2 by the fact that the measured dissolution rate at 1140°C for silica glass is similar to that reported by Donaldson (1985b) for quartz at the same temperature.

### **2.1.2 Cooling-rate experiments**

Controlled cooling of the furnace after a period of isothermal silica dissolution was performed for three experiments (details are given in table 2.4). This was achieved by adding a steadily increasing e.m.f. to the control thermocouple output, as if the furnace was heating up. The additional e.m.f. was supplied by a motor-driven potentiometer (Williams and Mullins, 1976). No attempt was made to maintain a constant oxygen fugacity during cooling; in R51 (1144-908°C) this decreases by 5 log units.

Table 2.4  
Silica dissolution cooling-rate runs.

Run	isothermal			cooling		quench	
	temp (°C)	duration	-logfO <sub>2</sub>	rate (°C/hr)	duration	temp (°C)	-logfO <sub>2</sub>
50	1143	5 days	8.59	0.33	10 days	1063	10.09
51	1143	6 days	8.59	0.4	25 days	907	13.76
53	1145	35 days	8.45	16.3	1 day	957	15.45

### 2.1.3 Orthopyroxene dissolution

The strong cleavages of the pyroxenes made it impossible to fabricate spheres, instead cut pieces or angular fragments of pyroxene were used in the experiments.

In one set of experiments large crystals of enstatite (en<sub>94</sub>) were cut into blocks 1\*1\*2mm, using a fine bench saw. These, however, tended to split easily along cleavage traces, so many of the pieces used were smaller than the intended size. Bronzite<sup>4</sup> (en<sub>78</sub>) was used for the other set of experiments. It had previously been broken into fragments about 1mm long; these were handsorted under a microscope to select approximately cuboid fragments. Both pyroxenes are from the St. Andrews collection. Details of enstatite experiments are given in table 2.5 and of bronzite experiments in table 2.6.

After some preliminary dissolution experiments, it was found to be extremely difficult to determine the orientation of the exposed section with respect to the original crystal, and that this would prevent measurement of post-dissolution crystal sizes (§2.2). Measurements were therefore restricted to the prepared from both halves, with a good chance that each half

---

<sup>4</sup> Following the IMA review of pyroxene nomenclature (Morimoto *et al.* 1988) the name "bronzite" has been discarded and is to be replaced by "enstatite". But, to prevent confusion in this report, the name "bronzite" will be retained to distinguish this composition (en<sub>78</sub>) from the more magnesian enstatite (en<sub>94</sub>).

Table 2.5  
Enstatite runs.

Run	Final conditions			Run duration	
	temp(°C)	-logfO <sub>2</sub>	δQFM	(hours)	(days)
124	1132	8.18	-1.02	74.75	3
88 q	1128	7.92	-1.28	143.98	6
101 q	1132	8.73	-0.47	268.85	11
91 q	1126	8.57	-0.63	480.50	20
115	1154	8.00	-0.90	11.22	0.5
80 q	1149	8.18	-0.72	23.50	1
76	1149	8.11	-0.79	24.23	1
143	1150	8.12	-0.80	72.33	3
74	1150	8.12	-0.78	72.42	3
79	1149	8.24	-0.64	76.20	3
75	1149	8.11	-0.79	143.47	6
110	1172	8.37	-0.23	5.83	0.25
139	1170	9.39	0.79	11.47	0.5
116	1174	7.48	-1.12	11.62	0.5
85 q	1168	7.88	-0.72	22.95	1
78	1169	7.70	-0.90	47.70	2
100 q	1173	8.90	0.30	96.00	4
122	1193	7.57	-0.83	5.70	0.25
121	1194	7.61	-0.79	13.02	0.5
120	1194	7.61	-0.79	22.58	1
136	1190	7.52	-0.88	23.87	1
84 q	1188	7.59	-0.81	24.20	1
130	1191	7.57	-0.83	28.13	1
82	1190	7.55	-0.85	41.58	2
135	1191	7.56	-0.84	48.20	2
145	1191	7.52	-0.88	50.33	2
99	1190	9.10	0.70	54.68	2
119	1192	7.59	-0.81	70.92	3
118	1193	7.58	-0.82	92.10	4

q - charge quenched into water.

widths of reaction rims, and to improve accuracy of these measurements, two or more pieces of pyroxene were put in each charge. The charge would then be cut in half and thin sections prepared from both halves, with a good chance that each half would contain pyroxene fragments, increasing the number of potential measurements from a single run.

The enstatite is pale green, with a well developed cleavage, parallel exsolution lamellae of clinopyroxene and garnet, and

Table 2.6  
Bronzite runs.

Run	Final conditions			Run duration		
	temp (°C)	-logfO <sub>2</sub>	δQFM	(hours)	(days)	
125	1134	8.23	-0.97	46.68	2	
144	1131	8.38	-0.82	93.70	4	
132	1132	8.42	-0.78	143.95	6	
128	1134	7.91	-1.29	185.92	8	
142	1151	8.49	-0.41	9.27	0.4	
114	1153	8.05	-0.85	11.43	0.5	
111	1152	8.63	-0.27	18.95	0.75	no basalt
77	1149	8.09	-0.81	23.62	1	
113	1153	8.09	-0.81	35.33	1.5	
112	1153	8.2	-0.70	48.83	2	
141	1151	9.34	0.44	100.13	4	
108	1172	8.37	-0.23	3.08	0.125	
109	1173	8.38	-0.22	7.30	0.3	
96 q	1171	9.59	0.99	11.57	0.5	
140	1170	9.54	0.94	12.07	0.5	
86 q	1169	7.87	-0.73	24.00	1	
81	1169	7.90	-0.70	24.58	1	
117	1173	7.37	-1.23	46.58	2	
95 q	1171	9.45	0.85	48.50	2	
137	1194	7.52	-0.88	≈0.10		
107	1193	8.27	-0.13	3.47	0.125	
106	1193	8.13	-0.27	6.73	0.25	
94 q	1190	9.09	0.69	15.30	0.5	
93	1191	9.18	0.78	21.92	1	
138	1189	8.24	-0.16	22.00	1	
129	1194	8.29	-0.11	23.93	1	no basalt
123	1194	7.72	-0.68	28.12	1	

q - charge quenched into water.

exsolved chromite grains (plate 2.1c). In some sections the enstatite displays curved exsolution lamellae and straight cleavages, showing that exsolution predates a deformation event which, in turn, preceded cleavage formation. The compositions of enstatite and its exsolved phases are given in table 2.7.

The **bronzite** shows slight pale-green to pale-brown pleochroism and good cleavage. It too has exsolution lamellae parallel to cleavage, but the lamellae are not of constant width along their length, and tend to separate into granules. These are composed mostly of clinopyroxene, but have subsequently exsolved

Table 2.7  
Compositions of pyroxenes and included phases.

	Enstatite	1	2	3	Bronzite	4	5	6
SiO <sub>2</sub>	57.38(18)	42.24(33)	55.44	0.34	52.58(39)	48.37	44.74	0.0*
TiO <sub>2</sub>	-	-	-	-	0.27 (2)	1.62	1.70	-
Al <sub>2</sub> O <sub>3</sub>	0.83 (2)	22.24 (2)	1.86	15.72	4.64(19)	6.31	12.19	58.03
Cr <sub>2</sub> O <sub>3</sub>	0.21 (5)	2.42(12)	1.27	51.27	na	0.41	0.05	6.56
FeO	4.56(12)	7.05(11)	1.62	16.47	13.70(33)	4.62	6.52	20.40
MnO	0.10 (4)	0.35 (3)	0.07	0.21	0.24 (4)	0.09	0.05	0.14
MgO	36.18(46)	20.18(30)	19.26	13.02	27.67(18)	14.23	18.65	13.85
CaO	0.25 (3)	5.05 (5)	18.69	0.08	0.80(20)	23.63	10.15	-
Na <sub>2</sub> O	-	-	1.31	-	-	0.23	2.55	-
	99.51	99.53	99.52	97.11	99.90	99.51	96.60	98.98

Numbers in parentheses denote one standard deviation; hence 0.27 (2) = 0.27 ± 0.02

#### Phases

enstatite (6 analyses), 96.8% quad,  $wo_{0.5}en_{94.2}fs_{5.3}$

1) chrome pyrope (3 analyses),  $py_{72}alm_{14}sp_{1}gr_{6}uv_{7}$

2) chrome diopside, 88.6% quad,  $wo_{40}en_{57}fs_3$

3) chromite,  $sp_{18}herc_{13}mgchr_{40}chr_{29}$

bronzite (9 analyses), 87.7% quad,  $wo_{1.6}en_{78.2}fs_{20.2}$

4) clinopyroxene, 78.5% quad,  $wo_{52}en_{44}fs_4$

5) edenitic hornblende, 79% pargasite, Na-A = 0.71

6) spinel,  $sp_{50}herc_{43}mgchr_4chr_3$ : \* analysis calculated from mixed bronzite-spinel analysis assuming that the spinel contains no SiO<sub>2</sub>.

na - not analysed

amphibole (plate 2c). This appears to be the result of a secondary exsolution event; the first is inferred to be the exsolution of a hydrous clinopyroxene from the bronzite. Exsolved lamellae of clino-amphibole in augite have been documented by Smith (1977). The amphibole will probably decompose first on heating, releasing volatiles that may depress the bronzite solidus. Backscattered electron imaging also reveals thin lamellae of Mg-Fe spinel. The compositions of the host pyroxene and the exsolved phases are given in table 2.7.

Neither pyroxene contains fluid inclusions.

## **2.2 Thin section preparation**

Water quenched samples were vacuum-impregnated with epoxy resin to hold them together, affixed to a microscope slide and ground using 600 grade carborundum to reveal a suitable section. For pyroxene charges the plane of the section was required to pass close to the centre of the crystal, and for charges containing silica rod it was sufficient to reveal an elliptical section of the rod. Sections were finished with 1200 grade carborundum, then glued (with the glass slide still affixed) face down onto another slide with epoxy resin. After setting, the remainder of the charge was ground away, using first the boart and subsequently 600 grade carborundum, until the section was about 100 $\mu\text{m}$  thick, thinned to 50 $\mu\text{m}$  with 1200 grade carborundum and polished with SnO<sub>2</sub> for microprobe analysis. It was realised later that use of SnO<sub>2</sub> adversely affected the quality of the backscattered electron images, after which all samples were polished with diamond paste.

Samples quenched in air were mounted, with known orientation, onto microscope slides using Lakeside cement, then prepared as above. Charges containing more than one piece of pyroxene were first mounted in a block of epoxy resin and cut in half with a 0.5mm bench saw. Each half was ground to expose a suitable section, mounted on a microscope slide with epoxy resin and finished as above.

## **2.3 Measurements of crystal sizes**

Crystals and silica rods were measured before and after experiments to obtain kinetic data for each dissolution system.

Pre-experimental crystal sizes were measured with a binocular microscope and eyepiece graticule, accurate to  $\pm 25\mu\text{m}$ .

The length of rod in silica dissolution experiments was measured only to aid thin section preparation.

Post-experimental measurements were made after a thin section of the charge had been prepared. Each charge was photographed using the backscattered electron imaging (BEI) facility of the microprobe (§2.4.1), and these micrographs were used for the majority of measurements. To check the accuracy of magnification and the scale bars printed on BEI micrographs, a piece of silica glass rod was mounted in epoxy resin, and photographed at ten different magnifications between x40 and x94. Within the errors generated by measuring the scale bar, the BEI agreed on the diameter of the rod, but this diameter was 30 $\mu$ m larger than measured by a microscope graticule scribed every 10 $\mu$ m. This is equivalent to overmeasuring of 3.5% by the BEI.

Along its length, the diameter of the silica-glass rod was found to vary slightly from its nominal diameter of 1mm, but the variance of the diameter of a single piece or even several consecutive pieces does not exceed measurement errors. The diameter of silica rod used for these experiments is 990 $\pm$ 30 $\mu$ m.

The irregular fragments of pyroxene were measured as above and sketched, but it was extremely difficult to ascertain the exact orientation of the pyroxene in a thin section and this prevented calculation of the change in size of the pyroxene fragment during dissolution. This problem is not as significant as it may appear, as there is no development of a glass-rich zone around the pyroxene as in silica dissolution experiments, and the olivine reaction product replaces the dissolved pyroxene volume directly (§5.1.2, §5.2.2).

### 2.3.1 Silica dissolution experiments

Charges were measured to obtain the size of the rod, the width of the pyroxene reaction rim and the width of the glass-rich zone around the rod (§3.2). Knowledge of the orientation of the silica rod with respect to the plane of the thin section is not required, as explained below.

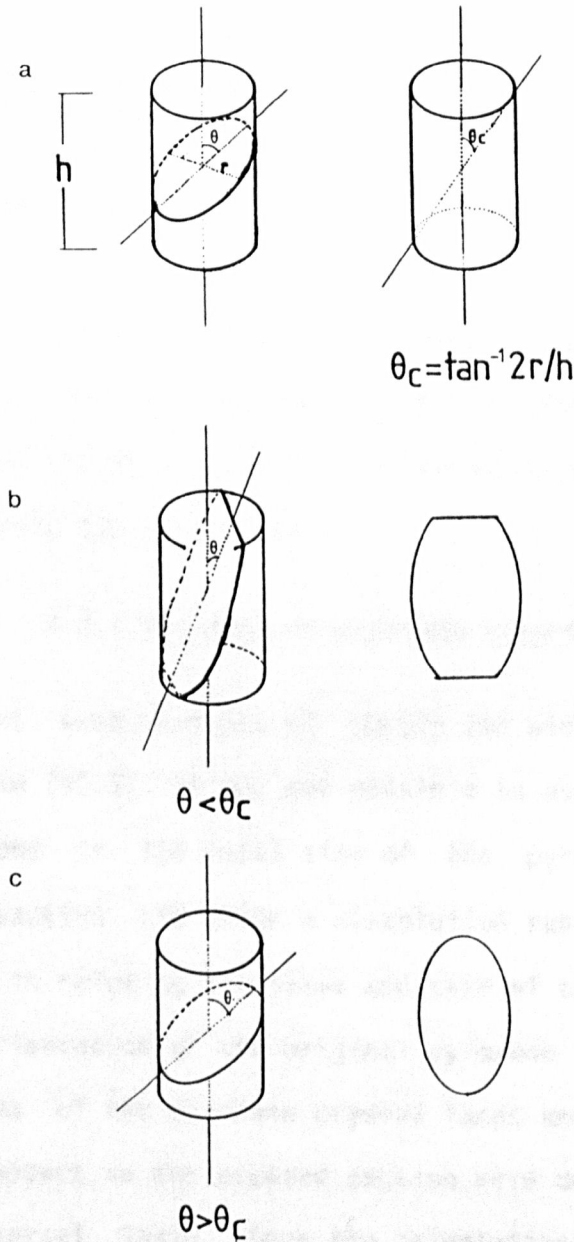
In general, the shape of a section through a cylinder depends on the angle between the plane of the section and the axis of the cylinder ( $\theta$ ) (figure 2.1a). There is a critical value of  $\theta$ , ( $\theta_c$ ), below which any section through the rod will be a truncated ellipse (figure 2.1b). In such a section, careful grinding may expose a section containing the cylinder diameter. Above this critical angle ( $\theta > \theta_c$ ), it is possible to expose a complete elliptical section of the rod (figure 2.1c). The probability of achieving a complete elliptical section from a random plane of sectioning increases with longer pieces of silica rod. Shorter pieces of rod are more likely to yield truncated elliptical sections (figure 2.1b).

During grinding with carborundum, unless the plane of the section is perpendicular to the axis of the cylinder, the first sections through the cylinder will be approximately triangular with two curved sides (fig 2.2a). As sectioning continues, the section will increase in size and the ends of the longer of the curved sides will become parallel and then move together (figures 2.2b,c,d), as an elliptical section is approached. A complete ellipse (figure 2.2e) is the goal in this stage of thin section preparation, but an elliptical section where either or both ends are truncated is also usable.

The principal disadvantage of this method is that the most accurate measurements must be taken in the direction of the semi-minor axis of the ellipse, which is the diameter of the

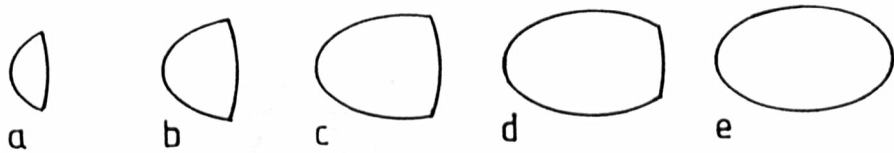
---

Figure 2.1



- a) Elliptical section through a cylinder, with the plane of the section at an angle  $\theta$  to the cylinder axis.  $\theta_c$  is the critical angle separating truncated elliptical sections (b) from complete elliptical sections (c).
- b)  $\theta < \theta_c$ ; exposed section (right) is a truncated ellipse.
- c)  $\theta > \theta_c$ ; exposed section (right) is a complete ellipse.

Figure 2.2



Progressive views of the exposed elliptical section, as seen during section preparation.

---

cylinder. An average value can thus only be obtained from several identical runs. If the eccentricity of the ellipse<sup>5</sup> can be accurately determined then measurements may also be made in the direction of the semi-major axis (the long dimension) and scaled accordingly. However, this introduces additional errors involved with measuring the eccentricity.

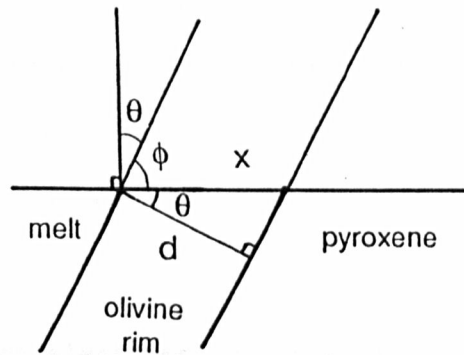
### 2.3.2 Pyroxene dissolution experiments

Charges were measured to obtain the width of the olivine reaction rim (§5.3). It was not possible to ascertain the size of the pyroxene or the total size of the pyroxene crystal and olivine reaction rim after a dissolution run, because of the difficulty in relating the shape and size of the exposed section to the orientation of the original pyroxene crystal (§2.1.4). Orientations of the pyroxene crystal faces and olivine reaction rim with respect to the exposed section were determined by means of a Universal Stage. Once the orientation of a particular crystal face was known, measurements obtained from backscattered electron micrographs were corrected so that the thickness of the

---

<sup>5</sup> The eccentricity of an ellipse is the ratio of its longest and shortest dimensions.

Figure 2.3



Method for calculating actual widths of olivine reaction rims.

$x$  = measured width from compositional images.

$d$  = actual rim width =  $x \cdot \cos\theta$

$\theta$  = orientation angle between edge of pyroxene crystal and perpendicular to section, measured on the Universal Stage.

$\phi = 90^\circ - \theta$

---

olivine reaction rim perpendicular to that particular crystal face could be calculated (figure 2.3).

The accuracy of orientations determined with the Universal Stage is  $\pm 3^\circ$ , but the majority of sections displayed pyroxene faces at a high angle ( $\phi > 35^\circ$ ) to the plane of the section, involving small or negligible angular correction factors. Angles of  $\phi$  greater than  $35^\circ$  introduce a correction factor smaller than 0.9 ( $\approx \cos 35^\circ$ ) and such correction starts to have a detrimental effect on the accuracy of measurements. For some thin sections the angle  $\phi$  was greater than  $60^\circ$  and not measurable with the Universal Stage, necessitating a repeat run at those conditions.

#### **2.4 Electron microscopy and microprobe investigations**

All of the analytical work for this project was carried out using the JEOL 733 Superprobe at the University of St. Andrews, which is equipped to examine X-rays, secondary electrons and backscattered electrons.

### 2.4.1 Electron microscopy

**Secondary electrons** are emitted from the surface of a sample, and describe the surface topography in great detail, but provide only limited compositional information. Since the samples examined were polished flat this facility was not extensively used.

**Backscattered electrons** are incident electrons which rebound elastically off the sample. The intensity of backscattered electrons (the backscatter coefficient, or BSC) is simply a function of the atomic number of the sample. Areas with high mean atomic numbers have high BSC and backscatter more electrons (appearing brighter). If the incident electron beam is rastered across the sample, a video image can be built up and photographed. This technique can be used to resolve phases of differing composition on the surface of a polished specimen as small as  $1\mu\text{m}$ , and to display and highlight zoning patterns within individual crystals (eg Paterson *et al.*, 1989). Operating conditions for backscattered electron imaging (BEI) were 15kV, at 4 or 20nA. Lower currents provide less contrast, but improved resolution at grain boundaries,

### 2.4.2 Chemical analysis

a) Two types of **qualitative scans** were performed. The first, employed mostly to assess zoning in pyroxenes, was a continuous traverse achieved by setting the three spectrometers to the peak positions for the required elements, moving the stage under computer control and measuring the X-ray intensities on a strip-chart recorder. The second, for measuring silica concentration

gradients, involved three element partial analyses<sup>6</sup> (10s peak count and two 5s background counts) at spots every 2 or 5 $\mu$ m along a traverse. Both scans of were operated at 15kV, 20nA.

**b) Quantitative analysis** of major elements was performed (by wavelength dispersive spectrometry) on a representative selection of experimental charges, to determine glass and mineral compositions. Operating conditions were 20nA at 15kV. Minerals were analysed with a 1 $\mu$ m beam spot, glasses either with the 1 $\mu$ m beam spot or with the beam rastered over an area 25-100 $\mu$ m<sup>2</sup>. The raster method was used for glass analyses in compositionally uniform areas to prevent migration of Na, but analyses in a compositional gradient were obtained with the spot, as measurement over a larger area would obscure the detail of a gradient. The standards used for analysis are given in table 2.8 and were counted for 60s peak (30s for Na, K) and 10s background. Unknowns were counted for 20s peak and 5s background. All microprobe analyses obtained are contained in appendix 2.

Table 2.8  
Microprobe standards.

Element	Standard	Detection limit (wt%)	Typical 2 $\sigma$ error	
			in opx.	in ol.(wt%)
Si	Wollastonite	0.02	0.33	0.28
Ca	Wollastonite	0.02	0.10	0.06
Ti	Rutile	0.03	0.08	0.06
Al	Corundum	0.01	0.09	0.03
Fe	Fe metal	0.04	0.37	0.43
Mn	Ferrite	0.04	0.08	0.08
Mg	Periclase	0.01	0.24	0.30
Na	Jadeite	0.03	0.10	-
K	Orthoclase	0.03	0.10	-
Si, Mg	Olivine fo <sub>90</sub>		(olivines only)	

<sup>6</sup> Data used were in the form of raw count values. No ZAF correction was applied to this data.

### 2.4.3 Quality control of microprobe analysis

Generally, analyses with totals outside the range 98.5-101% were discarded, unless they were of glass, biotite or amphibole, where the presence of volatiles would lower the measured total.

Specifically, **pyroxene** analyses were run through a computer program to calculate their structural formula (Papike *et al.*, 1974), testing five criteria before accepting an analysis. These are:

- (i) total cations (Si+Al<sup>IV</sup>) on the tetrahedral site (per six oxygens) =  $2 \pm 0.02$
- (ii) octahedral cations (Al<sup>VI</sup> Ti Fe<sup>III</sup> Fe<sup>II</sup> Mg Mn Cr) > 0.98 (to fill the M1 site)
- (iii) octahedral cations on M2 (left over from (ii)) + Ca  $\leq 1.01$  (typically <2%, Nelson and Carmichael, 1973).
- (iv) total cations on M2 =  $1 \pm 0.02$
- (v) residual (excess charge after allocating some Fe to Fe<sup>III</sup> to minimise cation charge imbalance) < 0.001. Most pyroxene neocrysts in the silica dissolution experiments failed solely on this criterion (possibly due to vacancies in the crystal structure), so this was relaxed to < 0.01.

**Olivines** were tested by a computer program which simply calculated total cations per four oxygens. If this was outside the range  $3 \pm 0.02$  the analysis was discarded. Due to problems finding suitable standards for olivine analysis, some totals approach 102%. If such analyses met the total cation requirement

\* Fractionation density is defined as the ratio of molecular weight to molar volume of the chemical components in the liquid phase that are removed by fractional crystallization (Sparks and Huppert, 1984), that is, the mol/equivalent density of the crystalline phase.

and were obviously not olivine-glass mixes<sup>7</sup>, they were retained.

**Amphiboles** were tested by a computer program similar to the pyroxene program (Papike *et al.*, 1974).

## 2.5 Calculation of melt properties from microprobe data

### 2.5.1 Density calculations

Densities of melts and fractionation densities<sup>8</sup> of crystalline phases are calculated from microprobe data by the empirical method of Bottinga and Weill (1970), using partial molar volume and thermal expansion coefficient data from Nelson and Carmichael (1979). The data of Bottinga *et al.* (1982) are used to calculate the partial molar volume of Al<sub>2</sub>O<sub>3</sub>, which is composition dependent. Other oxide partial molar volumes are assumed to be independent of composition within experimental accuracy (typically <<2%, Nelson and Carmichael, 1979).

There are a number of errors associated with the determination of density in silicate melts which arise from experimental uncertainties in calculating partial molar volumes, from inaccuracies in sample analyses, and from uncertainties concerning the oxidation state of iron. Sparks and Huppert (1984) computed standard 2 $\sigma$  errors for calculated densities of basalts as being around 1%. Comparison of calculated and measured densities indicate that density calculations on common basaltic melts have an accuracy of about 0.5%.

---

<sup>7</sup> Al and Ti in an olivine analysis are good indicators of olivine-glass mixture within the electron excitation volume.

<sup>8</sup> Fractionation density is defined as the ratio of molecular weight to molar volume of the chemical components in the liquid phase that are removed by fractional crystallization (Sparks and Huppert, 1984), that is, the melt-equivalent density of the crystalline phase.

## 2.5.2 Viscosity calculations

Viscosities of melts in the experiments were calculated from microprobe analyses of glasses by the empirical method of Shaw (1972). Values predicted by this method are in close accord with laboratory measurements, at least for low pressures, low water contents and temperatures above the liquidus, where basalts behave as Newtonian fluids (McBirney and Murase, 1984). Addition of about 3 wt% water decreases viscosity of a highly polymerized liquid such as andesite by about 2 orders of magnitude at 1150°C (Shaw, 1963). However, because this method was constructed for crystal-free melts, corrections may be required to adjust for the presence of gas bubbles or suspended crystals, which increase the effective viscosity of a crystal-liquid mixture.

The effect of crystal content on the viscosity of a crystal-rich magma is commonly estimated from the Einstein-Roscoe equation, but large differences are encountered between predicted and measured viscosities (Marsh, 1981). This equation assumes that the suspended solid fraction has no physico-chemical relationship to the host liquid, which is obviously not the case for magmas where crystals nucleate and grow during cooling. Measured viscosities, either obtained in the field or in a laboratory, usually increase as the melt remains at subliquidus temperatures for increasing periods of time (eg Scarfe, 1973). Most of this increase is attributable to crystal growth, but part may be due to ordering and polymerization of the liquid. In addition, the rheological behaviour of partially crystalline basalts agrees well with the Bingham model of fluids, and becomes increasingly non-Newtonian with increasing crystal contents (Shaw *et al.*, 1968; Shaw, 1969).

In consequence, it is to be expected that the viscosity of

melt in equilibrium with crystalline phases at constant temperature will increase with time. For this study, the viscosity value required is that of a melt, rather than that of a crystal-liquid mixture, since crystals around a dissolving phase do not appear to move. It is, however, difficult to measure the viscosity of a liquid in equilibrium with crystals, in contrast to the viscosity of a crystal-liquid mixture. Existing methods of viscosity calculation developed for superliquidus melts and corrections for partially crystalline mushes may not be applicable at subliquidus temperatures, and the viscosity values calculated for use in this study should be treated with healthy scepticism. The relative differences between values calculated for similar temperatures at similar crystal contents should still be valid.

## **2.6 Projection of melt and crystal compositions**

Glass (melt) and crystal compositions were projected using the modified CMAS projection scheme of O'Hara (1968) for multiply saturated liquids (Grove and co-workers; 1984, 1982); see figure 3.15. All iron in the glass was taken to be  $Fe^{2+}$ . Analyses were recalculated in terms of the molar mineral components olivine, clinopyroxene, quartz, plagioclase, orthoclase and spinel (Grove *et al.*, 1982). This six component system is simplified by projection from orthoclase and spinel into the tetrahedron ol-cpx-qz-pl. Field boundaries were constructed using data from plagioclase-saturated experimental liquids (see figure 1 of Grove and Baker, 1984). The molar components of the projection were multiplied by the number of oxygen atoms in each mineral component and renormalized, as the oxygen projection enhances volume relations among phases and coexisting liquids (Grove *et*

al., 1983). Finally, compositions are projected from plagioclase into the pseudoternary ol-cpx-qz.

The topology of the pseudoternary is similar to that of the system fo-di-qz (Kushiro, 1972), with the exception of the absent protoenstatite field. The most important difference is that this projection removes the effect of variable plagioclase content on projected liquids in ol-cpx-qz. The effects of Fe-Mg and Ca-Na variations in phases are also suppressed.

Melt compositions can be used to predict the pyroxene polymorph with which they would be in equilibrium. Projected melt compositions lie in all three pyroxene fields determined by Grove and Baker (1984), shown by figure 3.15.

## 2.7 Pyroxene thermometry

Three models for pyroxene thermometry are applied to natural examples of pyroxene-bearing reaction textures (eg around quartz), enabling the temperatures at which the reactions occurred to be estimated.

In the past fifteen years, several different thermometric models have been presented in the literature. Early models (eg Wood and Banno, 1973; Wells, 1977) assumed ideal mixing of  $Mg_2Si_2O_6$  over the opx and cpx phases and calibrated this against available data for the diopside-enstatite miscibility gap. Wells (1977) pointed out that the large entropy change for  $Mg_2Si_2O_6^{cpx} = Mg_2Si_2O_6^{opx}$  demonstrated the inadequacy of this assumption, but the model fitted the available data over quite a wide temperature range. Improvements in solution models for the di - en join have since rendered these thermometers obsolete (Turnock and Lindsley, 1981; Lindsley, 1983). Later models (Lindsley, 1983; Saxena, 1983; Davidson, 1985) assumed non-ideal but disordered site

models, which require experimental data on site occupancy in pyroxenes and/or phase equilibrium of coexisting pyroxenes.

Inaccuracies generated by these models are due to some combination of the inapplicability of the models used, inaccuracies in measuring phase compositions, and disequilibrium in experimental products or in natural assemblages.

Most two-pyroxene thermometers have been derived for pyroxene pairs whose compositions plot near the di-en-fs-hd quadrilateral ( $w_o + e_n + f_s > 90\%$ ) and do not account for the effects of non-quadrilateral components. A (mainly empirical) projection scheme for approximating the activities of  $w_o$ ,  $e_n$  and  $f_s$  components in natural pyroxenes is given by Lindsley (1983), permitting use of quadrilateral phase relations for thermometry.

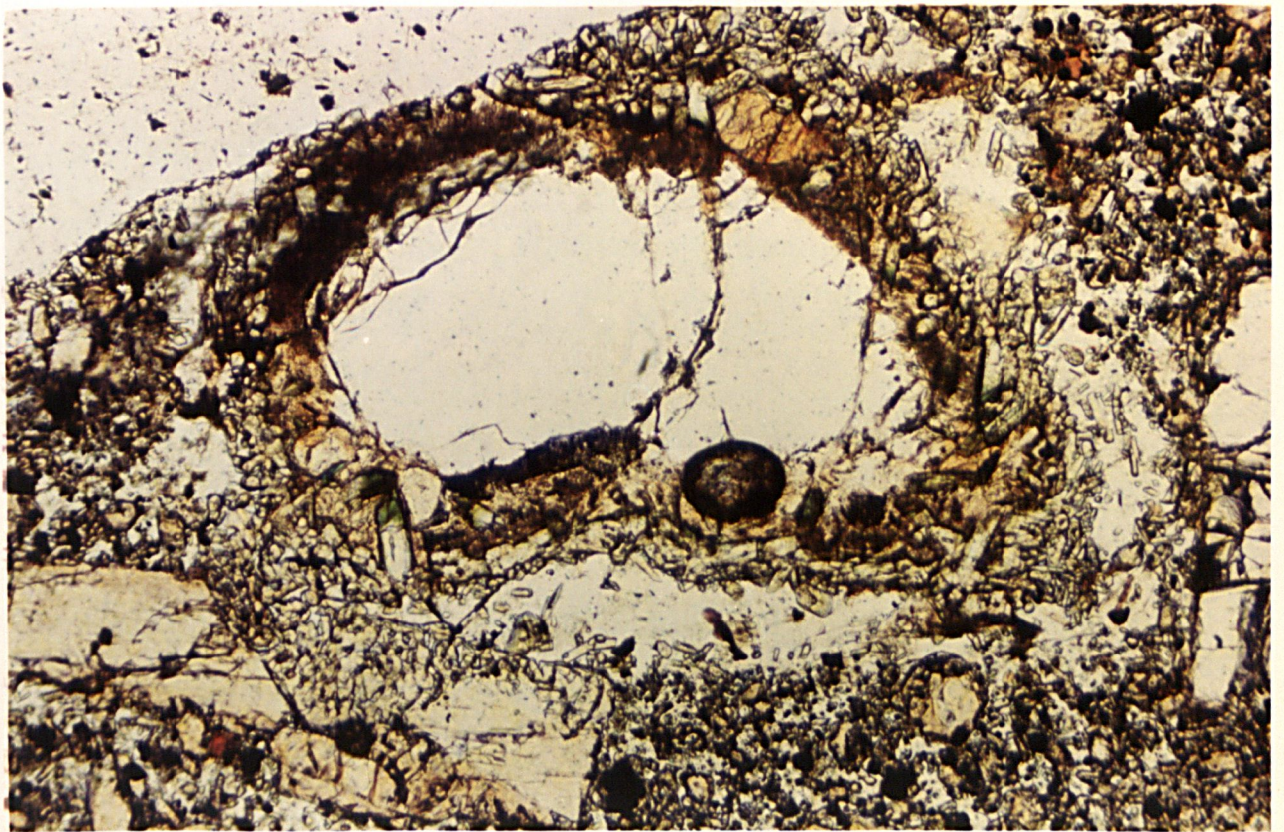
In this work, temperatures of pyroxene crystallization are estimated using the two-pyroxene graphical thermometer of Lindsley (1983), the solution model of Davidson (1985) with isotherms from Nabelek *et al.* (1987), and the two-pyroxene thermometer of Saxena *et al.* (1986). These may also be used to estimate minimum temperature for augite that does not coexist with orthopyroxene. Data were corrected for non-quadrilateral components by the method of Lindsley (1983).

Estimated uncertainties for the method of Lindsley (1983) are about  $\pm 50^\circ\text{C}$  for pyroxenes with low contents of non-quadrilateral components. Of this,  $20\text{--}30^\circ\text{C}$  is from placement of isotherms and  $20\text{--}30^\circ\text{C}$  from errors in composition. Correction for (projection from) non-quadrilateral components will introduce additional uncertainties that will generally be proportional to their content, but are difficult to quantify. Errors for the thermometers of Saxena *et al.* (1986) and the model of Davidson (1985) are typically  $\pm 30^\circ\text{C}$ .

**Frontispiece two**

- a) H100428 Embayed quartz rimmed by pyroxene and glass.
- b) BM16 Rounded quartz rimmed by aegirine-augite and glass.

Each quartz is about 1mm across.



## Chapter three

### The experimental dissolution of silica

Part of this project is an experimental investigation of the kinetics and resultant textures of quartz dissolution into basalt under subliquidus conditions, in order to understand the textures shown in frontispiece two. Here the results of these experiments are reported, investigating the dissolution of silica glass, the growth of pyroxene neocrysts, the influence of buoyancy and surface tension on melt transport, the chemistry of glasses and their relationships to the crystalline phases present. Chapter four examines the petrography of some natural samples, and compares their textures with those produced in these experiments.

This chapter is split into three sections which deal with the petrography, the kinetics, and the phase relations of the experimental system investigated.

#### 3.1 Petrography

##### **3.1.1 General features of experimental charges**

Plate 3.1 shows examples of sections through silica dissolution charges after a variety of run durations and temperatures, including cooling rate experiments. Many of the charges are cracked, resulting from shrinkage during quenching. From the plate it can be seen that dissolution of silica into this partially molten basalt leads to the crystallization of a reaction rim of pyroxene. With increasing time this fringe of pyroxene enlarges and a glass-rich zone (free of crystals) develops around the silica.

Due to the small sizes of crystals in these experiments (<100 $\mu$ m), both remnant from partial melting and newly nucleated,

Plate 3.1  
Photomicrographs of quartz dissolution charges.  
Scale bars are 1mm.

(a) R30 (1142°C for 2 days) Silica rod sectioned nearly perpendicular to its axis, giving an elliptical section. The glass-rich zone and pyroxene fringe are quite well developed, while the surface of the rod is noticeably cusped near vesicles. The rod contains two cracks filled by basalt glass (formed prior to cooling), one across the top left portion of the rod section, and the other almost vertical on the right hand side. Tiny pyroxene needles have crystallized in the latter.

(b) R36 (1143°C for 4 days) The silica rod has broken the surface of the charge (right), forming a large bump on the surface of the rod. Acicular pyroxenes are present at the edge of the groundmass (top centre, bottom centre).

(c) R105 (1142°C for 8 days) One end of the silica rod (top) has undergone extensive crystallization to form "curved crack" domains (see §3.1.5).

(a), (b) and (c) show the evolution of the reaction texture with time. The silica rod becomes smaller, while the pyroxene neocrysts grow longer and thicker. Any crystal still present in the glass-rich zone dissolve out.

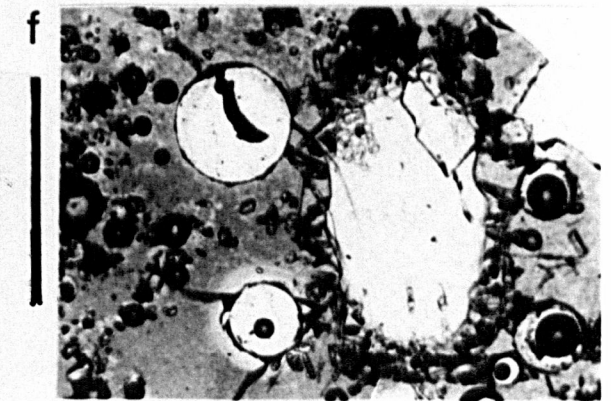
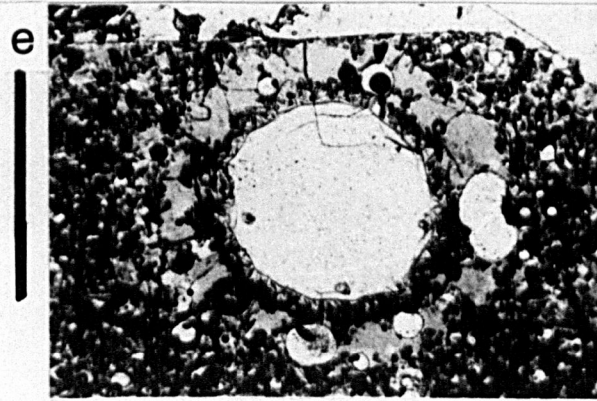
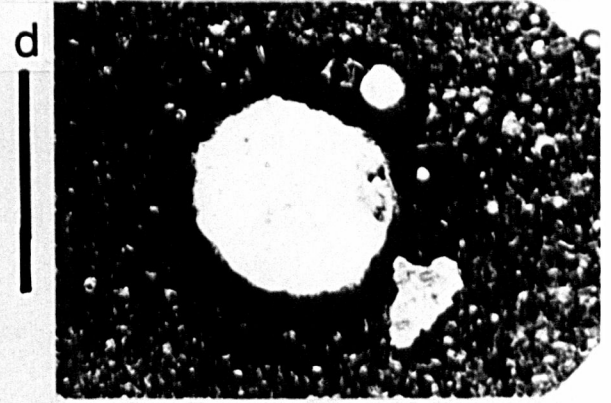
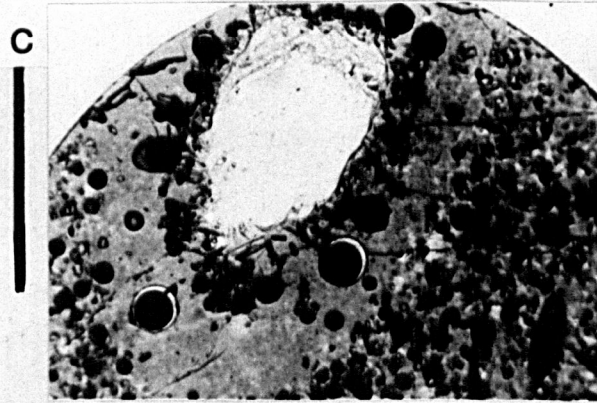
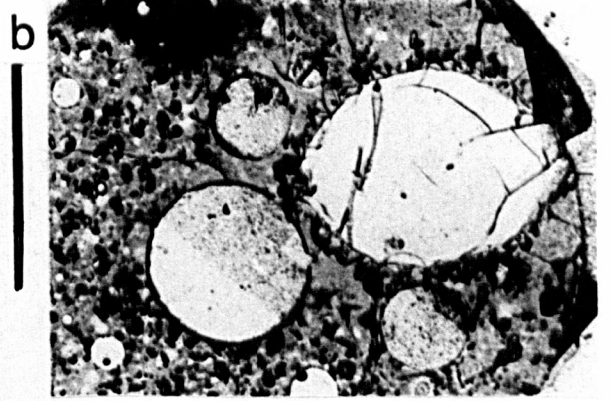
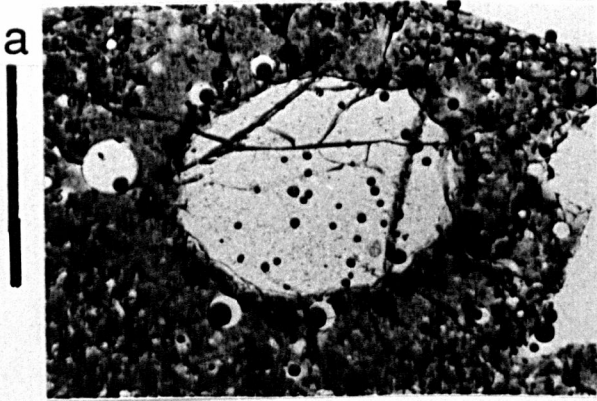
(d) R51 (cooling-rate experiment quenched at 907°C) The glass-rich zone around the silica has become opaque, after immiscibility resulted in the formation of tiny droplets of iron-rich glass. Large, radial pyroxene prisms are visible.

(e) R62 (Also plate 3.2a) (1123°C for 24 days) The pyroxene fringe is dense at its outer margin, with a larger fraction of glass near the enclosed silica. Around the fringe is a well developed glass-rich zone.

(f) R57 (1164°C for 8 days) At higher run temperatures the rod is more cusped and irregularly shaped. Pyroxene growth is also coarser than in 1120°C runs (cf (e)), with fewer and larger crystals.

# Plate 3.1

Photomicrographs of quartz dissolution charges.



most of the petrography was accomplished using backscattered electron imaging (BEI). Examples of sections through typical 1120°C and 1140°C charges are shown in plate 3.2. Definitions of the terms **fringe**, **glass-rich zone** and **groundmass** are given in the figure caption.

The degree of melting of the basalt is steady after six hours at 1140°C. This is in agreement with Donaldson (1985b), who reports 1-3 hours for equilibrium partial melting at this temperature. In 1120°C experiments, the degree of partial melting is low ( $\approx 30\%$ ; plates 3.1e, 3.2a) and charges retain their initial cylindrical shape. Charges run at 1140°C have undergone considerably more melting (50-60%; plates 3.1a,b,c, 3.2b) and become spherical, suspended from the Pt wire loop by surface tension (Donaldson *et al.*, 1975a). The 1160°C experiments have undergone almost complete melting ( $> 90\%$ ; plate 3.1f).

In the groundmass of 1140°C and 1160°C charges, partial melting results in rounded grains of olivine and plagioclase surrounded by melt. In shorter runs some of these grains still display evidence of their initial fragmental shape. In longer runs olivines are well rounded, but plagioclase crystals have evolved from fragmental shapes to become equant and euhedral.

Close to the silica rod, the crystal content of the groundmass decreases with increasing time, due to diffusion of silica into the groundmass causing further dissolution of remaining crystals and exaggerating the degree of melting.

In 1120°C charges the groundmass contains residual, rounded augite and euhedral, equant pigeonite, which has overgrown both augite and olivine (and is visible in the shortest runs at this temperature (1 day)). The euhedral morphology of this groundmass pigeonite strongly suggests that it has grown during partial

Plate 3.2

Compositional images of quartz dissolution charges.

Scale bars are 100 $\mu$ m.

- (a) R62 (24 days at 1123°C) Around the silica rod (dark grey, centre) is a reaction rim, or fringe, of pyroxene neocrysts (light grey) embedded in glass (medium grey). The outer limit of the fringe is deemed to be the thin band of equant, granular pyroxenes just inside the vesicles. Outwith the fringe is the glass-rich zone, containing a few well-rounded olivine and pyroxene grains in glass, and large (200 $\mu$ m) vesicles. The glass-rich zone extends out to where plagioclase (dark grey) becomes common. The groundmass is the part of the charge apparently unaffected by silica dissolution, and is composed of plagioclase (dark grey), olivine (light grey) and glass (medium grey). Rare pigeonite needles are present at the edge of the groundmass. Note that vesicles may be absent in the fringe, and larger in the glass-rich zone than in the groundmass.

The literature on reactions is confused by the use of various synonyms. The term corona is equivalent to the combined fringe and glass-rich zone, while the terms reaction rim and corrosion border are equivalent to the fringe.

- (b) R67 (8 days at 1144°C) Silica rod (dark grey, centre) surrounded by melt (medium grey) and pyroxene (light grey). At the edge of the image is the groundmass, composed of plagioclase grains (dark grey) and rounded olivines (light grey). In the lower half of the image several melt-filled cracks are visible traversing the lower half of the rod. These are associated with a region characterised by slightly lower backscatter coefficient and curving cracks. Some recrystallization to acicular tridymite has occurred within these cracks.
- (c) R51 (as plate 3.1d). This charge contains many zoned pyroxene and olivine grains (medium grey). Euhedral plagioclase crystals (dark grey) in the groundmass are normally zoned.
- (d) R51 (as (c), plate 3.1d). The zonation of pyroxene from pigeonite cores to augite overgrowths is abrupt and, compared to the cores, the overgrowths have quite complicated growth shapes. Between plagioclase crystals are areas of fine acicular plagioclase needles and liquid immiscibility droplets (white). Slight recrystallization along the margins of the silica rod is evident by its irregular outline, although the irregularities are no more than 5 $\mu$ m in size. Small (15 $\mu$ m) feldspar spherulites (bottom left) also appear to have nucleated on the rod surface, radiating out into the matrix.

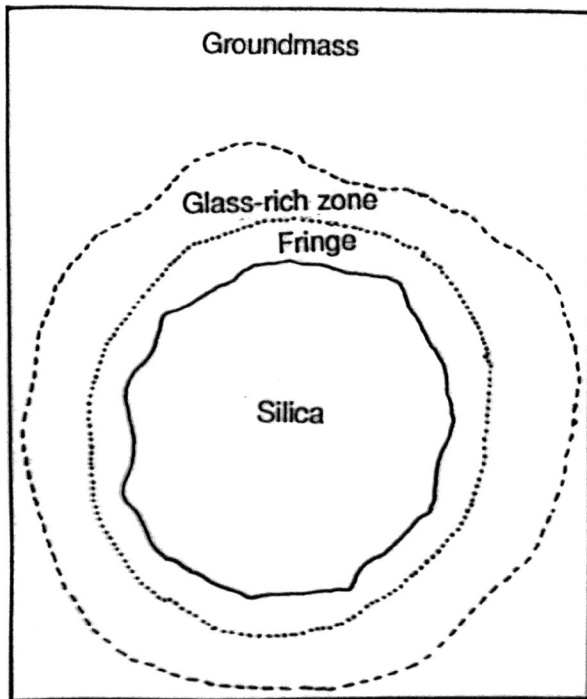
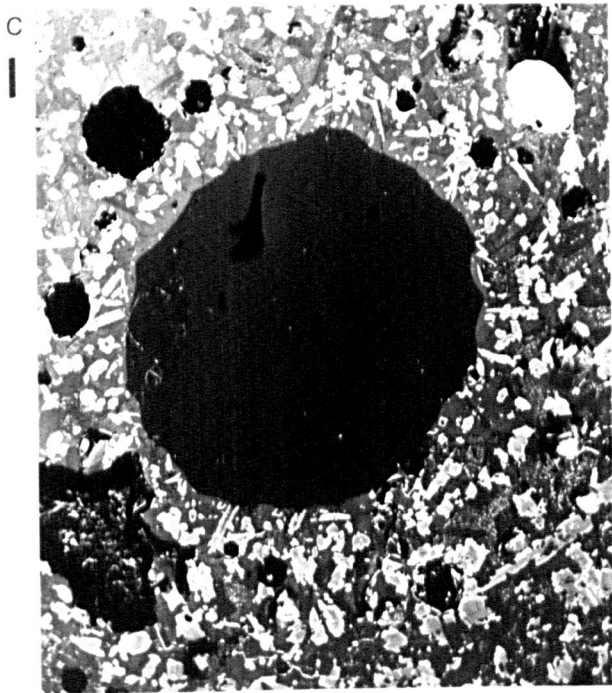
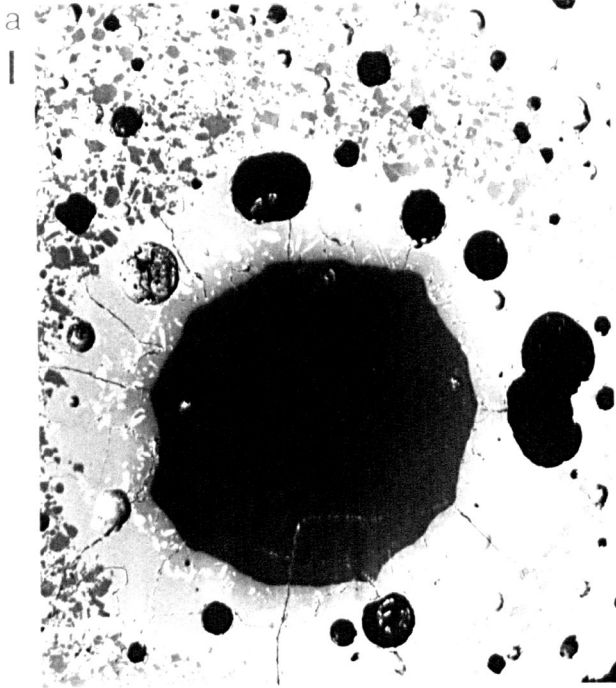


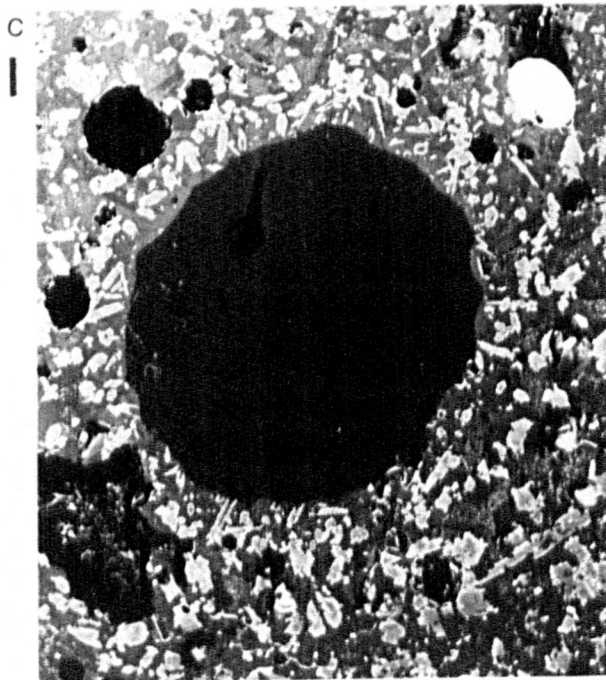
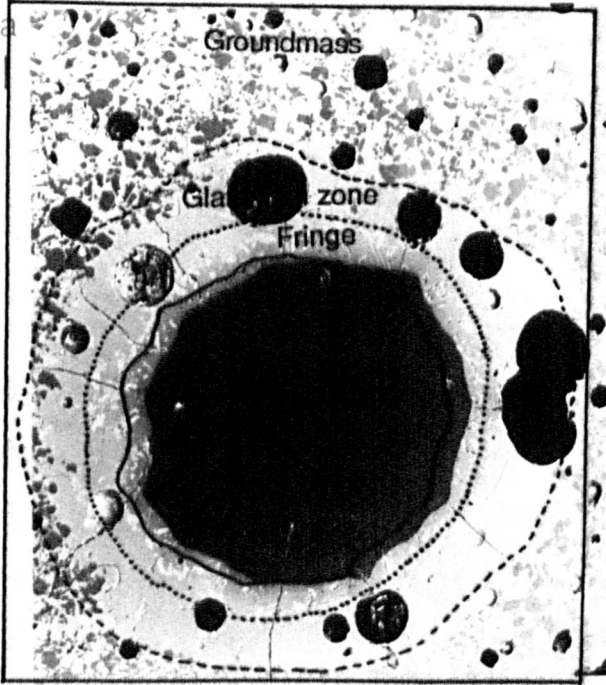
Plate 3.2

Compositional images of quartz dissolution charges.



# Plate 3.2

Compositional images of quartz dissolution charges.



melting of the basalt and is thus a stable groundmass phase, although it was not present in the original basalt. Pigeonite is not present as a crystalline phase in Servilleta basalt of the Taos Plateau (appendix A12; Basaltic Volcanism Study Project, 1981). Its presence in the experiments may be due to differences in composition between the melt that exists during partial melting, and that which existed during crystallization. Alternatively, kinetic effects (eg suppression of nucleation) may have prevented pigeonite crystallization during natural cooling (eg Grove and Bryan, 1983). No pyroxene is found in the groundmass of 1140°C and 1160°C charges, supporting the proposed pyroxene liquidus for the Servilleta basalt at about 1133±5°C (Lofgren, 1983). To test whether crystallization of pigeonite in the groundmass and glass-rich zone is a result of silicification, one charge (R102) was run for six days at 1144°C without any silica rod. No pigeonite was developed.

In all but one experiment (R42: 18 hours at 1175°C,) pyroxene neocrysts are found close to the dissolving silica rod, even in runs as short as six hours at 1140°C. With increasing time these develop into a fringe of acicular crystals and melt surrounding the rod (eg plate 3.2a).

New pyroxene has overgrown particles of augite or olivine in the basalt, or nucleated on the surface of the rod with apparently no consistent orientation (plate 3.3a). Pyroxene overgrowth on olivine or augite is more common in lower temperature runs (1120°C; plate 3.3a), where dissolution of these phases close to the rod is slower. Very small pyroxenes also nucleate on the rod within melt-filled cracks across the rod (plate 3.1a).

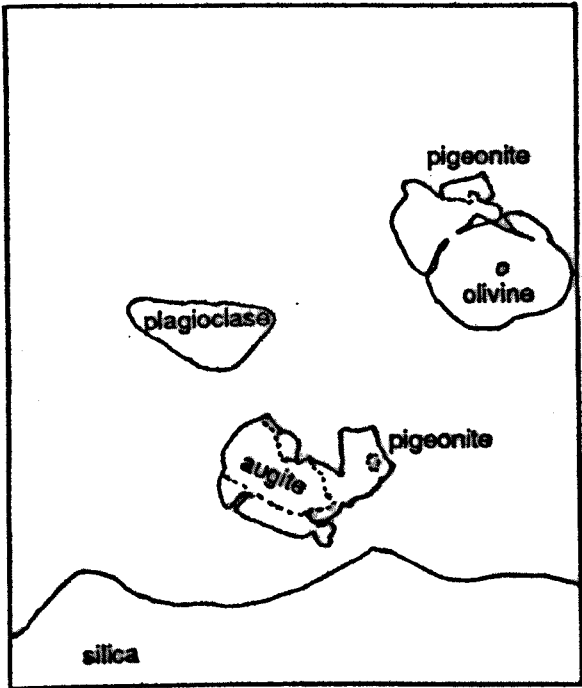
All charges show a locus of highest pyroxene density

Plate 3.3

Compositional images of pyroxene neocryst morphologies.

Scale bars are 100 $\mu$ m.

- (a) R71 (1 day at 1127°C) Plagioclase grains (dark grey) exhibit rounded corners, olivine (light grey) is well rounded, while pyroxenes consist of irregular augitic cores (light grey) with euhedral pigeonite overgrowth (medium grey) (eg below centre, near the rod), as well as euhedral pigeonite crystals. Olivine, at the edge of the groundmass (right centre), may be partly overgrown by pigeonite. Close to the silica (bottom), pigeonite exists as small skeletal neocrysts, with cusps on the surface of the silica adjacent to concentrations of pyroxene crystals.
- (b) R62 (24 days at 1123°C) Hollow or skeletal crystals have well formed external faces and irregular or rounded internal faces. The pyroxene at the top has a small (10 $\mu$ m) olivine core. Pyroxenes further from the rod are slightly rounded and mutually attached. The black object at the top right is part of a vesicle.
- (c) R67 (8 days at 1144°C) Skeletal pyroxene crystal with well-formed external faces and irregular rounded internal faces, enclosing an "island" of silica, with extremely bulbous margins. The rod displays a slight cusp near the pyroxene. At the bottom left is the end of a melt-filled crack running through the rod. The margins of the silica along this crack are slightly bulbous, in contrast to the outer surface of the rod (horizontal in this image).
- (d) R57 (8 days at 1164°C) Skeletal and hollow pyroxenes, some including silica, some including melt. Note that melt inclusions have varying backscatter coefficient implying differing melt compositions, and that the silica inclusions have bulbous margins.



# Plate 3.3

Pyroxene neocryst morphologies.

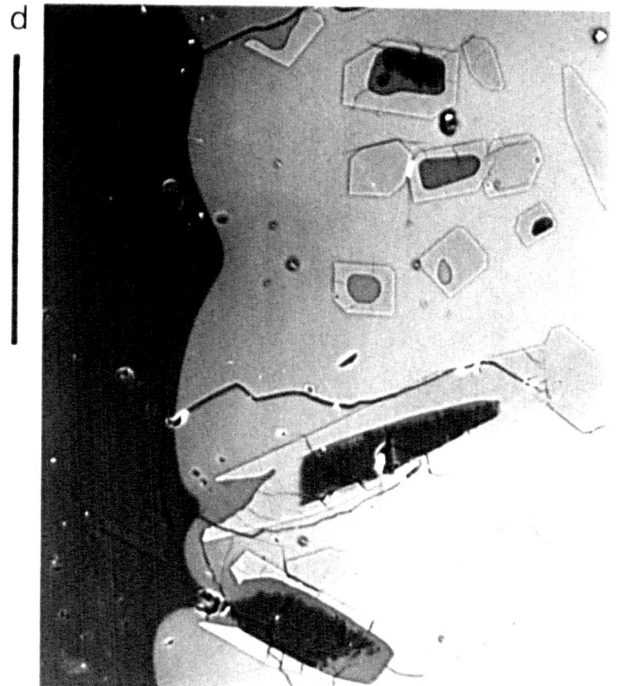
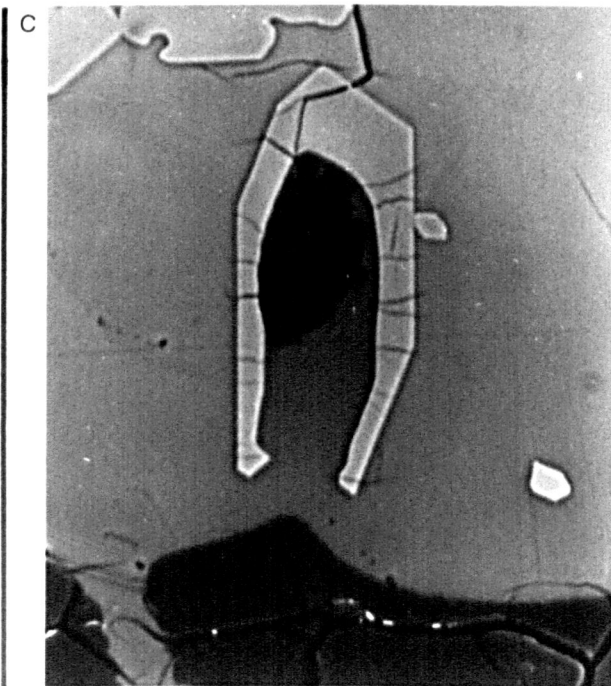
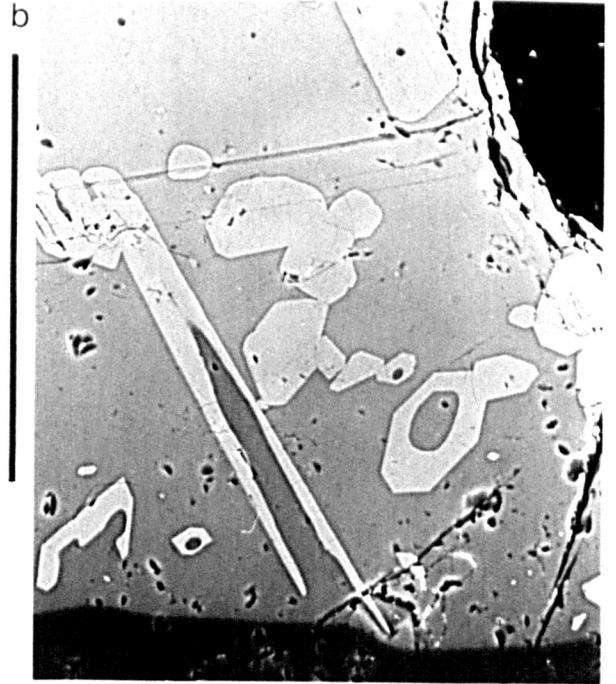
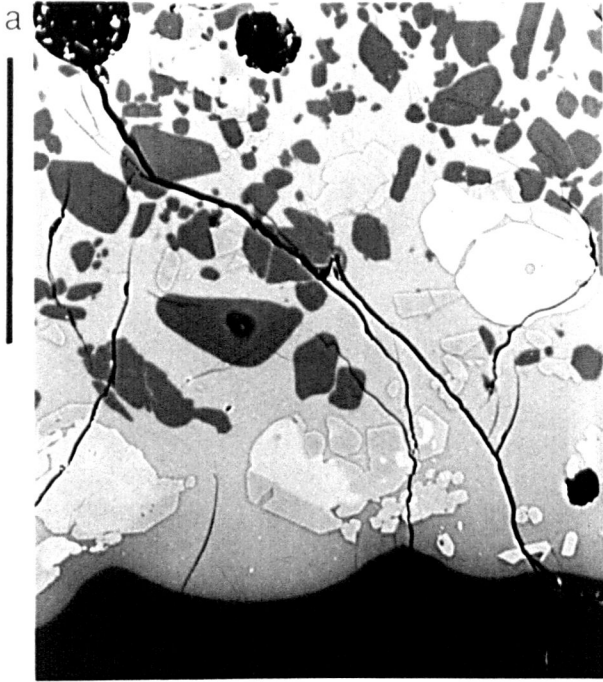
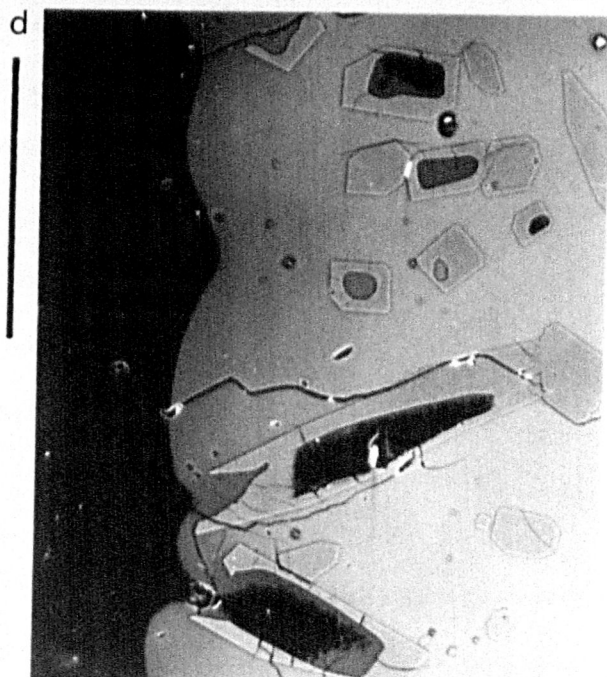
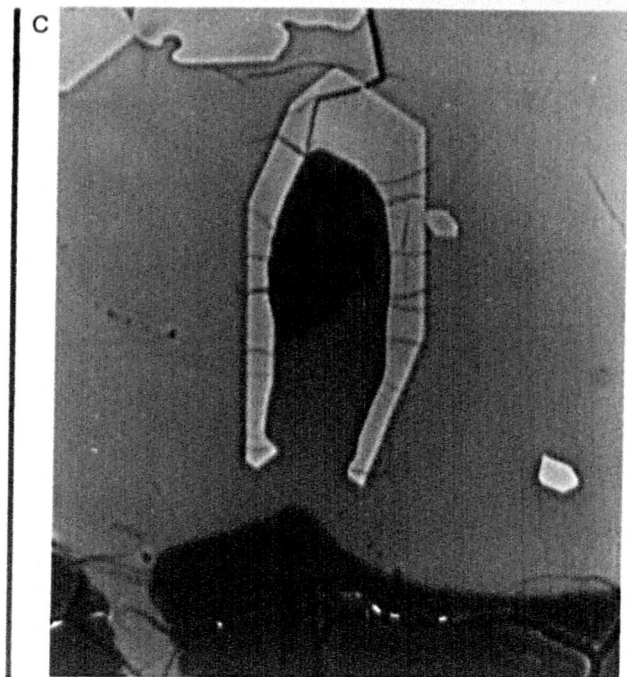
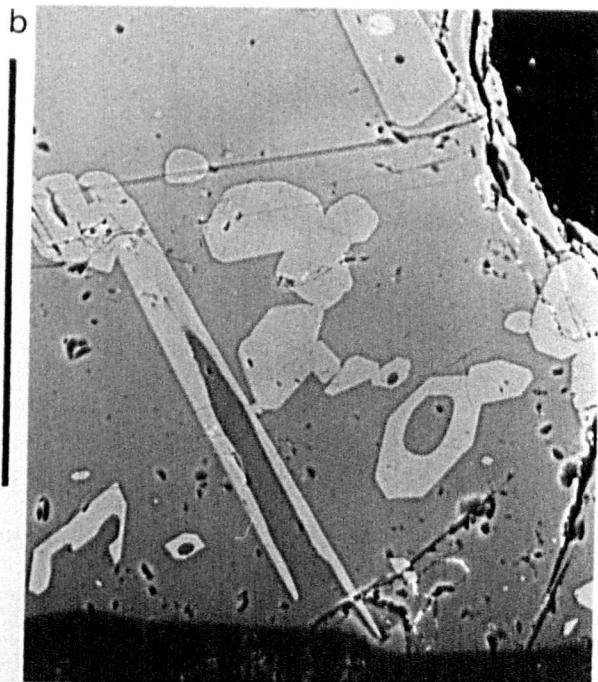
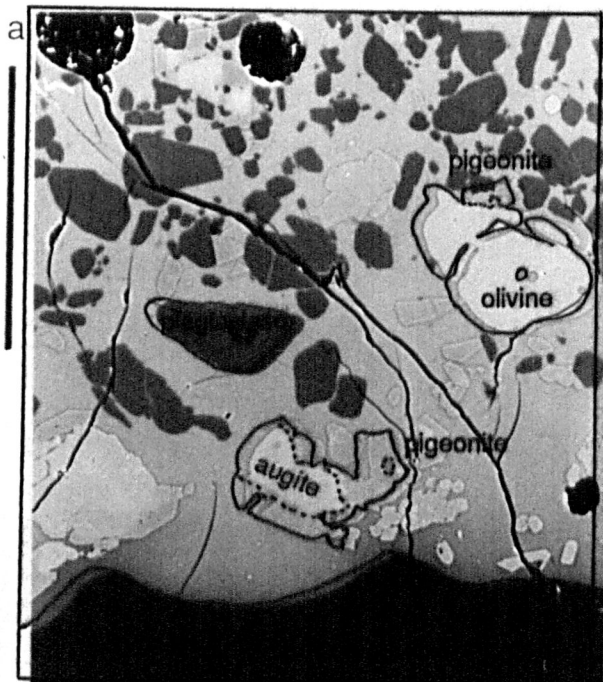


# Plate 3.3

Pyroxene neocryst morphologies.



(number of grains per unit volume) at the outer edge of the fringe that corresponds to the original limit of the rod. Both inside and outside this locus the density of crystals is lower, indicating a reduced nucleation rate. The high initial nucleation rate is due to surface imperfections on the rod and the presence of suitable substrates (augite and olivine) in the groundmass, but diminishes as imperfections on the rod surface are dissolved and original augite and olivine are either dissolved or overgrown by new pyroxene.

In 1140°C and 1160°C charges, new pyroxene is initially only found adjacent to the rod, having nucleated either on the rod or on nearby remnants of olivine or augite, since these run temperatures are above the pyroxene liquidus. In longer runs, large (100µm) equant or prismatic pigeonites are also found in the glass-rich zone and at the edges of the groundmass.

Pigeonite crystallizing in short runs (1-2 days) has well-developed crystal faces, compared to the well-rounded olivine and augite grains, and to the irregular cores of olivine and augite overgrown by pigeonite (plate 3.3a). Close to the rod, pyroxene crystals are often skeletal and open towards the rod (plate 3.3b,c,d). External faces of pyroxenes are perfectly flat, except for some crystals distant from the rod which are slightly rounded (plate 3.3b). In contrast, hollow, box-shaped pyroxenes usually display well-rounded or irregular internal surfaces and flat faces at the mouth of the crystal (plate 3.3c). Some hollow pyroxenes partially enclose, and may still be in contact with, cusps on the surface of the silica rod (eg plate 3.3d), while others apparently enclose patches of silica (plate 3.3c).

Pyroxene neocrysts are more equant further from the rod, and the skeletal shapes close to the rod are less pronounced, with

rounding and thickening of the limbs of crystals (plate 3.3b). Many simple, equant, euhedral crystals are present at the site of the original rod-melt interface, where the greatest pyroxene nucleation occurred.

Although the initial orientations of pyroxene neocrysts appear random, some of the neocrysts have become elongate and radially oriented about the rod after extended run durations. The habit of growing crystals is controlled by the nature of the compositional boundary layer (CBL) in which they grow. Elongate crystals are predicted to form when the thickness of the CBL is small compared to the crystal size (Martin *et al.*, 1987). The habit of the elongate, skeletal pigeonites suggest that the melt within 50 $\mu$ m of the rod is pyroxene-saturated. Those pigeonite neocrysts with their c-axes pointing at the silica are able to grow rapidly enough to keep their growing faces in this saturated melt (Fleet, 1975). More tangentially orientated pyroxenes are not able to keep up with the CBL and are left behind, resulting in little growth, or even resorption.

Cellular morphologies develop in situations where the growth rate is large with respect to the diffusion rate (Lofgren, 1974; Kirkpatrick, 1975; Donaldson, 1976; Naslund, 1984), and can form in any supersaturated melt where these conditions hold, regardless of how the supersaturation was achieved. The hollow or skeletal morphology develops when melt transport processes are unable to operate rapidly enough to maintain an equilibrium melt composition along crystal surfaces (Kirkpatrick *et al.*, 1981). Melt adjacent to the corners of crystals is more easily replenished from the bulk, allowing increased crystal growth compared to the centre of faces. Faster rates of crystal growth (due to higher supersaturation) may lead to dendritic

morphologies (Kirkpatrick *et al.*, 1981), but this not been observed in any of these experiments. Supersaturation is often associated with rapid cooling, but the isothermal furnace conditions and small size of the charges probably prevent significant temperature variations from existing within charges.

Where crystals have grown together into mutual contact, they appear to have coalesced. Rounding of crystals is rare at the outer edge of the rim, and non-existent close to the silica even after 32 days, suggesting that pyroxene does not texturally equilibrate (§5.5; Waff and Bulau, 1979). Clusters of several contacting grains are extremely common, and may imply self-nucleation (eg plates 3.2, 3.3).

Optically, the pyroxene neocrysts are monoclinic, with maximum extinction angles ( $z^{\wedge}c$ ) for the three sets of experiments ranging from 39-44°. These data were obtained from 106 measured angles taken from 12 experimental charges spanning the complete range of run temperatures. Deer *et al.* (1978) quote 32-44° as the range of extinction angles for pigeonite. Compositions of the pyroxenes are discussed in §3.3.1.

### 3.1.2 Vesicles

Air is trapped within experimental charges during their fabrication and collects as vesicles during partial melting. In general, vesicles are not present in the fringe, and are fewer and larger in glass-rich zones and in charges run at higher temperatures (plate 3.1f), probably as a result of migration and coalescence. This does not occur in the groundmass of 1120°C and 1140°C runs, where high viscosity due to substantial crystal content prevents movement of the bubbles. Vesicles are fewer in number in 1160°C runs, and may have been able to migrate to the

surface of a charge and escape to the atmosphere. Migration of vesicles will significantly contribute to mechanical mixing within a charge.

### 3.1.3 Development of the glass-rich zone

During dissolution, a glass-rich zone free of olivine and plagioclase crystals, and thus distinct from the groundmass, develops between the fringe and the groundmass (plate 3.2a). Some large, well-rounded crystals are present in shorter runs, but these were still dissolving at the time of quenching and would eventually have disappeared as a consequence of silica diffusion into the partial melt.

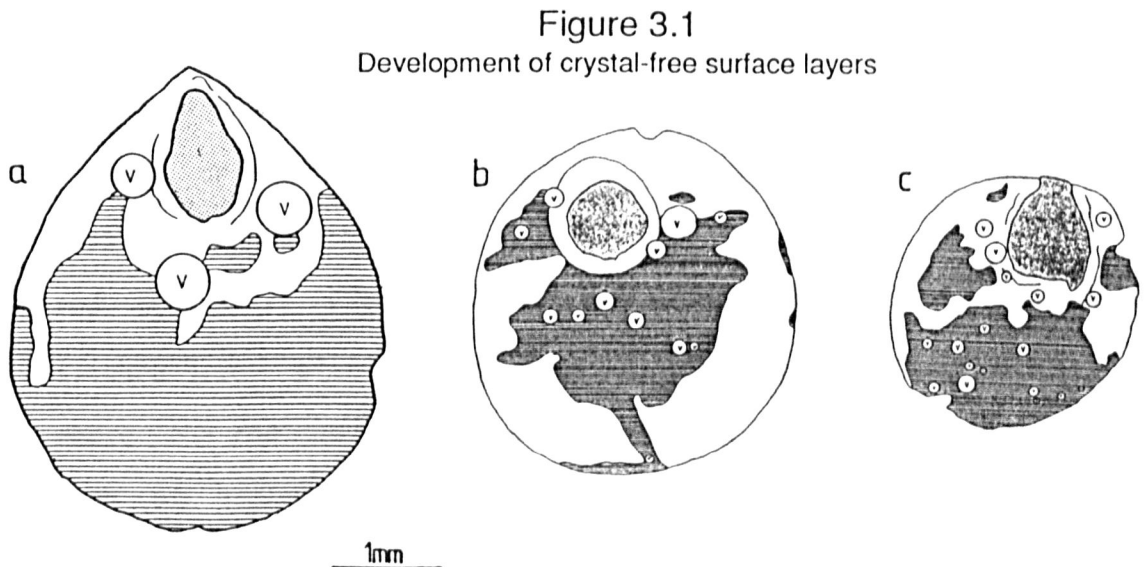
In lower temperature (1120°C) runs, where transport of silica in the melt is restricted by the high viscosity of the small melt fraction, the glass-rich zone is limited in size, and concentric around the rod and pyroxene fringe (plate 3.2a). In higher temperature (1160°C) runs, the silica rod is often at the top of the charge and residual olivine and plagioclase are at the bottom (figure 3.1). In these, the glass-rich zone is irregular in thickness.

In the majority of runs, even at higher temperatures, actual sinking of residual olivine and plagioclase grains does not seem to have occurred. Where the silica rod has risen to the top of the charge, the paucity of olivine and plagioclase in the upper parts of the charge is most easily explained by dissolution brought about by diffusion of silica from the rod. In no charge is there a concentration of crystals found at the bottom of the charge as would be expected to result from crystal settling. Apparently, the groundmass melt has a yield strength exceeding the stress exerted by the weight of the crystals. Alternatively,

convective velocities in the melt may exceed crystal settling velocities.

In highly molten charges crystal-free melt ponds at the top of the charge near the rod, and migrates around the edges of the charge (figure 3.1a,c) until the margin is glassy and relict crystals only remain at the centre (figure 3.1b).

In several runs the glass-rich zone is wider around vesicles, extending into the groundmass (eg plate 3.2a, top). This could be due to shrinkage of the vesicles during cooling, sucking melt out of the groundmass of the charge, or to convection around the vesicle, enhancing the transport of siliceous melt away from the rod and causing additional dissolution of the groundmass. The latter suggestion is in contradiction to the fact that vesicles apparently hinder



Line drawings of three 1160°C charges, showing the silica glass rod (stipple) and partly crystalline groundmass (horizontal hachure). The circles represent vesicles and the thin line (often incomplete) around the rod delineates the outer edge of the pyroxene fringe. The remainder of the white areas are crystal-free melt. In each case the sections are approximately vertical and the silica rod has risen to the top of the charge.

- a: R65, 3 days at 1167°C,
- b: R64, 2 days at 1166°C,
- c: R43, 3 days at 1167°C.

dissolution close to the rod, allowing cusps to form on its surface (§3.1.4).

In runs of short duration (< 4 days), the glass-rich zone may contain large relict olivines ( $Fe_{0.76}$ ; up to  $100 \times 50 \mu\text{m}$  in section). It is possible to estimate a rate of dissolution for these, since after 4 days at  $1140^\circ\text{C}$  they have fully dissolved. This implies a minimum dissolution rate of about  $0.3 \mu\text{mhr}^{-1}$  in the siliceous melt close to the rod. This rough estimate is very similar to Donaldson's (1985b) value for quartz at the same temperature ( $0.4 \mu\text{mhr}^{-1}$ ). By comparison, extrapolation<sup>1</sup> of his superliquidus experimental data for olivine H19 ( $Fe_{0.89}$ ) down to  $1140^\circ\text{C}$  suggests a rate of  $4 \mu\text{mhr}^{-1}$ . This order of magnitude discrepancy confirms that superliquidus dissolution rates may not be extrapolated usefully to subliquidus conditions.

#### 3.1.4 Dissolution shape of the silica rod

Where a vesicle is trapped close to the surface of the rod, a cusp or bump may occur (plate 3.1a,f), indicating reduced dissolution near the vesicle. Similarly, notching of the silica rod occurs if it is partly exposed at the surface of a charge (figure 3.1c, plate 3.1b), especially in highly molten charges where the rod can rise buoyantly. In such examples there is no sign of preferential dissolution caused by variations in melt surface tension ie flux-line attack (Donaldson and Hamilton, 1987). Dissolution of the silica rod continues within the charge but not at the surface, where the silica is in contact only with the atmosphere. Notching of the rod just below the surface of the charge is attributed to dissolution being hampered as the surface

---

<sup>1</sup> using the Arrhenius relationship:  $\text{rate} = A \exp(-E_A/RT)$ , (§3.2.3).

is approached. Even if the rod is not exposed it may be so close to the surface of the charge that dissolution is impeded (figure 3.1a), resulting in a non-elliptical section of the rod.

Similar cusps on the surface of the silica rod also occur close to skeletal pyroxenes (plate 3.3c) or may even embay them (plate 3.3 d). Other skeletal pyroxenes may contain inclusions of silica, possibly still connected to the rod. Inclusions of silica now completely enclosed by pyroxene have developed highly crenulate margins (plate 3.3 c,d), whereas surface cusps still mostly attached to the rod show smooth surfaces. The surfaces of these silica inclusions are irregular where they are more isolated from the exterior melt and close to the surface of the pyroxene, but towards the exterior melt the interface is still smooth. A similar irregular surface occurs along the edge of a melt-filled crack through the silica rod (plate 3.3c).

These cusps form because the proximity of pyroxenes to the surface of the rod inhibits the removal of Si-rich melt from the solid-melt interface, which leads to a shallower silica concentration gradient and slows dissolution of the rod. Dissolution is also hampered by the release of melt depleted in pyroxene components as a result of pyroxene crystallization. Failure to remove these siliceous melts causes a cusp to form on the silica surface. As the pyroxene grows, it further encloses and protects the cusp from dissolution.

Thornber and Huebner (1985) reported similar cusps developed on the surface of olivine crystals during experimental dissolution, where droplets of iron liquid locally impeded olivine dissolution.

### 3.1.5 Crystallization of silica and "curved crack" domains

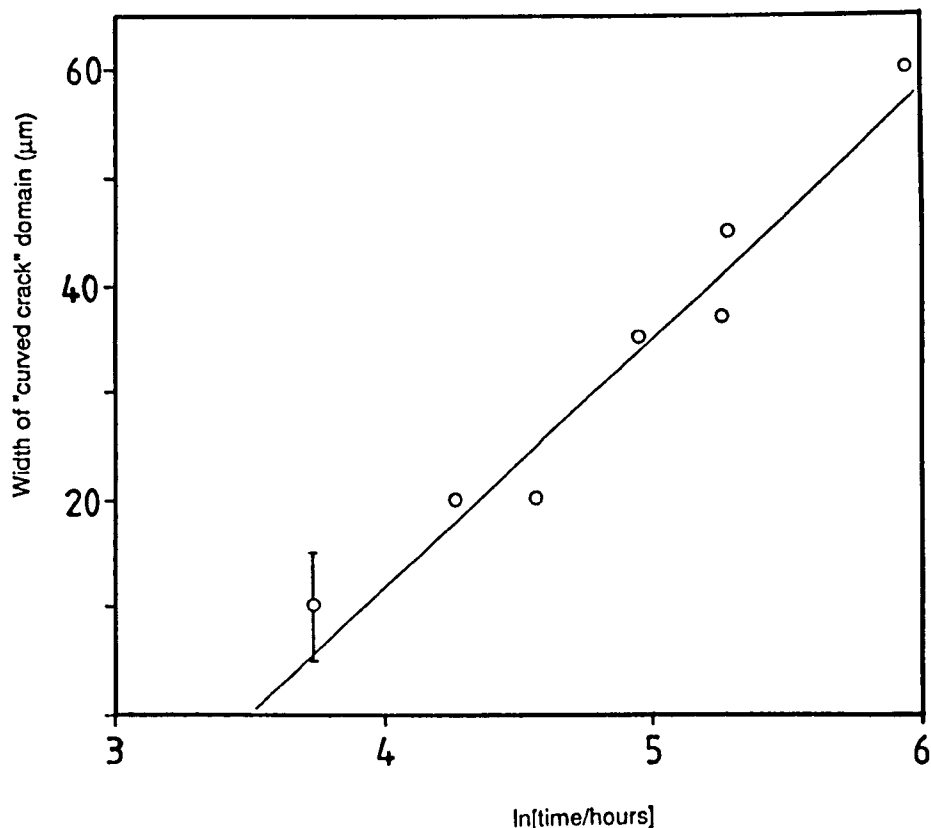
Where the silica rod has cracked (either during pressing or heating of the pellet) and filled with melt, a high-temperature polymorph (probably tridymite) has crystallized replacing the silica. As in some natural examples (§4.3), crystallization of tridymite occurs only along internal cracks, not on the outer surface of the rod.

In addition to tridymite, the melt has caused some alteration of the silica rod, forming domains of material with a low backscatter coefficient bounded by curving cracks (plate 3.2b). Some melt veins become broken up into rows of tiny melt inclusions as the silica anneals.

These "curved crack" (CC) domains are optically isotropic, like the rod, and their nature and origin are obscure. They are related to damage and defects in the rod, spreading from melt-filled cracks. They are present in runs at all temperatures where the rod is damaged. In samples where no defects exist no crystallization has occurred, even after 24 days at 1123°C (plate 3.2a).

The growth rate of CC domains is proportional to  $\ln[\text{run duration}]$  (figure 3.2), suggesting that the process is controlled by diffusion through the silica, and that there is an incubation period for 1140°C runs of 33 hours before these domains develop. From the approximation for typical diffusion distances ( $x^2=4Dt$ ; Crank, 1975), a diffusion coefficient of  $8 * 10^{-16} \text{m}^2 \text{s}^{-2}$  is estimated. This is several orders of magnitude lower than values for tracer diffusion in silicate glass (Hofmann, 1980) and is lower than the diffusion coefficient for silica in melt calculated in §3.2.4.

Figure 3.2  
"Curved crack" domains



Widths of "curved crack" domains plotted against  $\ln(\text{time/hours})$ . Errors given are the same for all points. Data from R30, R31, R36, R63, R105, R67 and R37. The x-intercept is at 33 hours.

---

Microprobe analysis of CC domain material reveals no discernible difference from unaltered rod. Excluding silica, all major elements analysed were below detection limits (<0.1wt%).

The processes of cracking the silica rod, filling the cracks with melt and crystallization of the silica phase result in a change in the volume of the rod. Allowances must be made for this where present, and runs where these features are highly developed are not suitable sources of kinetic data.

### 3.1.6 Cooling-rate experiments

These were carried out to investigate what would happen to isothermally developed textures if they were cooled slowly (table

2.4). It was hoped that this would shed some light on some of the reasons for pigeonite crystallization in experimental runs, whereas natural samples contain only augite.

The textures developed in R50 (cooled to 1062°C) are very similar to those developed in isothermal runs, except that the pyroxene neocrysts are strongly zoned with pigeonite cores and augite rims.

R51 (plates 3.1d, 3.2c) was run similarly to R50, except that cooling was continued to 907°C. Rims of augite on pigeonite neocrysts (plate 3.2d) are irregular in thickness and outline. Pyroxenes with similar rims are found throughout the charge. Near the rod, zoned skeletal pyroxenes have been little affected by cooling of the charge. Euhedral plagioclase crystals in the groundmass are normally zoned.

The surface of the silica rod is not smooth as in isothermal experiments, but shows evidence of the growth of another silica phase. Very close to the rod the charge is still glassy, but from 50 $\mu$ m out are areas of fine acicular plagioclase needles and iron-rich droplets of glass resulting from liquid immiscibility (plate 3.2d). The onset of liquid immiscibility is between 907 and 1062°C.

R53 was run isothermally for over a month, then cooled rapidly (16°C/hr) to well below the solidus. The major differences between this run and isothermal experiments is the development of acicular plagioclase and pyroxene crystals in the groundmass and glass-rich zone of the charge, and the development of liquid immiscibility in all but the most siliceous glass adjacent to the rod.

Pigeonite crystallizes under the isothermal conditions prevalent at the start of each cooling-rate experiment, but is

subsequently overgrown by augite. Augite crystallization probably began when it became the stable pyroxene phase at lower temperatures. It is not clear from the experiments which pyroxene would crystallize if there were no isothermal period and cooling was initiated immediately.

### **3.2 Kinetics of silica dissolution and fringe growth**

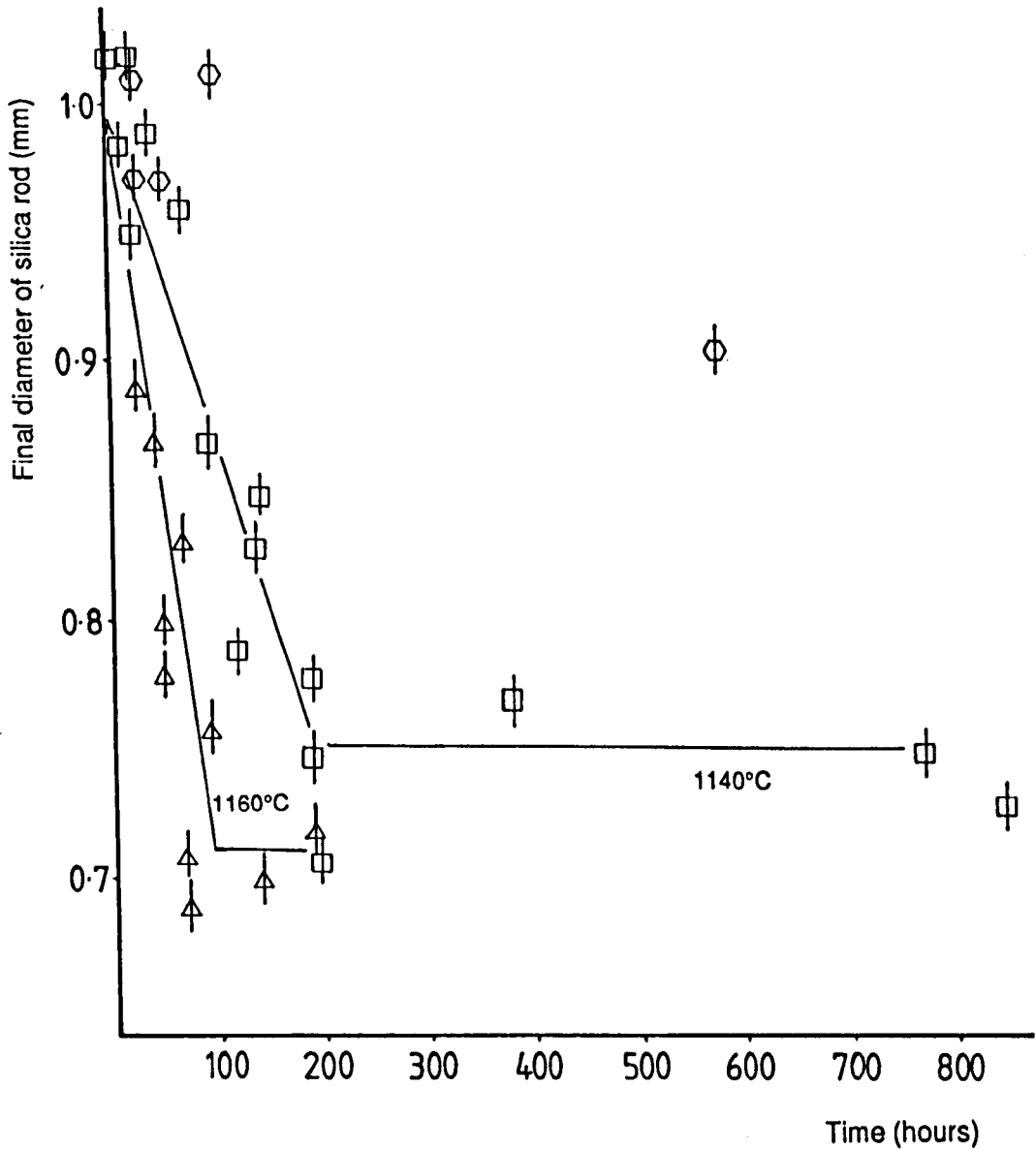
In natural examples where quartz crystals are surrounded by reaction rims of pyroxene, it is not always possible to tell the pre-dissolution size of the quartz. Quartz dissolution occurring at temperatures above the pyroxene liquidus will not be recorded by the pyroxene fringe. Below its liquidus, pyroxene first nucleates on the surface of the quartz, and the locus of high crystal density in a fringe represents the size of the quartz at the time of first pyroxene crystallization. Hence, the kinetics of fringe growth are potentially more useful than those of silica dissolution in estimating the residence times of pyroxene-rimmed quartz crystals in mafic melts.

In this section, the kinetics of silica dissolution and fringe growth are investigated, and the rates found to be independent of time. The rate-controlling step for dissolution is found to be convection probably driven by surface-tension variations around the charge.

### 3.2.1 Rates of silica dissolution

Post-dissolution diameters of silica-glass rods were measured with a microscope graticule. These values are considered accurate to  $\pm 10\mu\text{m}$  and are presented in figure 3.3. Some of the

Figure 3.3  
Dissolution of silica rod



Rod diameters plotted against run duration (linear time scale). Note the constant dissolution rate, then the apparent cessation of dissolution, resulting in no further change of the rod diameter. Data from 1160°C runs (triangles), 1140°C runs (squares) and 1120°C runs (hexagons). Vertical lines are error bars.

scatter of points can be attributed to reduced dissolution in cases where the rod was close to the surface of a charge.

In 1140°C runs the rod diameter decreases at the uniform rate of  $0.6\mu\text{mhr}^{-1}$  ( $1.7 \times 10^{-10}\text{ms}^{-1}$ ) for run durations less than 8 days, and for 1160°C experiments the rod diameter decreases at the uniform rate of  $1.6\mu\text{mhr}^{-1}$  ( $4.4 \times 10^{-10}\text{ms}^{-1}$ ) for runs less than four days long. In both cases the fit to a straight line is better for plots in which the abscissa is "time" rather than " $\sqrt{[\text{time}]}$ ". Insufficient successful 1120°C runs allowed no satisfactory distinction to be made between "time" or " $\sqrt{[\text{time}]}$ " as the abscissa; an estimated dissolution rate of  $0.1\mu\text{mhr}^{-1}$  ( $2.8 \times 10^{-11}\text{ms}^{-1}$ ) was obtained assuming a constant dissolution rate throughout the 24 days of the run (R62). The value of  $0.6\mu\text{mhr}^{-1}$  (1140°C) is in good agreement with Donaldson's (1985b) value of  $0.4\mu\text{mhr}^{-1}$ , highlighting the fact that the form of the silica, whether as glass or as quartz, is not significant.

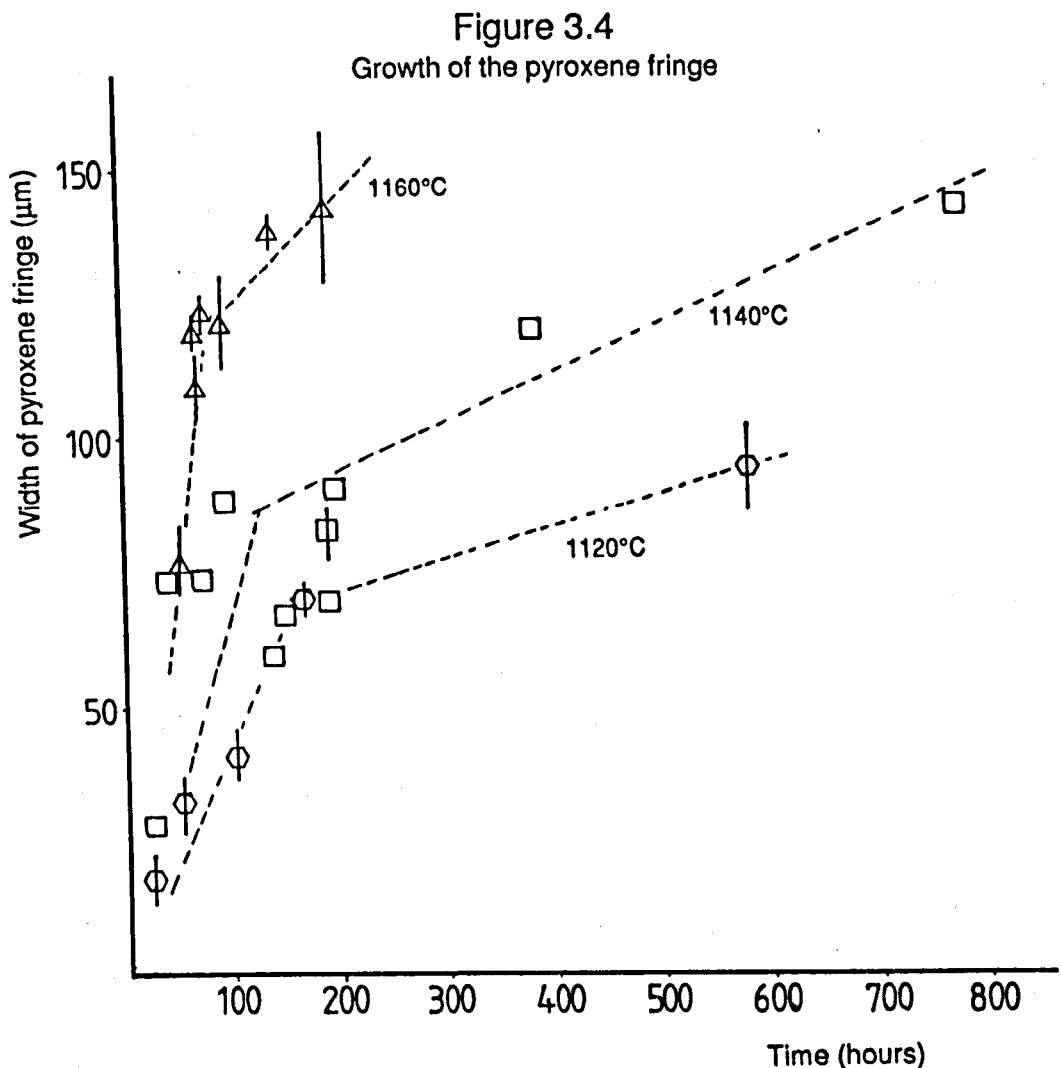
Although the initial dissolution rates for 1140°C and 1160°C runs are constant, for each data set there is an abrupt hiatus, after which dissolution ceases and the size of the silica rod remains roughly constant. This occurs at 3-4 days for 1160°C charges and 8 days for 1140°C charges. Again, data from 1120°C runs are insufficient to establish whether a similar break exists for these experiments.

### 3.2.2 Fringe growth

Widths of pyroxene fringes were obtained from backscattered electron images. For short run durations, approximately linear fringe growth rates of 0.4 and  $0.6\mu\text{mhr}^{-1}$  were obtained for 1120°C and 1140°C runs (figure 3.4). The value of  $0.6\mu\text{mhr}^{-1}$  for 1140°C experiments of 8 days and shorter agrees well with the measured

silica dissolution rate of  $0.6\mu\text{mhr}^{-1}$  for durations less than 8 days (§3.2.1). The value of  $0.4\mu\text{mhr}^{-1}$  for the fringe growth of  $1120^\circ\text{C}$  charges, (which assumes that there is no pyroxene growth on the outer part of the fringe), may be a better estimate of silica dissolution rate than the estimate of  $0.1\mu\text{mhr}^{-1}$  obtained in §3.2.1. The agreement of the  $1140^\circ\text{C}$  rates substantiates this. So, fringe growth is strongly dependent on silica dissolution.

There appear to be breaks in the graphs depicting growth of the pyroxene fringes (figure 3.4) at the same times as breaks in the silica dissolution graphs (ie 3-4 days at  $1160^\circ\text{C}$ , 6-8 days at



Widths of pyroxene fringes plotted against time. Data from  $1160^\circ\text{C}$  runs (triangles),  $1140^\circ\text{C}$  runs (squares) and  $1120^\circ\text{C}$  runs (hexagons).

1140°C and about 10 days at 1120°C (inferred)). At these breaks the fringe growth rates decrease, but growth continues, probably controlled by diffusion.

During the first few days it appears that fringe growth keeps pace with silica dissolution and thus the overall size of the silica rod and pyroxene rim together remain constant. However, once the silica stops dissolving (§3.2.1), pyroxene growth continues at the outer edge of the fringe and the overall size increases.

### 3.2.3 Activation energy of dissolution

Using the Arrhenius relationship<sup>2</sup>, a plot of  $\ln$ [dissolution rate] against reciprocal temperature ( $1/T$ ) should yield a straight line of slope  $-E_A/R$ , from which the activation energy may be calculated.

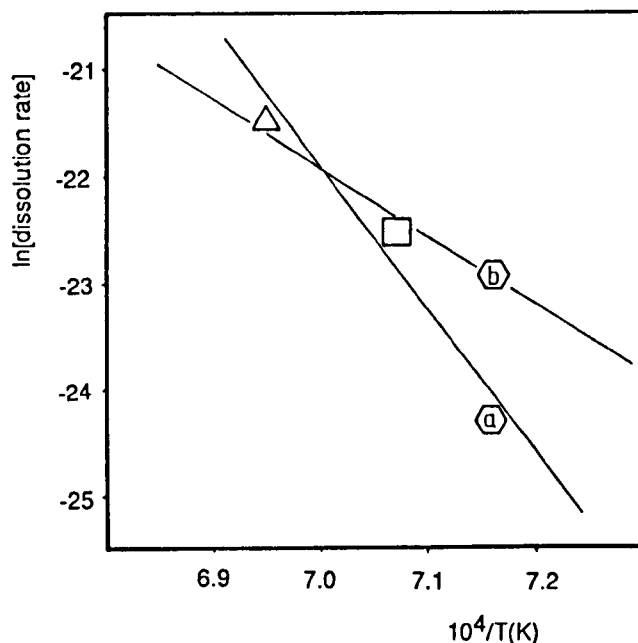
Two values were obtained from figure 3.5. The first,  $E_A = 1.1 \text{ MJmol}^{-1}$  was calculated using the three dissolution rates measured from figure 3.3, and the second,  $E_A = 530 \text{ kJmol}^{-1}$ , used the fringe growth rate instead of the measured, but poorly constrained, dissolution rate for 1120°C runs (§3.2.2).

These values are both considerably higher than published literature values (169  $\text{kJmol}^{-1}$ , Donaldson, 1985b; 190  $\text{kJmol}^{-1}$ , Watson, 1982) for superliquidus dissolution systems involving crystalline quartz. This suggests that the rate-determining step in subliquidus dissolution systems involves the breaking of more bonds than in superliquidus systems, implying that subliquidus melt is more polymerised. Alternatively, the bonds broken may be

---

<sup>2</sup> rate =  $A \exp(-E_A/RT)$ , where  $E_A$  is the activation energy of the dissolution reaction,  $A$  is a constant ("the frequency factor") and  $R$  is the gas constant.

Figure 3.5  
Arrhenius plot to determine activation energies



Arrhenius plot of  $\log_e$ [dissolution rate] against  $1/T$ . Data from 1160°C runs (triangles), 1140°C runs (squares) and 1120°C runs (hexagons). Point A is the estimated dissolution rate from figure 3.3, while point B is the measured fringe growth rate from figure 3.4.

different or stronger. At higher temperatures and in iron-free melts, activation energies for quartz dissolution of 1.25 - 1.9 MJmol<sup>-1</sup> have been calculated from the data of Kuo and Kirkpatrick (1985a).

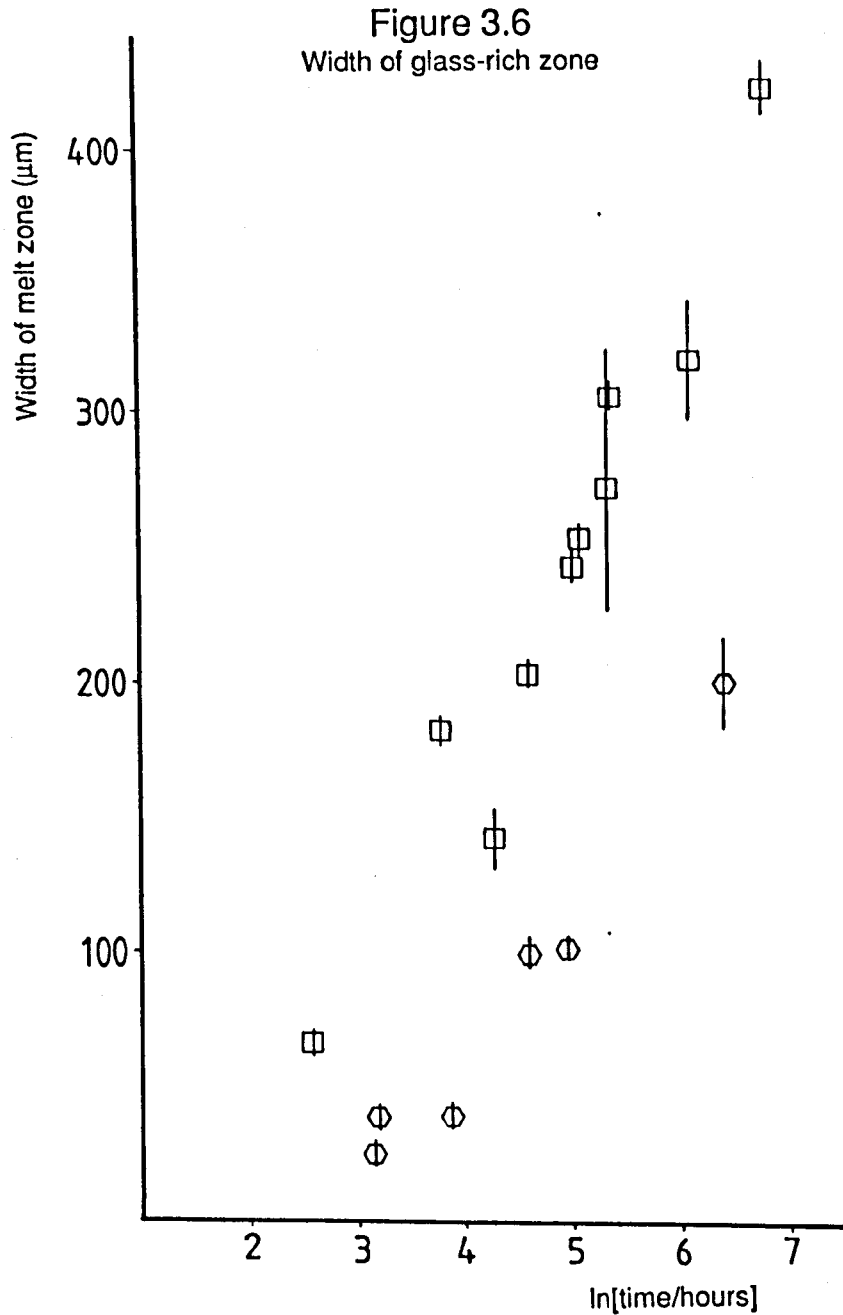
### 3.2.4 Growth of the glass-rich zone

The width of the glass-rich zone is related to  $\ln$ [time] (figure 3.6), and thus is probably related to diffusion of silica from close to the rod out into the groundmass.

Using the approximate relationship for typical diffusion distances ( $x^2 = 4Dt$ ; Crank, 1975), values for  $D$  of  $1.1 \cdot 10^{-14} \text{m}^2 \text{s}^{-1}$  and  $6.0 \cdot 10^{-15} \text{m}^2 \text{s}^{-1}$  were calculated for 1140°C and 1120°C runs respectively, assuming that only a slight increase in silica content is required to cause dissolution of the groundmass crystals. If, however, a substantial increase in silica content

is required to cause this dissolution, these values are minimal and the estimated values of  $D$  should be higher.

---



Width of glass-rich zone plotted against  $\ln[\text{time}]$ . Data from  $1140^{\circ}\text{C}$  runs (squares) and  $1120^{\circ}\text{C}$  runs (hexagons). Where a range of values was obtained, this is presented as a vertical line.

### 3.2.5 Silica-rich boundary layers

If the compositions of melt and crystal differ, the melt composition adjacent to a crystal is altered during crystallization or dissolution, resulting in an exponential composition gradient being set up in a liquid adjacent to the crystal face (eg Donaldson, 1975; Coriell *et al.*, 1980; Coriell and Sekerka, 1981). The width of such compositional boundary layers (CBL) and their time dependence are characteristics of the transport processes operating in the melt. If the diffusivity and concentration difference between crystal and melt are fixed, the dissolution rate depends entirely on the effective CBL thickness. Various rate-controlling processes in diffusion-controlled dissolution can be distinguished in terms of their effective CBL thickness (Kuo and Kirkpatrick, 1985a).

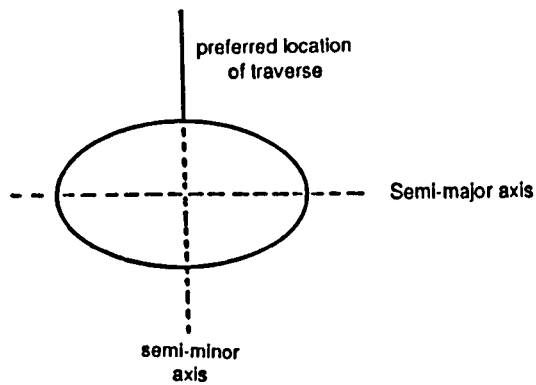
Dissolution will continuously supply material to the boundary layer. Under conditions of convection, a steady state will be achieved between convection removing boundary layer material, and dissolution replacing this boundary material so that the CBL thickness will remain constant.

Compositional boundary layers around dissolving silica glass rods were investigated to see whether their widths were dependent on orientation or time.

The following measurements were made:

- (1) Stepwise traverses (count rates) across the CBL of several 1140°C charges (not oriented with respect to gravity).
- (2) Stepwise traverses (full analysis) across and around the rim of a charge in an attempt to detect a CBL encircling the charge.

Figure 3.7  
The location of the semi-minor axis



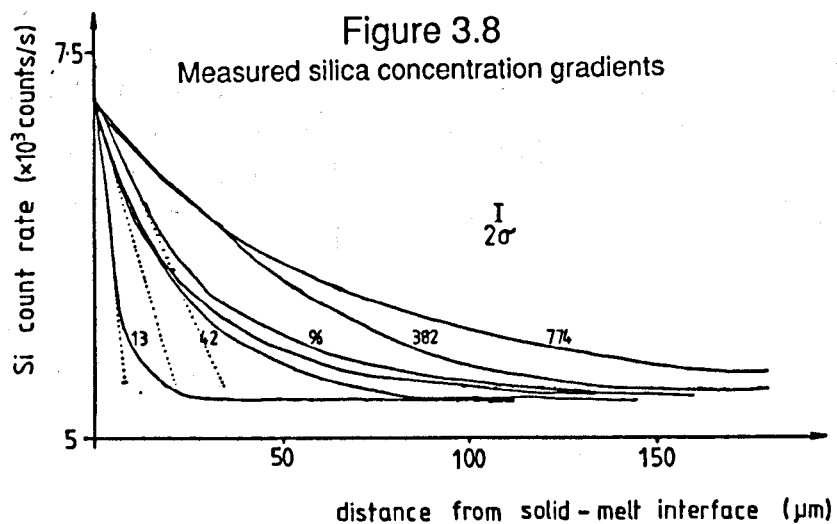
Sketch of elliptical section through a rod, showing the semi-major and semi-minor axes of the ellipse and the preferred location of the microprobe traverse.

---

### 3.2.5a Around the rod

Stepwise traverses were made by taking peak and background counts for Si at  $5\mu\text{m}$  steps across charges run at  $1140^\circ\text{C}$  (§2.4.2a). As far as possible, traverses were performed along the extension of the semi-minor axis of the rod section (figure 3.7) because these would be perpendicular to the rod surface in three dimensions. Although it was possible to perform these traverses in similar orientation with respect to gravity, the random orientation of the rod within a charge would have necessitated correction for traverses not performed along the semi-minor axis of the elliptical section, since the semi-minor axis is not necessarily parallel to gravity. In this respect, charges run with spheres of quartz would have been more useful, since all exposed sections would have been circular.

Figure 3.8 is a composite presentation of data for charges run for 13-774 hours (0.5-32 days). All of the traverses extrapolate to the same silica count rate at the interface between silica rod and melt; this is approximately 71% of the



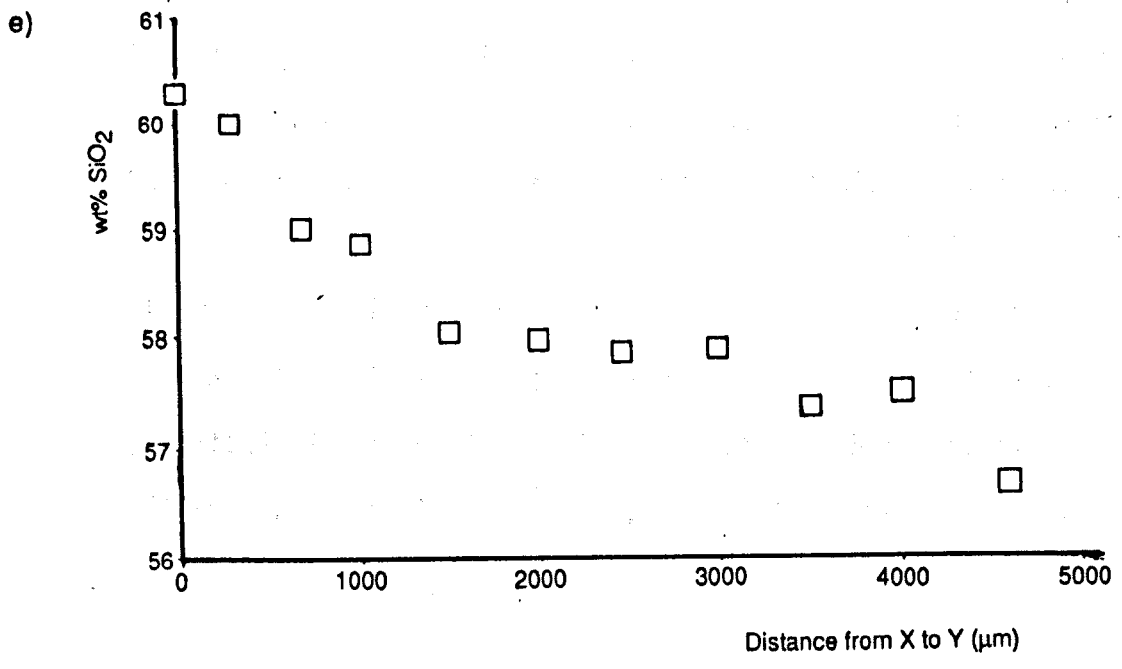
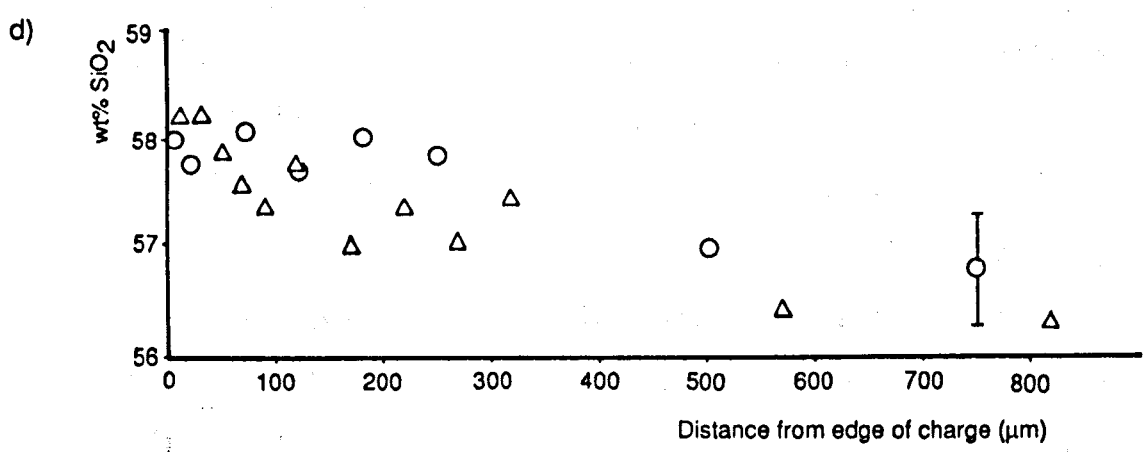
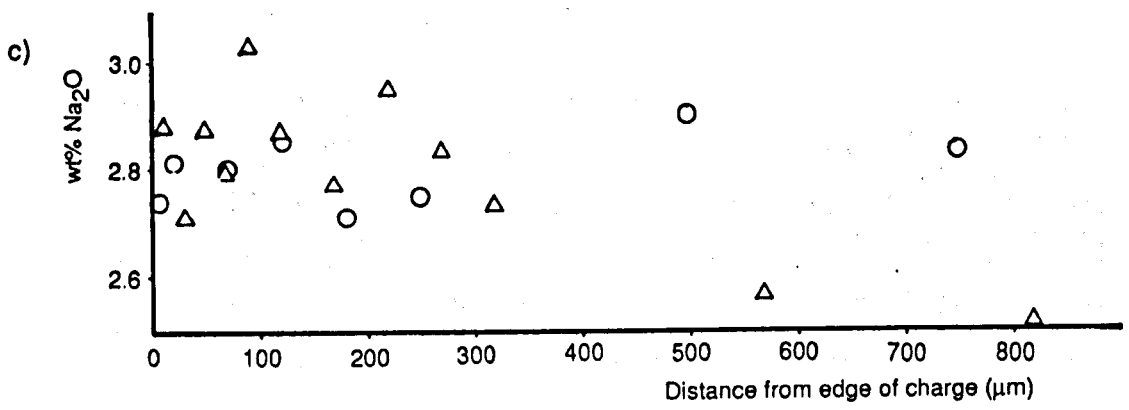
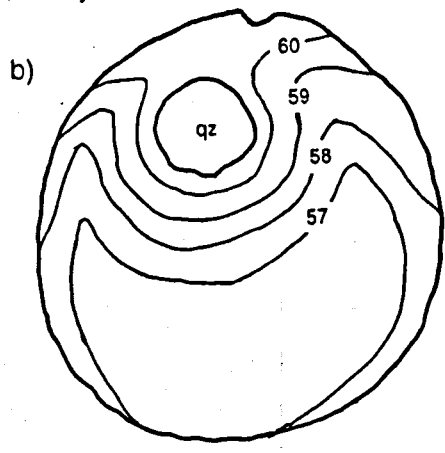
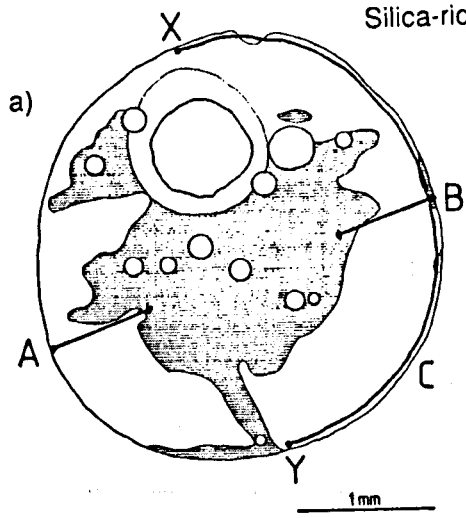
Silica count rate data from 1140°C experiments. Ordinate is silica count rate (peak minus background). Abscissa is distance from the glass - melt interface. The numbers beside each curve denote the run duration (in hours) of the charge from which the traverse was taken. The unlabelled line is for 192 hours. The profiles for 42, 96 and 192 hours are considered almost equivalent within experimental error. The dotted lines indicate the interfacial gradients. Data from R35, R30, R38, R36, R37 and R49. The bar shows the error inherent in each traverse.

rod's silica count rate. Measured count rates decrease rapidly from this interfacial value and define the silica-enriched CBL around the rod as they asymptotically approach the count rate for the groundmass melt.

Because the compositional gradient asymptotically approaches the horizontal, it is difficult to accurately define the thickness of the compositional boundary layer. Instead, the thickness of the boundary layer is defined as the compositional difference between interface and groundmass melts, divided by the compositional gradient at the rod-melt interface (Kuo and Kirkpatrick, 1985a).

There is a transient period over the first 42 hours while the thickness of the CBL increases; this is not always characteristic of dissolution experiments (Kuo and Kirkpatrick, 1985a). Between 42 and 192 hours, the rate of thickening of the

Figure 3.9  
Silica-rich surface layers.



boundary layer decreases substantially, but may not halt altogether, since the profiles for 96 and 192 hours may be interchanged within error. This period suggests that natural convection maintains the CBL at almost constant thickness (Kuo and Kirkpatrick, 1985a; Donaldson, 1985b). More rapid thickening of the CBL after 192 hours suggests that natural convection no longer has such a dominant effect on the width of the CBL. This change in behaviour can be related to the apparent halt in dissolution discussed above, which in turn can be related to the reaction rim of pyroxene neocrysts hindering convection close to the rod.

### 3.2.5b Around the charge

One 1160°C charge (R43) was selected to test for a silica-rich surface melt layer. Groundmass crystals are very scarce near the surface of this charge (§3.1.3, figure 3.1b), and this is believed to be caused by dissolution due to silica-enrichment, as in the glass-rich zone. This effect is not obvious in any 1140°C or 1120°C charges.

Two full-analysis traverses (A and B of figure 3.9a) were made from the margin of the charge towards the centre, perpendicular to the direction of gravity during the run. A third traverse (C of figure 3.9a) was made around the rim of the charge. Traverse A was 820µm long, B was 750µm and C was 4500µm.

Figure 3.9d shows the variation in melt silica content for

---

Figure 3.9 (facing page)

Results of traverses to detect compositional zoning in an experimental charge.

- a) Location of traverses on R43.
  - b) Approximate contours of silica content of melt (wt%).
  - c) wt% Na<sub>2</sub>O as a function of distance, traverses A,B.
  - d) wt% SiO<sub>2</sub> as a function of distance, traverses A,B.
  - e) wt% SiO<sub>2</sub> as a function of distance, traverse C.
- Triangles are traverse A, circles are traverse B.

each of the traverses A and B. The profiles show enrichment of the surface melt by 1 - 1.5wt% SiO<sub>2</sub> compared to the bulk. These data allow the charge to be contoured with respect to silica content of the glass (figure 3.9b). Na profiles (figure 3.9c) decrease slightly towards the bulk (as does K). The other major oxides Ti, Al, Fe, Mn, Mg, Ca increase towards the bulk.

Silica contents around the margin (traverse C; figure 3.9e) show a steady decrease from 60.3wt% at X, down to a groundmass value of 56.6wt% at Y, where some plagioclase is present. Na contents are approximately constant.

The increased silica content of the surface melt cannot be attributed to alkali volatilization from the charge (Donaldson, 1979) as the Na and K contents of the surface melt are both higher than melt nearer the centre of the charge. These higher alkali contents indicate "uphill" diffusion of alkalis into the silica-rich melt (eg Sato, 1975).

It is possible that the formation of a silica-enriched melt layer around a charge could result from the silica-rich layer being surface active (ie having a lower surface tension) relative to the bulk melt and displacing it at the surface of the charge to reduce the total surface energy. This is supported by Appen (A95, in Eitel, 1965) who showed that the partial molecular surface tension for Si is lower than most of the other major oxides, and hence that increasing the silica content of a melt would decrease its surface tension. The same is also true for Na. Such a melt would therefore attempt to encircle the charge in order to lower the total surface energy of the system.

### 3.2.6 Summary of kinetic data

Initially, the rates of silica dissolution and fringe growth, and the widths of the CBLs, are constant at all temperatures investigated, as was found for superliquidus experiments by Watson (1982), Donaldson (1985b), and Kuo and Kirkpatrick (1985a), who attributed the fact to convection in the melt removing siliceous interfacial melt. Likewise, the constant dissolution rates in these experiments can be attributed to natural convection of some sort. However, the convection does not appear to be primarily buoyancy-driven, as a silica-rich boundary layer develops around the surface of a charge.

The hiatuses in silica dissolution and fringe growth rates strongly suggest that a major change in melt transport occurs at these times. The cessation of dissolution suggests that the rate-controlling step, believed to be convection in the melt, has halted, probably because of the continued growth of pyroxene.

### 3.2.7 Convection in the charges

Natural convection of melts within these experimental charges is inferred by constant dissolution rates and boundary layer thicknesses. Scenarios involving forced convection on short timescales are also possible. For example, flotation of the silica rod (§3.1.4) and the migration and coalescence of vesicles (§3.1.2) are two other possible causes of convection, especially in runs at higher temperatures, where the crystal content, and hence viscosity of the groundmass melt, is lower.

Buoyancy-driven natural convection must occur as a result of unstable density gradients in a liquid, which may form as a result of temperature or compositional variations in the liquid. A statically unstable density profile will not automatically

cause convection to occur unless the density gradient exceeds a critical value sufficient to overcome the yield strength of the melt<sup>3</sup>. Once convection is initiated there is no "stagnant" layer adjacent to the crystal (Coriell and Sekerka, 1981; Wilcox, 1983). Convection will occur right up to the edge of the crystal, driving non-depleted melt to the dissolving crystal face. Since there is no apparent motion of neocrysts near the silica, the crystal content of the charges appears to do little except physically obstruct the passage of melt. Convection therefore only involves the melt fraction of a charge.

The only temperature variation present in these experiments will be a small contribution from the latent heats of pyroxene crystallization and silica dissolution, but since the charges are small and run under isothermal conditions, the effect of these contributions is assumed to be negligible. A temperature increase would cause a slight decrease in melt density, but since basalts have a small volumetric coefficient of thermal expansion, a temperature increase of 50°C would, on its own, only cause a decrease in density of 10kgm<sup>-3</sup> (Sparks *et al.*, 1980). It is inconceivable that a temperature variation of this magnitude exists within one of these small charges.

---

<sup>3</sup> Above their liquidus, silicate liquids behave as Newtonian fluids, without measureable strength. However, below their liquidus, they are examples of "plastic fluids", of which the Bingham body is a simple case, and have a finite strength (the yield strength), so that the shear rate vanishes below a certain stress. The existence and time dependence of the yield strength may be important in determining the rheological behaviour of the melt phase, as convection will not occur in a magma until the yield strength is exceeded. Yield strengths measured in the laboratory show less correlation with silica content than with cooling below the liquidus, but no simple relation between yield strength and the volumetric proportions of crystals has been found (McBirney and Murase, 1984).

### 3.2.7a Compositional convection

Much larger variations in density can result from compositional variation in melts. In these experiments, there is a significant difference in composition between interface and groundmass compositions such that the interface melt has a density about  $150\text{kgm}^{-3}$  (range  $120\text{-}180\text{ kgm}^{-3}$ ) less than that of the groundmass partial melt (§2.6.1; table 3.1). Crystallization of pyroxenes also releases buoyant, depleted fluid<sup>4</sup>, increasing

Table 3.1  
Calculated melt properties

Run	Density ( $\times 10^3\text{kg m}^{-3}$ )			gm	Viscosity ( $\times 10^4\text{ Pa.s}$ )			gm
	int.gl	fringe	melt		int.gl	fringe	melt	
<b>1120 runs</b>								
R61*	2.33	2.48	2.48	2.46	34000	64	15	6.7
<b>1140 runs</b>								
R32	2.33	2.42	2.48	2.51	2900	76	4.7	3.1
R30	2.38	2.48	2.45	2.51	240	13	5.6	3.2
R31	2.35	2.45	2.46	2.47	620	15	8.4	3.3
R36*	2.37	2.49	2.50	2.54	1100	7.9	8.8	6.4
					2500	13	11	3.2
R38*	2.39	2.52	2.50	2.53	1600	9.8	4.3	2.7
					2700	94	2.7	2.8
								2.6
R37	2.38	2.47	2.47	2.53	3900	19	17	3.9
mean (8 analyses)	2.37	2.48	2.48	2.52	1500	15	8	3.3
<b>1160 runs</b>								
R43*	2.36	2.45	2.46	2.51	130	3.4	2.4	1.7
					870	3.6	2.3	1.8
R44*	2.36	2.45	-	2.47	3600	4.4	-	2.9
					100	3.8	-	2.3
mean (4 analyses)	2.36	2.45	2.46	2.49	450	5.8	2.3	2.1

\* Mean density values calculated from double analyses.

int.gl - glass composition close to the interface  
fringe - glass at boundary between fringe and glass-rich zone  
melt - glass at boundary between glass-rich zone and groundmass  
gm - groundmass partial melt.

<sup>4</sup> The fractionation density (§2.5.1) of the pigeonite is typically  $2740\text{ kgm}^{-3}$ , greater than the density of the melt in which they grow.

the volume of buoyant melt close to the rod and enhancing the probability of convection.

A horizontal film of fluid above or below a dissolving or growing crystal face will convect if the density gradient is unstable and a critical Rayleigh number is exceeded (Sparks *et al.*, 1984). Values of the compositional Rayleigh number were calculated using experimental data to test whether buoyancy-driven natural convection might occur within these experimental charges. The data used and values for  $Ra_c$  obtained are given in table 3.2. All of these values are 3-4 orders of magnitude less than the critical value of 1000, suggesting that buoyancy-driven convection is not possible. This suggests that the length-scale of the experiments is too small to allow buoyancy-driven convection. In natural systems, where the dissolving crystals and reaction rims are of similar sizes to those in the experiments (§4.3; plate 4.1), the relevant length-scale will still be too small for buoyancy-driven convection.

It must be remembered that these calculations have been performed for the case of a horizontal crystal face and boundary

Table 3.2  
Computed compositional Rayleigh numbers

run temp	$D \cdot 10^{-15}$	$\beta$	$\mu \cdot 10^4$	$V \cdot 10^{-10}$	$\delta \cdot 10^{-6}$	Ra(a)	Ra(b)
1120°C	6	130	6.7	1.1	100	0.54	1.8
1140°C	11	150	3.9	1.7	100	1.2	2.3
1160°C	25	130	2.1	4.4	100	0.46	1.4

$$Ra(a) = gD^2\beta/\mu V^3 \quad (\text{Sparks } et \text{ al. } 1984).$$

$$Ra(b) = g\delta^2\beta/\mu V \quad \text{using } \delta \approx D/V \text{ to eliminate } D$$

$\beta$  = difference in calculated densities between interface and groundmass melts ( $\text{kgm}^{-3}$ ).

$\mu$  = calculated viscosity of groundmass melt (crystal-free) from table 3.1 (Pa.s).

$V$  = measured dissolution velocities, from §3.2.1 ( $\text{ms}^{-1}$ ).

$\delta$  = measured boundary layer thicknesses, from §3.2.5; 1120°C value guessed (m).

$D$  = measured diffusion coefficients, from §3.2.4, 1160°C value estimated using  $D = D_0 \exp(-E_A/RT)$  ( $\text{m}^2\text{s}^{-1}$ ).

layer, which represents the most kinematically stable configuration, and convection is least likely to occur in this situation. For vertical or inclined faces, no stable condition exists. Consequently, there will always be some tendency for the compositional boundary layer to detach from the crystal surface and flow away from its point of origin (Tait *et al.*, 1984; Sparks and Huppert, 1984) if the yield strength of the liquid is exceeded.

### 3.2.7b Surface tension-driven phenomena

§3.2.5b demonstrated the existence of a crystal-free melt layer enriched in silica around the surface of a charge. Such a layer is presumably surface active, and will try to cover the entire surface of the charge to reduce its total surface energy. This would drive convection of silica-enriched melt away from the rod and around the charge.

Similar behaviour, termed "dynactive" (Jebsen-Marwedel, 1956), occurs where two liquid phases with differing densities and surface tensions are in contact. For dynactive behaviour to occur the differences in density and surface tension must be of opposite sign. The most characteristic phenomenon is the possibility that a liquid of high density may rise to the surface of a lighter melt, if the first has a lower surface tension. As a result, melt of low surface tension tends to subdivide melt with a higher surface tension into a cellular network by capillary action. A difference in surface tension of only 1% is sufficient to make this effect evident. This is followed by swirling because of the density disequilibrium attained by the cellular arrangement. The resultant mixing by flow of melts of differing densities thus efficiently enhances the diffusion process.

These phenomena are seen in glass manufacture between the bulk melt and the alumina-enriched reaction glass derived from dissolution of tank block material, which has lower density, but higher viscosity and surface tension than the bulk melt (Jebsen-Marwedel, 1956). Intense enveloping, dynactive rotation currents and spreading phenomena are observed between the two melt phases.

In the experiments reported here, the siliceous melt is apparently surface active (§3.2.5b) and hence lower in surface tension than the bulk melt, but also has a lower density, and, as defined above, dynactive behaviour should not strictly occur. However, the siliceous melt does not start at the top of the charge, and the surface of the charge is not only at the top, as is the case for tanks, but all around, enabling the possibility of complex interaction of the surface melt with the groundmass melt once it has reached the sides or bottom of the charge.

### 3.2.7c Cessation of convection

As shown above, the rates of fringe growth and silica dissolution become time-dependent after an initial constant period and the compositional boundary layers thicken (figure 3.8), showing that convection has been restricted. Convection might be inhibited by the presence of crystals in the melt increasing the effective viscosity of the melt. However, the pyroxenes in the fringes show no sign of movement, except possibly their radial orientations, which could be argued to result from radial fluid flow around the rod. No movement of pyroxenes is expected after they have formed a rigid interconnected skeleton around the silica, which is, in effect, a porous layer around the rod through which melt must travel while convection continues. It is difficult to estimate the

permeability of such a layer, but differences would arise from variations in size, shape and packing of crystals, preferred orientation, extent of crystallization, porosity and tortuosity of channels between crystals. Continued growth of the pyroxenes will increase the tortuosity and decrease both the porosity and the permeability of the layer. As this continues, the Rayleigh number for convection in the fringe will decrease until the critical value is reached, at which point convection stops (Tait *et al.*, 1984). Silica-rich melt is trapped adjacent to the rod and dissolution ceases. Growth of pyroxene at the outer edge of the fringe may continue by diffusion of material from the groundmass, further increasing the volume of pyroxene present.

#### 3.2.7d Summary

Convection occurs within experimental charges but is not predominantly buoyancy-driven. It has already been shown, theoretically, that surface tension is more important as a driving force for fluid flow than gravity in all laboratory experiments (Stevenson, 1986). The dominant effect of surface tension is the spreading of siliceous melt over the surface of a charge. This usually occurs towards the top of a charge because in many cases the rod itself has floated there. The possibility of surface tension-driven flow along crystal-melt boundaries in the groundmass of a charge should not be ruled out as a further mechanism operating.

In natural examples, the dimensions of the partly dissolved quartz and the pyroxene reaction rim are similar to those in the experiments, and melt transport will presumably be very similar. Buoyancy-driven natural convection is thus not expected to occur around dissolving quartz grains in natural rocks.

### 3.3 Pyroxenes and coexisting melts

#### 3.3.1 Pyroxene compositions

Typical pyroxene analyses from each set of isothermal experiments are given in table 3.3 and all analyses obtained are given in appendix 2. In general, with increasing temperature of crystallization, the Si, Al and Mg contents increase, while Ti, Fe, Mn and Ca decrease. Na is below detection limits. The neocrysts are almost pure (96-99%) Ca-Mg-Fe pyroxenes, with very low Al and Ti contents (0.2-0.7 wt%, 0.2-0.4 wt%, respectively). In the pyroxene quadrilateral (figure 3.10) they plot in the field of pigeonite, with the exception of some of the 1160°C neocrysts, which plot below the pigeonite-clinoenstatite boundary (placed at Wo<sub>5</sub> by Morimoto *et al.*, 1989). Augites analysed in 1120°C charges plot in the augite field. Pigeonite analyses with

Table 3.3  
Typical fringe pyroxene analyses

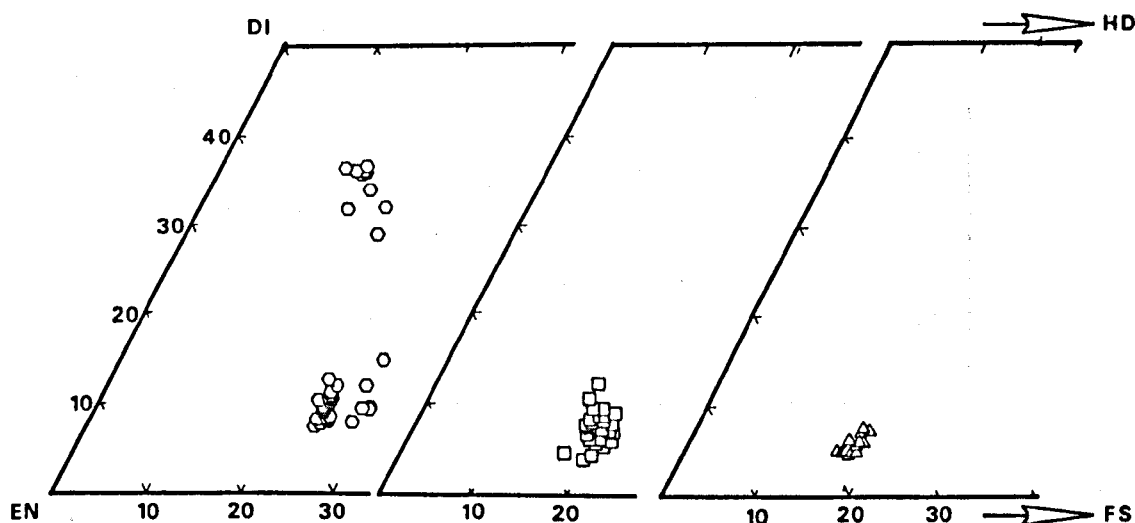
Run	R62	R49	R57	R27
Analysis	33	9	23B	24
Distance (µm)	10	10	20	30
Temperature (°C)	1123	1143	1164	1070
SiO <sub>2</sub>	54.14	54.74	55.49	52.78
TiO <sub>2</sub>	0.23	0.16	0.14	0.70
Al <sub>2</sub> O <sub>3</sub>	0.26	0.32	0.60	1.06
FeO	15.97	14.03	12.62	12.55
MnO	0.36	0.28	0.22	0.59
MgO	24.40	27.22	28.59	15.32
CaO	3.96	2.71	2.41	16.18
Na <sub>2</sub> O	nd	nd	nd	0.22
Total	99.32	99.46	100.07	99.40
%Quad	99	99	98	
%wo	8	5	5	34
%en	67	73	77	45
%fs	25	22	18	11

%Others = 100 - %Quad

wo + en + fs = 100%

nd = not detected

Figure 3.10  
Pyroxene compositions in experimental charges



Pyroxene compositions projected from non-quadrilateral components by the method of Lindsley (1983) and plotted in part of the pyroxene quadrilateral. Units are mol%.

- (a) Pigeonite and augite from 1120°C runs,
- (b) Pigeonite from 1140°C runs,
- (c) Pigeonite from 1160°C runs.

---

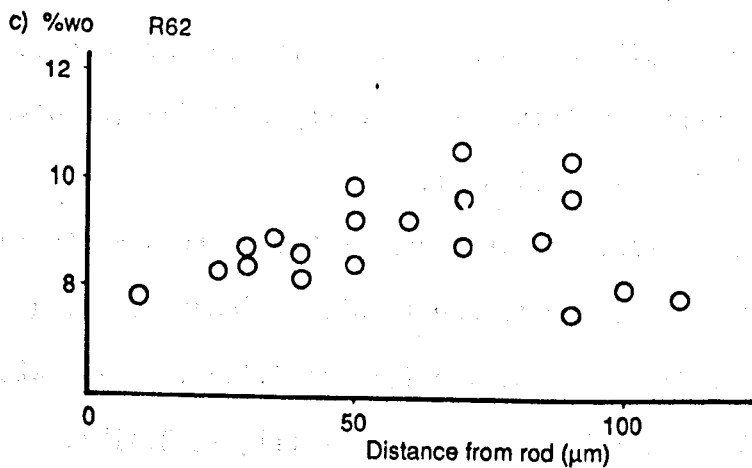
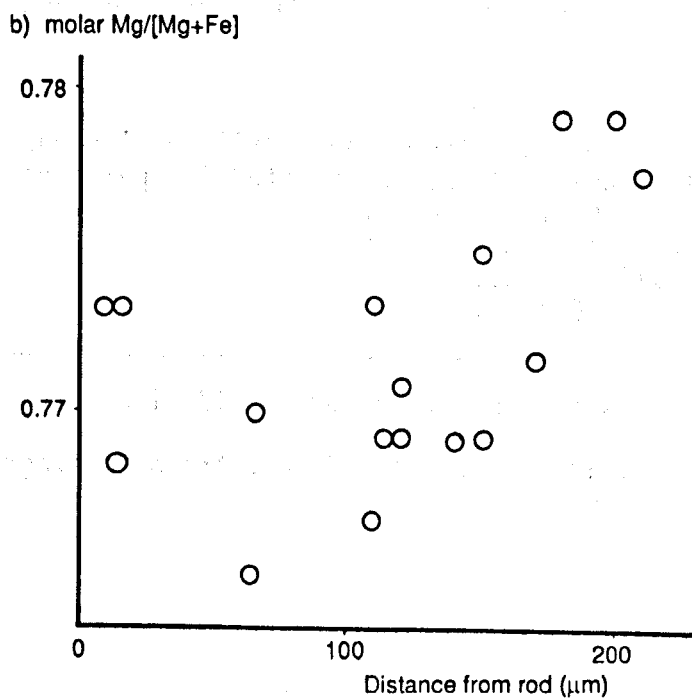
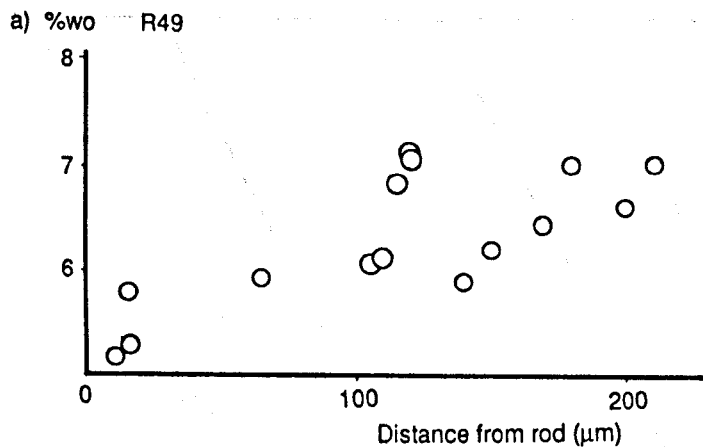
Wo > 10% may be mixtures incorporating some residual augite, but this is only apparent in backscattered electron micrographs (plate 3.3a).

### 3.3.1a Variation in individual experiments

Compositional variation of pyroxenes as a function of distance from the silica rod was investigated by microprobe traverses across pyroxene fringes, in charges on R49 (32 days at 1143°C) and R62 (24 days at 1123°C).

The calcium content of pyroxenes in R49 decreases steadily from the outer edge of the fringe ( $\approx 200\mu\text{m}$ ) inwards, with the lowest values closest to the silica (figure 3.11a). This pattern is followed by the molar  $\text{Mg}/(\text{Mg}+\text{Fe})$  values (figure 3.11b).

Figure 3.11  
Variation in pyroxene compositions  
with distance from the rod



The same general trend is shown by R62, but in this case some pyroxenes crystallizing at the outer edge of the fringe also have low wollastonite contents (figure 3.11c). These may be the earliest neocrysts, which nucleated before the completion of partial melting and establishment of convective melt transport.

Hence, pyroxene neocrysts initially crystallize with high %Wo and molar Mg/(Mg+Fe). As crystallization proceeds, melt transport around the dissolving silica is hindered (§3.2), so that melt close to the silica becomes isolated, evolving to Ca-poor and Fe-rich compositions, because the crystallizing phase has higher Ca contents and Mg/Fe ratios than the melt. These trends are reflected in the compositions of later crystallizing pyroxenes nearer the rod, which have higher Fe and lower Ca contents.

### 3.3.1b Pyroxenes from cooling rate experiments

Pigeonite cores to pyroxene crystals plot within the range of pyroxenes from 1140°C isothermal runs (figure 3.12). The rims of the crystals are augitic, Fe-rich compared to the residual augites analysed in 1120°C runs. Intermediate points may represent mixed analyses, or possibly a narrowing of the miscibility gap during cooling.

### 3.3.2 The nature of the pyroxene phase

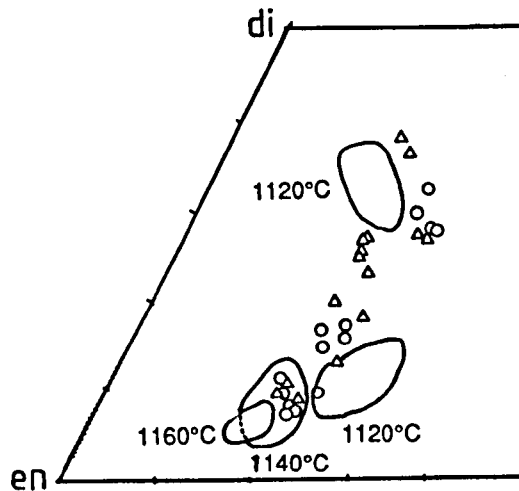
As will be seen in chapter four, all of the natural examples studied in this work and by other authors from a wide

---

Figure 3.11 (facing page)

Variations in (a) %wollastonite component and (b) mg# of pyroxenes in R49, and (c) the variation in %wollastonite component of pyroxenes in R62, as a function of distance from the silica glass rod.

Figure 3.12  
Pyroxene compositions from cooling-rate experiments



Pyroxene compositions from cooling rate experiments plotted in part of the pyroxene quadrilateral. Fields of pyroxene compositions from figure 3.10 are also given. Data from R50 (triangles) and R51 (circles).

range of host rocks contain augite as the pyroxene phase in the reaction rim. No mention is made of pigeonite or orthopyroxene (except by Sato (1975) and Lacroix (1893) - and in Sato's example the orthopyroxene was growing into the reaction rim from the groundmass). It is strange, therefore, that the dissolution of quartz and silica glass into a tholeiite (this work), and quartz into an alkali olivine basalt (Donaldson, unpublished) under isothermal experimental conditions should lead to the crystallization of pigeonite instead of augite.

A preliminary set of partial melting and dissolution experiments using a ferrodiorite (RC342, from Harker's Gully, Marsco, Skye; see table 2.2) were originally carried out to determine the suitability of this system for investigating quartz dissolution kinetics. Although the reaction was too slow to allow procurement of accurate kinetic information, some microprobe analyses of pyroxene and melt compositions were obtained.

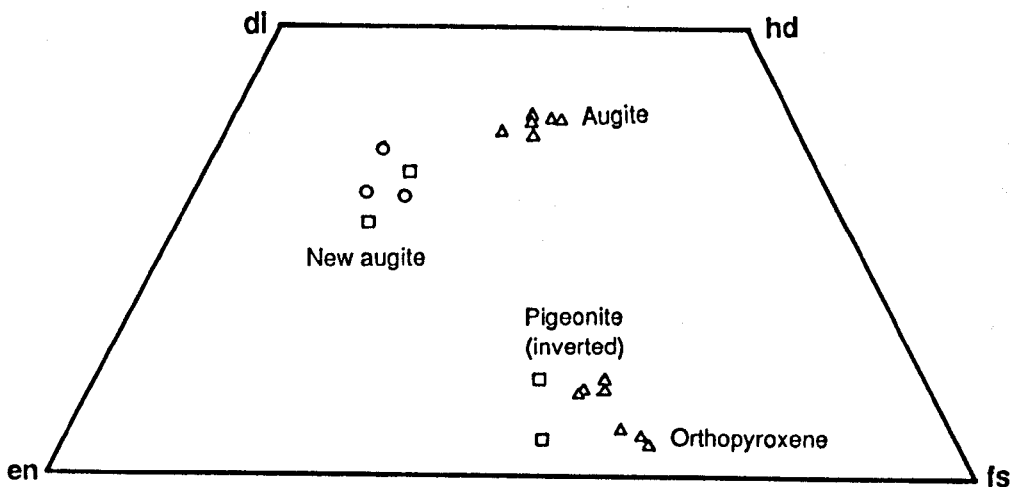
Partial melting of the ferrodiorite for shorter run durations (< 1 day at 1070°C; eg R19) reveals two different

pyroxene textures. The first consists of clusters of many tiny euhedral pyroxene neocrysts resulting from amphibole breakdown, and the second is the development of sieve textures (partial dissolution) on larger pyroxene crystals. After increased run duration (> 2 days; R25) the former texture has become coarser via coalescence and recrystallization, but the sieve texture has completely obliterated original pyroxene shapes.

Analysed pyroxene compositions from the shorter runs (R19, R26) are similar to those in the original ferrodiorite (augite, orthopyroxene and inverted pigeonite; Wager and Vincent, 1962) but are significantly different from those in the longer run (R25) where recrystallization of pyroxene has caused more Mg-rich augite and orthopyroxene compositions to form (figure 3.13).

A reconnaissance experiment dissolving quartz spheres (R27: 230 hours at 1070°C) produced a narrow fringe of equant, rounded,

Figure 3.13  
Pyroxenes from ferrodiorite experiments.



Pyroxene compositions from ferrodiorite experiments (at 1070°C) plotted in the pyroxene quadrilateral. Circles are pyroxenes around dissolving quartz (R27), triangles are groundmass pyroxenes from short duration partial melting experiments (R19, R26) and squares are groundmass pyroxenes from a longer partial melting experiment (R25).

interconnected but not skeletal pyroxene crystals. Microprobe analysis revealed these to be augite, similar in composition to the augites analysed from longer partial melting runs (figure 3.13).

### 3.3.2a Metastable crystallization?

Although augite has been grown experimentally as fringes around quartz, it is possible that either this augite or the pigeonite from the other experiments is a metastable phase. The elongate and skeletal crystal shapes exhibited by the pigeonites (§3.1.1) are often associated with metastable growth.

The crystallization of pigeonite (as in the groundmass of 1120°C runs; §3.1.1) has been documented from melting experiments on basalts, replacing augite in the original starting material (Schiffman and Lofgren, 1982; Grove and Bryan, 1983). Pigeonite nucleation may have been suppressed in such examples by rapid cooling under natural conditions, so that the basalt continued to crystallize olivine and plagioclase, until the residual liquid moved into the augite phase volume. In addition, the replacement of equilibrium pigeonite as the initial pyroxene by augite or augite and pigeonite during dynamic crystallization is clearly demonstrated by the cooling-rate experiments described above (§3.1.6, §3.3.1), by Baker and Grove (1985) and Schiffman and Lofgren (1982), and has also been observed for a number of lunar bulk compositions (Walker *et al.*, 1976).

Calculated values for the iron-magnesium distribution coefficient ( $K_D$ )<sup>5</sup> between liquid and pyroxenes may indicate

---

<sup>5</sup>  $K_D = (X_{Fe}^{PX} / X_{Mg}^{PX}) * (X_{Mg}^{LIQ} / X_{Fe}^{LIQ})$ , where X is the mole fraction of an element in either liquid (LIQ) or pyroxene (PX).

Table 3.4  
Values of  $K_D$  from published experiments

System	Run temp(°C)	$K_D$	Reference
aug-liq	1137-1243	0.23*	Grove+ 1983, Tormey+ 1987
pig-liq	1173-1196	0.27	Kinzler+ 1985
pig-liq	1059-1137	0.25(1 $\sigma$ = 0.03)	Grove+ 1982
pig-liq	1075-1175	0.25(1 $\sigma$ = 0.04)	Baker+ 1987
pig-liq	1123-1127	0.24	this work
" "	1141-1146	0.26	" "
" "	1163-1167	0.28	" "
pig-liq	1143-1152	0.27-0.29	Donaldson (unpublished)

All values calculated from data presented in reference, except \*.

whether the pyroxenes nucleated stably or otherwise. Existing values of  $K_D$  either published, or calculated from published experimental data, are given in table 3.4, along with data from these experiments and others by Donaldson (unpublished). The data from these experiments clearly fall in the same range as those published by other workers. The attainment of consistent results for exchange equilibria does not prove equilibrium, but probably demonstrates a close approach. Metastable crystallization may result in disequilibrium partitioning, and, under conditions of rapid growth, distribution coefficients approach unity (Grove and Bence, 1979), so that pyroxene compositions would become more Fe-rich (eg Grove and Bryan, 1983). However, the possibility that variations in  $K_D$  may be caused by analytical errors should not be forgotten. A 2% analytical error for major elements by microprobe analysis would result in a variation of  $\pm 0.2$  in values of  $K_D$ . The slight variation present in table 3.4 is ascribed here to analytical error, rather than disequilibrium partitioning resulting from rapid crystallization.

### 3.3.2b Pigeonite stability

When pigeonites from these experiments and other experimental systems run at atmospheric pressure (referenced in

figure caption) are plotted in terms of  $Mg/(Mg+Fe)$  against temperature (figure 3.14), they lie close ( $\pm 25^\circ C$ ) to the line of minimum stability for pure Ca-Mg-Fe pigeonites relative to orthopyroxene and augite (figure 8 of Lindsley, 1983). Correlation with the estimated minimum stabilities of "natural pigeonites" (Lindsley, 1983) and "all pigeonites" (Davidson and Lindsley, 1985) is much poorer ( $-60^\circ C$ ,  $-100^\circ C$  respectively). Pigeonites grown in this study are nearly pure Ca-Mg-Fe pyroxenes, and as such their agreement with Lindsley's (1983) data for pure pigeonites is not surprising and suggests stable crystallization in these experiments. If, however, the more recent stability curve of Davidson and Lindsley (1985) is correct, most pigeonites shown on figure 3.14 appear to have crystallized metastably, instead of orthopyroxene and augite.

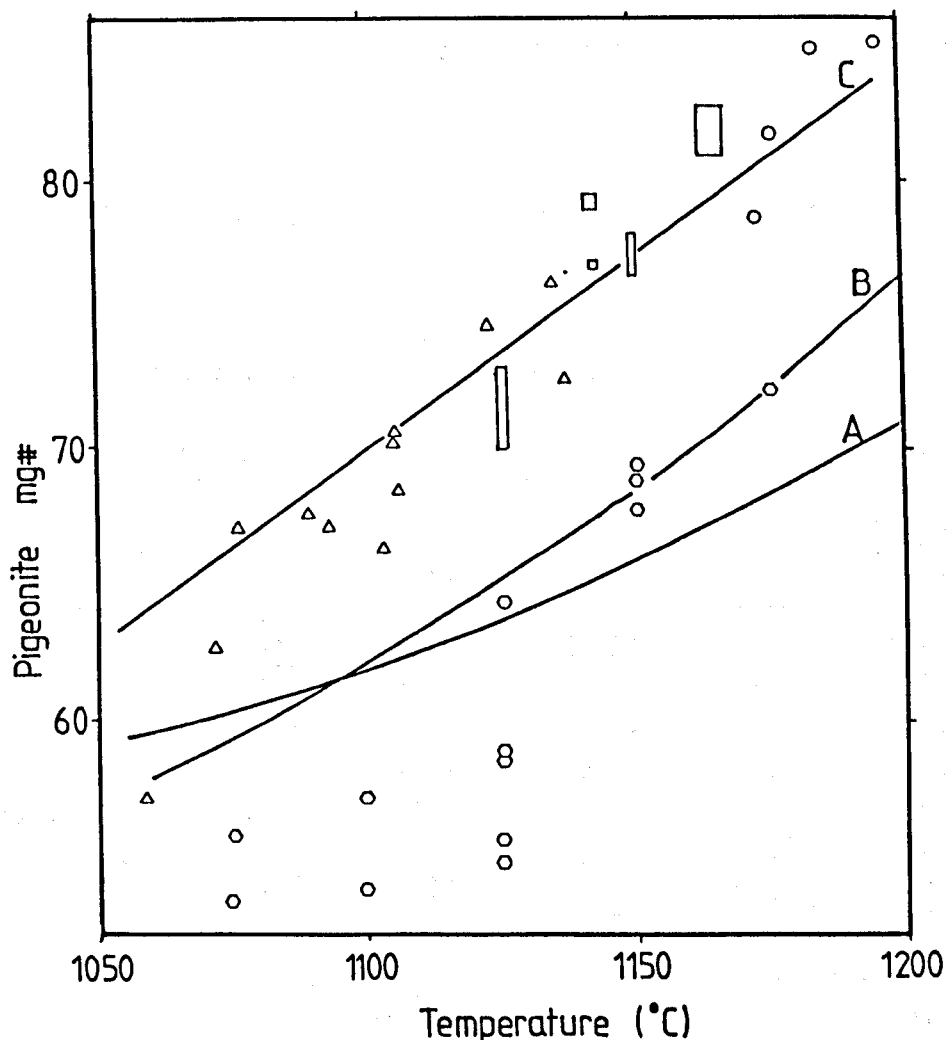
Pigeonite crystallized in the high pressure experiments of Baker and Egglar (1987) corresponds more closely to the higher temperature stability curves.

### 3.3.2c Other factors

There are two other possible influences on the composition of the crystallizing pyroxene.

- i) The effect of increasing pressure on the simple system fo-di-qz (Morse, 1980) is to eliminate the pigeonite field by 1GPa. This is unlikely to be significant in many rock samples since the presence of tridymite restricts the depth of reaction to less than 3km ( $\approx 100MPa$ ).
- ii) For each set of experiments, the total variation in  $fO_2$  was 0.8 log units around the QFM buffer, and for this range no significant variation in pyroxene chemistry was noted. The effect of larger variations in  $fO_2$  was not investigated.

Figure 3.14  
Pigeonite stability.



Plot of experimental pigeonite compositions ( $\text{mg\#} = 100 \cdot \text{Mg}/(\text{Mg} + \text{Fe})$ ) against run temperature. Data from:

- (circles) Kinzler and Grove (1985), 1 atmosphere crystallization experiments, synthetic starting materials.
- (triangles) Grove *et al.* (1982), 1 atmosphere melting experiments, natural starting materials.
- (hexagons) Baker and Egglar (1987), 0.8 MPa melting and crystallization experiments, natural starting materials, graphite/platinum capsules.
- (rectangles) Range of values from this work and Donaldson unpublished data.

Line A is the minimum stability of pigeonite at atmospheric pressure (figure 6 of Davidson and Lindsley, 1985).

Line B is the estimated minimum stability of natural pigeonites (figure 13 of Lindsley, 1983).

Line C is the minimum stability of pure Ca-Mg-Fe pigeonites, relative to orthopyroxene and augite (figure 8 of Lindsley, 1983).

Schiffman and Lofgren (1982) reported that variations of  $fO_2$  within 1 log unit of the QFM buffer were not sufficient to prevent pigeonite crystallization in favour of augite.

### 3.3.3 Melt compositions

Table 3.5 lists typical groundmass and interface melt compositions from experimental charges at each run temperature.

Table 3.5  
Interface and groundmass melt compositions

	1070°C Ferrodiorite			1120°C Tholeiite		
	groundmass	interface	calculated interface	groundmass	interface	calculated interface
Si	61.34	75.40	75.40*	56.90	75.21	75.21*
Ti	2.08	1.20	1.32	2.43	1.07	1.40
Al	13.13	11.36	8.35	13.12	11.10	7.55
Fe	10.61	4.31	6.75	11.31	4.50	6.51
Mn	0.39	0.11	0.25	0.17	0.07	0.10
Mg	2.19	0.86	1.39	4.20	1.56	2.42
Ca	5.48	2.35	3.49	7.84	2.58	4.51
Na	2.30	1.19	1.46	3.38	1.23	1.94
K	2.48	3.21	1.58	1.05	2.69	0.60
scalar	1.033	1.029		1.035	1.025	
mg#	0.27	0.26	0.27	0.40	0.38	0.40
ca#	0.33	0.34	0.33	0.35	0.31	0.35
nk#	0.49	0.48	0.49	0.51	0.44	0.51

	1140°C Tholeiite			1160°C Tholeiite		
	groundmass	interface	calculated interface	groundmass	interface	calculated interface
Si	56.60	72.84	72.84*	55.55	73.88	73.88*
Ti	1.53	0.75	0.96	1.23	0.49	0.72
Al	13.88	12.09	8.69	14.96	11.74	8.80
Fe	10.08	4.66	6.31	9.60	4.35	5.64
Mn	0.20	0.05	0.13	0.11	0.11	0.06
Mg	5.25	2.45	3.29	6.19	2.63	3.64
Ca	8.79	4.07	5.50	8.67	3.67	5.10
Na	2.87	1.37	1.80	2.95	1.53	1.73
K	0.80	1.72	0.50	0.74	1.60	0.44
scalar	1.018	1.025		1.005	1.019	
mg#	0.48	0.48	0.48	0.54	0.52	0.54
ca#	0.37	0.37	0.37	0.35	0.34	0.35
nk#	0.40	0.34	0.40	0.38	0.36	0.38

\* = defined value; calculated interface composition assuming simple mixing of silica and groundmass melt.

mg# = molar Mg/(Mg+Fe); error  $\pm 0.01$

ca# = molar Ca/(Ca+Mg+Fe); error  $\pm 0.01$

nk# = molar (Na+K)/Al; error  $\pm 0.02$

scalar = 100/(analysis total), used to normalize analyses to 100%

The interface melts were analysed 5-10 $\mu$ m from the rod-melt interface. The calculated interface compositions are estimated assuming that the interface melt is a mixture of groundmass melt and pure silica. The calculated interface composition underestimates the Al and K contents, while overestimating Fe, Mg and Ca. Pyroxene crystallization cannot account for these differences, as the ratio ca# remains constant.

The large discrepancies between actual and calculated interface melt compositions shows that the interface melt does not result from simple mixing of groundmass melt and silica. Instead, it must arise from differences in diffusion rates in the melt. The ratios mg#, ca# and nk# are fairly constant, but the slight variations may be critical in determining the nature of the crystallizing pyroxene phase.

### 3.3.3a Why does augite crystallize?

To explain the crystallization of augite in pyroxene-glass fringes around quartz in orthopyroxene andesite containing no groundmass clinopyroxene, Sato (1975) stated that the activity of Ca must be higher in the fringe than in the groundmass. Since ca# is constant in natural fringes (see table 3.4; Sato, 1975; respectively), Sato suggested that an increase in Ca activity could be brought about by decreasing the activity of Al, with which Ca may complex to form anorthite molecules in the melt. Decrease of the activity of Al in the melt may be related to the uphill diffusion of Na and K into silica-rich melt near the quartz. Al would then complex with Na and K to form alkali feldspar molecules rather than anorthite molecules in the melt. The overall result would be an increase in Ca activity, resulting in crystallization of Ca-rich pyroxene.

To check whether the activity of Ca is increased in natural samples due to a decrease in Al activity, the ratio  $n_{k\#}$  was calculated for glass analyses from the present experiments and from Sato's (1975) paper. Groundmass glass analyses from Sato's paper have similar  $n_{k\#}$  (0.38-0.46) to those from the present experiments (0.38-0.51; table 3.5), whereas the interface melt analyses from Sato's paper have much higher  $n_{k\#}$  than those in the present experiments (0.84-0.96 vs 0.34-0.48). Sato's theory would thus predict low-Ca pyroxene for all of the present experiments, even those in the ferrodiorite, in which augite crystallizes.

In the present experiments, the increased activity of Ca in fringe glasses may be prevented by efficient homogenization of melts by convection in charges which are mostly liquid. It must be remembered, however, that the natural samples studied by Sato were not isothermal, and the glass compositions record the conditions at quenching, which are not necessarily the same as present when pyroxene first nucleated around the quartz.

### 3.3.3b Melt chemistry

Compositions of analysed glasses (listed in appendix 2) were projected into the pseudoternary ol-cpx-qz (§2.7)<sup>6</sup> to test whether crystallizing pyroxene polymorphs were in equilibrium with surrounding glass (figure 3.15). The fields within this pseudoternary system (figure 3.15a) indicate which polymorph is expected to be in equilibrium with a particular melt composition. Groundmass melts from 1120°C and 1140°C runs plot near the ol-pig

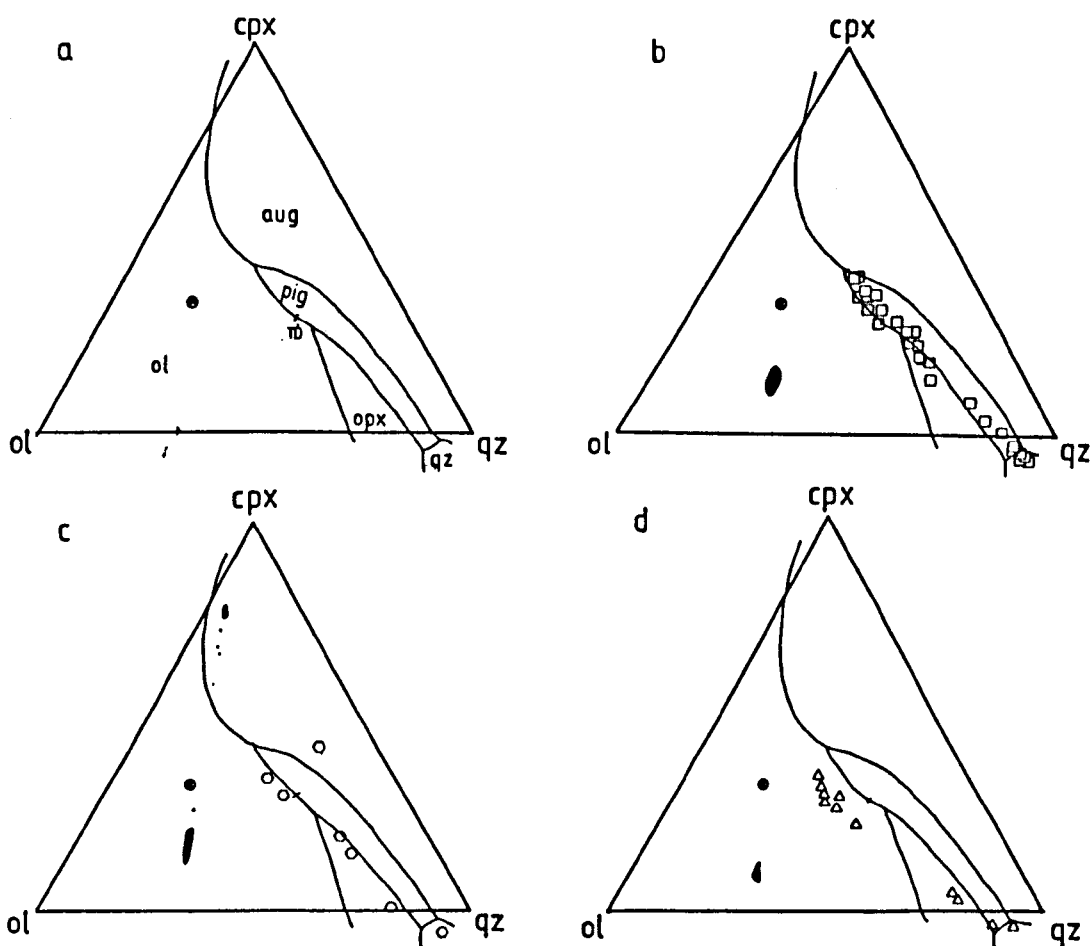
---

<sup>6</sup> One limitation of the ol-cpx-qz subprojection is its requirement for plagioclase saturation, since in the experiments there is no plagioclase present near the silica or in the glass-rich zone, although melts close to the silica may be close to saturation since the groundmass is still saturated. Thus the subprojection may not be strictly valid in these examples.

boundary curve, but the groundmass glass analyses from 1160°C charges plot in the olivine-plagioclase field. In these runs, all of the groundmass pyroxene has dissolved, and the composition of the liquid has moved away from the boundaries involving groundmass pyroxene into the ol-pl field.

Melt compositions adjacent to the rod-melt interface all lie close to the quartz-pigeonite field boundary. If any analyses are

Figure 3.15  
Projected melt compositions



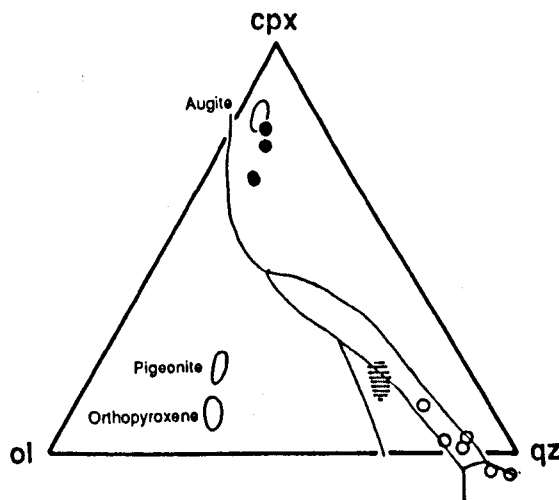
- a) Phase boundaries in the pseudoternary ol-cpx-qz from Grove and Baker (1984; figure 1). The fields labelled are olivine, augite, pigeonite, orthopyroxene and quartz. TD represents a thermal divide on the ol-pig boundary. All fields are in equilibrium with plagioclase. The circle with a cross marks the projected position of the Servilleta basalt composition.
- (b) Experimental data for 1140°C runs projected into the pseudoternary. Squares depict melt compositions, while black areas depict pyroxenes.
- (c) Data for 1120°C runs, hexagons represent melts.
- (d) Data for 1160°C runs, triangles represent melts.

mixes of groundmass melt and silica rod, projection into the pseudoternary will simply move them towards or into the quartz field. Since the interface melt must be saturated with silica (the dissolving phase) and with pigeonite (the crystallizing phase), the experimental data is in good accord with the location of the phase boundary proposed by Grove and Baker (1984). Projection of interface melts into the pigeonite field suggests pigeonite is stable rather than metastable in isothermal experiments. Intermediate compositions define mixing lines between endmember groundmass and interface glass compositions.

Melt compositions from adjacent to quartz dissolved in ferrodiorite plot for the most part in the pigeonite field (figure 3.16), but the melts closest to the quartz (5, 10 $\mu$ m) plot

---

Figure 3.16  
Projected melt compositions  
for ferrodiorite experiments



Melt and pyroxene compositions from the ferrodiorite experiments projected into the pseudoternary ol-cpx-qz. Fields as in figure 3.15. Fields labelled "augite", "pigeonite" and "orthopyroxene" represent pyroxenes and the shaded area represents melt from partial melting experiments. Filled and open circles represent pyroxenes and melts (respectively) from the quartz dissolution experiment (R27).

very close to the quartz-augite boundary. Interface melts in these charges are more Ca-rich than similar melts from experiments using the Servilleta basalt. In contrast, the melts from the groundmass of the ferrodiorite charges plot in the pigeonite field. This highlights the fact that the composition of the interface melt is critical in determining the composition of the pyroxene phase, and also that the composition of the interface melt is not uniquely determined by the groundmass melt chemistry.

### **3.3.3c Theoretical considerations regarding the composition of interfacial melts.**

Simple dissolution of a phase leads to the formation of an interface melt. If matter transport in the melt is fast, there will be little or no compositional distinction between bulk and interface melts. If, however, dissolution is slow by comparison with reaction at the crystal-melt interface, there will be a significant difference between the two compositions, with the interface melt composition displaced towards that of the dissolving phase. Experimental work on dissolution in silicate systems (simple and complex) favours mass transport as the dominant control on dissolution, rather than interface reaction (Oishi *et al.*, 1965; Kuo and Kirkpatrick, 1985a; Donaldson, 1985b; this work), but melt transport processes do not operate rapidly enough to eliminate the compositional variations. In simple systems, the interface melt composition is that, or nearly that, expected for equilibrium between the dissolving phase and melt in the relevant system at that temperature (Oishi *et al.*, 1965a). However, there is opportunity for differences in melt species mobility to affect the interface melt composition, because faster moving species are less depleted at the interface

than slower ones. As a result, the interface composition is not necessarily on a straight line between the bulk composition and the dissolving phase; in general the path of bulk to interface melt compositions is curved rather than straight, because the ratio of species diffusivities is not equal to the ratio of their concentration gradients. This is borne out by dissolution experiments involving silica and alumina (Oishi *et al.*, 1965), and by dissolution of olivine and quartz in melts from the system fo-di-si (Kuo and Kirkpatrick, 1985a).

This difference in interface chemistry, which will determine the pyroxene chemistry in the fringe, may be controlled by the chemistry of melts in the bulk of the charge, by the differing diffusivities for various chemical species into and out of the boundary layer (Oishi *et al.*, 1965), or by both. In these experiments it appears that diffusion of Ca in the melt and its resultant concentration in the interface melts is crucial to the formation of augite or pigeonite as the neocryst phase.

#### 3.3.4 Summary

Since all known examples of pyroxene fringes around quartz xenocrysts (see chapter four) are composed of augite and not pigeonite, one of the aims of this study was to ascertain whether the pigeonites grown in these experiments are the stable equilibrium phase that would be expected to crystallize from the interface melt.

It appears likely that pigeonite is the stable pyroxene phase in these experiments, but the absence of pigeonite in any natural samples is yet to be explained. It is possible that the crystallization of pigeonite in these experiments is fortuitous, as other experimental studies have shown pigeonite to be very

sensitive to melt composition (Kinzler and Grove, 1985; Grove and Juster, 1987). Kinetic effects are possibly responsible for this, although it is more likely that augite is the stable pyroxene phase in the majority of samples studied because of differences in melt chemistry.

### 3.4 Summary of experimental quartz dissolution

Dissolution of quartz occurs at constant rates below the liquidus and is accompanied by the crystallization of elongate, skeletal pyroxene neocrysts. Dissolution rates are kept constant by convection in the melt, and the presence of a silica-rich surface layer around the charge suggests that this convection is driven by differences in surface tension. The composition of the neocrystic pyroxene is probably critically dependent on small variations in melt chemistry at the interface.

## Chapter four

### Quartz-melt reaction textures in mafic and intermediate rocks

This chapter is concerned with natural examples of the reactions of quartz with host magmas, especially the incongruent dissolution textures experimentally investigated in chapter three. A brief survey of the literature is given, followed by the petrography of such textures in the 12 samples studied. The localities and general petrographic descriptions of these are given in appendix 1. Pyroxene compositions are used to estimate the temperatures at which the reaction textures formed. Comparison of data for these natural samples with the experimental results is used to estimate the duration of the incongruent dissolution reaction.

#### 4.1 Documented examples

Numerous descriptions of inferred reactions of quartz crystals with their host magma exist in the petrological literature, but these are mostly brief and uninformative. Four exceptions, providing extensive petrological detail of pyroxene fringes around resorbed quartz grains, are given by Wilshire (1961), Wilkinson (1962), Searle (1962a) and Sato (1975). Table 4.1 is a compilation of references to igneous rocks with resorbed and reacted quartz, with emphasis on the incongruent dissolution reaction. The approximate geographical occurrences of these are shown on figure 4.1.

The most common evidence of reaction is the resorbed and embayed forms shown by quartz in a great variety of igneous rocks. Resorption may be evidenced simply by rounding of the crystal, or by the formation of a glass-rich zone and crystallization of pyroxene (incongruent dissolution). Such

# Table 4.1

## Described quartz reactions.

#	Area	Host magma	Phases in rim	Reference	#	Area	Host magma	Phases in rim	Reference
1	Umnak Is.	AK ol. andesite	augite	Byers 1961	11	W.Ethiopia	ol.basalt	px, fsp	Augustithis 1978
2	Glacier PK.	WA dacite	(resorbed)	Eichelberger 1978a,b	11	Uganda	alkali basalt	px,gl, trid, Kfsp, ne	Holmes 1936
3	Nevada	rhylolite	(rounded) <sup>1</sup>	Coats 1968	12	Itinomegata	basalt	clinopyroxene	Aoki+ 1982
3	Nevada-Oregon	rhylolite	(resorbed), fsp	Conrad 1984	12	Nijijima Japan	basalt	px, hb	Koyaguchi 1986b
4	Sierra Nevada	bas. andesite	pyroxene	Al Rawi+ 1967	12	Shikoku, Japan	bas./andesite	augite, <sup>10</sup> glass	Sato 1975
4	Cinder Cone CA	andesite	augite	Eichelberger 1975	12	Oki Is, Japan	basalt	cp, brown glass	Uchimizu 1966
4	Clear Lake CA	andesite	augite	Finkelberger 1975	13	New Britain	(bas.)andesite	(highly embayed)	Lowder+ 1970
4	Cinder Cone CA	andesite	glass, augite	Finch+ 1930	14	NSW Aust	basalt	cp (mostly)	Binns 1969
4	Chaos Crags CA	basalt	augite, glass	Heiken+ 1980	14	NSW Australia	basalt (analc)	cp, gl, alkfsp	Wilkinson 1962
4	Owens Valley CA	basalt	augite, brown glass	Knopf 1938	14	NSW Australia	basalt (analc)	di, pl, alkfsp, ilm, ap	Wilshire 1961
4	Lassen CA	basalt	pyroxene	Macdonald+ 1965	15	Tauhara TVZ	basalt	pyroxene, glass	Eichelberger 1978a,b
4	Cinder Cone CA	andesite	augite, glass	Smith+ 1968	15	Tauhara TVZ	basalt	clinopyroxene	Eichelberger 1975
4	California	ol.basalt	clinopyroxene	Webb 1941	15	TVZ	hybrids	glass, clinopyroxene	Graham+ 1987
4	Chaos Crags CA	bas. incl.	augite <sup>8</sup> , hb	Williams 1931	15	TVZ	basalt	(rounding), cpx <sup>11</sup>	Lewis 1968
5	Arizona	NM ol. tholeiite	sericite, chlorite	Anderson 1968	15	Auckland NZ	basalt	Ti-mt, (augite)	Rafferty+ 1979
5	Taos	qz-porphry <sup>3</sup>	aug, crist, Na-plag	Aoki 1967	15	TVZ	basalt	pyroxene	Reid+ 1983
5	Utah	bas. andesite	clinopyroxene, glass	Hause+ 1977	15	Auckland NZ	basalt	glass, pyroxene	Searle 1962a
5	Colorado	bas./andesite	augite	Larsen+ 1936	16	Moeraki NZ	thol.dolerite	augite	Nakamura+ 1973
5	Taos	basalt	thin px rim	McMillan+ 1988					
5	Colorado	basalt	(rounded, embayed)	Thomson+ 1985					
5	Montana	rhylolite	(resorbed)	Conrad 1984					
6	Yellowstone WY	basalt	augite, glass	Wilcox 1944					
7	Soufrière <sup>4</sup>	andesite	glass, augite	Eichelberger 1978a,b					
7	Mt Pelé	"dacite" <sup>5</sup>	augite, tridymite	MacGregor 1938					
8	Arran	comp. dyke	clinopyroxene	Carmichael 1962					
8	Skye	basalts etc	clinopyroxene	Kanaris-Sotirion+ 1985					
8	Ballachulish	granodiorite	feldspar, pyroxene	Harker 1904					
8	Skye	"marscoite" <sup>6</sup>	aug, olig, hb	Muir 1953					
9	Maxain BRD	alkali basalt	pyroxene	Wager+ 1965					
9	Puy de Dome	basalt	pyroxene	Augustithis 1978					
9	Massif Central	diorite	biotite, amphibole	Augustithis 1978					
9	Massif Central	basalt	clinopyroxene	Barbarin 1988					
9	Auvergne	FR basanite	clinopyroxene	Hutchison+ 1975					
9	Trégastral	FR olivine norite	augite, glass <sup>9</sup>	Lacroix 1893					
10	Anatolia	basalt	cp, glass	Maury+ 1974					
10	Santorini	bas. andesite	augite, fsp, bi	Thomas+ 1932					
10	Aegina, Greece	calc-alkaline	pyroxene	Keller 1974a					
			augite	Nicholls 1971					
			clinopyroxene	Pe 1973					

# = map reference on figure 4.1.  
 The reference cited is given in terms of the first author only, followed by a "+" if there is more than one author, and the year of publication.

Abbreviations used:  
 Area: AK California, USA  
 CA New Mexico, USA  
 NM Wyoming, USA  
 WY Taupo Volcanic Zone, NZ  
 TVZ alk. bas.  
 bas. ol.  
 thol. tholeiitic  
 alkfsp alkali feldspar  
 bi biotite  
 cord cordierite  
 crist cristobalite  
 gl glass  
 Kfsp K-feldspar  
 ne nepheline  
 plag plagioclase  
 Si silica phase

BRD West Germany  
 FR France  
 NZ New Zealand  
 WA Washington, USA  
 analc. analcime  
 comp. composite  
 qz. quartz

augite  
 chlorite  
 clinopyroxene  
 feldspar  
 hornblende  
 magnetite  
 oligoclase  
 pyroxene  
 tridymite

<sup>1</sup> Quartz traversed by melt-filled tubes, often blind.  
<sup>2</sup> Olivine with augite rims may be seen in the same section.  
<sup>3</sup> Precambrian.  
<sup>4</sup> Also at Martinique.  
<sup>5</sup> The presence of corroded quartz crystals with augite rims and the presence of labradorite suggest that this "dacite" is an inhomogeneous mixed rock of dubious parentage.  
<sup>6</sup> eg France, West Germany, West Indies, Somalia etc.  
<sup>7</sup> eg basalts, andesites, nephelinites.  
<sup>8</sup> Also (orthopyroxene), spinel, nepheline, cordierite, tridymite and cristobalite. Augite closest to the quartz is occasionally zoned to aegirine.

<sup>9</sup> In both the basalt and the dacite these reaction rims were overgrown by later quartz.  
<sup>10</sup> Also tridymite, cristobalite, sanidine, biotite, oxides, clays, (orthopyroxene) and plagioclase.  
<sup>11</sup> present in crystalline rocks, absent in glassy rocks.

textures are seen in rocks ranging in composition from basanites, through basalts and andesites to dacites, and are widely accepted as resulting from chemical disequilibrium between the quartz and the host magma.

In basalts and andesites, quartz grains and highly siliceous xenoliths often have irregular outlines and are rimmed by minute prismatic augite crystals, often in association with brown glass. Tridymite or sodic plagioclase may also be present in the reaction zone. Augite in reaction rims is Mg-rich, and Ti-, Al-poor compared to augite in the groundmass of a rock (Smith and Carmichael, 1968; Nakamura and Coombs, 1973; Sato, 1975; Eichelberger, 1978a), and is present in rims even where the groundmass of the host contains orthopyroxene and no augite (Muir, 1953; Sato, 1975).

Quartz crystals in dacites are often well rounded with substantial embayments indicative of resorption, and in some dacites quartz crystals may be surrounded by reaction rims of

---

Figure 4.1  
Referenced localities



Approximate localities of rocks containing dissolving quartz referred to in table 4.1.

glass and augite. Rimmed and unrimmed quartz may be present together in the same section. This, and the fact that dacites often exhibit reaction rims on other minerals (eg olivine), suggests that some of these "dacites" (eg MacGregor, 1938) may be hybrids resulting from the contamination of a magma with either a solid, or a partially molten or a liquid contaminant.

Quartz phenocrysts in rhyolites are largely anhedral and embayed. Arran pitchstones (72-73wt% SiO<sub>2</sub>) contain quartz phenocrysts with irregular boundaries, surrounded either by spherulitic birefringent material (a devitrification product) or by minute fringes of pyroxene microlites (Carmichael, 1962). With this exception, there are no reported instances of quartz in rhyolites with a reaction rim.

There are exceptions to pyroxene being the principal mineral rimming quartz. Table 4.1 also documents instances of amphibole and mica in the reaction rims. In some samples these are inferred to be primary magmatic phases (eg Barbarin, 1988), as they may be overgrown by quartz during regrowth (§4.3.3; Koyaguchi, 1986b). In others, the presence of hornblende may be due to magmatic or hydrothermal replacement of pyroxene (§4.3.1). The presence of rims of sericite and chlorite around quartz (Anderson, 1968) is probably the result of hydrothermal or meteoric alteration of a pyroxene and alkali feldspar reaction rim.

#### 4.2 Origin of the quartz

Review of the literature suggests several origins for quartz in mafic and intermediate magmas.

Quartz may occur as xenocrysts derived from crustal rocks encountered and assimilated by the magma, for example, lumps of quartzite (Harker, 1904; p351) or gneiss (Maury and Bizouard,

1974). If the temperature of a typical mafic magma is higher than the solidus of incorporated xenoliths, partial melting will occur initially at quartz-feldspar boundaries and extending in some examples to more than half of the xenolith (eg Al-Rawi and Carmichael, 1967; Maury and Bizouard, 1974). Once the xenolith has achieved about 45% partial melting it loses its rigidity and may easily disaggregate<sup>1</sup> (Kovach and Marsh, 1981), releasing residual solid material (eg grains of quartz) into the host magma (eg Al-Rawi and Carmichael, 1967; Bogoyavlenskaia, 1972)<sup>2</sup>. The presence and composition of inclusions within the quartz may provide information on its source. For example, rhyolitic glass inclusions imply quartz derived from granite (Mies and Glazner, 1987).

Xenocrysts of quartz may also be derived from a contemporaneous magma by magma mixing (eg Eichelberger, 1978a,b; Sakuyama, 1981). These may be recognised in the resultant hybrid as pseudomorphs after high quartz (eg Koyaguchi, 1986b), suggesting that the quartz phenocrysts originally nucleated and grew in a silicic magma.

A third possibility is that the quartz is a phenocryst phase

---

<sup>1</sup> Obviously the viscosity of the partial melt phase and that of the host magma will exert some control on the degree of partial melting required for disaggregation. Grapes (1986) documents xenoliths which have achieved 40% partial melting and are still largely intact. For the inverse situation, solidification of a crystallizing liquid is thought to occur at about 60% crystallinity (Sparks and Marshall, 1986).

<sup>2</sup> Theoretical studies of melt distribution within a porous solid (Cheadle and McKenzie, 1988) suggest that, for monomineralic xenoliths with a crystal-melt-crystal dihedral angle of 59° (for quartz, Jurewicz and Watson, 1985) disaggregation could occur at ≈30% liquid, and for a dihedral angle of 40° the volume fraction of liquid required would be ≈25%. However, these studies require ideal melting (along all grain edges), whereas a polymineralic xenolith will melt along quartz-feldspar boundaries before quartz-quartz boundaries. If partial melt were to pool or escape, the estimates above would be low.

of the magma. Nicholls *et al.* (1971) demonstrated that the activity of silica in a magma increases with pressure such that mafic liquids could become saturated with silica. Hence, quartz may be stable in mafic liquids at elevated pressures and cognate in the same way as high pressure pyroxene phenocrysts (eg Binns *et al.*, 1970).

To support this, Carmichael *et al.* (1974) proposed that melting of quartz eclogite at depth would give a basaltic or andesitic liquid in equilibrium with quartz. If there was any growth of quartz under these conditions, inclusions of trapped melt would be expected. On depressurization (magma ascent) the quartz would become unstable, not only with respect to its host magma, but also with respect to any melt inclusions it might contain. No mention is made of the existence of such melt inclusions, or their reaction with the host quartz, by authors proposing a cognate status for quartz. However, if the quartz were residual from partial melting of quartz eclogite and no regrowth occurred, no inclusions would be expected, and the grain would be rounded rather than euhedral. In any case, melting of quartz eclogite has been shown inappropriate for the production of basalt or andesite, since quartz is never a liquidus phase during the experimental crystallization of andesite. It occurs near the liquidus at  $P > 30$  kbar (dry) but increasing water content increases silica solubility (Green and Ringwood, 1968).

The common round shape of quartz phenocrysts in rhyolite and dacite is often ascribed to a decrease in silica activity (increase in silica solubility) in the magma as it rises through the crust (eg Nicholls *et al.*, 1971). This reasoning is not generally applicable to more mafic liquids carrying resorbed quartz crystals, which often betray other evidence of magma

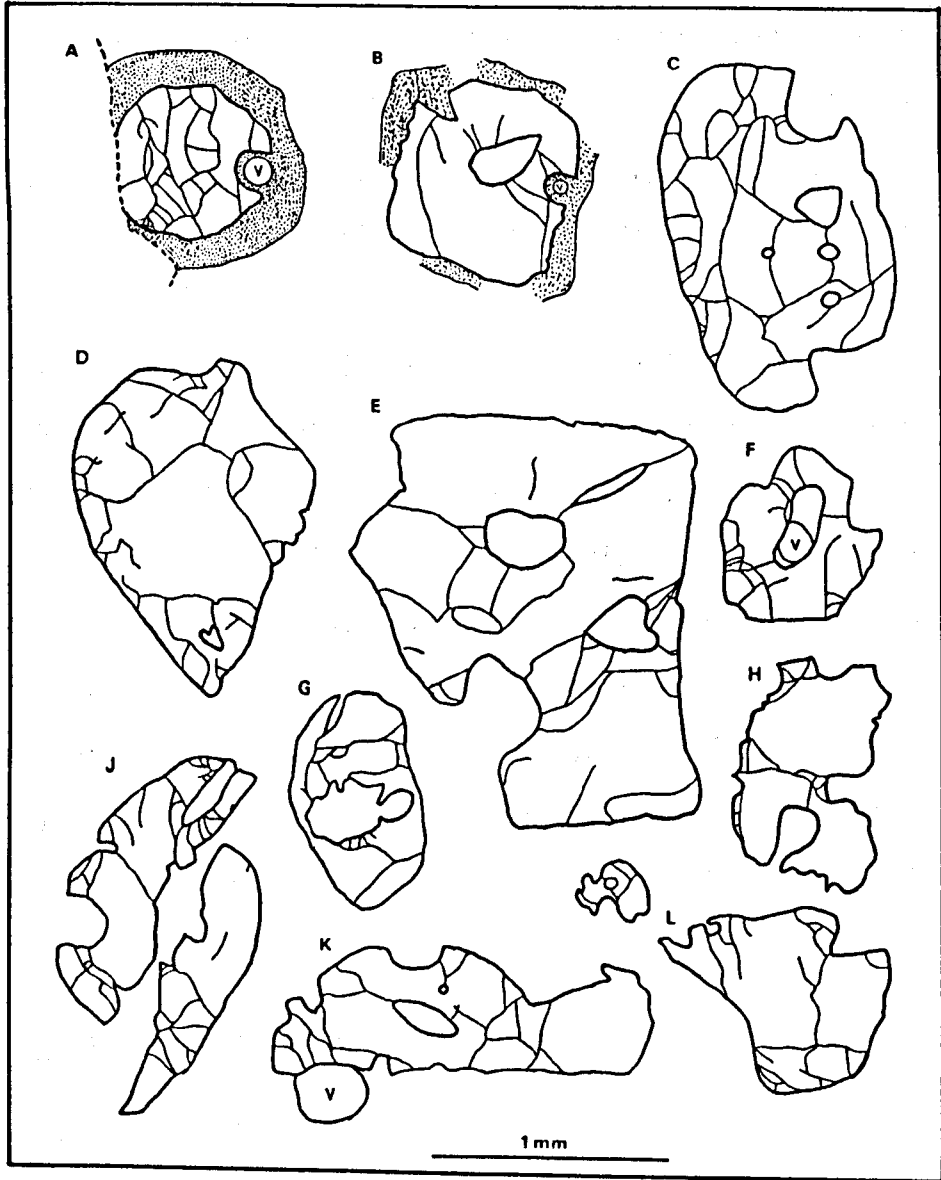
hybridization, eg sponge-textured sodic plagioclase (Tsuchiyama, 1985). Koyaguchi (1986b) showed that the composition of such plagioclase is inconsistent with its derivation from basement material and concluded that magma mixing was the only viable explanation. In addition, xenocrystal plagioclase may only be derived from depths equivalent to pressures  $\leq 800\text{MPa}$  (Wyllie, 1984) and therefore cannot be derived from melting at greater depth. It would seem that in these examples a non-cognate status for the quartz should be preferred.

Donaldson (1985b) has shown that, regardless of provenance or condition, there is essentially no difference in the dissolution rates of quartz under superliquidus conditions, whether in the form of phenocrysts (from rhyolite), crystals from hydrothermal veins, or strained crystals. However, since superliquidus dissolution rates are much higher than subliquidus rates, it is possible that slight differences in rates between quartz grains of different derivations may be masked at superliquidus conditions, in the same way that crystallographic dependence of dissolution rate may be (eg for olivine; Jurewicz and Watson, 1988b). Following the work of Donaldson (1985b), it is assumed here that the origin of the quartz bears little on calculations of residence ages.

#### **4.3 Petrography of some samples containing reacted quartz**

For this project a collection of samples containing reacted quartz was made, some collected and some donated by other departments. The samples and their sources are described in appendix 1. Reaction textures around quartz in mafic liquids are described from observations of the sample collection, and compared to experimental analogues (chapter three).

Figure 4.2  
Quartz grains in RC404.



### 4.3.1 General features

Quartz crystals are often well rounded and cracked (eg figure 4.3k), sometimes with an irregular jagged face where a rounded crystal has split along a crack (eg figure 4.2j). Some quartz crystals are irregular and angular (eg figure 4.2h). Large cracks through quartz are filled by brown glass, often intersecting circular pockets where fluid or melt inclusions have been invaded by exterior melt. These melt pockets may be cross sections through melt tunnels (plates 4.1g, 4.2c). Angular fragments of quartz often have irregular edges with hemispherical embayments (sites of inclusions) and form by the separation of grains along cracks. Several quartz grains observed have round surface embayments, sometimes truncated by later embayments still containing gas vesicles (eg figures 4.2a,b,f, 4.3f,h). The best example (plate 4.2c) is a quartz grain with a long blind embayment containing a vesicle, now carbonate-filled. This is consistent with the embayment being formed by "upward drilling" of the vesicle into the quartz (Donaldson and Henderson, 1988).

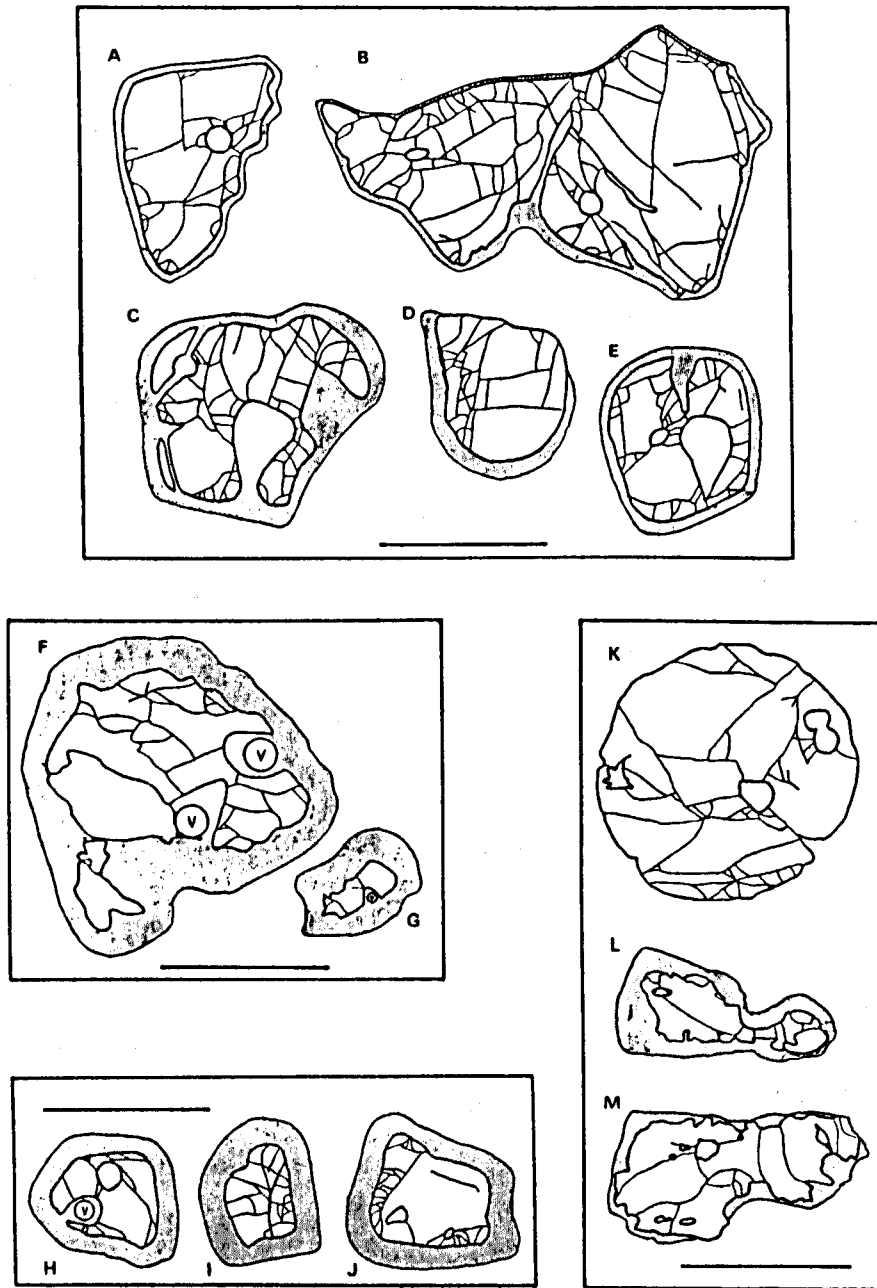
The quartz is usually surrounded by a fringe of prismatic clinopyroxene and brown glass. Small skeletal pyroxenes are embedded in brown glass close to the quartz surface on which they nucleated. Cusps on the surface occur where pyroxenes are still in contact with the quartz, each capped by or embaying a skeletal pyroxene (plates 4.1a, 4.2a,b). Some cusps are visible as inclusions of quartz within hollow pyroxenes and may have become

---

Figure 4.2 (facing page)

Line diagrams of quartz grains found in mixed dacite (RC404). Stippled areas denote pyroxene fringe, where present. V denotes a gas-filled vesicle. g is well rounded, a,c are well rounded and embayed, d,j are round and fractured, b,f are subround, h,k are angular and embayed while e,l are angular with rounded edges.

Figure 4.3  
Quartz grains in other samples.



detached from the quartz. This texture is often developed in experimental runs (§3.1.5), but never to the same extent. Further from the quartz the pyroxenes become stouter and more equant, and the ratio of pyroxene to interstitial glass increases from about 1:1 to 5:1. Around a quartz there may be several clusters of pyroxenes towards the outer edge of the fringe, each composed of acicular crystals radiating from a single point (plate 4.2d). Continued growth of the outer part of the fringe, using pyroxene components from the groundmass, brings the pyroxenes into contact with one another, whereupon they become connected, and start to form a rigid network. If this occurs to a large degree, the outermost pyroxenes will form a barrier that is impermeable to melt transport, isolating the quartz and adjacent silica-rich glass, and preventing chemical communication between the host basalt and interface melt. Tridymite needles projecting from the quartz into the brown glass are only observed in examples where the pyroxene fringe has become sealed.

Broadly, pyroxene fringes can be subdivided into three main textural types:

- 1) A glassy fringe containing discrete euhedral or skeletal crystals, similar to those developed experimentally (§3.1), eg plate A1a. The glass is continuous through the crystals - ie the fringe was porous with respect to melt.

---

Figure 4.3 (facing page)

Line diagrams of quartz grains. Stippled areas denote pyroxene fringes. V denotes a gas-filled vesicle. Each scale bar is 1mm long. e,i,j,k are well rounded, c,h are well rounded and embayed, d is round and fractured, b is angular, and a,f,g,l,m are angular and embayed.

a-e: H121372; f,g: H100428; h-j: H74389; k-m: H121594

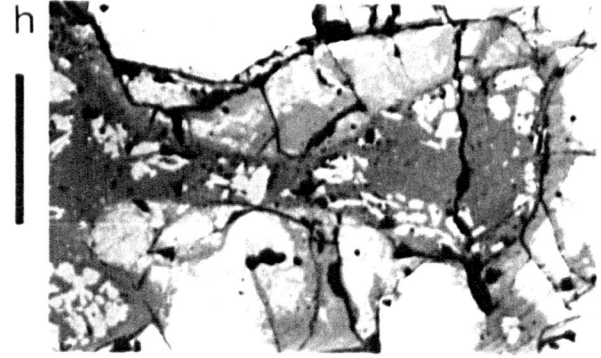
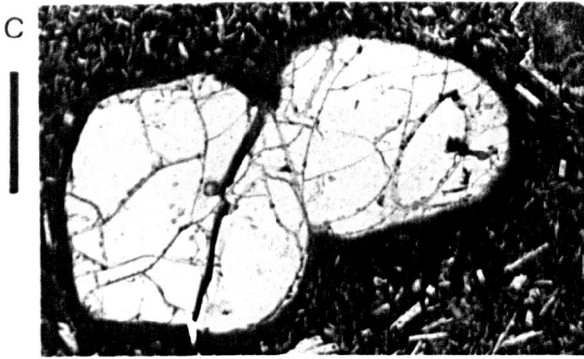
Plate 4.1

Photomicrographs of quartz grains with reaction rims.

Scale bars are 500 $\mu$ m.

- a) RF15 Quartz xenocryst, surrounded by a fringe of pyroxene and glass. Close to the quartz the pyroxenes are radial and acicular, whilst against the groundmass they are equant and stubby.
- b) H59909 Quartz crystal, surrounded by radially arranged augite prisms intergrown with feldspar, biotite and hornblende. Further from the quartz, slightly altered, equant pyroxenes form a solid continuous band, isolating the quartz from the host rock.
- c) H121372 Two grains of quartz, still attached, showing preferential dissolution along their mutual grain boundary (notching) and fracture of one grain, after the formation of the reaction rim of pyroxene and glass. Pyroxenes are generally radially oriented and prismatic. At the top right is a sponge-textured plagioclase.
- d) RC324 Quartz grain with pyramidal facets, included pyroxene and a rim of hornblende.
- e) H121592 Well rounded quartz grain with a hemispherical embayment, from which radiate two melt-filled tubes.
- f) H121592 (As (e)). Reflected light view of fringe pyroxenes, which are acicular, skeletal, and include quartz, or surround cusps on the quartz surface (bottom).
- g) H100429 Quartz with an incomplete reaction rim of pyroxene and glass. The crystal contains a tunnel and several inclusions of glass, some pyroxene and occasional tridymite. The similarity of this mineralogy to that of the reaction rim suggests that the round inclusions are connected to the external reaction rim, and may even be sections across melt tunnels through the quartz.
- h) H100429 (As (g)). Reflected light image of a pyroxene and melt inclusion within the quartz xenocryst, connected to the encircling reaction rim via a crack or tunnel.

Plate 4.1  
Quartz grains with reaction rims.



- 2) A fringe of interconnected pyroxenes which isolates melt and skeletal pyroxenes close to the quartz, eg plates 4.2a,c; A4a.
- 3) A fringe of texturally equilibrated and interconnected pyroxenes, isolating (often devitrified) glass with equant pyroxenes adjacent to the quartz, eg plates 4.1b; A3d.

In rocks containing quartz xenocrysts with reaction rims, similar textures of pyroxene and glass lacking a central quartz are often present (eg plate A4c,d). These structures are either sections through the edge of a fringe without including any quartz, or examples where the quartz crystal has completely dissolved.

A number of natural examples exhibit rims of amphibole rather than pyroxene. Quartz crystals in RC324 are rimmed entirely by amphibole crystals (plates 4.1d; A3b). However, the quartz includes small crystals of ferroaugite, which probably crystallized as the quartz was dissolving and were subsequently overgrown by quartz during cooling, thus protected from alteration to amphibole (plate A3a). In RC394 (plate A3c) marginal alteration of fringe pyroxenes to amphibole has occurred, but the process is incomplete (also Muir, 1953). It is possible that amphibole may crystallize directly around a dissolving quartz in a hydrous magma, but the pyroxene inclusions within quartz in RC324 suggest that the amphibole here has replaced pre-existing pyroxene.

#### 4.3.2 Regrowth features

In some of the rocks studied, the surface of rounded quartz grains may be covered by faceted pyramids about 100 $\mu$ m high (eg

Plate 4.2

Compositional images of reacted quartz with pyroxene rims.  
Scale bars are 100 $\mu$ m.

- a) RC417 Quartz (black), partly plucked, with a reaction rim of glass (grey) and pyroxene (white). There are many cusps on the quartz and inclusions of quartz completely enclosed by hollow pyroxene crystals.
- b) RC417 (As (a)). Inclusions of quartz (dark grey) sheltered within hollow pyroxene crystals.
- c) H121592 Part of a quartz xenocryst, surrounded by a rim of euhedral pyroxene prisms in glass. The fine network of cracks across the quartz have trapped SnO<sub>2</sub> (white) during polishing of the section. Larger cracks contain glass and must have opened during reaction with the magma. The crystal is deeply embayed in several places, and one of the embayments contains two carbonate-filled vesicles (centre). Along the margins of embayments and cracks the quartz has partially recrystallized, forming fine needles of tridymite.
- d) LP14 A radiate cluster of several acicular pyroxene crystals (light grey) in a reaction rim around quartz (black, bottom). Tridymite needles (black, 10-50 $\mu$ m long) form an irregular layer on the quartz surface (bottom).

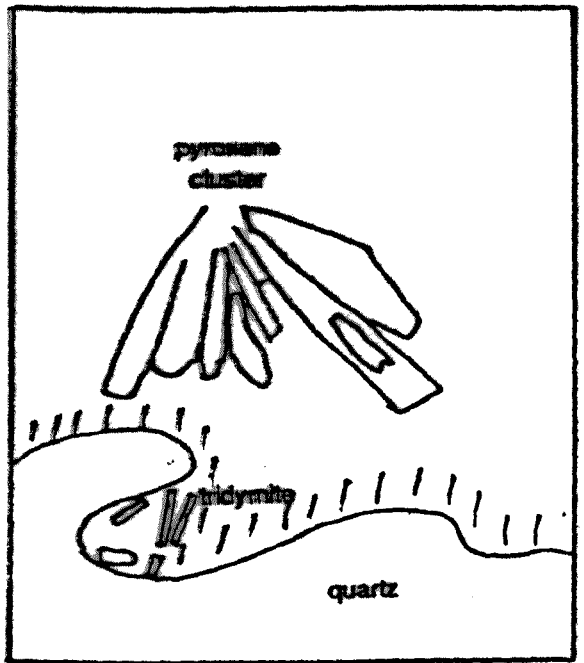
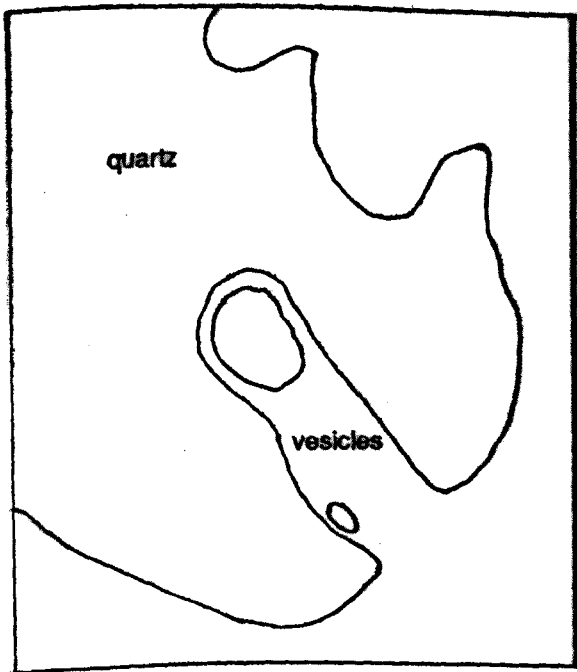


## Plate 4.2

Compositional images of reacted quartz with  
pyroxene rims.

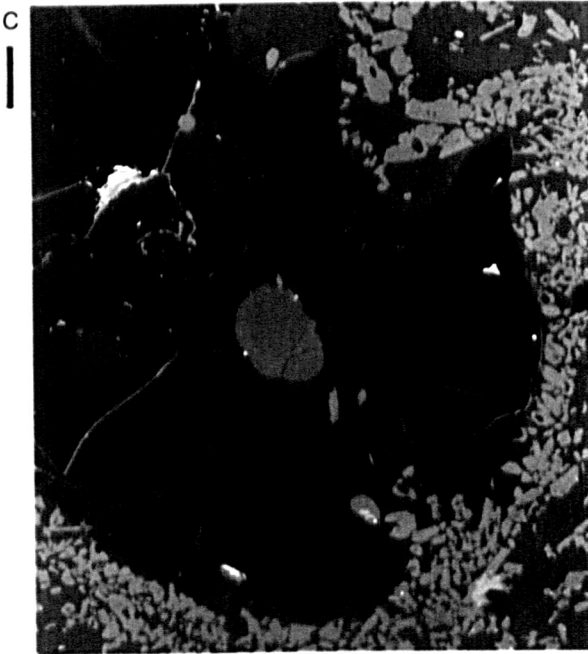
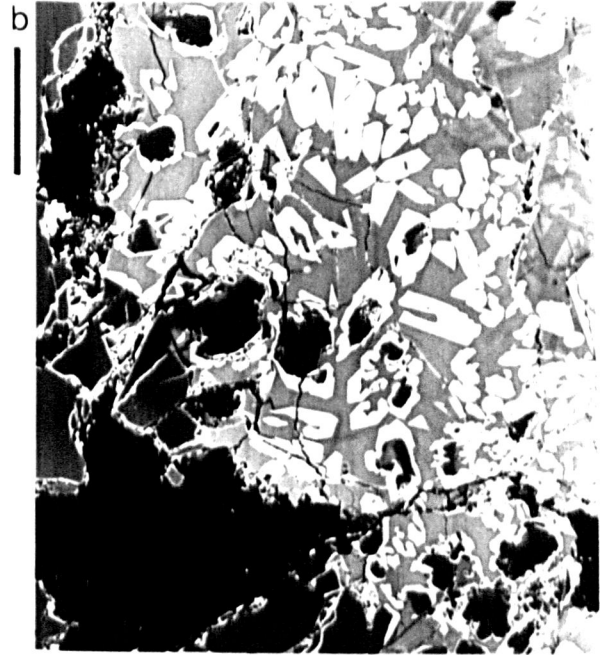
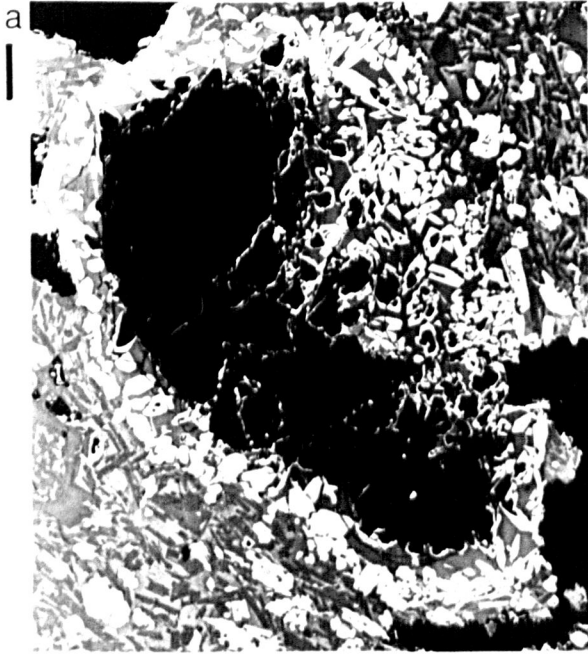
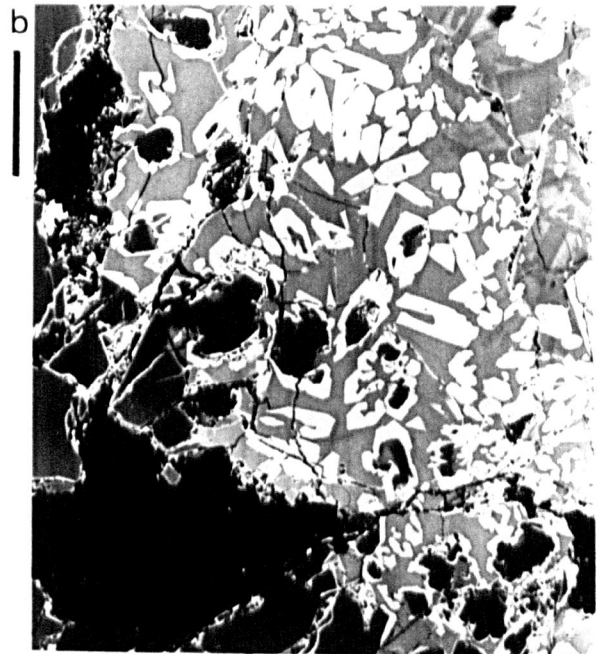
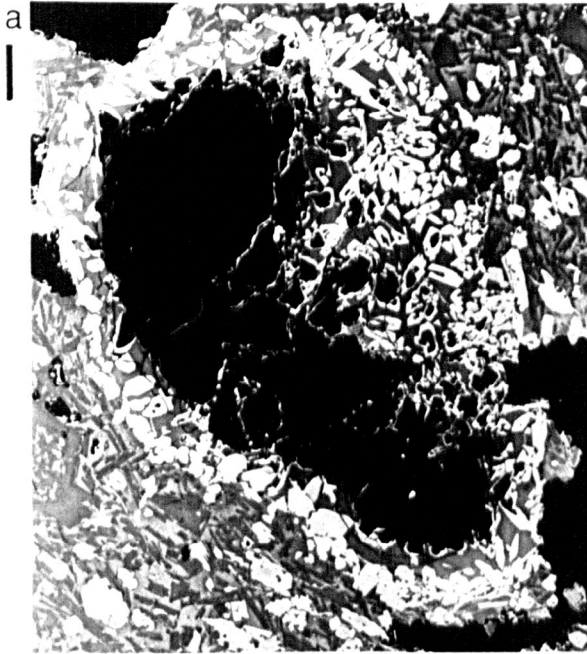


# Plate 4.2

Compositional images of reacted quartz with  
pyroxene rims.



plates 4.1d; A3b). These overlie an inclusion-rich zone in the quartz, which preserves the rounded form of the post-dissolution quartz grain. Some of the inclusions may be pyroxene (plate A3a). Pyramids indicate that some crystallization of quartz has occurred from the siliceous melt trapped between the pyroxene fringe and the relic quartz during cooling. The regrowth hypothesis is preferred to the formation of faceted crystals by dissolution (§1.2.4).

In other rocks, quartz crystals are covered by tridymite needles that have crystallized from the trapped siliceous melt (eg plate 4.2d). Other quartz crystals show no regrowth at all. Tridymite needles are only seen on quartz crystals where the surface of the quartz is sheltered from the external melt. They often occur in melt-filled cracks or tunnels within a quartz grain (plate 4.2c), but will only occur on the external surface if the pyroxene fringe has completely sealed off the microsystem within (eg plate 4.2d). The variation, from no silica regrowth, through needles of tridymite to quartz growth pyramids, is dependent on the pressure and temperature conditions prevailing after dissolution ceases, although it is likely that the silica content of the trapped siliceous glass, the rate of cooling and the water content of the melt will also be relevant. Rapid cooling may not allow the nucleation of a silica phase because of their complex framework structure (Swanson and Fenn, 1986). The temperature of the quartz inversion to tridymite increases rapidly with pressure (229°C per kilobar; McBirney, 1984, p213-4). Tridymite is stable at low pressures and higher temperatures such that growth of tridymite from liquids at 1100°C must have occurred within 3km of the Earth's surface.

### 4.3.3 Comparison with experimental textures

In many respects the petrography of natural samples mirrors the features of experimentally dissolved silica (§3.1); in particular, the morphologies and orientations of pyroxene crystals (§3.1.1), and the development of cusps where pyroxene neocrysts are close to the surfaces of quartz crystals (§3.1.4). The major differences are

- (a) the presence of deep embayments in the quartz, sometimes clearly associated with vesicles, whereas vesicles in the experiments hinder dissolution and lead to cusp formation (§3.1.2, §3.1.4);
- (b) the occurrence of radiate clusters of pyroxene needles in natural samples;
- (c) the fracture of quartz grains, which has been observed in experiments dissolving crystalline quartz (Kuo and Kirkpatrick, 1985a; Donaldson, 1985b). The silica glass rod used in the experiments (chapter three) does sometimes fracture, but this may be ascribed to pellet pressing.

### 4.4 Shapes of quartz

The diversity of shape of quartz crystals in mafic and intermediate rocks is shown in figures 4.2 and 4.3. In this section various processes that may account for this diversity are discussed.

#### 4.4.1 Mechanisms of rounding

Previous experiments have demonstrated that dissolution of quartz grains into a magma at high undersaturations typically results in rounding and smooth embayment-free interfaces being developed against melt (Watson, 1982; Donaldson, 1985a,b; Kuo and Kirkpatrick, 1985a). Under these conditions dissolution is relatively fast and any slight variations in dissolution rate with crystallographic direction will be obscured.

Curved faces can form by growth of a crystal and are often found in metamorphic rocks (Holmes, 1921), but crystal growth in experimental studies typically involves flat faces (eg Donaldson, 1976).

Another possibility is that a rounded form may result from mechanical abrasion, that is, the gentle rubbing of crystals against others in a magma. If the crystals are already in contact with one another, movement within the magma might lead to abrasion, or to crystal fracture. If the crystals are not in contact with one another, impact must occur before abrasion or fracture are possible. To consider whether this mechanism is plausible it is necessary to contemplate the processes involved. Around any moving particle in a viscous fluid there will be a velocity boundary layer (VBL), such that adjacent to the crystal there will be no movement of the fluid relative to the crystal face. Viscous shear stresses from the bulk of the fluid cause the fluid velocity to increase with distance from the crystal, until the bulk velocity is achieved at the edge of the VBL. During movement within a partly crystalline magma, this boundary layer will cushion the suspended crystal from impact against other particles, or against a fixed object with which the magma is in contact (eg the walls of a magma chamber). Two particles in

suspension are unlikely to come into mutual contact because of the presence of their VBLs. It is conceivable that a particle might be able to "burst through" its cushioning VBL and impact a stationary object, by having sufficient momentum to displace the intervening boundary layer. However, the displacement of fluid (sideways with respect to the relative motion of the particle and stationary object) will tend to deflect the particle sideways, decreasing the probability of direct impact. A higher crystal content of a magma might enhance the possibility for abrasion, but at the same time would increase the viscosity of the fluid and decrease the possibility of movement.

#### 4.4.2 Mechanisms of fracture

Cracking and separation of quartz during heating occurs because quartz has different coefficients of thermal expansion in different crystallographic directions (Kingery *et al.*, 1976). Lines of fracture in quartz grains are irregular and often intersect inclusions (eg figure 4.2c). Melt inclusions are often present in rounded quartz grains found in rhyolite or dacite (Mies and Glazner, 1987) and will tend to disrupt its crystal structure, providing weaknesses along which a fracture may propagate. Fluid inclusions within a crystal will have a similar effect. Rapid temperature changes experienced by such a crystal, either upon incorporation into a magma, or upon eruption, may result in pressure build-up within inclusions or thermal shock causing crystals to fracture along lines of weakness, ie through the inclusions. This will result in quartz crystals with one or more fractured surfaces containing rounded embayments (the original locations of the inclusions), as seen in figure 4.2h,j,k. In some examples, both halves of a quartz crystal are

still adjacent to one another (figure 4.2j).

Mechanical impact between crystals (§4.4.1) might also cause crystal fracture, but the paucity of broken crystals in lavas and intrusions suggests that this mechanism is not important. However, if the magma has a yield strength at subliquidus temperatures (McBirney and Murase, 1984), viscous shear stresses in the magma may be transmitted through the velocity boundary layer to the crystal and cause fracture.

#### 4.4.3 Mechanisms of embayment

Embayments have traditionally been interpreted as either an unstable growth feature or (more usually) as a consequence of dissolution. Under experimental conditions, rapid growth of quartz usually leads to crystal shapes that are either skeletal with well-formed faces or euhedral (Swanson and Fenn, 1986). The problem with the dissolution interpretation has been the overriding tendency for experimental dissolution to impose on a crystal a rounded form and smooth interface with the melt (§4.4.1).

Surface embayments are often visible at the margin of a crystal where a fracture has intersected a fluid or melt inclusion, and the result is an embayment at the location of the inclusion (Mies and Glazner, 1987) eg figures 4.2h,j,k, 4.3f,l,m. Similar embayments have been experimentally reproduced by the action of gas bubbles (Donaldson and Henderson, 1988). Vapour bubbles, either as vesicles or released from fractured fluid inclusions, are capable of locally enhancing dissolution at the surface of a quartz crystal to form hemispherical embayments. Figures 4.2a,b,f and 4.3f,g,h are examples of rounded embayments in quartz still containing gas bubbles. However, cavities formed

by either of these proposed mechanisms will be unstable, because of the tendency of dissolution to round corners and create a more equant form with a lower surface area (Donaldson, 1985a).

#### 4.4.4 Summary

The rounded forms of quartz grains in mafic rocks are most likely to result from dissolution, because such grains are often accompanied by pyroxene reaction rims. Grains fracture along lines of weakness in a crystal, which are often due to the presence of melt and fluid inclusions. Separation of a crystal along such lines leaves angular faces with hemispherical embayments. Rarely, a large embayment may preserve a vesicle (filled by gas or secondary minerals), indicative of embayment formation by enhanced dissolution around the vesicle.

Highly angular quartz grains (eg figures 4.2h,j,k,l and 4.3b,c,f,l,m) are extremely unstable with respect to dissolution into an undersaturated melt because of their high surface area relative to a sphere. In examples where both rounded and angular faces exist, the mechanism that produced the angular surfaces must have occurred late compared to rounding, and may be related to the eruption and cooling of the rock.

### 4.5 Chemistry of pyroxenes and coexisting phases

#### 4.5.1 Chemistry of pyroxenes from reaction rims and groundmass

Microprobe analyses of pyroxenes and glasses (where present) in reaction rims around quartz were obtained for samples LP14, H100426, H100428, H100429, H121372, H121592, H74389, RC324, RC404, RC417, RC420 and BM14. Typical analyses are given in table 4.2.

All of the pyroxene compositions obtained in this study are

Table 4.2  
Typical pyroxene compositions.

Rock	Distance* ( $\mu\text{m}$ )	Analysis	SiO <sub>2</sub>	TiO <sub>2</sub>	Al <sub>2</sub> O <sub>3</sub>	FeO	MnO	MgO	CaO	Na <sub>2</sub> O	Total	others
BM16	10	PX1BD52	53.43	0.38	0.11	8.66	0.29	12.47	23.27	0.44	99.05	
BM16	30	PX2BD58	53.19	0.20	0.12	8.80	0.37	13.25	23.40	0.21	99.89	0.15 Zr
BM16	55	PX3DD50	52.85	0.77	1.08	6.52	0.22	13.97	23.98	0.62	100.01	
BM16	GM core	PXGM5	47.83	2.30	6.08	6.14	0.17	13.37	23.24	0.29	99.64	0.22 Cr
BM16	GM rim	PXGM9	40.01	4.88	12.23	8.26	0.07	10.14	23.77	0.31	99.77	0.1 Cr
H74389	10	PXC10C	52.91	0.46	0.39	11.50	0.30	14.81	18.83	0.36	99.56	
H74389	GM	GMPXD	50.18	1.34	2.32	13.08	0.25	14.00	17.55	0.44	99.16	
H74389	XC	PXRND4	51.84	0.56	2.80	8.64	0.27	17.70	17.79	0.24	99.84	
H100426	30	PXC30A	52.76	0.51	0.82	10.84	0.29	15.38	18.44	0.26	99.30	
H100428	25	PXC25A	53.29	0.22	0.58	8.68	0.33	16.76	19.41	0.10	99.37	
H100428	GM	PXGMB	48.38	1.05	5.12	7.73	0.20	15.47	19.86	0.32	98.27	0.14 Cr
H100428	GM	PXGMD	55.17	0.21	0.67	13.23	0.29	28.37	1.88	0.0	99.82	
H100429	25	PX225A	53.82	0.18	0.27	8.69	0.22	16.91	19.42	0.17	99.82	0.14 Ni
H100429	130	PX2130C	51.55	0.43	1.47	10.97	0.35	17.20	16.83	0.22	99.36	0.34 Ni+Cr
H106444	16	PX237/1	53.46	0.21	0.67	7.68	0.20	15.90	20.62	0.28	99.02	
H106444	GM	PX237/7	51.20	0.65	4.23	6.38	0.16	17.25	19.01	0.31	99.19	
H121372	35	PXC35	52.17	0.64	1.75	9.89	0.27	16.82	16.65	0.29	98.59	0.11 Ni
H121372	GM	PXGME	51.54	1.01	3.66	7.52	0.23	16.42	19.10	0.42	100.16	0.26 Cr
H121592	20	PX1C20D	52.77	0.53	0.45	10.01	0.47	15.76	19.06	0.34	99.49	0.1 Cr
H121592	130	PX1C130A	52.72	0.42	0.52	10.79	0.26	15.83	18.46	0.30	99.45	0.15 Cr
H121592	90	PX1090A	51.36	0.32	2.63	23.49	0.95	19.79	1.18	0.11	99.83	
H121592	GM	PXOGMA	53.25	0.37	2.29	16.19	0.37	25.37	1.78	0.10	99.72	
LP14	33	PX11/4	53.35	0.13	0.36	7.53	0.14	16.75	20.99	0.23	99.48	
LP14	130	PX11/3	53.13	0.23	1.09	6.46	0.18	18.42	19.56	0.22	99.29	
LP14	GM	PX11/18	53.31	0.43	1.16	18.21	0.39	24.16	2.32	0.0	99.98	
LP14	GM	GMPX5	52.05	0.76	1.57	10.56	0.42	16.03	18.08	0.42	99.89	
RC324	INCL	PX#35	51.08	0.40	0.29	21.02	0.70	9.48	17.73	0.22	100.92	
RC404	10	PX229/10	53.56	0.18	0.26	10.16	0.33	14.73	20.65	0.23	100.10	
RC404	GM	PX229/17	53.63	0.34	0.93	10.35	0.37	16.92	17.46	0.19	100.19	
RC404	GM	PX229/16	53.70	0.37	2.43	14.25	0.30	26.76	2.30	0.0	100.11	
RC404	GM	PX229/15	54.34	0.11	0.62	18.60	1.04	24.98	0.63	0.0	100.32	
RC417	41	PX243/24	53.73	0.40	0.55	8.09	0.21	17.43	19.48	0.21	100.10	
RC417	GM	PX243/34	54.41	0.31	0.77	14.80	0.38	27.31	2.03	0.0	100.01	
RC417	GM	PX243/16	51.68	0.67	2.81	8.23	0.30	16.53	19.12	0.27	99.93	0.32 Cr
RC420	52	PX224/1	53.82	0.10	0.25	7.17	0.22	16.33	21.03	0.20	99.12	
RC420	GM	PX224/10	52.57	0.34	2.45	5.26	0.17	17.81	20.08	0.22	98.90	

Typical glass analyses (between quartz and fringe)

Rock	Distance	Analysis	SiO <sub>2</sub>	TiO <sub>2</sub>	Al <sub>2</sub> O <sub>3</sub>	FeO	MnO	MgO'	CaO	Na <sub>2</sub> O	K <sub>2</sub> O	Total
H106444		GL237/5	83.73	0.22	6.81	1.82	0.0	0.45	0.80	2.50	2.69	99.02
H121372	20	GL20	74.57	1.21	12.38	1.91	0.0	0.0	0.28	1.29	6.17	97.81
LP14		GL3Aa	79.58	0.62	11.35	0.94	0.06	0.09	0.30	1.18	3.28	97.40
RC404	18	GL229/2	79.21	0.37	10.89	1.61	0.0	0.11	0.48	1.28	4.23	98.18
RC417	10	GL243/33	78.10	0.48	10.92	2.78	0.63	0.36	0.75	1.02	3.94	98.48
RC420	10	GL224/11	80.97	0.23	7.56	2.03	0.05	0.56	0.88	2.53	3.34	98.15

Typical amphibole analysis

Rock	Analysis	SiO <sub>2</sub>	TiO <sub>2</sub>	Al <sub>2</sub> O <sub>3</sub>	FeO	MnO	MgO	CaO	Na <sub>2</sub> O	K <sub>2</sub> O	Total
RC324	AM#33	49.81	0.49	2.66	25.41	0.40	9.40	9.89	0.95	0.31	99.32

INCL - included pyroxenes      GM - groundmass pyroxenes      XC - xenocrystic pyroxenes

\* Distance of the analysis point from the surface of the quartz crystal.



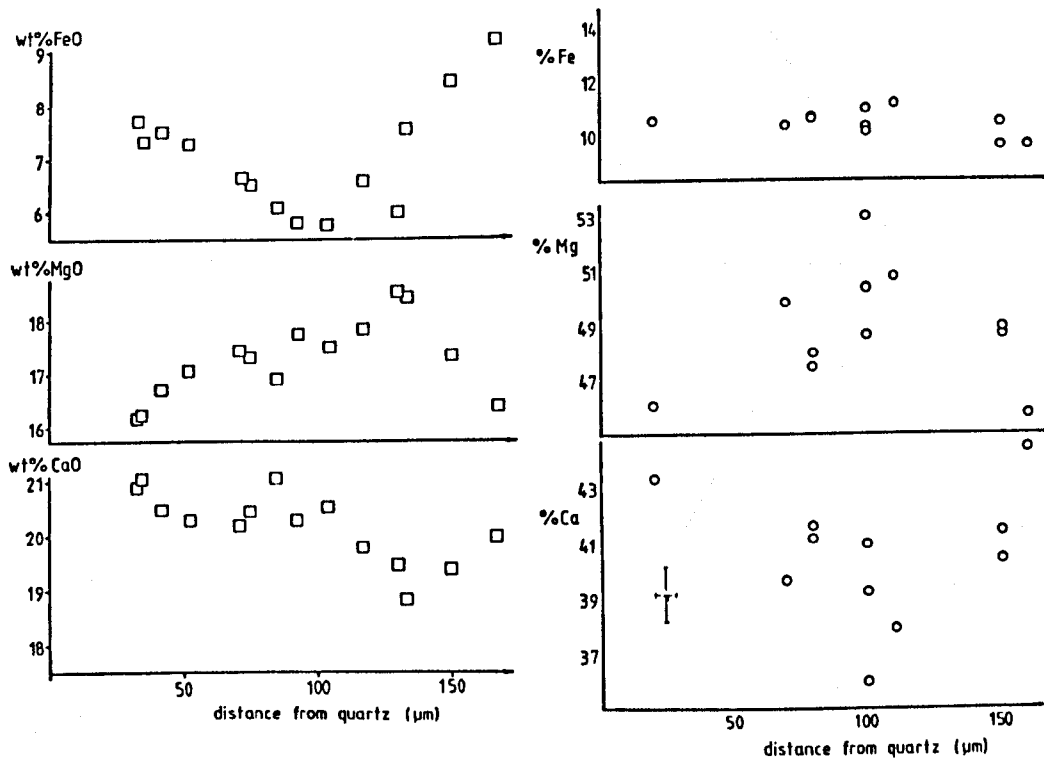
Existing pigeonite close to dissolving quartz was overgrown by augite and thereby protected from reaction with the siliceous melt (cf pigeonite overgrowing augite in experiments; §3.1.1; plate 3.3a).

Detailed microprobe traverses of pyroxene compositions across two reaction rims were carried out. Relative molar proportions of Ca, Mg, Fe were computed and plotted against distance from the quartz.

Pyroxenes from LP14 (figure 4.5a) exhibit a minimum FeO content at 100 $\mu$ m from the quartz, as well as a minimum CaO content and a maximum MgO content at 130 $\mu$ m from the quartz. Pyroxenes from H100428 (figure 4.5b) show a maximum for Mg and a minimum for Ca at about 100 $\mu$ m from the quartz, whereas Fe shows no significant variation. These maxima and minima represent the location of first pyroxene nucleation (the initial size of the quartz (§3.1.1)), with higher Mg and lower Ca contents suggesting higher temperatures of crystallization. Pyroxene growth continued during cooling, as indicated by increasing Ca and decreasing Mg/Fe, both towards and away from the quartz. This highlights that care must be taken when assuming that the width of the pyroxene fringe corresponds to the width of dissolved quartz (cf §3.2.2), since in LP14 approximately 25% of fringe growth has occurred outside the zone of first pyroxene nucleation.

In the pyroxene quadrilateral the compositions of pyroxenes from LP14 vary with distance from the quartz (figure 4.6). The trends of pyroxene compositions are parallel both towards and away from the quartz from the locus of first pyroxene nucleation, with crystals towards the quartz being richer in Ca. Within 40 $\mu$ m of the quartz, there is a sudden change in the crystallization

Figure 4.5  
Variation in pyroxene compositions across rims.

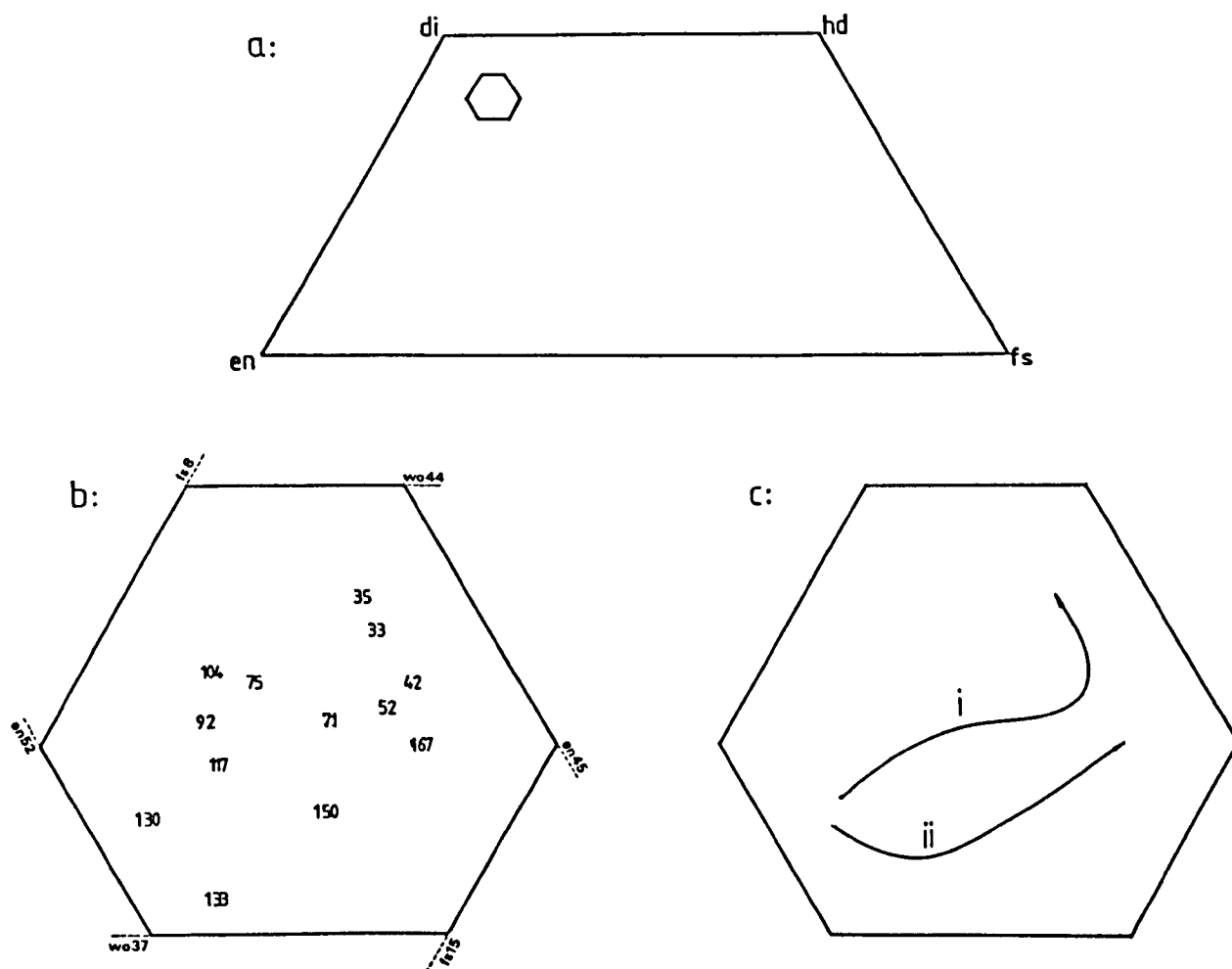


- FeO, MgO and CaO contents of pyroxenes from a reaction rim against their distance from the central quartz (LP14). Errors are included within the size of the squares.
- Molar proportions of Fe, Mg and Ca of pyroxenes from a pyroxene fringe against their distance from the central quartz (H100428). Typical errors are given.

trend, with a sharp enrichment in Ca at constant Mg. This may be due to rapid cooling on eruption.

Fringe pyroxenes closer to the quartz typically have higher Fe/Mg ratios and Ca contents than those towards the outer edge (table 4.3), implying lower temperatures of crystallization, consistent with the bulk of pyroxene growth occurring towards the retreating quartz during cooling (figures 4.5, 4.6). If the quartz was simply a site for pyroxene nucleation and underwent no

Figure 4.6  
Trends in pyroxene composition across a rim.



Fringe pyroxenes from LP14 projected into the pyroxene quadrilateral (a).

b) Location of pyroxene compositions; numbers refer to the distance of the analysis point from the surface of the quartz ( $\mu\text{m}$ ).

c) Trends of pyroxene composition from the inferred point of first pyroxene nucleation ( $\approx 130\mu\text{m}$ ). (i) Towards quartz; (ii) away from the quartz.

---

dissolution (Muir, 1953), pyroxene compositions should signify decreasing temperatures of crystallization away from the quartz, rather than towards it.

Compositional gradients of pyroxene chemistry across a fringe were noted in §3.3.1 for longer experimental runs, where the composition of the melt varies across the fringe. It is

Table 4.3  
Trends in fringe pyroxene chemistry

Rock	Ca increase towards quartz	Fe/Mg increase towards quartz	Al,Ti decrease towards quartz
LP14	yes	yes	yes
RC404	?	?	yes
H121372	?	?	yes
RC417	?	?	yes
H121592	yes	yes	yes
H100428	yes	yes	yes
H100429	yes	yes	yes
H74389	yes	yes	yes
RC420	yes	yes	yes
H100426	?	yes	yes
H106444	flat	yes	yes
BM16	?	?	yes

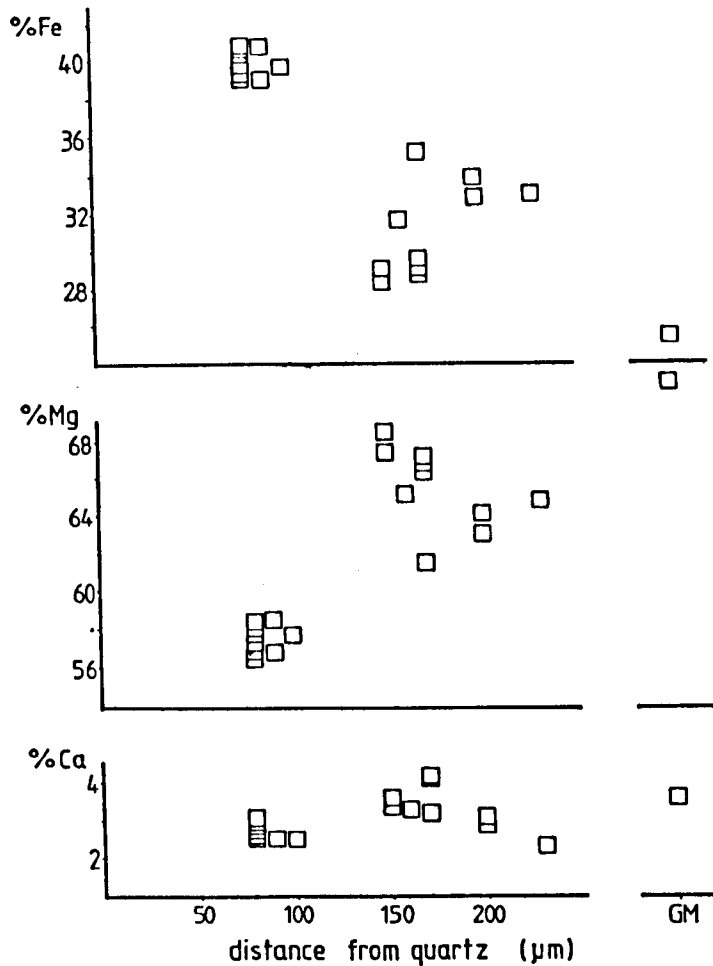
possible that these isothermal effects (Ca contents and Mg/Fe ratios both decreasing towards the silica) might account for the compositional effects attributed above to decreasing temperature of pyroxene crystallization. In the natural examples described here, pyroxene Mg/Fe values also decrease towards the quartz, but by 2 to 6 times more than in R49 (32 days at 1143°C). However, Ca contents of pyroxenes in natural reaction rims increase towards the quartz, indicating that the isothermal effect on Ca contents has been reversed.

Orthopyroxenes in the groundmass of H121592 exhibit little systematic variation in Ca, Mg and Fe contents (figure 4.7), except that a chemically distinct generation of orthopyroxene has crystallized close to the quartz at the edge of the groundmass, but outside the augite fringe. This reflects the local change in melt chemistry brought about by the dissolution of quartz, which would have depressed the orthopyroxene liquidus and locally delayed crystallization to lower temperatures.

Pyroxenes close to quartz in BM16 have colourless cores with bright green rims. Microprobe analysis (in appendix 2) reveals that the cores are augite, and the rims have aegirine contents of

Figure 4.7

Variation in groundmass orthopyroxene chemistry.



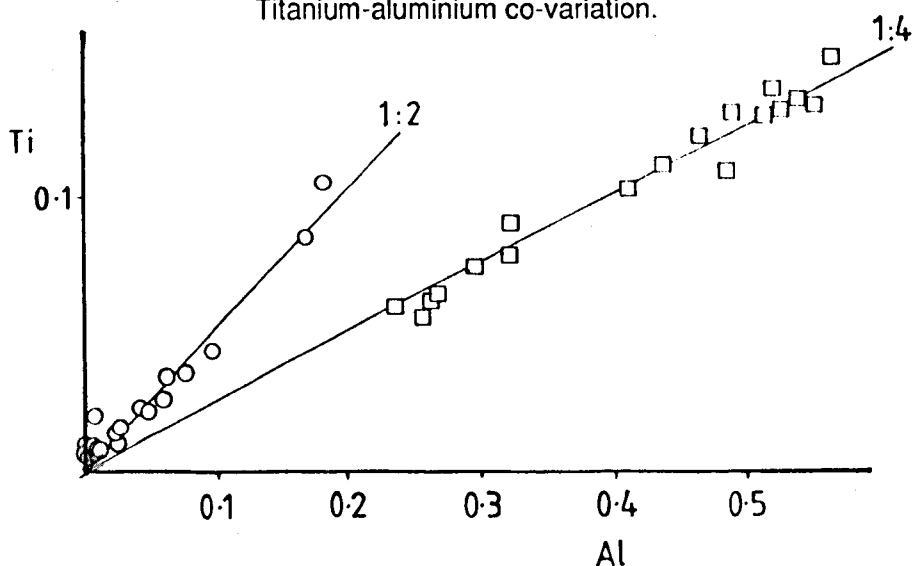
Molar proportions of Fe, Mg and Ca of orthopyroxenes against their distance from a nearby quartz grain (H121592). The closest pyroxenes (70-100μm) impinge on the outer edge of the reaction zone, and appear to be compositionally distinct from the others.

up to 30% in most instances, with one analysis of a pyroxene rim recognized as a titanian aegirine (5.11 wt%  $\text{TiO}_2$ , 24.67 wt%  $\text{FeO}^*$ , 14.52 wt%  $\text{Na}_2\text{O}$ ). These rims, mentioned by Lacroix (1893; p18-19), are thickest on faces towards the quartz, especially on radial acicular crystals, suggesting that these were growing towards the quartz from the enclosing band of pyroxene. A sharp compositional discontinuity (within the resolution of the imaging technique; about 1μm) between core and rim of pyroxenes suggests a sudden change in crystallization conditions (plate A4). This

late aegirine crystallization could have been brought about either by a sharp temperature decrease on eruption, or by depletion of melt close to the quartz in augite components after growth of the pyroxene fringe isolated this innermost melt from the host basanite.

The Ti:Al plot for fringe and phenocrystic pyroxenes from BM16 reveals two different relationships between Ti and Al (figure 4.8). Fringe pyroxenes follow the trend  $Ti=Al/2$ , suggestive of the substitution  $R^{2+}_2Si_2O_6 \rightleftharpoons R^{2+}TiAl_2O_6$ . However, pyroxene phenocrysts follow the trend  $Ti=Al/4$ , suggesting that the two substitutions  $R^{2+}_2Si_2O_6 \rightleftharpoons R^{2+}TiAl_2O_6$  and  $R^{2+}_2Si_2O_6 \rightleftharpoons R^{2+}AlSiAlO_6$  occur together. The change in Ti/Al ratio from 1/4 to 1/2 has been interpreted to be due to the onset of plagioclase crystallization removing Al from the melt (Bence and Papike, 1972), but more recently the substitution of Ti into clinopyroxene has been shown to dramatically affect  $Fe^{2+}$ -Mg partitioning (Sack and Carmichael, 1984).

Figure 4.8  
Titanium-aluminium co-variation.



Molar proportions (per six oxygens) of Ti and Al in fringe (circles) and phenocrystic pyroxenes (squares) from BM16.

In general, pyroxenes (even the orthopyroxenes in H121592) crystallizing in the silica-rich melt zone around a dissolving quartz are enriched in Si and depleted in Ti and Al compared to groundmass and phenocrystic pyroxenes (tables 4.2, 4.3; also Sato, 1975) because of the high silica activity of the melt from which the fringe pyroxenes grew (Kushiro, 1960; Le Bas, 1962; Nakamura and Coombs, 1973). This feature will also be characteristic of pyroxene-glass ocelli formed by the complete dissolution of quartz.

#### 4.5.2 Relationships between pyroxenes and coexisting melts

Holmes (1936) demonstrated that the quartz xenocrysts in a basic melt are surrounded by a rhyolitic glass, and not simply melted directly to a liquid of their own composition (the melting point of silica is 1713°C; Kushiro, 1972); this is substantiated by the analyses of interface glasses in appendix 2. Across the pyroxene fringe and the glass-rich zone, there is a complete spectrum of glass compositions formed by some mixing mechanism. This complete spectrum is illustrated for silica in figure 3.8.

Mixing of silicate liquids, even on a small scale around a dissolving quartz, will not generally result in straight-line variation diagrams. The intermediate compositions may still diverge from a simple pattern of proportional mixtures, and compositional gradients may not be linear (eg Yoder, 1973), because rates of diffusion vary for different elements, and according to the water content of the system (Johnstone and Wyllie, 1988). This is discussed in §3.3.3b.

Where possible, the composition of glass trapped between a quartz and its pyroxene reaction rim was analysed. These melt compositions were projected into the pseudoternary ol-cpx-qz

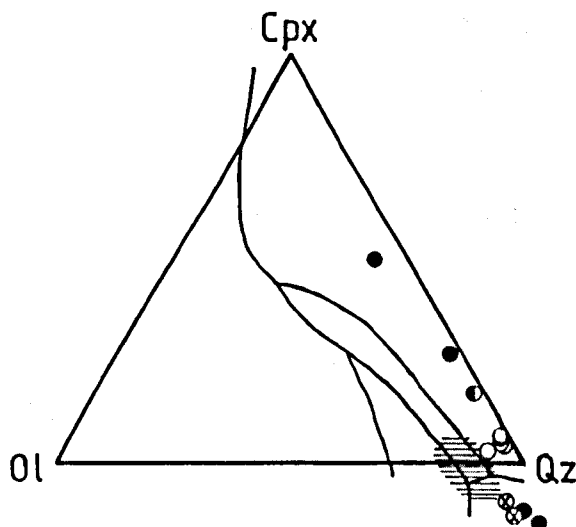
(§2.6). Whereas the interface melts from experimental charges plot in the pigeonite field or at the pigeonite-quartz phase boundary (§3.3.3a; figure 3.15), the interface melts from natural charges plot either in the augite field or in the quartz field (figure 4.9). This suggests that a significant difference in major element chemistry is responsible for the difference in pyroxene polymorphs between fringes in natural examples and fringes produced in the present experiments.

#### 4.5.3 Pyroxene thermometry

Analysed pyroxene compositions were used to estimate temperatures of reaction texture formation. Values obtained from three methods are summarised in table 4.4. The two-pyroxene thermometers record temperatures ranging from 1220 - 850°C, with the dacite (RC404) recording lower temperatures than the basalts

---

Figure 4.9  
Projected melt compositions.



Melt compositions from various natural samples projected into the pseudoternary ol-cpx-qz (§2.6). The hachure denotes the projection of interface melts from quartz dissolution experiments in SK918 (figure 3.15). Data from H121372 (half-filled circle), LP14 (filled circles), RC417 (crossed circles), RC420 (open circles).

(LP14, H121372, RC417, H100428), and the andesite (H121592) being intermediate. Temperatures from the three thermometers are mutually consistent, and are averaged when estimating the temperature of the dissolution reaction.

For those rocks without orthopyroxene, the temperatures calculated using the thermometers must be regarded as minimum estimates, since the clinopyroxene is not constrained to solvus compositions. The errors for these one-pyroxene estimates are not calculable, but comparison with two pyroxene temperatures for similar rocks (eg H100429 with H100428, RC420 with RC417) suggests that the estimates may still be fairly accurate. Measured temperatures range from 1170 - 870°C, except for the rounded pyroxene "xenocrysts" from H74389 (1230°C). The maximum temperature recorded in a fringe is again used to model the dissolution reaction.

These estimates compare well with field measurements of temperatures of andesite magmas, which range from 1110-1050°C (Gill, 1981). BM16 pyroxenes project close to the di-hd join and for the most part are too Ca-rich to permit thermometric calculations. Two analyses of fringe pyroxenes allow temperature estimates of around 900°C to be obtained; however, these seem implausible as temperatures from the crystallization interval of such an olivine-rich rock, and are interpreted as resulting from post magmatic re-equilibration of the pyroxene compositions at lower temperatures. No thermometry is possible on the pyroxene phenocrysts in this rock because they are too Al-rich.

These temperature estimates are used in conjunction with measurements of the widths of reaction rims in chapter eight to calculate residence times for reacted quartz.

#### 4.6 Summary

Natural examples of pyroxene reaction rims around quartz are similar in many respects to experimentally developed textures, with skeletal pyroxene prisms often radially oriented about a rounded quartz grain. However, many of the natural textures have evolved beyond the limits of this laboratory investigation. Pyroxene growth has continued at the outer edges of the fringes, which have become sealed. One major difference between the experiments and the natural examples is the nature of the pyroxene phase in the reaction rim. Even in one sample (H100426) where pigeonite was a groundmass phase, it only occurs in the fringe as cores to augite crystals. This is not a consequence of equilibration and recrystallization because even porous and glassy fringes (rapidly quenched) are composed of augite.

## Chapter five

### The experimental dissolution of orthopyroxene

This chapter reports experiments investigating the dissolution into an alkali olivine basalt of two orthopyroxenes. The two compositions are an enstatite ( $en_{94}$ ) and an aluminous bronzite ( $en_{78}$ ) (56 experiments in total).

#### 5.1 Petrography of enstatite experiments

As discussed in §2.1.3, the enstatite contains garnet, clinopyroxene and chromite; all are chrome-rich and usually exsolved as blades or plates parallel to {100}. Deformation followed exsolution in some enstatite fragments, with the result that the exsolution lamellae are now bent, whilst remaining parallel to one another (plate 2b).

In the terminology of Dawson and Stephens (1976, 1975) for kimberlitic garnets, the composition of the garnet lamellae is that of chrome pyrope. Garnet is not stable at low pressure, and atmospheric pressure experiments by Donaldson (1984) showed that a chrome-poor pyrope decomposes rapidly at temperatures above 1100°C to melt and either olivine or orthopyroxene, such that 100µm lamellae (the maximum size present in this enstatite) would decompose in 30 minutes at 1120°C, and 2.5 minutes at 1180°C.

##### **5.1.1 Heating in the absence of basalt**

Upon heating the crystal, the garnet lamellae in the enstatite decompose, but the new phases present within the lamellae are not identifiable by backscattered electron imaging because of their fine-grained nature (R130: 28 hours at 1191°C). After prolonged heating, olivine neocrysts form within the lamellae (148 hours at 1215°C; Donaldson, unpublished data).

Both the enstatite and its included garnet are metastable with respect to olivine plus melt at run temperatures, but reaction of the enstatite to olivine and melt only occurs in the presence of melt, which acts as a flux. Decomposition of garnet to olivine or orthopyroxene also releases a melt (Donaldson, 1984), which may flux the decomposition of enstatite to olivine, although it is difficult to tell whether such decomposition has occurred. The decomposition of the garnet in these partial melting experiments is not rapid either, but is enhanced by the presence of melt. The exsolved clinopyroxene and chromite are both stable in these experiments.

### 5.1.2 Heating in the presence of basalt

Partial melting of the basalt leaves angular plagioclase and rounded olivine grains rich in melt inclusions surrounded by partial melt. Euhedral-subround inclusion-free overgrowth occurs on olivines in the groundmass, while plagioclase fragments become euhedral with time. Large groundmass olivines close to the reaction rim are reverse-zoned, with Fe-rich cores (residual from the original basalt) overgrown by new olivine material.

In all of the dissolution charges examined, decomposition of the garnet has been rapid, for there is no remnant garnet within the enstatite. It has been replaced by a mass of fine olivine needles and melt, surrounded by small grains of plagioclase and chromite (plate 5.2b). The products of garnet decomposition are much coarser in dissolution experiments than after a comparable period of partial melting, suggesting that the influx of basalt melt speeds garnet decomposition and textural equilibration (§5.5) of the breakdown products.

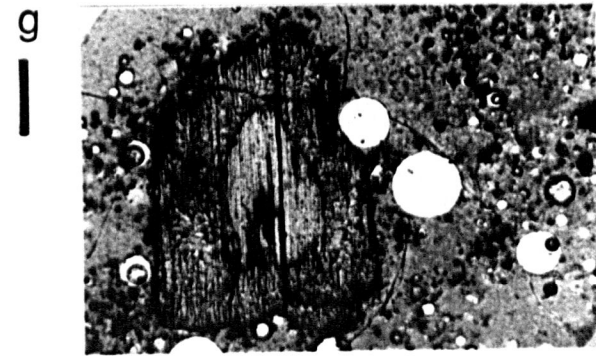
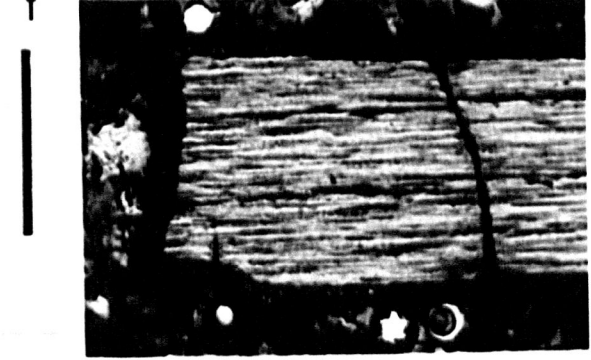
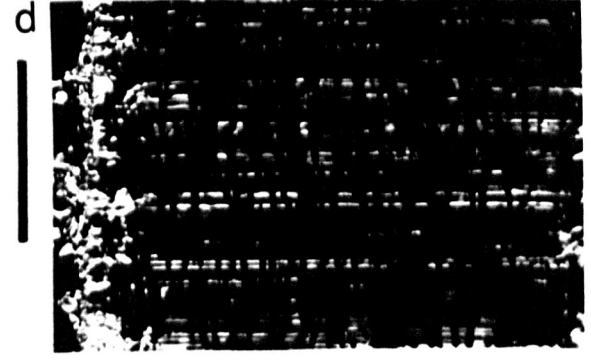
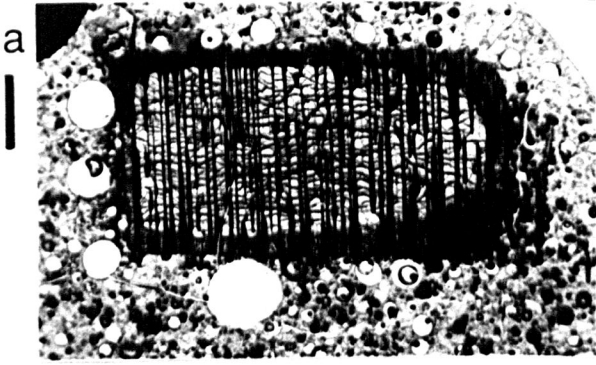
During dissolution, the shape of the enstatite crystal is

Plate 5.1  
Photomicrographs of orthopyroxene dissolution charges.  
Scale bars are 500 $\mu$ m.

- a) R85 (1 day at 1168°C) Enstatite with granular olivine fringe.
- b) R74 (3 days at 1150°C) Detail of edge of enstatite (bottom, at extinction) with clinopyroxene caps from reaction with melt clearly visible. Due to the thickness of the section, the clinopyroxene caps appear wider than suggested by measurements from backscattered electron images.
- c) R85 (1 day at 1168°C) Part of enstatite with a fringe of granular olivine and melt.
- d) R85 (1 day at 1168°C) (As (c), crossed polars). Enstatite and oriented olivines have gone into extinction together, leaving clinopyroxene exsolution lamellae and randomly oriented olivines birefringent.
- e) R111 (19 hours at 1152°C, no basalt) Partially melted bronzite crystal (at extinction) with horizontal clinopyroxene exsolution lamellae and trails of granular olivine neocrysts.
- f) R108 (3 hours at 1172°C) Bronzite with thin (45 $\mu$ m) fringe of granular olivine and melt.
- g) R117 (2 days at 1173°C) Bronzite with fringe of granular olivine and melt.
- h) R117 (8/16) (As (g), crossed polars). Bronzite and oriented rod-shaped olivines are at extinction, while the clinopyroxene lamellae and the randomly oriented olivine grains within the bronzite and around the edge of the fringe show birefringence.

# Plate 5.1

Photomicrographs of orthopyroxene dissolution charges.



controlled principally by its original shape, and by the presence of the garnet lamellae. Decomposition of the garnet has allowed penetration of basalt melt into the enstatite interior, creating separate parallel plates of enstatite (plates 5.1a; 5.2c,d) and allowing access of melt from the sides as well as from the ends of these plates. This results in deep notches forming on the pyroxene surface, where dissolution is enhanced by increased melt access. In 1170°C and 1190°C charges, the rounding of corners on the pyroxene is noticeable, both of the whole crystal and of the ends of the strips (plates 5.1a; 5.2c,d).

Reaction with melt leads to incongruent dissolution of enstatite with the formation of olivine neocrysts. At first, small equant olivines crystallize in a band parallel to the original face of the crystal. Within this, a substantial fraction of the olivine growth is concentrated along the ex-garnet planes, where faces on the enstatite of {100} are exposed for epitaxial olivine nucleation (plate 5.1c,d). These olivine neocrysts share a common optical orientation, such that the c-axes of the olivines are aligned with the a-axis of the enstatite, and all go into extinction together. Within the former garnet lamellae the neocrysts are small, faceted and equant, and become larger, more connected and rounded towards the edge of the fringe. In longer runs at 1190°C, where the enstatite is mostly dissolved, the development of trains of olivine neocrysts with identical orientation is well developed (plate 5.2d).

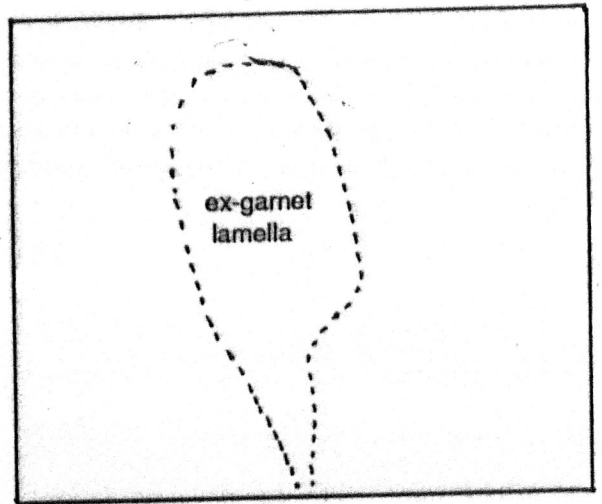
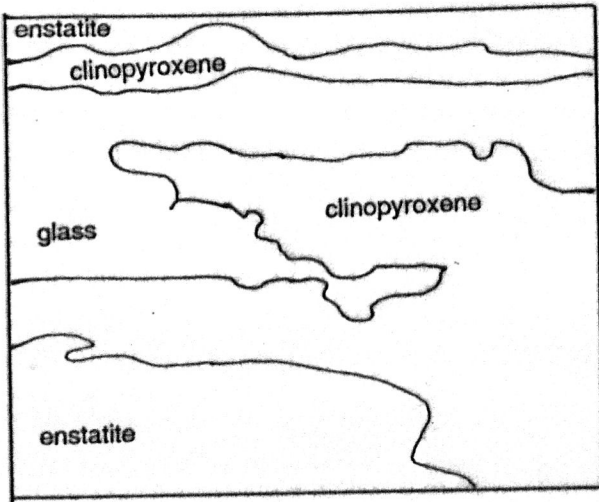
Growing in the gaps between the rows of aligned crystals, the remaining olivines are randomly orientated, larger in size, and fewer in number than the others; adjacent to the pyroxene these olivines are euhedral, but are subhedral and rounded further away. The olivines nucleated on the outer surface of the

Plate 5.2

**Compositional images of enstatite dissolution charges.**

Scale bars are 100 $\mu$ m.

- a) R91 (20 days at 1126°C) Olivine grains (light grey) within ex-garnet lamellae are mostly overgrown by clinopyroxene (medium grey) adjacent to plates of enstatite (black), or are exposed to melt (medium grey), against which the olivines show evidence of slight growth during quenching (black rims).
- b) R74 (3 days at 1150°C) Remnant of exsolved garnet at edge of enstatite crystal, now replaced by fine olivine needles in a matrix of plagioclase and melt. Towards the groundmass (right) the plagioclase, olivine and chromite grains all become coarser, and the olivine needles lose their acicular shapes. Olivines grains which nucleated around the garnet are highly interconnected.
- c) R85 (1 day at 1168°C) Margin of enstatite crystal showing clinopyroxene and chromite lamellae. Clinopyroxene lamellae are more resistant to dissolution than enstatite, and project about 5 $\mu$ m into the melt. The ex-garnet lamellae are not of constant width, and the fine-grained decomposition products of garnet evolve to coarser grains of olivine as the outer surface of the enstatite is approached.
- d) R135 (4 days at 1191°C) Rounded enstatite remnant with blades of chromite partly exposed or completely released into the fringe. Note olivine growth concentrated along ex-garnet planes (marked by fine-grained chromite).
- e) R122 (6 hours at 1193°C) Close-up of edge of enstatite crystal (black). Garnet lamellae are now composed of fine-grained, interconnected, euhedral olivine crystals and chromite particles. Between lamellae the olivines are larger and fewer in number.
- f) R82 (2 days at 1190°C) Enstatite (left) with clinopyroxene lamellae (horizontal, medium grey) and a thin boundary layer of Fe-rich orthopyroxene. Olivines have nucleated on and are now embayed by enstatite (arrowed). Along the ex-garnet lamellae, the fine-grained olivines are euhedral close to the enstatite, but quite rounded near the groundmass.



# Plate 5.2

Compositional images of enstatite dissolution  
charges.

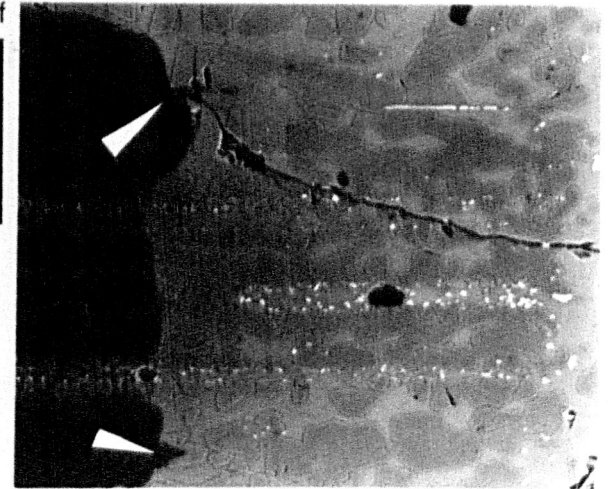
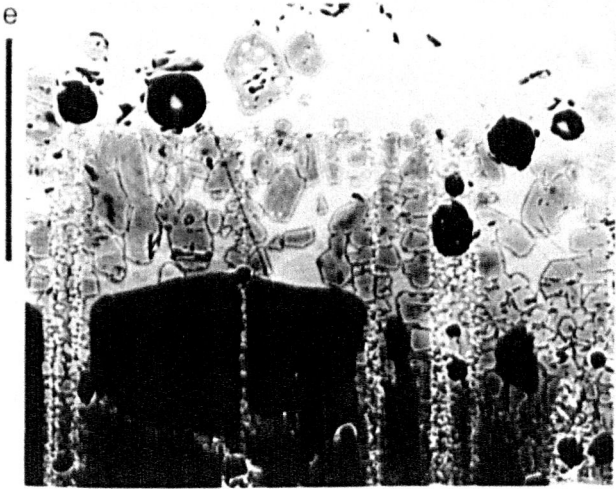
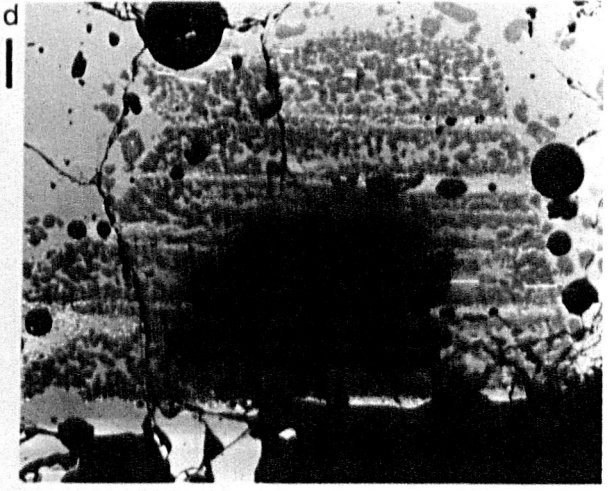
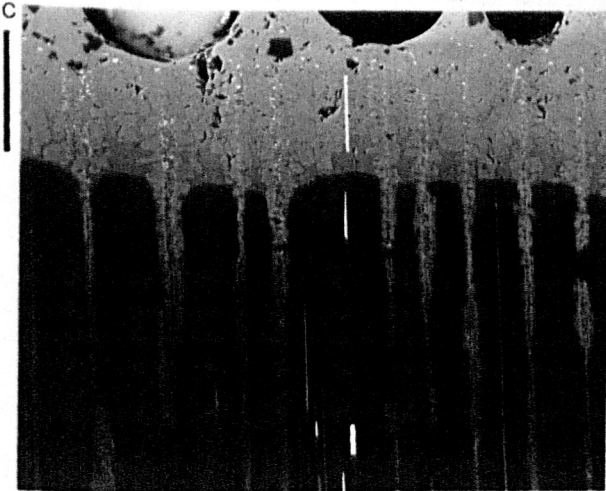
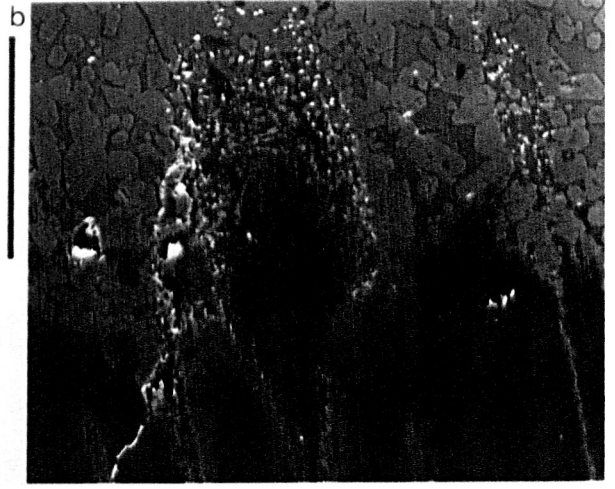
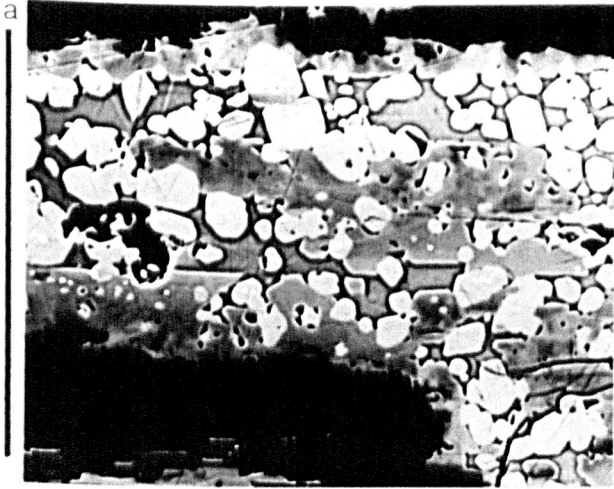
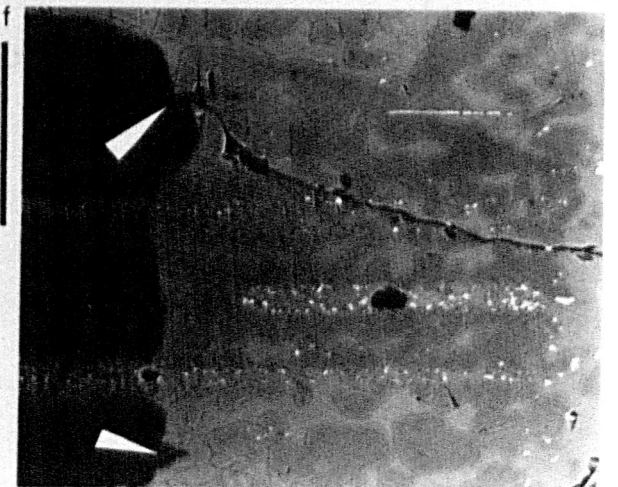
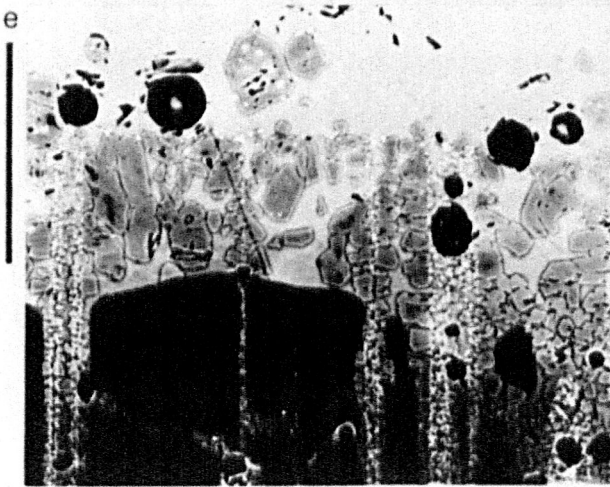
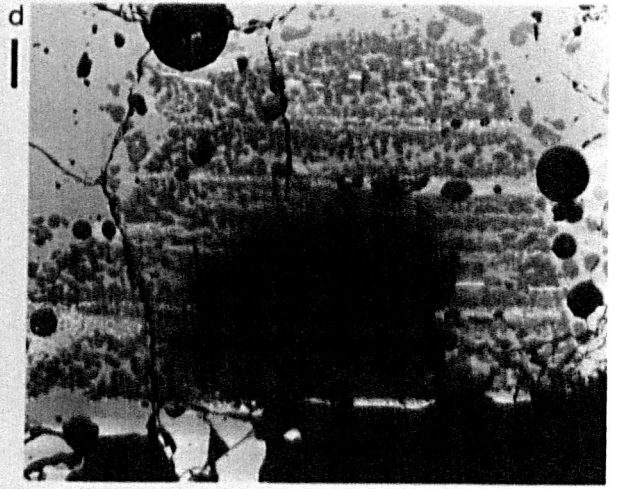
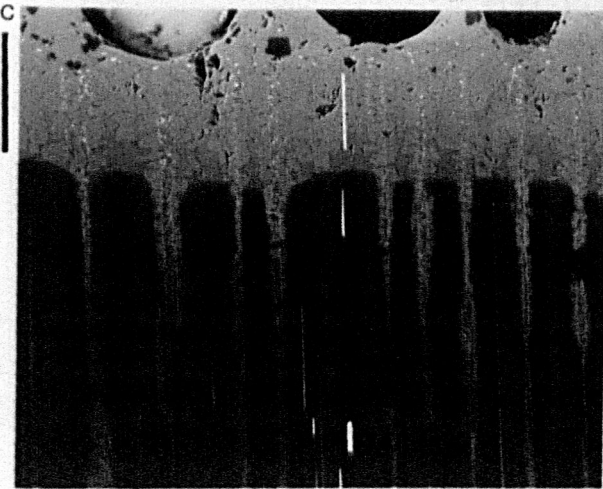
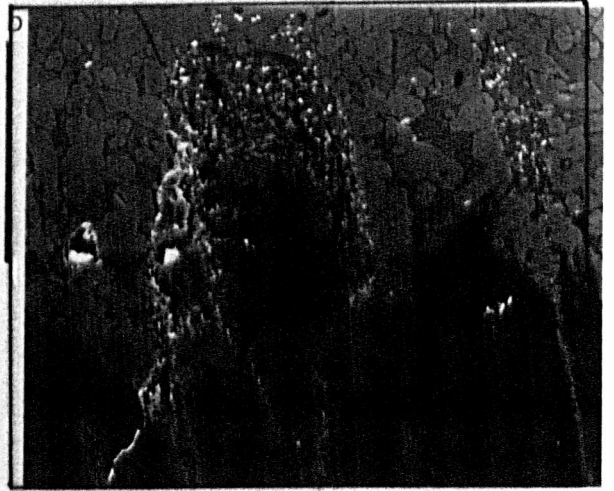
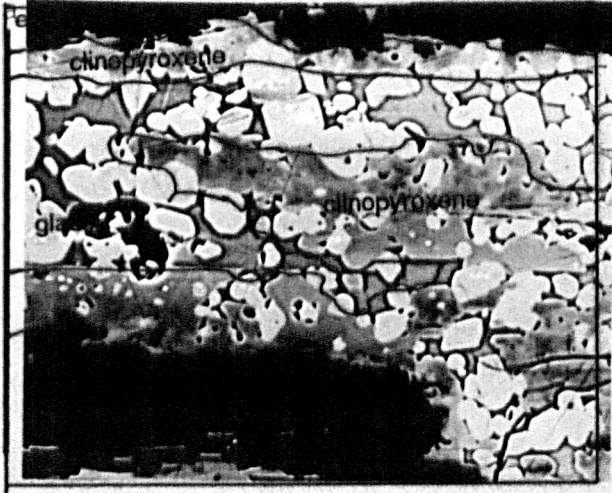


# Plate 5.2

Compositional images of enstatite dissolution charges.



enstatite, and are embayed by and still in contact with the pyroxene in some sections (eg plate 5.2e,f).

At 1170°C and 1190°C a thin (0.5 - 5µm) layer of orthopyroxene ( $\text{wo}_3\text{en}_{85}\text{fs}_{12}$ ) is seen on the surface of the enstatite ( $\text{wo}_1\text{en}_{95}\text{fs}_5$ ) (plate 5.2f). This probably forms by diffusional exchange across the melt-pyroxene boundary during dissolution, rather than by overgrowth.

The chromite plates and grains are unaffected upon exposure to the basalt, and lamellae stranded in the melt after dissolution of the host maintain the same alignment as lamellae within the enstatite (plate 5.2c,d). Larger plates may have separated into several smaller crystals (eg plate 5.2d).

The clinopyroxene exsolution lamellae dissolve at a similar rate to the host enstatite at 1190°C, and are not seen as sites of preferential or restricted dissolution. However, at 1170°C, as the clinopyroxene liquidus is approached, exsolved clinopyroxene lamellae dissolve more slowly than the enstatite, and project 5-10µm into the melt (plate 5.2c). By 1150°C, clinopyroxene is a stable phase in the melt layer closest to the enstatite and forms a thin (10µm) overgrowth as caps. The clinopyroxene is only present at interfaces between enstatite and melt, and does not extend into the ex-garnet lamellae (plate 5.1b). At 1130°C, however, clinopyroxene does occur within the ex-garnet lamellae and encloses earlier olivine neocrysts (plate 5.2a).

It is not clear exactly when the clinopyroxene overgrowth crystallized. It is not a quench phase, because it exhibits none of the growth shapes characteristic of rapid growth (eg Lofgren, 1980), and is even present in runs quenched into water. A change in melt chemistry in the reaction rim due to olivine crystallization, and the difficulty in replenishment from the

bulk melt caused by the high tortuosity of melt channels through the olivine fringe may have caused clinopyroxene crystallization. Once clinopyroxene has crystallized, dissolution of the orthopyroxene is restricted by diffusion through the clinopyroxene layer.

Longer run durations lead to complete replacement of the enstatite by numerous olivine neocrysts and melt (eg after 3 days at 1190°C). Charges which have undergone substantial dissolution afford an overview of the processes of grain-shape equilibration (§5.5), from the youngest neocrysts near the enstatite, to the oldest at the outer edge of the reaction rim.

## **5.2 Petrography of bronzite experiments**

The bronzite contains lamellae of exsolved spinel and clinopyroxene, with amphibole subsequently exsolved from the latter (§2.1.3).

### **5.2.1 Heating in the absence of basalt.**

Heating the bronzite (R111: 19 hours at 1152°C) results in reaction of the bronzite at clinopyroxene-amphibole exsolution sites, with the resultant production of olivine, melt and a new Al-poor bronzite composition ( $\text{wo}_4\text{en}_{80}\text{fs}_{16}$ , 1.5 wt%  $\text{Al}_2\text{O}_3$ ; see appendix 2) (plate 5.1e). Upon heating the hydrous mineral decomposes and releases vapour, triggering melting of the bronzite by depressing its solidus. This reaction is not rapid at lower temperatures; in some 1130°C experiments exsolved clinopyroxene is still visible and has not participated in the internal breakdown reactions (plate 5.3a). The reaction also has a marked effect on the subsequent development of the dissolution and neocryst textures. Exsolved spinel does not participate in

Plate 5.3  
Compositional images of bronzite charges.  
Scale bars are 100 $\mu$ m.

- a) R128 (8 days at 1134°C) Detail of edge of bronzite crystal (left) with some exsolved clinopyroxene (medium grey), internal breakdown to low-Al bronzite (dark grey), olivine (light grey) and melt (black). Surrounding the bronzite is a fringe of rounded olivine grains, and close to the bronzite is a band of clinopyroxene, which is euhedral towards the bronzite and anhedral towards the groundmass. There is quite a strong compositional gradient in the melt external to the bronzite, as indicated by its backscatter coefficient. Close to the bronzite the melt appears dark grey, grading out to very light grey.
- b) R112 (2 days at 1153°C) Bronzite, showing internal breakdown to low-Al bronzite (dark grey), melt and olivine, with complex grain shapes where internally nucleated olivines are released into the melt.
- c) R141 (4 days at 1151°C) Olivine fringe around bronzite. The original bronzite-melt interface is at the right. Within this, the bronzite has undergone a high degree of internal breakdown, leading to a large number of smaller olivine crystals in the fringe. By comparison with (d), the number of neocrysts in the fringe per unit volume is higher.
- d) R141 (4 days at 1151°C) The bronzite has undergone little internal breakdown to olivine plus melt. The original bronzite-melt interface is marked by the small (50 $\mu$ m) olivine crystals at the right. Within the fringe, the olivines are larger (>100 $\mu$ m) and far more complicated in shape (compare with (c)).
- e) R137 ( $\approx$ 10 minutes at 1194°C) Initial nucleation of many 5-10 $\mu$ m olivine crystals around bronzite.
- f) R138 (1 day at 1189°C) Detail of complex olivine shapes both within and outwith bronzite. The darker pyroxene is the new, Al-poor bronzite composition. Internally nucleated olivines are apparently coalescing to form large grains with complex shapes.

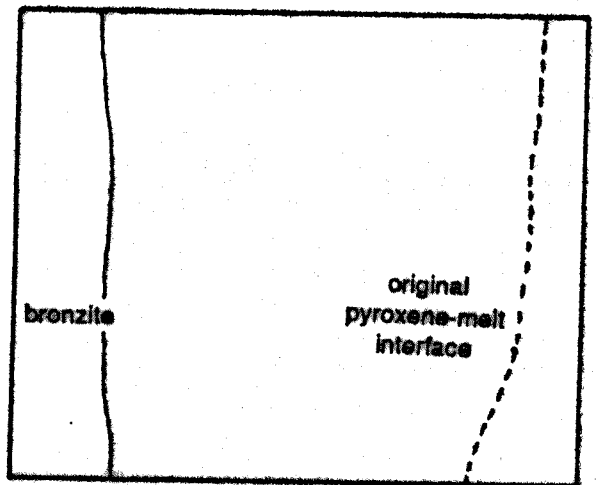
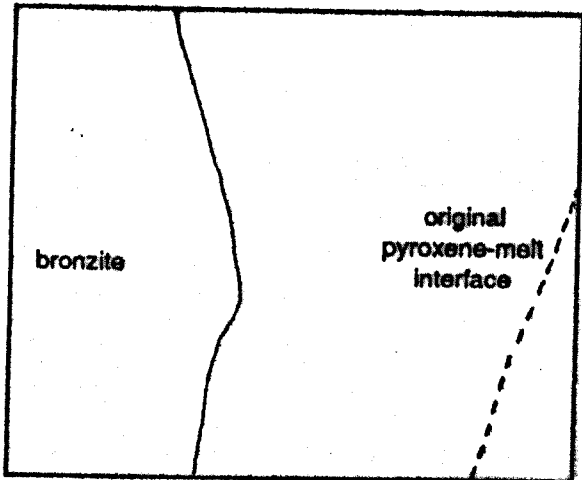
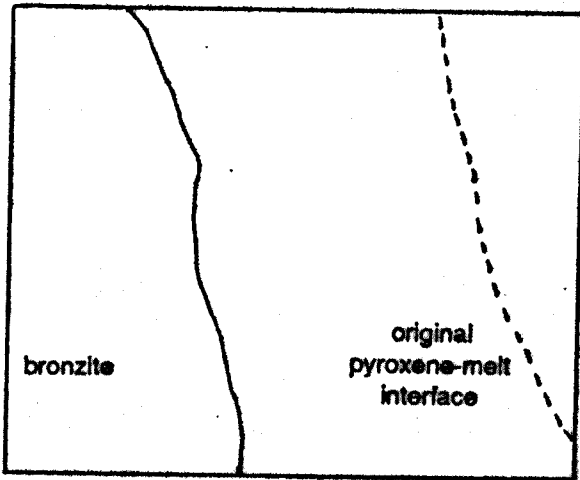


# Plate 5.3

Compositional images of bronzite dissolution charges.

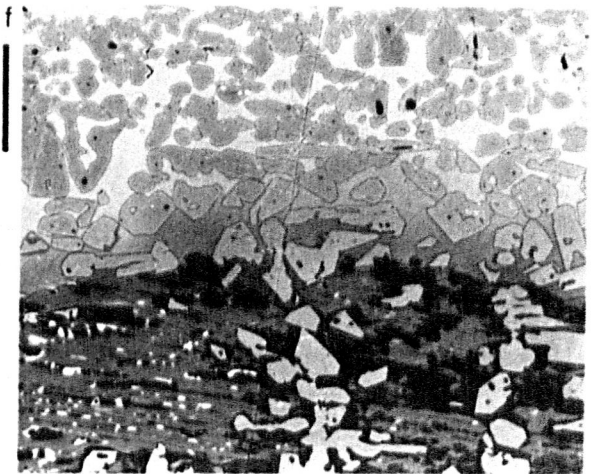
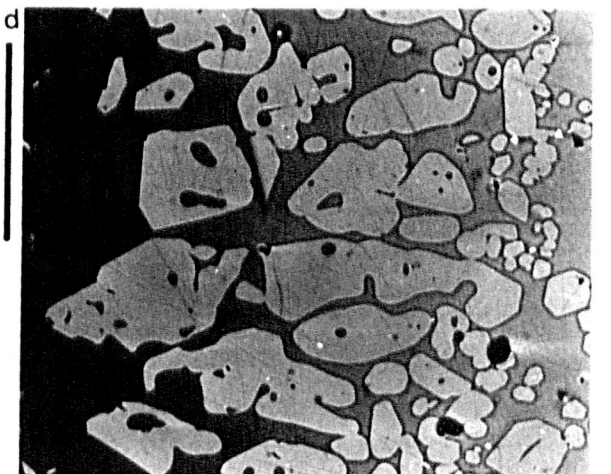
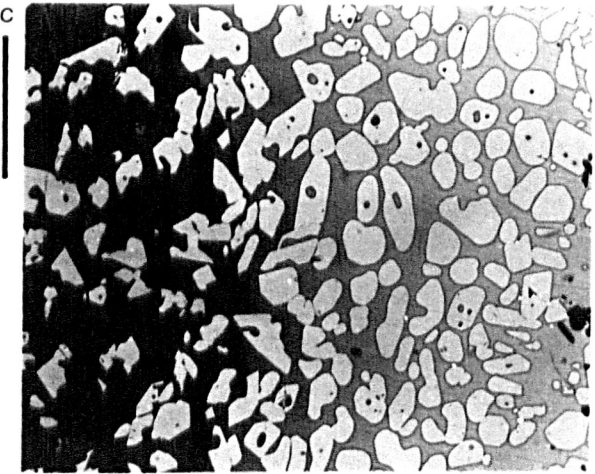
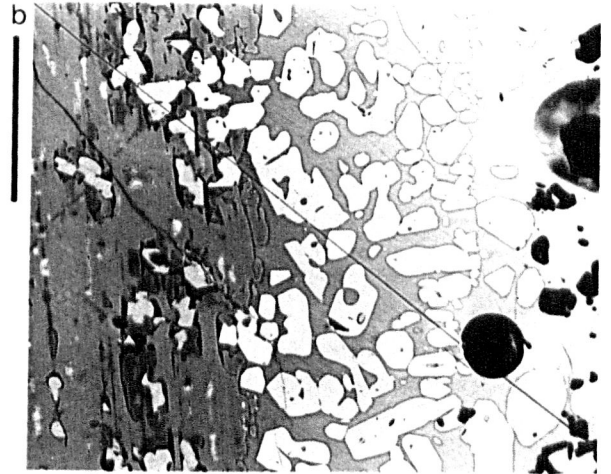
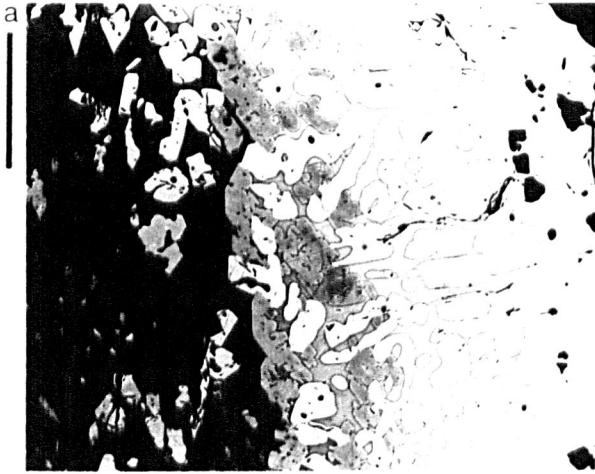
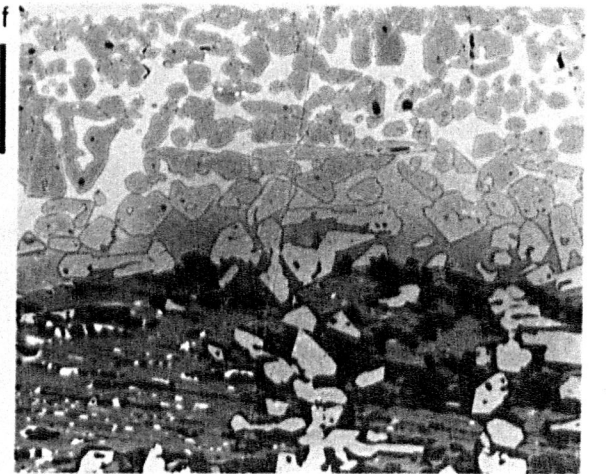
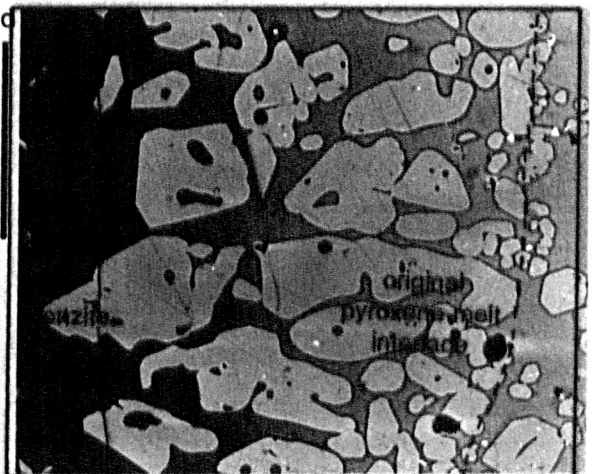
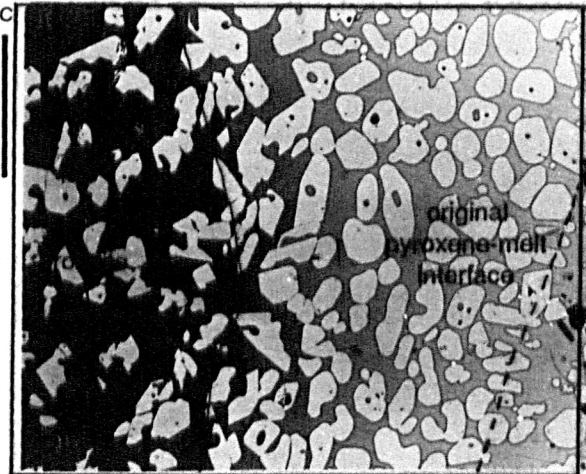
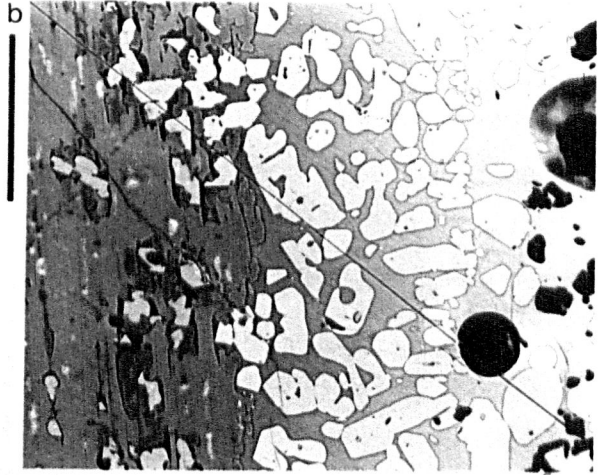
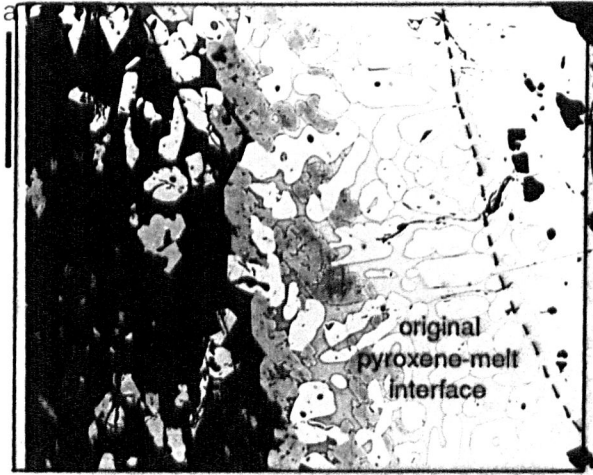


# Plate 5.3

Compositional images of bronzite dissolution charges.



the internal breakdown reactions, but dissolves simply upon exposure to the melt.

### 5.2.2 Heating in the presence of basalt.

At each temperature investigated, incongruent dissolution of the bronzite by reaction with melt leads to the formation of a rim of olivine and melt (eg plate 5.1f,g). At 1130°C this is accompanied by the crystallization of ragged and inclusion-rich clinopyroxene close to the bronzite surface (not an overgrowth layer), with euhedral faces towards the bronzite (plate 5.3a). The development of anhedral clinopyroxene around the bronzite is very limited in 1150°C runs, and is absent in 1170°C or 1190°C runs. The clinopyroxene is similar (in form and composition) to that seen in the enstatite dissolution experiments (§5.1.2).

The dissolution shape of the bronzite is little affected by the presence of cleavage or exsolved phases. The bronzite becomes rounded and dissolves uniformly, with no noticeable crystallographic dependence of dissolution, even in 1130°C runs.

The ten minute experiment at 1194°C demonstrates virtually instantaneous and extensive olivine nucleation *around* the bronzite (plate 5.3e), but no reaction to form olivine and melt *within* the bronzite. The surface of the bronzite is a good surface for olivine nucleation at this time.

A longer experiment (3 hours at 1172°C) demonstrates some internal breakdown of the bronzite to form olivine plus melt. After the initial nucleation of many olivine crystals outside the bronzite, the style of olivine crystallization has changed to one of vigorous growth rather than nucleation. Within a band of small (<20µm) olivines, the number of olivine crystals decreases, but their size increases. (Similar textures are shown in plate

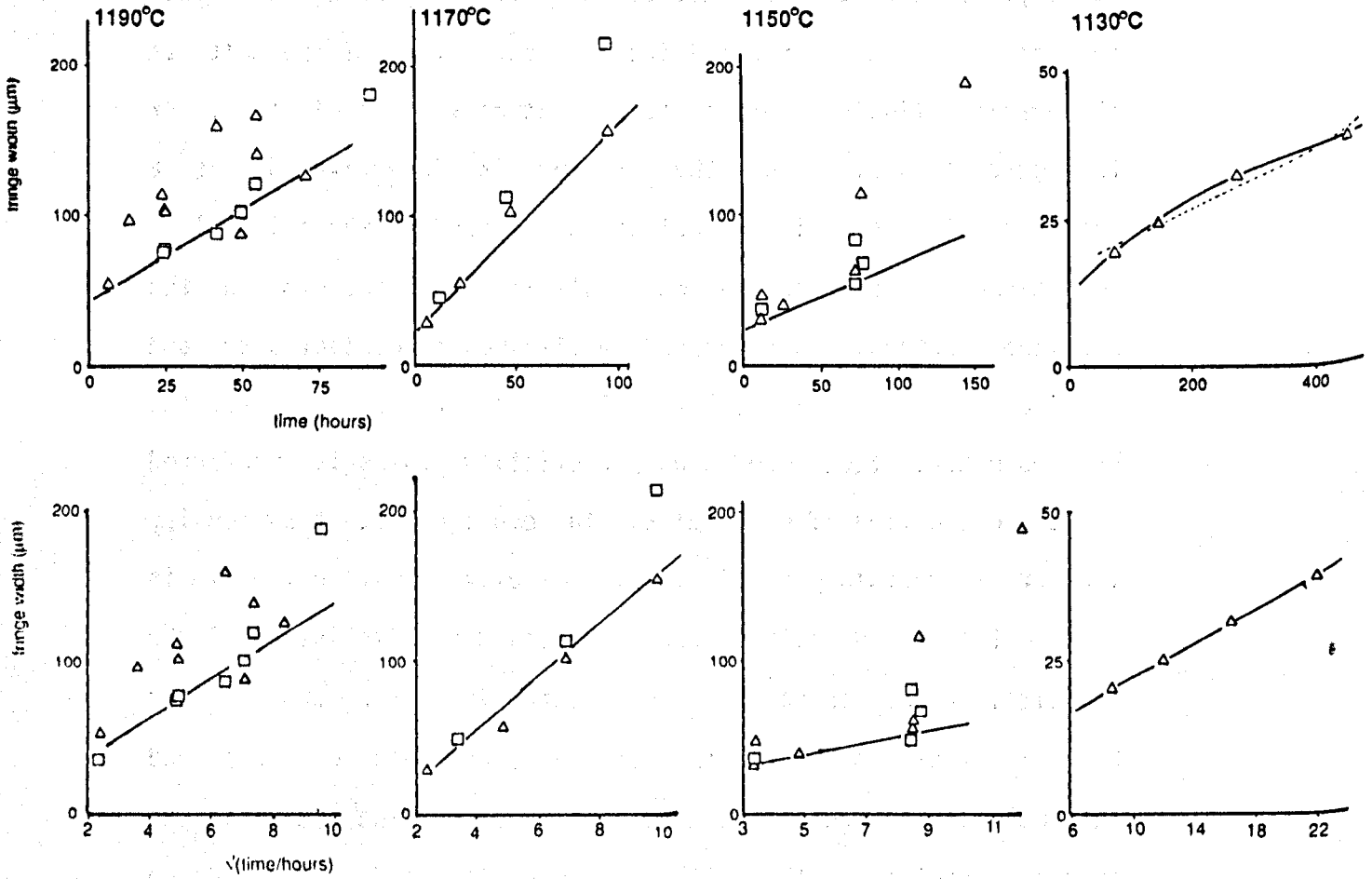
5.3b,d). Either the presence of the large, growing neocrysts sufficiently reduces the olivine supersaturation of the melt at the pyroxene-liquid interface to prevent olivine nucleation, or the current surface of the pyroxene is "deactivated" as a potential site for olivine nucleation compared to the original.

Although some nucleation of olivine still occurs on the pyroxene surface, as evidenced by olivines in contact with and overgrowing the bronzite (plate 5.3f), once the bronzite surface becomes deactivated, growth on pre-existing grains is preferred to the nucleation of new grains. In consequence, the density (number of crystals per unit volume) of olivine within the rim is dependent on the density of grains released by dissolution of the bronzite. Where there has been extensive breakdown of the bronzite (perhaps where the crystal has been damaged) and internal olivine nucleation, the density of olivine grains in the fringe is similar to that within the bronzite, and grains undergo little further growth upon exposure to external melt (plate 5.3c). Where there is little internal breakdown of the bronzite and therefore few olivines released in the same charge, olivine grains in the fringe are fewer and larger (plate 5.3d). The extent of bronzite breakdown is probably controlled by the local density of exsolved clinopyroxene-amphibole lamellae.

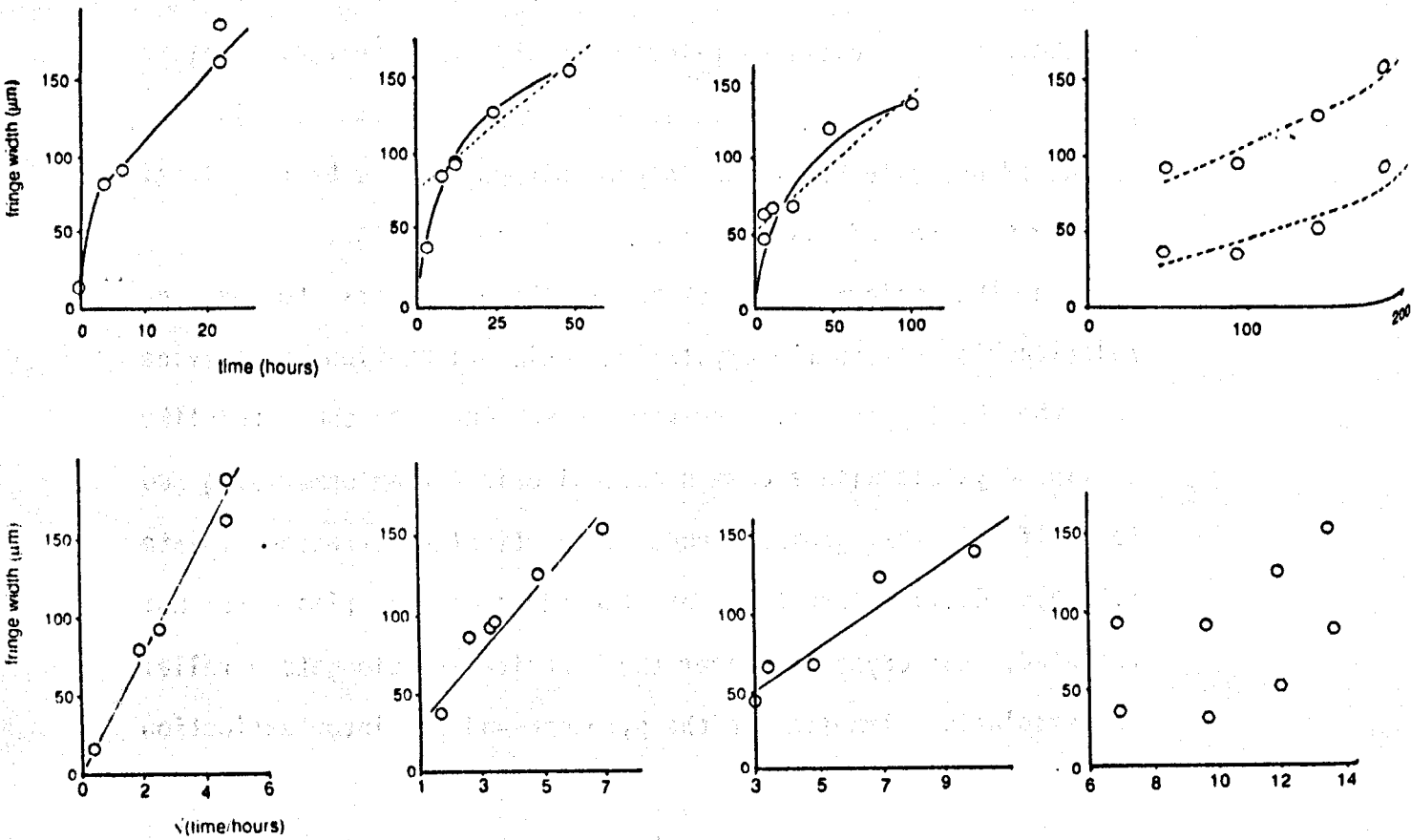
In the majority of examples there appears to be no relationship between the crystallographic orientations of olivine and the host pyroxene. However, some charges show rod-like olivine crystals with a common optical orientation comprising up to half of the grains around a particular pyroxene (plate 5.1g,h). Olivine crystals at the edges of the rims are not oriented, but crystals nearer the bronzite are elongate parallel to exsolution lamellae in the pyroxene and go into extinction

Figure 5.1  
Olivine fringe widths

Enstatite dissolution



Bronzite dissolution



with the host. Since these oriented olivines are only found near the centre of the reaction rim they are probably internally nucleated, but this orientation is apparent optically only in sections where the olivines appear as rods, ie perpendicular to the olivine c-axes. The crystallographic relationship is that the olivine c-axes are parallel to the pyroxene a-axis.

### 5.3 Kinetics

#### 5.3.1 Dissolution rates of orthopyroxene

Measured widths of olivine reaction rims were plotted against run duration to ascertain dissolution rates (figure 5.1). The original face of the pyroxene crystal is taken as the boundary between high and low olivine grain densities. Where there is a wide scatter of fringe widths at a particular duration the lowest value has been used, in case the higher values have not been fully corrected for inclination of the fringe from perpendicular to the plane of the section (§2.3.2).

Measurements from the enstatite experiments were made both parallel and perpendicular to the ex-garnet lamellae. The dissolution rates in these two directions appeared to be indistinguishable, within the errors inherent in measuring the widths of olivine reaction rims.

---

#### Figure 5.1 (facing page)

Widths of olivine reaction rims around dissolving orthopyroxenes are plotted against both linear and parabolic timescales. Each column represents one investigated temperature. For enstatite dissolution experiments, measurements of fringe widths parallel to ex-garnet lamellae are denoted by triangles, and those perpendicular to the lamellae by squares. For bronzite experiments the width of the olivine fringes are denoted by circles, and widths of clinopyroxene layers by hexagons. Solid lines were visually fitted through the lowest values at each duration. Where this best-fit line is curved, the dotted line represents the estimated constant dissolution rate (table 5.1a).

For enstatite, the results are not always conclusive enough to distinguish between time-dependent and time-independent crystal dissolution. A straight-line plot against time suggests that dissolution is time-independent and convection-controlled (eg at 1190°C and at 1170°C), whereas a straight line against  $\sqrt{(\text{time})}$  suggests that dissolution is time-dependent and diffusion in the melt is the dominant control (eg at 1130°C).

Dissolution rates given in table 5.1a have been calculated from graphs plotted against linear time scales, assuming that the rate of fringe growth equals the rate of pyroxene dissolution, and that there is no significant growth of olivine outside the original volume of the pyroxene.

Data from the bronzite experiments fit the  $\sqrt{(\text{time})}$  relationship better, suggesting that diffusion is the rate-controlling factor. Parabolic rate constants ( $k_p$ ) for the equation:

$$\text{fringe width} = k_p \sqrt{t}$$

are given in table 5.1b.

For both pyroxenes the dissolution rates increase with increasing temperature, except that the rates for enstatite at 1170°C and 1190°C are almost identical. These data are taken to

Table 5.1  
Orthopyroxene dissolution rates

Temp °C	enstatite		bronzite	
	$\mu\text{mhr}^{-1}$	$*10^{-11}\text{ms}^{-1}$	$\mu\text{mhr}^{-1}$	$*10^{-11}\text{ms}^{-1}$
a) 1190	1.3 ± 0.2	36 ± 5	4.3 ± 0.5	120 ± 14
1170	1.4 ± 0.2	39 ± 5	1.7 ± 0.1	47 ± 3
1150	0.47 ± 0.1	13 ± 3	0.9 ± 0.1	25 ± 3
1130	0.06 ± 0.02	1.7 ± 0.6	0.4 ± 0.05	11 ± 1
b)			$k_p (*10^{-7}\text{ms}^{-1/2})$	
1190			6.2 ± 0.5	
1170			4.1 ± 0.3	
1150			2.5 ± 0.2	
1130			1.8 ± 0.2	

indicate that at higher temperatures convection in the melt is the dominant control on dissolution rate. Since there is no significant thermal gradient across a charge, convection must be driven by compositional differences leading to variations in density and/or interfacial tension. At lower temperatures, diffusion across the reaction rim appears to dominate, leading to time-dependent behaviour.

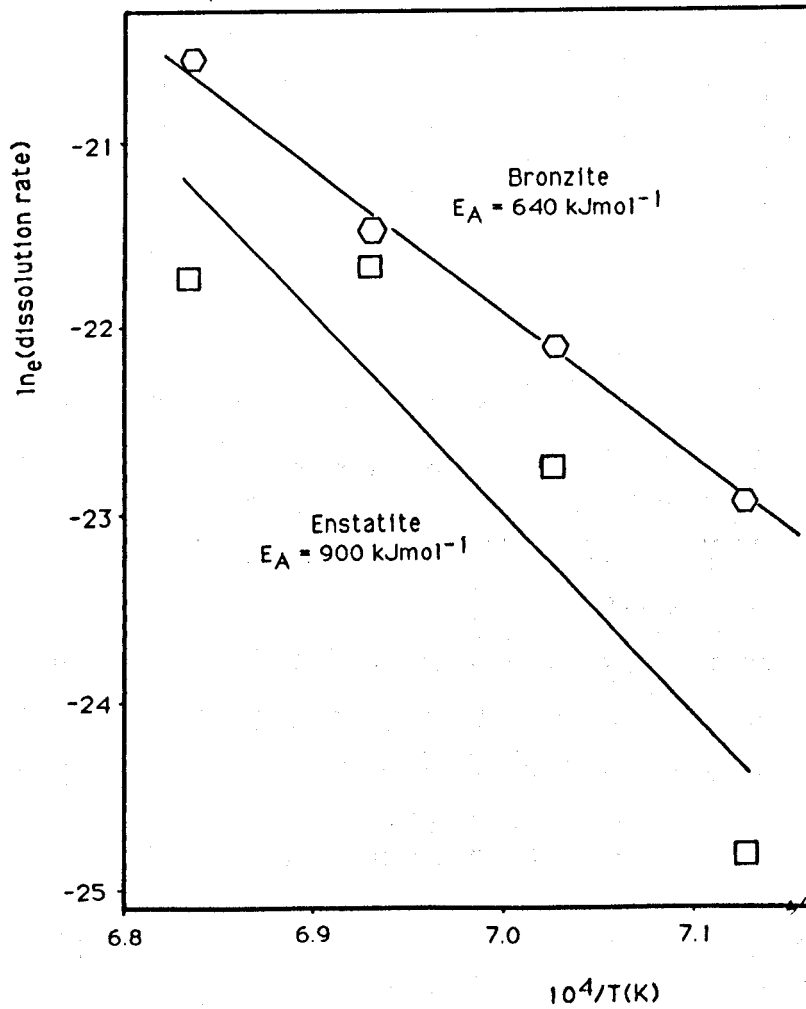
### 5.3.2 Activation energies of dissolution

Using the Arrhenius relationship (§3.2.3), activation energies may be calculated from the measured linear dissolution rates. Figure 5.2 yields values of  $640 \pm 60$  kJmol<sup>-1</sup> for bronzite and  $920 \pm 400$  kJmol<sup>-1</sup> for enstatite compositions.

For bronzite, a second activation energy may be calculated, if the dissolution rate is time-dependent and primarily diffusion controlled. Plotting the parabolic rate constant ( $k_p$ ) on an Arrhenius diagram (figure 5.3) yields an activation energy of  $370 \pm 40$  kJmol<sup>-1</sup>.

For comparison, other experimental data for orthopyroxene dissolution are plotted on figure 5.4, and values for activation energies are given in table 5.2. The large spread in values may reflect differences between different experimental procedures, or may indicate the extent of errors for calculated activation energies.

Figure 5.2  
Activation energies of orthopyroxene dissolution

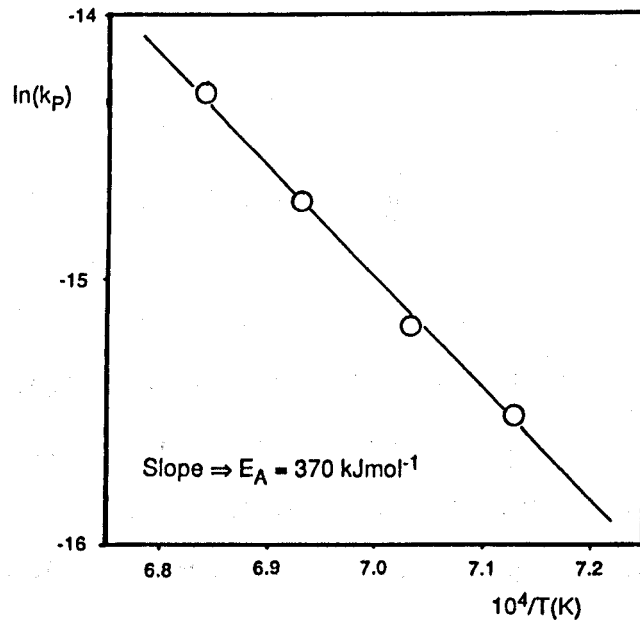


Arrhenius plot of dissolution rates against reciprocal temperature to estimate activation energies. Squares represent enstatite data, hexagons represent bronzite data.

Table 5.2  
Published activation energies of dissolution

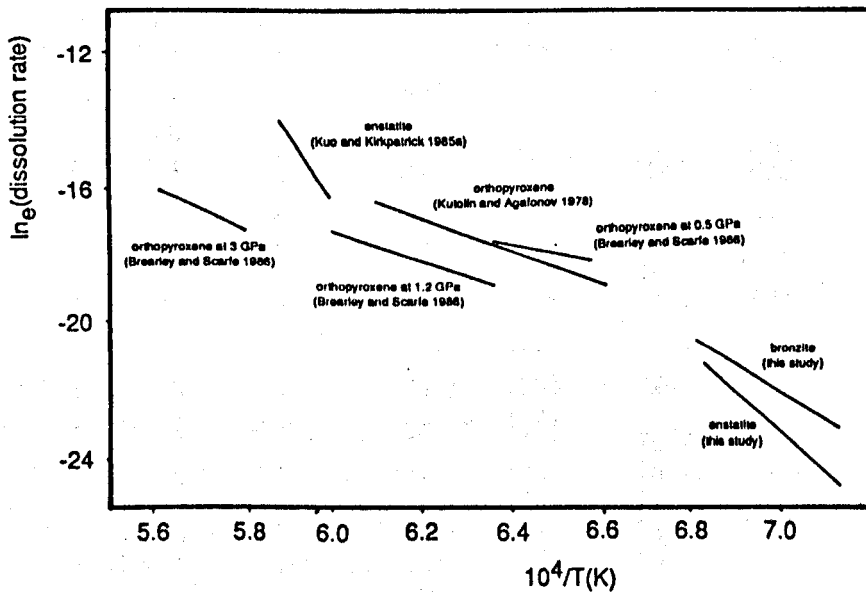
Comp.	Type	E <sub>A</sub> kJmol <sup>-1</sup>	Pressure	Temperature	Reference
en <sub>100</sub>	simple	1200	0.1MPa	1400°C	Kuo+ 1985a
en <sub>88</sub>	incongruent	276±21	0.5GPa	1250-1300°C	Brearley+ 1986
en <sub>88</sub>	simple	355±25/100	1.2GPa	1300-1400°C	"
en <sub>88</sub>	simple	460±176	3 GPa	1450-1500°C	"
		280			Kutolin+ 1978
en <sub>89</sub>	incongruent	420	0.1MPa	1220-1300°C	Tsuyhima 1986a
en <sub>78</sub>	incongruent	640±60	0.1MPa	1130-1190°C	this work
en <sub>94</sub>	incongruent	900±400	0.1MPa	1130-1190°C	"
en <sub>78</sub>	incongruent	370±40	0.1MPa	1130-1190°C	" (parabolic)

Figure 5.3  
Activation energy for time-dependent  
dissolution of bronzite



Parabolic rate constant ( $k_p$ ) plotted on an Arrhenius diagram.

Figure 5.4  
Orthopyroxene dissolution data



Arrhenius plot of published experimental dissolution data for magnesian orthopyroxenes. All data are from experiments at atmospheric pressure unless otherwise stated. All data are superliquidus except those from this study.

## 5.4 Chemical relationships in orthopyroxene dissolution charges

### 5.4.1 Fe-Mg contents of olivine.

For each orthopyroxene composition and run temperature, two charges of different run durations were analysed to determine olivine and melt compositions. Analyses are given in appendix 2.

Olivine formed by the breakdown of garnet lamellae in enstatite dissolution charges is more magnesian than olivine in the same charge resulting from orthopyroxene dissolution (table 5.3). Decreasing forsterite contents towards the outer edge of the fringe reflect equilibration of these olivines with groundmass melt.

Run duration at any particular temperature does not significantly affect the range of olivine compositions. This is,

Table 5.3  
Forsterite contents of olivines.

Run	temp (°C)	time days	internal (%fo)	inner fringe (%fo)	outer fringe (%fo)	groundmass (%fo)
<b>Enstatite</b>						
R88	1128	6	81 (80)	76-75	75	74
R91	1126	20	na (76)	77	na	na
R80	1149	1	na	81-80	80-79	77
R74	1150	3	na	81	80-79	na
R110	1172	0.25	na	84 (82)	84-83 (80)	83-82 (78)
R85	1168	1	85	83-80 (79)	80-79 (79)	80-78 (77)
R84	1188	1	na (84)	84-82 (82)	82-81 (82)	81-80 (82)
R82	1190	2	na	84-83 (85)	83-82 (83)	81-80 (83)
<b>Bronzite</b>						
R128	1134	8	80	79-78 (78)	77-76	76 (74)
R77	1149	1	79	78-76 (77)	75	na (77)
R112	1153	2	79-78(80)	77-76 (76)	76-75	76-75 (75)
R96	1171	0.5	81-80(81)	79-78 (79)	78-77	<77 (78)
R86	1171	1	na	78 (77)	77	na (77)
R94	1190	0.5	82-81(81)	82-81 (81)	81-80 (79)	81-80 (80)
R93	1191	1	81-80(82)	81-80 (83)	80	80 (80)

na = no analyses

Figures in parentheses are the computed values from the method of Roeder and Emslie (1970) (table 5.4).

Internal: olivines nucleated within the pyroxene.

Inner fringe: olivines immediately surrounding the pyroxene

Outer fringe: olivines at the outer edge of the fringe.

Groundmass: olivines from the bulk of the charge.

Table 5.4  
Computed temperatures for olivine fringes.

Run	Temp (°C)	time (days)	type	$K_D^{Ca_{90}}$ *10 <sup>-2</sup> (Jurewicz and Watson, 1988a)	Computed temp offset (°C)	Computed %fo temp offset (°C)	Computed temp offset (°C)	Computed temp offset (°C)	
<b>Enstatite</b>									
R88	1128	6	internal	2.95	1160	+32	80	1130	+2
R91	1126	20	internal	3.84	1180	+54	76	1070	-56
R110	1172	0.25	inner fr	2.87	1200	+28	82	1090	-82
			outer fr	2.60	1185	+13	80	1100	-72
R85	1168	1	groundmass	2.76	1200	+28	78	1140	-32
			inner fr	3.19	1180	+12	79	1080	-88
			outer fr	2.49	1175	+7	79	1120	-48
R84	1188	1	groundmass	3.20	1190	+22	77	1120	-48
			inner fr	3.16	1190	+2	82	1090	-98
			mid fr	2.84	1200	+12	82	1120	-68
			outer fr	2.20	1185	-3	82	1140	-48
R82	1190	2	groundmass	2.35	1185	-3	82	1140	-48
			inner fr	2.97	1210	+20	85	1090	-100
			outer fr	2.81	1210	+20	83	1130	-60
			groundmass	2.22	1190	0	83	1150	-40
<b>Bronzite</b>									
R128	1134	8	inner	3.31	1170	+36	78	1050	-84
			outer fr	2.88	1180	+46	78	1100	-34
			groundmass	3.43	1160	+26	74	1070	-64
R77	1149	1	fringe	4.55	1230	+81	77	1070	-79
			groundmass	3.92	1200	+51	77	1100	-49
R112	1153	2	internal	3.87	1225	+72	80	1040	-113
			fringe	3.19	1190	+37	76	1090	-63
			groundmass	3.22	1190	+37	75	1110	-43
R96	1171	0.5	internal	2.91	1190	+19	81	1070	-101
			fringe	2.65	1175	+4	79	1090	-81
			groundmass	3.13	1190	+19	78	1180	-41
R86	1171	1	inner fr	2.75	1180	+9	77	1090	-81
			outer fr	2.05	1165	-6	77	1110	-61
			groundmass	2.73	1175	+4	77	1120	-51
R94	1190	0.5	internal	3.49	1230	+40	81	1070	-120
			inner fr	2.83	1220	+30	81	1120	-70
			outer fr	1.95	1180	-10	79	1150	-40
			groundmass	3.14	1220	+30	80	1150	-40
R93	1191	1	internal	2.55	1220	+29	82	1090	-101
			fringe	1.79	1175	-16	83	1120	-71
			groundmass	2.75	1195	+4	80	1150	-41

The offset is the difference between computed and actual run temperatures.

however, not true for the two 1170°C enstatite charges, where the olivines in the shorter run (6 hours) are about 3 mol% more magnesian distant from the enstatite (table 5.3). These olivines have apparently not had sufficient time to equilibrate, suggesting that olivines (up to 50 $\mu$ m) are able to compositionally equilibrate with respect to iron and magnesium in about half a day at 1170°C.

Olivine formed by incongruent reaction within the bronzite is often a few percent more magnesian than that immersed in melt outwith the pyroxene (table 5.3), except in 1190°C runs, where the groundmass olivine composition is almost identical to that of those olivines nucleated internally. At other temperatures, olivines within the bronzite are uniform in composition, but once exposed to external melt their composition starts to change. Equilibration is quite rapid; crystals up to 50 $\mu$ m across apparently homogenize within a day at run temperatures (indicating an estimated diffusion coefficient of  $2 \cdot 10^{-15} \text{m}^2 \text{s}^{-1}$ , if diffusion in the olivine was responsible).

#### 5.4.2 Olivine-melt thermometry

Temperatures may be estimated for olivine-melt pairs by assuming olivine saturation for a melt of known iron and magnesium contents (figure 7 of Roeder and Emslie, 1970). This is valid since olivine is the first phase to crystallize in these reaction rims. Temperatures estimated by this method (given in table 5.4) are (with one exception) low by -32 to -120°C (mean -64°C). The difference between calculated and actual temperatures is largest for internal and inner fringe olivines, decreasing for olivines in the outer parts of the fringe and the groundmass.

A second thermometer, based on the Ca contents of olivine

(Jurewicz and Watson, 1988a) was also applied to the chemical data from these experiments, to test its validity and accuracy against the known run conditions. The authors assessed the sensitivity of this thermometer to be about 25°C (1σ) for quenched low pressure glasses. High estimates may arise if no correction is made for fluorescence<sup>1</sup> in olivines. The thermometer was applied to the data corrected for fluorescence by subtraction of 0.05wt% CaO.

Temperatures estimated for enstatite and bronzite experiments are given in table 5.4. The thermometer overestimates temperatures from the enstatite experiments by -3°C to +54°C (mean +16°C), and from the bronzite experiments by -16°C to +81°C (mean +26°C)<sup>2</sup>.

For both thermometers, the temperature offset for internal olivines is usually greater than for either fringe or groundmass olivines, and the temperatures computed for olivines and melts at the outer edge of the fringe are usually closest to actual run temperatures. Jurewicz and Watson (1988a) report good agreement between their thermometer and known run temperatures, so the discrepancies in this work are probably the result of

---

<sup>1</sup> Phase boundary fluorescence occurs when higher energy X-rays, generated within olivine, escape to adjacent clinopyroxene or melt and fluoresce additional Ca X-rays. This effect is important only in the analysis of fine-grained phases. Watson (1979) discovered that the effect is significant up to 15μm from the olivine-glass interface, ie for grains less than 30μm across, and assumed a correction factor of 0.05 wt% CaO. Adams and Bishop (1986) measured this effect to be equivalent to 0.022 wt% Ca in olivine grains 10-20μm in size in an olivine-clinopyroxene mix.

<sup>2</sup> Prior to data correction for Ca fluorescence, the thermometer had overestimated temperatures using uncorrected data from the enstatite experiments by 12 to 68°C (mean 34°C), and from the bronzite experiments by -1 to 111°C (mean 43°C).

disequilibrium between olivines and surrounding melt. Since both thermometers register large discrepancies from actual run temperatures, the olivines are unequilibrated with respect to Mg/Fe, as well as Ca. Estimated temperatures for the Ca-content thermometer result from excessive Ca in olivine (even after a generous correction for secondary fluorescence), which may result from (rapid) growth from a supersaturated melt (Donaldson *et al.*, 1975b).

The normalized Ca partition coefficient ( $K_D^{Ca_{90}}$ )<sup>3</sup> can be used to determine whether olivines are equilibrated with their host magmas. All of the melt compositions in these experiments contain < 9wt% CaO, and the olivines should therefore, according to the data of Jurewicz and Watson (1988a), exhibit a constant value for  $K_D^{Ca_{90}}$  of about 0.021. Values for  $K_D^{Ca_{90}}$  (table 5.4) range from 0.018-0.046 (corrected for fluorescence), with higher values corresponding to higher computed temperatures. Parts of charges showing  $K_D^{Ca_{90}} \approx 0.021$  exhibit estimated temperatures close to the actual run temperatures, and have reached equilibrium with respect to Ca. Parts of charges (eg internal olivine) with  $K_D^{Ca_{90}} \gg 0.021$  and high estimated temperatures have not equilibrated.

#### 5.4.3 Mechanisms of equilibration

From the computed values for  $K_D^{Ca_{90}}$  and estimated run temperatures, it is clear that olivine-melt equilibrium is not achieved for runs at 1130°C, 1150°C, and six hours at 1170°C (R110), but is achieved for all other runs analysed (all  $\leq 2$

---

<sup>3</sup>  $K_D^{Ca_{90}}$  = the ratio of Ca in the olivine to Ca in the melt, normalized to an olivine of composition  $fo_{90}$  (Jurewicz and Watson, 1988a).

days).

Using the data of Jurewicz and Watson (1988b) (1220°C,  $f_{O_2}=10^{-8}$ ), and the approximation  $t=x^2/4D$  (Crank, 1975; §3.2.4), homogenization of a 50 $\mu$ m crystal by diffusion through the olivine will typically take 5 days with respect to Fe, and 12 days for Ca. Since equilibration of olivine compositions (in 1170°C and 1190°C runs) is more rapid than this, some alternative mechanism for olivine equilibration is required. A likely candidate is solution and re-precipitation which operates during textural equilibration of the solid phases (§5.5).

## 5.5 Non-primary textures

By studying the backscattered electron images, it is apparent that the primary crystal shapes of olivine grains do not remain constant once exposed to melt. Here the changes in olivine textures with time are examined, with reference to enstatite and bronzite dissolution experiments at 1150°C and 1190°C.

### 5.5.1 Olivines in enstatite charges

In enstatite dissolution experiments, the larger, irregularly oriented olivine crystals undergo some rounding, but the very fine olivine crystals, resultant from garnet decomposition, experience extensive equilibration where exterior melt has penetrated a garnet lamella. The latter olivines become fewer and larger, until about halfway across the fringe there are none left, and olivine growth is concentrated on rounded and interconnected grains bounding the lamella (three days at 1150°C; plate 5.2b). After a further three days, olivine grains within a former garnet lamella are larger, interconnected and partly

rounded. Chromite grains in the fringe are larger away from the pyroxene, and even exhumed blades of chromite may start to break up into shorter sections (plate 5.2d; bottom left), reminiscent of Rayleigh instability (Hunter, 1986).

After six hours at 1190°C (plate 5.2e), the ends of the ex-garnet lamellae are filled with many small equant euhedral olivine crystals and tiny grains of chromite. Two days later (plate 5.2f) these small grains are larger, rounded and mutually attached. Note also that the chromite grains (white) become coarser away from the pyroxene.

### 5.5.2 Olivines in bronzite charges

In very short runs (R137, ≈10 minutes; plate 5.3e), many small euhedral olivine neocrysts have nucleated on the surface of the pyroxene. Occasionally two olivines are joined where they have impinged during growth (or self-nucleated), but no rounding of crystals is evident. After three hours the pyroxene contains many olivine crystals with flat faces where they are exposed to the melt. Some of the olivines are not fully detached from the pyroxene and still have irregular and uneven faces.

After a day (plate 5.3f) the textures have changed considerably. Olivine crystals still within the pyroxene are partly rounded and mutually connected, forming large, complexly shaped grains (plate 5.3f, bottom centre and bottom right). Outwith the pyroxene, similar textural modifications are occurring. At the outer edge of the fringe (the original edge of the pyroxene; eg plate 5.3f, top) small olivine crystals are well-rounded. Closer to the pyroxene, where the olivines are fewer and larger, the grains are well rounded with complex shapes, resulting from the coalescence of several smaller grains

(note for example the large, hollow, harp-shaped grain to the left of plate 5.3f).

Two of the most striking examples of textural equilibration are shown by 1150°C bronzite runs. Plate 5.3d shows large complex grain shapes formed by the coalescence of smaller grains, while in plate 5.3c, from the same charge, many olivine crystals exhumed from the dissolving pyroxene have become rounded and have not coalesced. Complex grain shapes formed by the coalescence of several adjacent grains (plate 5.3b, centre) have melt inclusions with complex shapes (plate 5.3b,d,f). In addition, contact flattening occurs where two grains have come into contact but have not coalesced, leading to the formation of a visible grain boundary devoid of melt (plate 5.3b bottom right, near the vesicle).

Despite the rounding of grains within reaction rims, facets are often developed on crystals towards the outer edges of rims (eg plate 5.3a,b,d). This is due to continued olivine growth supplied by material from the groundmass.

### 5.5.3 Textural equilibration.

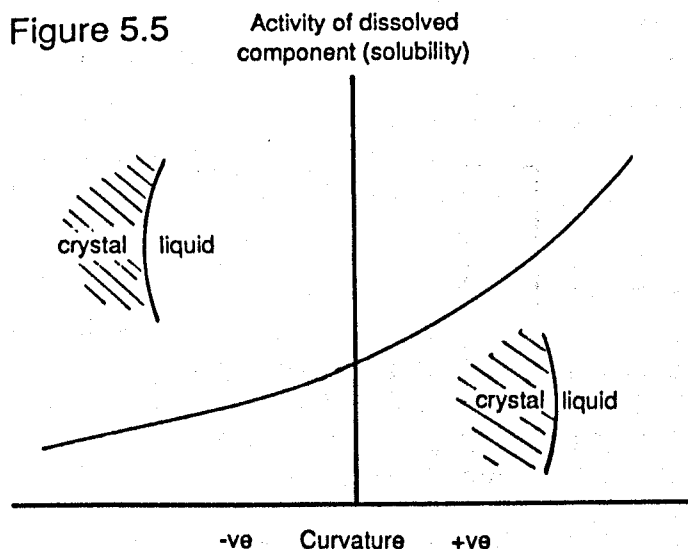
The process whereby crystal shapes evolve with time is known as textural equilibration, and has had a significant effect on the textures of all runs longer than three hours.

Surface energies play a major role in determining phase geometry in equilibrated silicate partial melts, just as they do in purely crystalline materials. The surface energy is assumed to be independent of crystallographic orientation, which is reasonable for minerals which exhibit typical granular textures and 120° grain intersection angles in high-grade metamorphic assemblages (eg Mercier and Nicholas, 1975), and is shown to be

the case for forsteritic olivine by the experiments of Waff and Bulau (1979).

The driving force for textural equilibration is the reduction in the surface energy of the solid phase. Highly skeletal grains with high surface area to volume ratios (SA/V) have high interfacial energies, since work, equal to the interfacial tension, is required to create a unit area of interface. As a result, such crystals are energetically unstable with respect to more equant crystals with lower SA/V. The equilibrium solubility of crystals is related to the surface curvature at any point (figure 5.5), assuming that the surface energy is constant everywhere, and negatively curved crystal faces will act as sinks for dissolved material, since they are less soluble than positively curved faces (Bulau *et al.*, 1979).

Liquid-phase sintering (German, 1985) encompasses a variety of processes involved in the textural equilibration of a particulate solid containing some interstitial liquid. Again the driving force for such textural rearrangement is the reduction in total surface energy. This is achieved: (1) by reducing the total



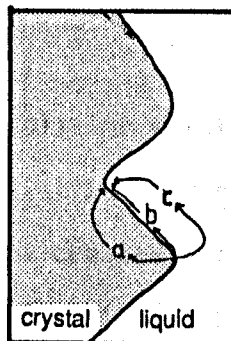
Activity of dissolved component as a function of surface curvature. (After Bulau *et al.*, 1979).

surface area of the solid, (2) by increasing the size and/or number of larger particles, (3) by simplifying skeletal grains to more equant habits, (4) by eliminating solid-liquid and solid-solid interfaces, or by any combination of these four processes.

This textural equilibration may be explained in terms of the following processes involved in liquid-phase sintering, by comparison with examples from the study of ceramic materials (Kingery *et al.*, 1976; German, 1985):

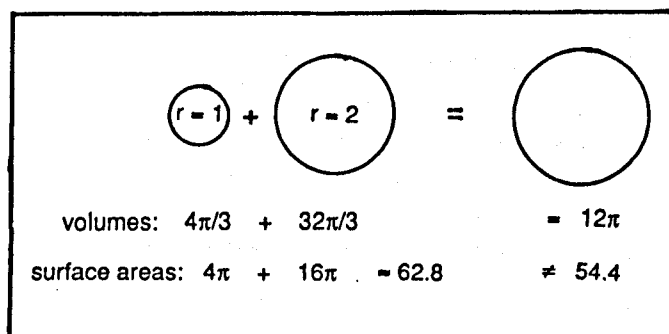
- 1) Highly curved regions of olivine-liquid interface will tend towards a constant low-curvature interface in the absence of anisotropic surface energies, in order to decrease the interfacial area. This is accomplished by diffusion within the crystal, diffusion along grain boundaries, or solution and reprecipitation via the melt phase (figure 5.6; eg plate 5.3b,f). During solution and reprecipitation, regions of high positive curvature dissolve, and the material is reprecipitated in regions of negative curvature, in order to reduce the total surface energy of the system. This leads to a more equant form; however, sharp corners on crystalline grains in contact with liquid will not exist under equilibrium conditions.

Figure 5.6



Material transport from regions of high positive curvature by (a) diffusion through the grain, (b) grain boundary diffusion, (c) solution-reprecipitation via the melt phase.

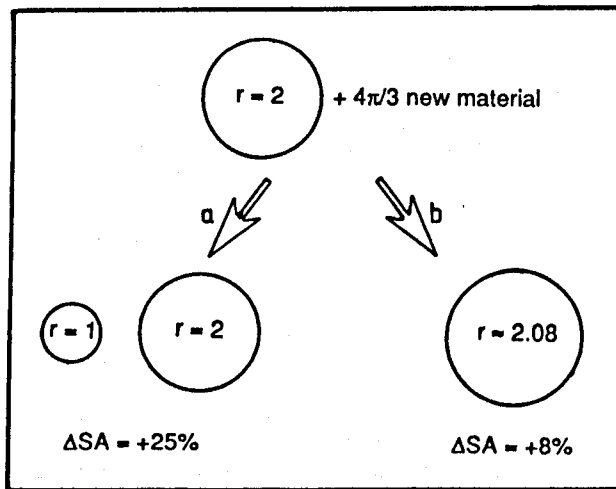
Figure 5.7



Effect of Ostwald ripening on the surface area of the solid phase. The surface area of the larger grain is less than the combined surface areas of the two separate grains.

- 2) As microstructures evolve during sintering, grains grow to lower the total energy stored in grain boundaries. Small grains are more soluble than large grains because of their higher SA/V, and preferentially dissolve. Diffusive transfer of crystal components from small to large grains via the intervening liquid allows further growth on the large grains. Although the resultant decrease in size of the smaller grains increases their surface energy per unit volume, this is more than offset by the decrease in surface energy per unit volume achieved by the large grains (figure 5.7; eg plate 5.2b). This coarsening of crystals suspended in a liquid is a specific example of the more general phenomenon of **Ostwald ripening**.
  
- 3) Similarly, growth of new olivine material occurs on larger rather than on smaller existing olivine crystals, because the extra interfacial area created per unit volume olivine added is less for a larger grain (figure 5.8). A smaller increase in surface area per unit volume requires less work and is therefore energetically favourable. Large grains

Figure 5.8

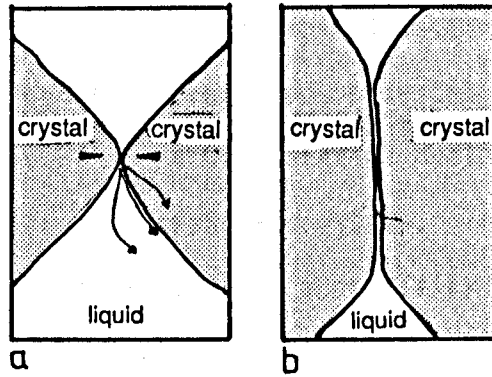


Change in total surface area of solid phase caused by the addition of new material (a) as new grains (b) added to existing grains.

become larger and the grain size distribution changes in favour of larger grains. This process is known as **secondary crystallization** or **discontinuous grain growth**. In bronzite dissolution experiments, olivine growth occurs on the large internally nucleated olivines in preference to the nucleation and growth of new small grains by this mechanism (eg plate 5.3d).

- 4) At points of contact between particles, high local stresses cause increased solubility, leading to plastic deformation and creep at these points. If the relative crystallographic orientations of two grains do not allow coalescence and the elimination of the solid-solid interface, material dissolved from the high stress point of contact will be reprecipitated far from the contact point - leading to flattening of the contact (figure 5.9, eg plate 5.3b). Such grain shape accommodation may also occur by diffusion through grains or along the grain boundaries. The driving force for this comes from the elimination of two liquid-solid interfaces and

Figure 5.9

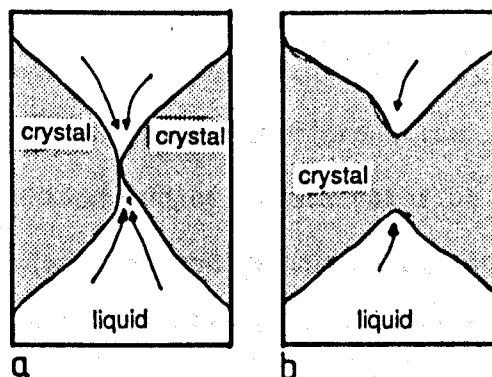


Contact flattening by transport of material as a consequence of increased solubility, caused by stress at contact (possibly due to capillary force) between two grains. (b) Result.

replacing them with a solid-solid interface of lower total energy.

- 5) When grains abut with a low-angle grain-boundary misorientation (ie the two lattices are nearly aligned with one another), complete coalescence may occur, by precipitation of dissolved material in the region of the contact, or by grain boundary migration. In the case of the former, a neck grows between the grains, eliminating the solid-solid interface (figure 5.10). Coalescence probably involves the cooperative recrystallization of two grains,

Figure 5.10



Neck growth by precipitation of material in region of high negative curvature at grain contact point (no applied stress). (b) Result.

and would require some rearrangement of atoms to accommodate any mismatch between the two crystal lattices. This would be facilitated by the preferred orientation of olivine neocrysts brought about by epitaxial nucleation in the ex-garnet lamellae of enstatite crystals, leading to a high degree of neck formation and connectivity between olivine grains (eg plate 5.2e,f). The complex nature of the larger olivines present in the bronzite runs appears to be the result of the coalescence of several internally nucleated olivine crystals (eg plate 5.3a,b,d,f). Here, coalescence leads to the formation of intricately shaped inclusions of trapped melt, which will themselves become rounded as solution-reprecipitation acts to remove regions of high curvature.

Similar solution-reprecipitation of olivine aggregates may also be driven by solubility variations in response to a thermal gradient (Walker *et al.* 1988). There is no measurable thermal gradient across the charge in these experiments, thus pointing to solution-precipitation driven by surface forces as the driving force for solution-reprecipitation (Walker *et al.* 1985).

#### 5.5.4 Summary of textural equilibration

Reaction between solid and liquid in a magma often leads to the formation of a supersaturated reaction melt, which may induce high nucleation and/or growth rates of the crystallizing phases. High nucleation and growth rates can lead to a solid phase having a high SA/V, either because it is composed of many small grains, or skeletal grains, or both. If the system is not quenched, the reaction textures may adjust by liquid-phase sintering processes, so that the initial textures may be

partially obscured, or completely replaced.

These mechanisms of textural equilibration also provide opportunity for the chemical equilibration of the olivine grains (§5.4). On the basis of the textural variations seen in these experiments, solution-precipitation is predicted to be the major mechanism of material transport; it will allow changes in chemical composition (decreasing forsterite and Ca contents) to be effected more rapidly than by simple diffusion through solid grains.

### 5.6 Summary

The incongruent dissolution of orthopyroxene yields olivine and melt as principal reaction products. Dissolution is controlled by transport processes operating in the melt, mainly diffusion at lower temperatures when most of the charge is crystalline, but convection driven by variations in the interfacial tension may dominate at higher temperatures and higher melt fractions. The formation of olivine as a reaction product is complicated; olivines crystallizing within the pyroxene are chemically and texturally out of equilibrium once exposed to exterior melt. The processes of liquid-phase sintering cause olivines to equilibrate both chemically and texturally, resulting in a variety of olivine textures, some primary and others the result of textural equilibration.

## Chapter six

### Orthopyroxene-melt reaction textures in mafic rocks

This chapter is concerned with natural examples of the reactions of orthopyroxene with host magmas, especially the textures resulting from incongruent dissolution which were experimentally investigated in chapter five. A brief survey of the literature is given, followed by the petrography of samples studied in this work. Where possible, pyroxene thermometry has been used as a guide to the temperature at which a dissolution reaction occurred.

#### 6.1 Documented examples

Numerous instances of reactions between xenocrystic or xenolithic orthopyroxene and magma exist in the petrologic literature. Table 6.1 lists references to incongruent reactions of orthopyroxene with magma, arranged with respect to reaction products. The geographical locations of these samples are shown on figure 6.1.

A first set of references (table 6.1a) relate to the reaction of orthopyroxene with magma to form clinopyroxene. These magmas range in composition from olivine-nephelinites to rhyolites. In some cases the clinopyroxene is polycrystalline and forms a granular reaction rim (eg Flett, 1908; Searle, 1961; Black and Brothers, 1965; Coats, 1968; Bryan *et al.*, 1972; Eiché *et al.*, 1987) and in others it may form a single crystal overgrowth on orthopyroxene (eg Coats, 1952; Carmichael, 1960; Byers, 1961; Muir and Long, 1965; Wise, 1969; Brothers and Searle, 1970). These may result from incongruent dissolution reactions, either between xenocrystic orthopyroxene and a foreign magma, or discontinuous reaction at a peritectic condition during

# Table 6.1

## Described orthopyroxene reactions.

### a) Reactions to clinopyroxene

# Area	Orthopyroxene <sup>1</sup>	Host magma	Phases in rim	Reference
1 Hawaii	hy	basalt	augite <sup>2</sup>	Muir+ 1965
2 Cold Bay	AK opx	bas. andesite	clinopyroxene	Brophy 1987
2 Aleutians	hy	andesite	augite	Byers 1961
2 Adak	AK hy (en <sub>85</sub> )	hy-basalt	clinopyroxene	Coats 1952
2 Aniak	AK opx	hy-andesite	augite	Coats 1952
3 Yukon, Canada	Al-brz	andesite	clinopyroxene	Marsh+ 1978
5 Nevada	opx	basalt	augite <sup>3</sup>	Eiché+ 1987
5 Nevada-Oregon	opx	rhyolite	(polyxt)cpz	Coats 1968
5 Mt. Hood	hy	dacite	pigeonite <sup>4</sup>	Conrad 1984
7 Mexico	en <sub>74-70</sub>	2 px andesite	augite	Wise 1969
8 Costa Rica	opx	ol. andesite	clinopyroxene	Luhr+ 1980
9 Soufrière	hy	basalt	clinopyroxene	Cigolini+ 1987
9 Mt. Pelé	hy	"bombs"	augite	Flett 1908
11 St. Paul's Rocks <sup>5, en<sub>85</sub></sup>	hy	"dacite"	augite	MacGregor 1938
13 Arran	opx	basanitoid	saite	Sinton 1979
16 Nisyros Greece	opx	acid glass	augite	Carmichael 1960
16 Santorini	hy	dacites	augite <sup>6</sup>	Di Paola 1974
16 Nisyros Aegean	opx	basic xenolith	pigeonite	Nicholls 1971
20 NE Japan	brz, hy	bas. andesite	clinopyroxene	Myers+ 1989
21 Chichi-jima	opx	tholeiitic	pigeonite	Kawan+ 1961
22 Marianas	opx	dacite	augite, Fe-pig	Kuroda+ 1988
23 Marianas	opx	boninite	clinopyroxene	Bloomer+ 1987
23 Banda Arc	hy <sup>9</sup>	bas. andesite	pigeonite	Dixon+ 1979
25 New Britain	hy	px. andesite	augite	Jezeck+ 1978
26 Tonga	hy	bas. andesite	augite	Lowder+ 1970
27 Kermadec	brz-hy	bas. andesite	pigeonite <sup>10</sup>	Bryant+ 1972
28 Northland	NZ opx (perid)	basalt	augite <sup>11</sup>	Brothers+ 1970
28 Auckland	NZ en, hy	ol. nephelinite basalt	pyroxene, glass Ti augite	Black+ 1965 Searle 1961

# = map reference on figure 6.1.

<sup>1</sup> This column presents the compositional information given by the author, which is usually only the name of the pyroxene.  
<sup>2</sup> Olivine has broken down to pigeonite in the same rock; augite only appears at least 50-100µm away from such olivines.

<sup>3</sup> Chemically similar to augite of the groundmass.

<sup>4</sup> Orthopyroxene also occurs in intergrowth with augite.

<sup>5</sup> Olivine may be rimmed by hypersthene or augite.

<sup>6</sup> Equatorial Mid-Atlantic Ridge.

<sup>7</sup> Sometimes with pigeonite cores.

<sup>8</sup> Hypersthene and augite both occur in dacite as phenocryst phases.

<sup>9</sup> A different hypersthene is also present rimming olivine.

<sup>10</sup> Hypersthene in andesite shows no reaction.

<sup>11</sup> In the same rock olivine is rimmed by granular pigeonite.

### b) Reactions to olivine

# Area	Orthopyroxene	Host magma	Phases in rim	Reference
1 Hawaii	opx	basalt	ol, gl, salite	White 1966
4 BC	opx	hawaiite	px, mt, ol, glass	Canil+ 1987
4 BC	hy	basanite	olivine	Nicholls+ 1982
6 Arizona	opx	basalt	olivine	Evans+ 1979
6 New Mexico	opx	alkali basalt	ol, alk. fsp. <sup>12</sup>	Fodor 1978
9 St Kitts	WI hy	basalt	cpz, ol, ores	Baker 1968
10 Main	opx	basalt	ol, pl, cpz	Wiebe 1986
12 Gough Island	hy (en <sub>70-75</sub> ) <sup>13</sup>	basalt	olivine	Le Maitre 1965
13 Derbyshire	opx	ankaramite	olivine, augite	Donaldson 1978
15 Finkenbergrd	opx	basalt	olivine	Augustithis+ 1975
15 Massif Central	opx	basalt	ol, br. glass	Hutchison+ 1975
17 W. Ethiopia	opx (mantle x)	ol. basalt	olivine	Augustithis 1978
17 Red Sea	opx	u/sat basalt	olivine	Hutchison+ 1971
19 Siberia	opx	alkali basalt	ol, br. glass	Kutolin+ 1970
28 Auckland	NZ en <sub>96-83</sub>	alkali basalt	ol, mt	Rodgers+ 1975
29 NSW Aust	opx (herz)	alkaline lava	ol, mt, salite	Binns+ 1970
29 NSW Aust	en <sub>75</sub>	thol. andesite	olivine, cpz	Duggan+ 1973
29 NSW Aust	en <sub>87-89</sub>	basalt	ol, mt, salite	Wilshire+ 1961
30 Tasmania	opx	basalt	olivine	Varne 1977
31 Kerguelen	opx (perid)	ol. basalt	olivine	Talbot+ 1963

### c) Other reactions

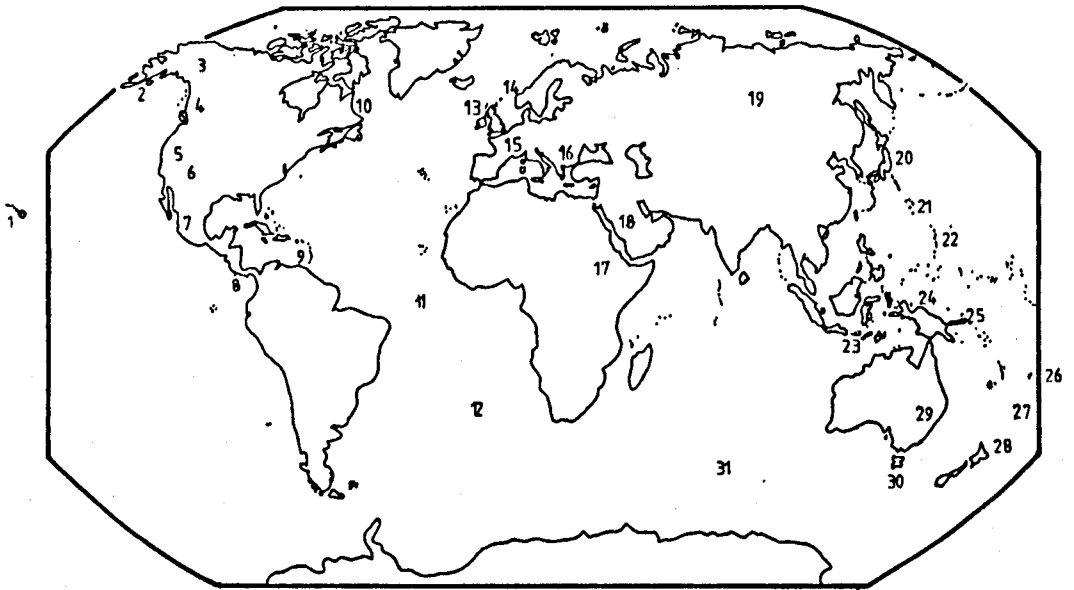
# Area	Orthopyroxene	Host magma	Phases in rim	Reference
5 Newberry	OR hy	rhyolite	hm, mt (oxid <sup>n</sup> )	Higgins 1973
5 Mt. St. Helens	hy	1980 pumice	sieve-texture	Pearce+ 1987
5 Mt. Hood	OR hy	hy andesite	hornblende	Wise 1969
14 Fen complex	opx	dankjernite	sponge zones	Griffin 1973
24 Papua	en <sub>83-66</sub>	andesite	amph + biotite	Arculus+ 1983
24 Papua	hy	"pumice"	hornblende	Heming+ 1973
28 Taupo	NZ opx	dacite	hornblende	Lewis 1968

Abbreviations as for table 4.1, except

BC	= British Columbia	WI	= West Indies
BRD	= West Germany	brz	= bronzite
Al	= aluminous	hy	= hypersthene
en	= enstatite	opx	= orthopyroxene
herz	= hercynite	xl	= xenolith
perid	= peridotite		
u/sat	= undersaturated		
hm	= haematite	oxid <sup>n</sup>	= oxidation reaction
Ti	= titanian		

<sup>12</sup> Also minor clinopyroxene and ilmenite.  
<sup>13</sup> Also a hypersthene resulting from olivine breakdown within a xenolith.

Figure 6.1  
Referenced localities



Approximate localities of rocks containing dissolved orthopyroxene referred to in table 6.1.

cooling. The distinction between these two processes is put forward in §1.4.

The second set (table 6.1b) of reaction products are polycrystalline rims containing olivine resulting from incongruent dissolution. Most such reactions are documented in alkali basalts carrying peridotitic nodules. Enstatite-bearing peridotitic inclusions are only found in the alkaline and highly alkaline basalts, which come from deeper source regions at pressures at which enstatite is stable (Green and Ringwood, 1968). Excellent descriptions of the textures resulting from these reactions are given by Wilshire and Binns (1961), White (1966), and Fodor (1978).

The third set (table 6.1c) is an amalgamation of references to various other textures where the development of sieve texture in a rim, or the presence of amphibole, biotite and oxides has been mentioned to distinguish these from the other reaction

textures.

All these reaction products are usually interpreted as resulting from reactions of the orthopyroxene with the enclosing magma. Two alternative interpretations of the olivine textures are as "crushed zones" around xenoliths (Augustithis, 1978), or the products of rapid crystallization from interface melt formed by simple orthopyroxene dissolution during eruption (Kuo and Kirkpatrick, 1985b). However, descriptions are often brief, and much information lacking. For example, many authors do not indicate whether the clinopyroxene reaction rim or "jacket" (table 6.1a) is continuous with the core crystal, or composed of many discrete crystals (eg Marsh and Leitz, 1978; Dixon and Batiza, 1979; Sinton, 1979; Cigolini and Kudo, 1987).

## **6.2 Petrography of some samples containing reacted orthopyroxene**

### **6.2.1 Reactions crystallizing olivine**

Orthopyroxene grains are usually rounded (plate 6.1b,d), and may contain exsolved lamellae of clinopyroxene, which are usually < 5 $\mu$ m but may bulge to 70  $\mu$ m (eg plate 6.2d). The outer surface of the orthopyroxene may be ragged, uneven and embayed, with embayments containing olivine, orthopyroxene, clinopyroxene and devitrified glass. Initial dissolution of the orthopyroxene leads to the nucleation of olivine (with or without clinopyroxene) on the orthopyroxene surface (plate 6.1). In some samples olivine may display hollow and skeletal habits (plate 6.2a; also Fodor, 1978; Kuo and Kirkpatrick, 1985b), but in most cases the olivine grains are equant and granular (eg plate 6.2b,c,d).

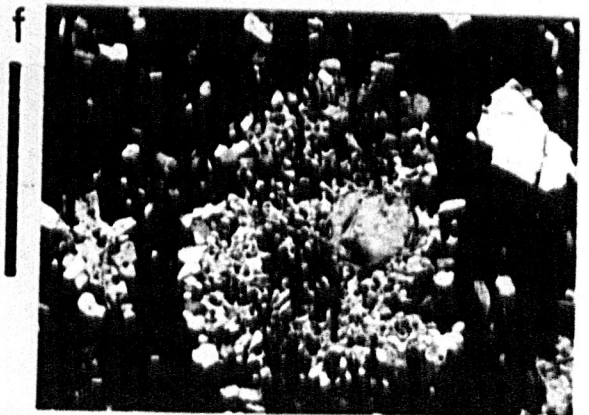
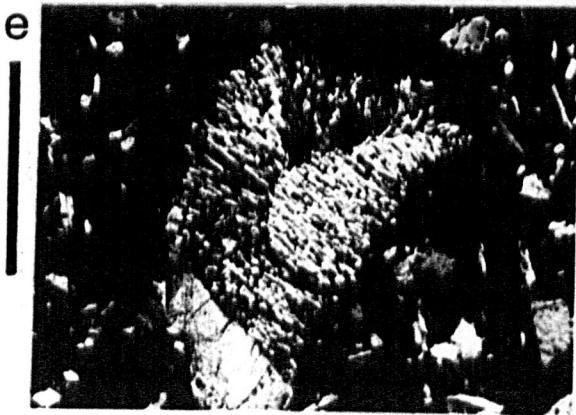
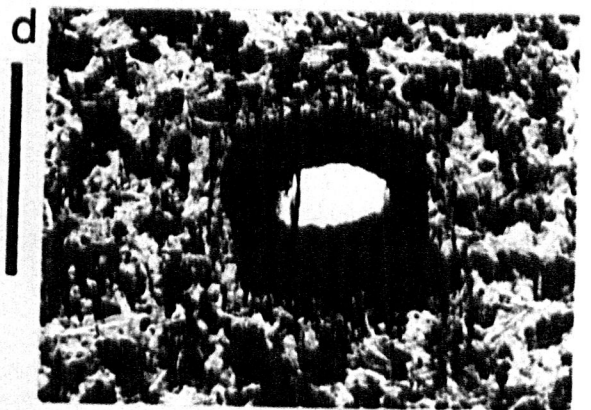
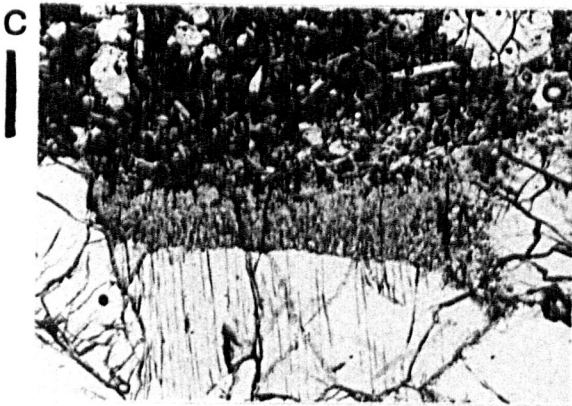
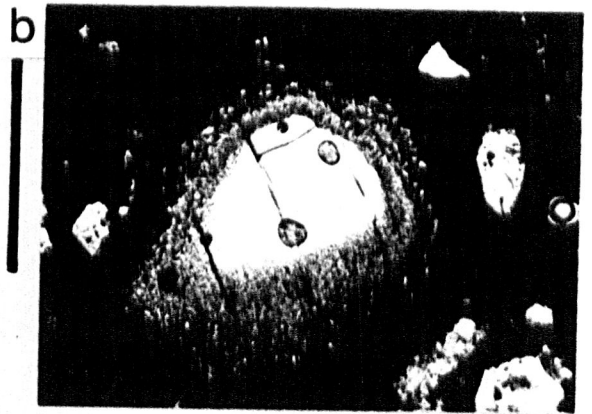
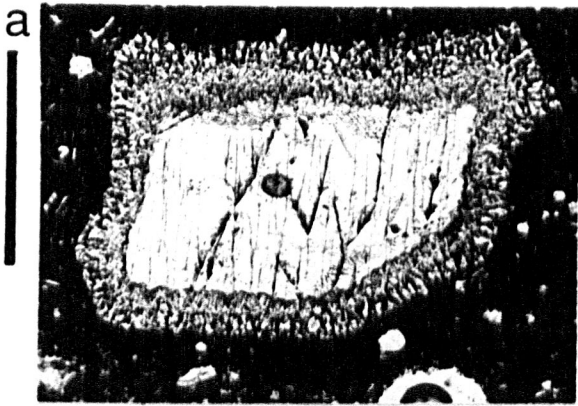
If olivine is the sole crystallizing phase at the onset of dissolution, very often it is joined at a later stage by clinopyroxene. The net result is an outer zone of olivine

Plate 6.1

Photomicrographs of orthopyroxene grains with reaction rims.  
Scale bars are 500 $\mu$ m.

- a) RF11 Rectangular orthopyroxene surrounded by an inner zone of fine-grained olivine and clinopyroxene, which is in turn surrounded by an outer zone of granular olivine. The olivines of this zone are elongate and radiating from the pyroxene.
- b) RF11 Orthopyroxene with olivine reaction rim.
- c) RF12 Orthopyroxene crystal, at the margin of an ultramafic xenolith, showing reaction against the host basalt to form a rim of olivine and clinopyroxene.
- d) RF15 Orthopyroxene grain, surrounded by reaction zone of clinopyroxene, olivine and glass, all overgrown by groundmass clinopyroxene.
- e) RF13 Clinopyroxene-olivine intergrowth, overgrown by groundmass clinopyroxene. Clinopyroxene of the intergrowth shows sector twinning.
- f) RF12 A rim of equant, granular olivines encloses a fine-grained crystalline mass of elongate, often skeletal olivine crystals with rounded corners, poikilitically enclosed in a matrix of clinopyroxene. In the centre of this mass is a large olivine crystal. Comparison with other textures (eg (a); plate 6.2c) suggests that this results from incongruent dissolution of orthopyroxene.

Plate 6.1  
Orthopyroxene grains with reaction rims.



surrounding an inner zone of olivine and clinopyroxene, where the clinopyroxene poikilitically encloses olivine crystals (plate 6.2b). Clinopyroxene lamellae may survive the demise of their host to be overgrown by clinopyroxene in the reaction zone (plate 6.2d). At the outer edge of the fringe olivine crystals are larger, more iron-rich, and there is little interstitial clinopyroxene. Olivines of all parts of the reaction rim equilibrate texturally, becoming rounded and changing shape to accommodate adjacent grains.

In other samples, olivine and clinopyroxene may co-precipitate immediately. These reaction textures are usually overgrown by clinopyroxene (eg White, 1961; plates 6.1d,e; 6.2d,e). Clinopyroxene may replace olivine as the phase crystallizing nearest the orthopyroxene (eg plate 6.1a), giving the appearance optically of a sieve texture on the orthopyroxene surface (eg Kuo and Kirkpatrick, 1985b). Orthopyroxene is sometimes enclosed and preserved by overgrowth of clinopyroxene (plate 6.2a,b), but is never overgrown by olivine.

### **6.2.2 Reactions crystallizing clinopyroxene**

No samples containing polycrystalline clinopyroxene rimming orthopyroxene were examined. One sample with clinopyroxene overgrowth on orthopyroxene is described in the appendix (H121372).

### **6.3 Textural equilibration**

The results of textural equilibration (§5.5.3) of olivine grains may be observed in some of the samples examined; however, textures are often complicated by the presence of clinopyroxene in the reaction rims.

Plate 6.2

Compositional images of orthopyroxenes with reaction rims.  
Scale bars are 100µm.

- a) RAW860 Close to the orthopyroxene (medium grey, bottom) are tiny clinopyroxene crystals (also medium grey) in a (black) matrix. Some clinopyroxene crystals are cored by (darker) orthopyroxene. Further out, olivine (white) is intergrown with clinopyroxene, before becoming the predominant mineral in the rim. The outer part of the rim consists mainly of feldspar (black) and olivine.
- b) CHD Olivine (dark grey) and clinopyroxene (medium grey) have nucleated on the orthopyroxene (black, bottom). Orthopyroxene sometimes survives as cores to clinopyroxene crystals. At the outer edge of the fringe (top) is a band of iron-rich olivine crystals (light grey), surrounding a zone of clinopyroxene poikilitically enclosing smaller olivine crystals.
- c) RF10 Partly dissolved orthopyroxene (black), surrounded by non-faceted, elongate and occasionally skeletal olivines in a matrix of clinopyroxene (darker grey) and glass, all enclosed by a band of olivines (light grey). White specks are probably spinel grains.
- d) RF16 Orthopyroxene (left, dark grey) with clinopyroxene lamellae (light grey) is embayed by reaction zone material, and passes into a zone of pockets of glass (black), irregular, elongate crystals of olivine (dark grey) and long, uneven strips of clinopyroxene (light grey). Olivine is more iron-rich (lighter) towards the groundmass (to the right), and the reaction rim is overgrown by groundmass clinopyroxene. At the right is a pyroxene phenocryst with an inclusion-rich core and inclusion-free rim. The inclusions (black) are probably glass.
- e) RF15 (As plate 6.1d) Rounded orthopyroxene grain (dark grey) showing (lighter) clinopyroxene lamellae, surrounded by a reaction zone composed mostly of elongate clinopyroxene (light grey), devitrified glass and small olivines (medium grey) visible close to the central orthopyroxene, all overgrown by a continuous rim of groundmass clinopyroxene.
- f) RF12 (As plate 6.1f) No original orthopyroxene is present in this view, except as inclusions at the edge of the central olivine. This is surrounded by a zone of rounded, skeletal olivines (light grey) enclosed by clinopyroxene (blotchy dark grey), all surrounded by a band of granular olivine. The olivines in the fringe have facets where they are in contact with the host, curved boundaries with 120° triple junctions against neighbouring olivines. They show rounding and contact flattening between adjacent grains, and complex shapes possibly due to the coalescence of adjacent grains.

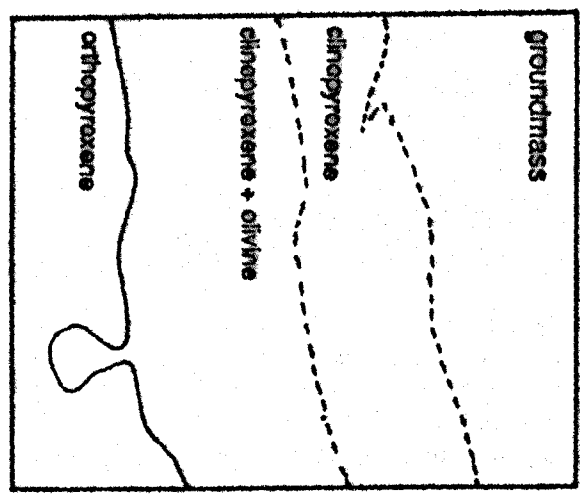
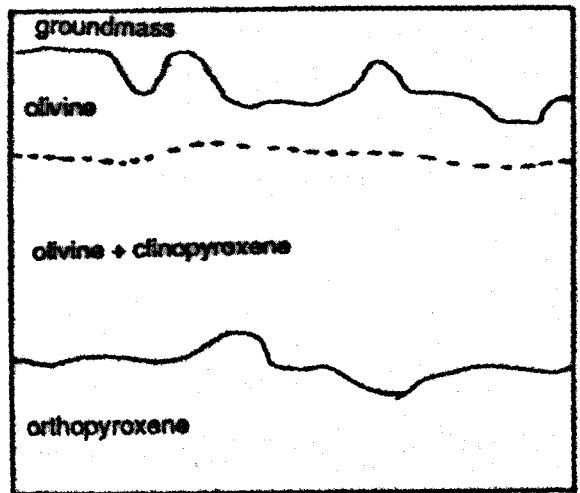
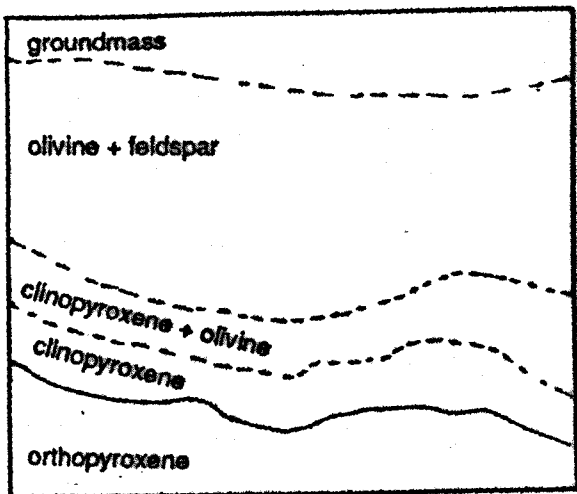


# Plate 6.2

Compositional images of orthopyroxenes with reaction rims.

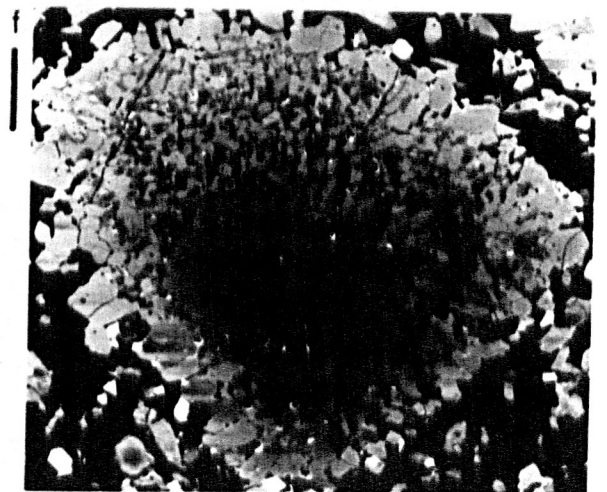
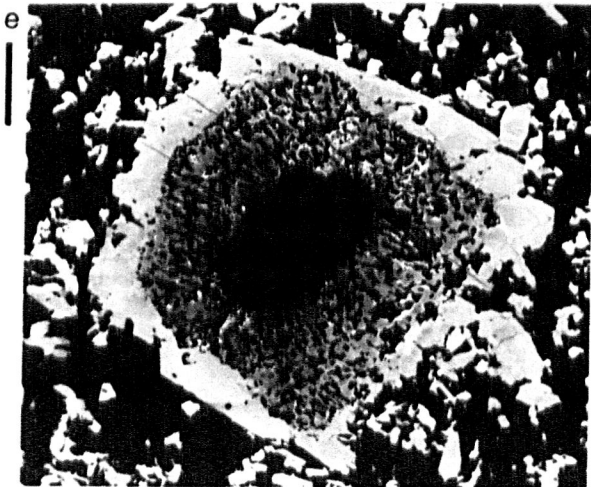
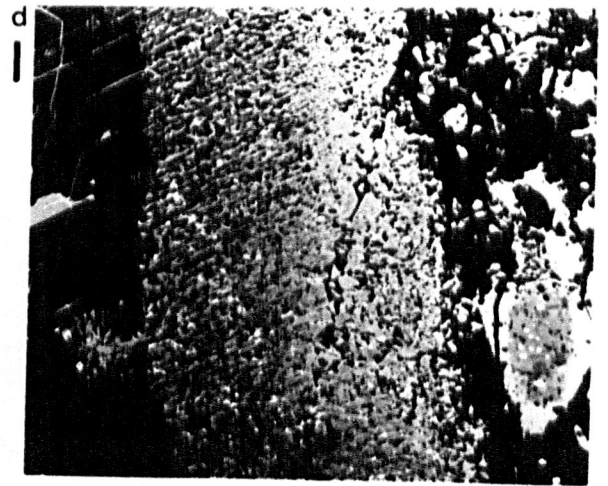
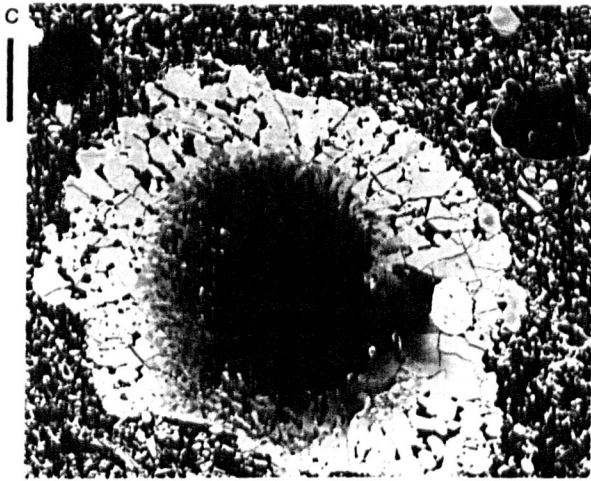
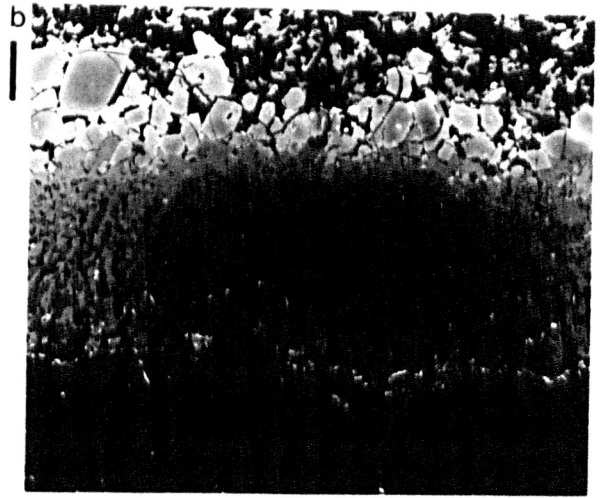
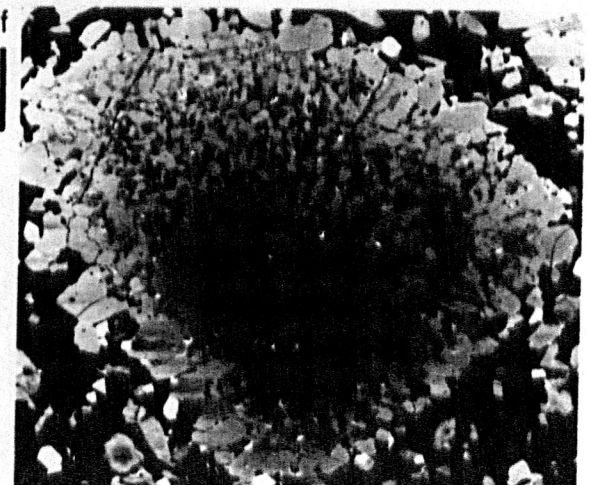
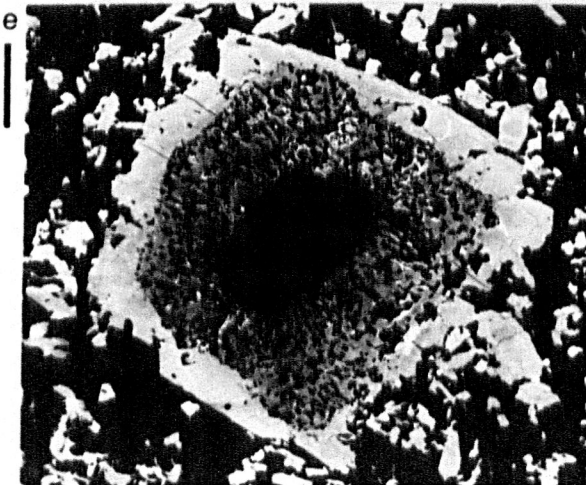
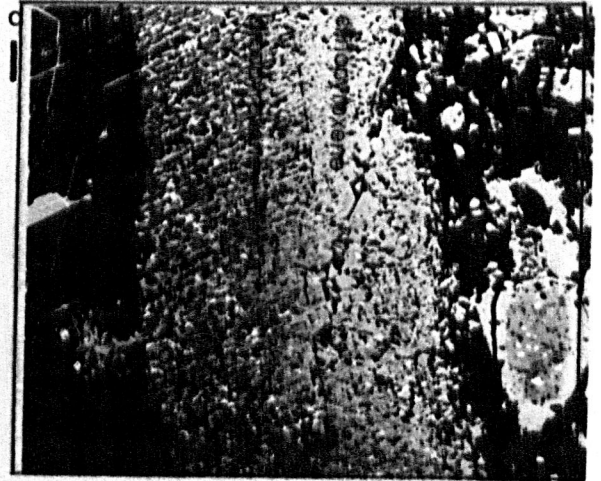
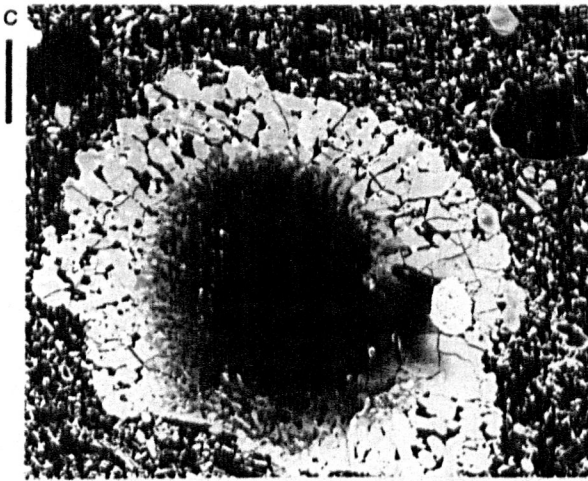
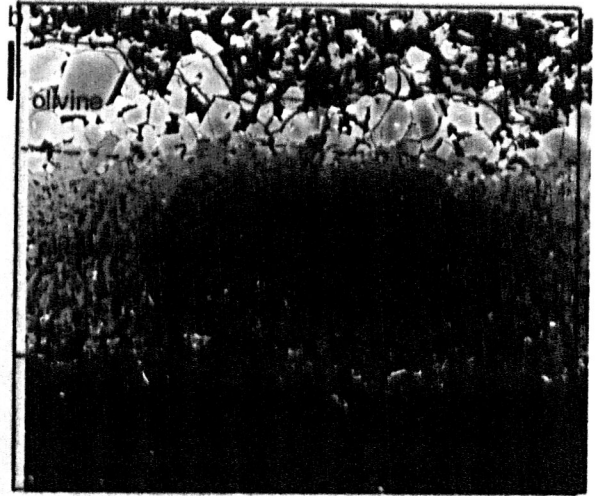
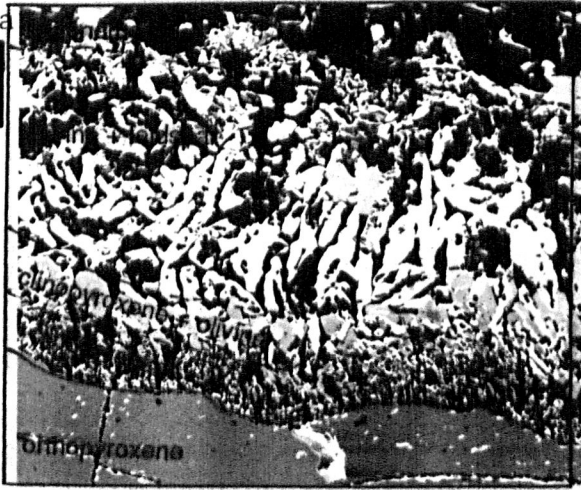


# Plate 6.2

Compositional images of orthopyroxenes with reaction rims.



Olivine grains at the limit of the reaction zone are faceted but change shape to accommodate adjacent grains and eliminate porosity. Their grain boundaries are often curved, showing contact flattening between adjacent grains, with 120° triple junctions where three grains meet. Olivine grains enclosed in clinopyroxene are rounded, sometimes irregular and complex in shape, composed of several originally distinct grains. Grain boundaries may be visible within these complex grains (plate 6.2b,c,f).

## 6.4 Chemistry

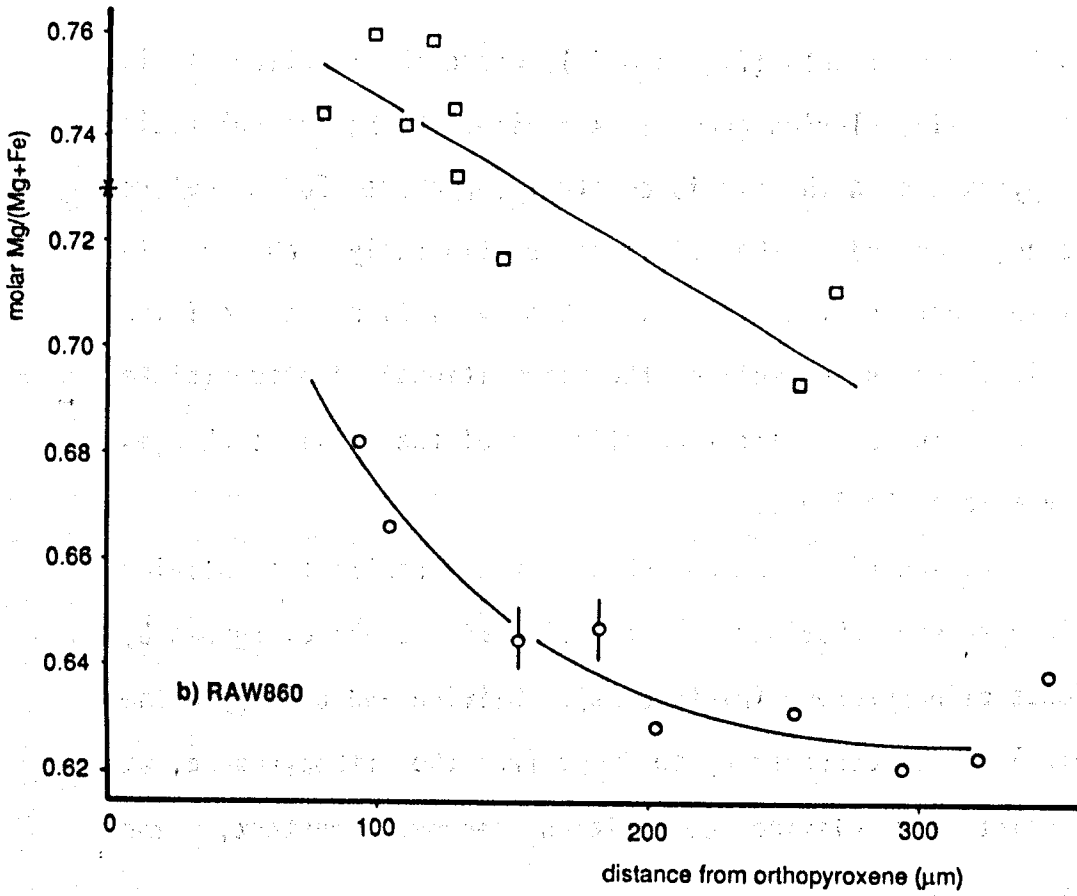
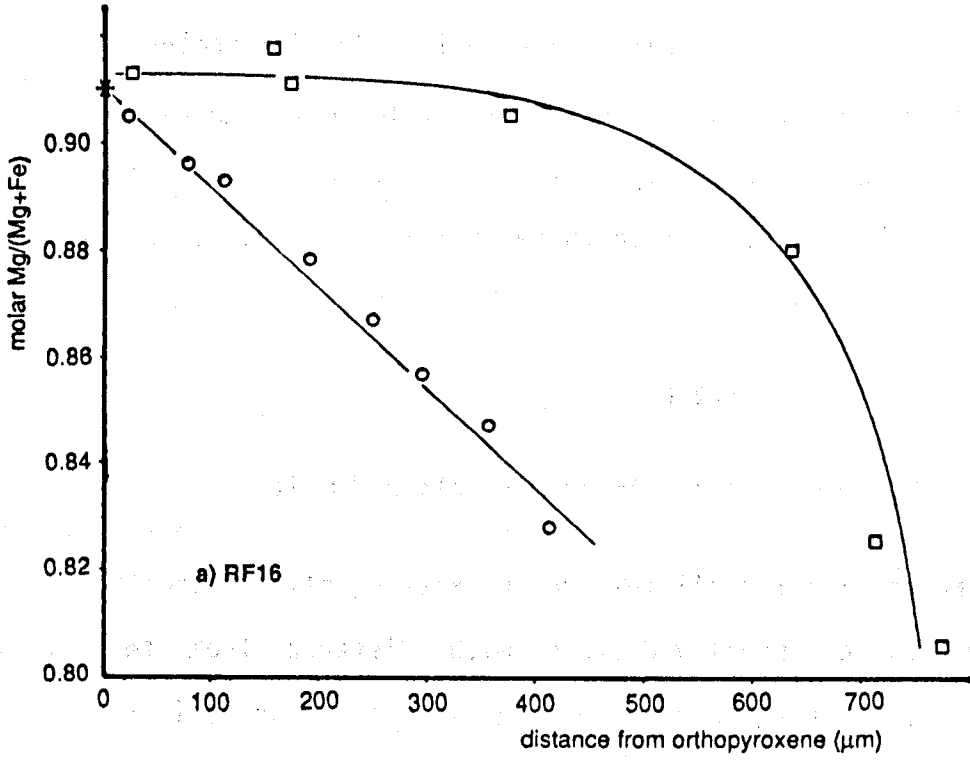
### 6.4.1 Mg-Fe exchange between minerals and melt

Mg/(Mg+Fe) ratios for olivines and coexisting clinopyroxenes in reaction fringes usually decrease with distance from the dissolving orthopyroxene towards the basaltic groundmass (figure 6.2).

In the case of RF16 (figure 6.2a), where the reaction rim is overgrown by Ti-, Al-rich groundmass augite, the Mg/(Mg+Fe) ratio of the pyroxenes in the rim is constant for about 500µm before decreasing, whereas the olivines continuously change in composition across the fringe. This variation in olivine compositions shows up well on the compositional images (plate 6.2d), where the backscatter coefficient of the olivines changes markedly across the image.

The reaction rim in RAW860 shows a total contrast of olivine and clinopyroxene behaviour. The reaction rim is not overgrown by groundmass clinopyroxene (plate 6.2a). Olivine and clinopyroxene Mg/(Mg+Fe) ratios decrease up to 200µm from the orthopyroxene, at which point the olivine composition becomes constant, and clinopyroxene is scarce.

Figure 6.2  
Olivine and clinopyroxene compositions



These compositional variations could be explained in two ways:

- 1) The observed chemical variation of olivine across the fringe (Fe-poor near orthopyroxene; figure 6.2) would ordinarily indicate that growth of olivine was from the surface of the orthopyroxene towards the host. This would result from the liquid becoming Fe-rich as a result of the removal of Mg-rich phases (olivine and clinopyroxene) during cooling of the magma, and the crystallizing olivines also becoming more Fe-rich.

It has already been shown by experiment (chapters three and five) that crystallization in these reaction rims is from the outside-inwards, towards the dissolving phase. For this situation, the effect of cooling would be to make the liquid, and thus the olivine, more Fe-rich towards the orthopyroxene. This was not observed. Apparently, this effect is more than negated by the chemical equilibration of Mg-rich olivines (next paragraph, §5.4).

- 2) Similar compositional zonation of olivine to that observed in these natural samples was developed in isothermal experiments, although with a smaller compositional range (§5.4.1). In the experiments the zonation was attributed to the crystallization of Mg-rich olivines from an Mg-rich melt adjacent to the orthopyroxene, and the subsequent

---

Figure 6.2 (facing page)

Molar Mg/(Mg+Fe) ratios of olivine and clinopyroxene in reaction rims plotted against their distance from the central orthopyroxene. Note the contrast between olivine and clinopyroxene with respect to curved or linear behaviour. Squares denote clinopyroxene, circles olivine and stars the dissolving orthopyroxene. Lines fitted by eye.

compositional equilibration of these olivines with liquid diffusing into the rim from the bulk of the charge. Diffusion of more Fe-rich melt from outside the reaction zone will lead to concentration gradients in the liquid across the reaction rim.

Such chemical equilibration was probably aided by the solution-precipitation mechanisms of textural equilibration (§5.5.3, §6.3). In addition, as cooling of the rock proceeds, the composition of the melt diffusing into the reaction rim to equilibrate with olivine becomes more Fe-rich, further increasing the Fe contents of olivines nearer the groundmass, and enhancing the gradient of olivine compositions across the rim.

Pyroxene compositions are much less susceptible to equilibration, partly because pyroxenes rarely undergo textural equilibration (eg Waff and Bulau, 1979), and because diffusion in experimental studies is much slower in pyroxenes than in olivine (eg Morioka, 1981; Brady and McCallister, 1983). Pyroxene compositions may therefore record the original compositional gradient in the reaction rim liquid more faithfully than olivine, and the difference between clinopyroxene and olivine compositions may indicate the extent of equilibration.

The compositional data for RF16 (figure 6.2a) are taken to indicate constant temperature across the fringe during dissolution, resulting in constant olivine and clinopyroxene compositions adjacent to the dissolving orthopyroxene; however, the olivines were able to compositionally equilibrate with melt or melt components transported into the reaction rim. The sharp tail-off in clinopyroxene compositions at the outer rim reflects

pyroxene growth during cooling.

The data for RAW860 (figure 6.2b) show uniform (equilibrated) olivine compositions at the edge of the rim, until sealing of the rim halted dissolution and prevented further melt access. The compositional gradient in the trapped melt is recorded in both the pyroxene and olivine compositions, although some equilibration of olivines further from the orthopyroxene has occurred.

#### 6.4.2 Olivine thermometry

Due to the lack of glass in the reaction rims of the samples studied, it has not been possible to apply the thermometers of Jurewicz and Watson (1988a) or Roeder and Emslie (1970) (§5.4.2).

Approximate temperatures from olivines in equilibrium with clinopyroxene and orthopyroxene may tentatively be calculated from the Ca contents of olivine:

$$\text{Ca(wt\%)} * 2500 + 1023 = T(\text{K})$$

(Koyaguchi, 1986c), once correction for fluorescence has been applied (§5.4.2). Temperatures estimated for olivines in reaction rims in RF16 range from 950°C near the orthopyroxene, to 1200°C towards the outer edge of the rim. However, RAW860 olivines are more calcic, and temperatures estimated using this equation are unrealistically high (1500 - 1750°C). These olivines retain hollow and skeletal shapes characteristic of rapid growth (plate 6.2a) and may not have equilibrated, thus retaining high Ca contents (eg Donaldson *et al.*, 1975b).

### 6.4.3 Pyroxene thermometry

The liquid from which clinopyroxene crystallizes close to the orthopyroxene will be saturated with orthopyroxene, because the dissolution of orthopyroxene is limited by ion transport in the melt. Hence the clinopyroxene composition should be constrained to the two-pyroxene solvus, and two-pyroxene thermometry (§2.7) can be applied to the compositions of pyroxene within the reaction fringe. Two-pyroxene temperatures for these dissolution systems were estimated using the atmospheric pressure isotherms of Davidson and Lindsley (1985; in Nabalek *et al.*, 1987) and are given in table 8.2. Some temperatures obtained by this means may be underestimates, since the clinopyroxene may not have crystallized during the dissolution reaction (as in experiments; §5.1, 5.2) but rather during subsequent cooling. The temperatures are used to estimate rates of dissolution reactions when calculating orthopyroxene residence ages (§8.2.2).

Pyroxenes crystallizing close to the orthopyroxene are poorer in Al and Ti compared to those in the host basalt, and are more suitable for thermometry, since projection from (ie correction for) non-quadrilateral components introduces larger errors to the temperature estimates. Temperature estimates for more aluminous pyroxenes may be low, as the projection scheme used overcompensates for the effect of Al.

### 6.5 Summary

Orthopyroxenes may react with magma by incongruent dissolution, either by up-temperature reaction (type b; §1.4) to form olivine, or by discontinuous reaction (type a; §1.4) forming, for example, clinopyroxene or amphibole. Clinopyroxene may co-crystallize with olivine in type (b) reactions. Such

reactions may occur at peritectic conditions, which will not necessarily lead to the formation of a reaction rim, because the whole magma will become saturated with the new phase.

If the reaction does not occur at a peritectic condition, the compositions of the neocryst phases will not necessarily be the same as those in the bulk of the melt. Olivine compositions and textures may adjust after nucleation and growth to approach chemical and textural equilibrium. Comparison of natural textures with those reproduced in experiments (chapter five) allows estimation of residence times, cooling rates, or magma ascent velocities (chapter eight).

## Chapter seven

### Reaction textures around other minerals

Survey of the literature and careful observation suggest that other minerals undergo incongruent dissolution reactions after incorporation in a foreign liquid, but the occurrence of incongruent dissolution has often not been recognized by the original author(s). Probable examples of incongruent reactions exhibited by olivine, spinel, clinopyroxene, amphibole and mica (biotite) are examined in this chapter.

At this point it may be helpful to recall the varieties of incongruent dissolution discussed in §1.4.6. These were defined as follows:

- a1) Down-temperature reaction occurring at a peritectic condition.
- a2) Down-temperature reaction not occurring at a peritectic condition.
- b1) Up-temperature reaction occurring at a peritectic condition.
- b2) Up-temperature reaction not occurring at a peritectic condition.

a1, a2 and b2 are judged to apply to textures considered here.

#### **A: Anhydrous minerals**

##### **7.1 Olivine**

The petrological literature contains many brief descriptions of reaction rims around olivine. These fall broadly into two categories:

(i) Metamorphic (solid state) reactions, where coronas of orthopyroxene and spinel are formed between grains of olivine and plagioclase (eg Aoki, 1968; Bevan, 1982; Wilson, 1982). Some authors are convinced that these textures are, in certain cases, magmatic in origin (eg Joesten, 1986). These rims are not considered further here.

(ii) Magmatic (discontinuous) reactions, either (type a1) reaction of olivine with liquid at the peritectic condition to form pyroxene, or (type a2) incongruent dissolution that may follow the incorporation of olivine crystals into a foreign magma. Since olivine is the first silicate mineral to crystallize from a wide range of mafic liquids it is not conceivable that it can react incongruently "up-temperature" (type b; §1.4.6). Many examples of incongruent dissolution at non-peritectic conditions have been mistakenly identified in the original descriptions as examples of discontinuous reaction at a peritectic condition. Tsuchiyama (1986b) suggests that "reaction rims are rarely formed by simple cooling of magmas, but more typically by reaction between disequilibrium pairs of olivine and melt due to xenocryst incorporation and magma mixing."

Olivine may react with a wide variety of igneous liquids to form reaction rims containing one or more of orthopyroxene, pigeonite, augite, amphibole, biotite, plagioclase and magnetite (table 7.1). The composition of the crystallizing phase(s) is(are) controlled by the local melt chemistry, which, in turn, is controlled by the local dissolution reaction. As a result, the pyroxene phase crystallizing during incongruent dissolution of olivine may not be the same as that crystallizing in the rest of

Table 7.1  
Described olivine reactions.

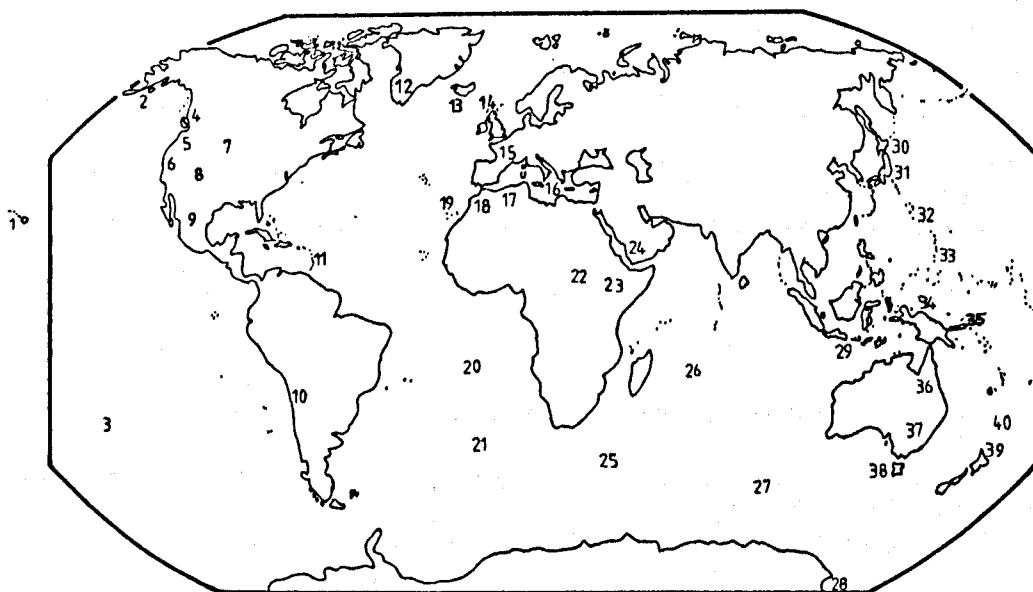
#	Area	Fo <sup>1</sup>	Host	Phases in rim	Reference	Fo	Host	Phases in rim	Reference
1	Hawaii	84	basalt	pigeonite <sup>2</sup>	Muir+ 1965	15	Massif Central	dacitic glass <sup>11</sup> , orthopyroxene	Maury+ 1974
2	Aleutians	AK 70 <sup>3</sup>	andesite	clinopyroxene	Byers 1961	16	Santorini	dacite	Barton+ 1986
2	Adak	AK	hy. basalt	clinopyroxene	Coats 1952	16	Aeolian Arc	opx (en <sub>70-84</sub> )	Keller 1974b
2	Aleutians	82-68	c-a andesite	amphibole, pl, mt	Conrad+ 1984	88-75	basalt	pig "rxn relation"	Nicholls 1971
2	Aleutians	89-87	andesite	amphibole or cpx	Conrad+ 1983	85-70	basalt	aug ± hy	Nicholls 1971
2	Shishaldin	AK 70 <sup>4</sup>	andesite	clinopyroxene	Fourmelle+ 1987	60	bas. andesite	clinopyroxene	Pe 1974
3	Tahiti		alkali gabbro	magnetite, biotite	McBirney+ 1968	ph	(rhyo) dacite	hornblende	Pe 1974
5	Mt. Hood	OR 78	andesite	hypersthene, mt	Wise 1969	gm	cpx, (opx, hb)	cpx, (hb) <sup>12</sup>	Pe 1973
6	Medicine Lake	76-63	hb. gabbro <sup>5</sup>	opx (wo <sub>2</sub> en <sub>68</sub> -wo <sub>3</sub> en <sub>4</sub> s)	Grove+ 1986	31	trachyandesite	clinopyroxene	Di Paola 1974
6	Lassen	CA 70-60	dacite	hypersthene	Macdonald+ 1965	90	alkali basalt	hypersthene (en <sub>63</sub> )	Baker 1969
6	Medicine Lk CA		basalt	opx "rxn relation"	Smith+ 1968	21	basalt	radial pyroxene	Le Maitre 1965
6	California		glass <sup>6</sup>	clinopyroxene	Webb 1941	22	basalt	clinopyroxene	Augustithis 1978
6	Lassen summit		dacite	hy or aug <sup>7</sup>	Williams 1931	27	basalt	hypersthene	Talbot+ 1963
7	Leucite Hills	90	orendite	phlogopite	Carmichael 1967	perid	px. andesite	hypersthene	Jezeck+ 1978
8	Taos	NM 87-78	dacite	cpx or opx	McMillan+ 1988	74-68	andesite	opaques	Jezeck+ 1978
8	Taos	NM ph	sil. andesite	pyroxene	McMillan+ 1988	83-78	andesite	tholeiitic	Kawano+ 1961
8	Colorado		rhyodacite	clinopyroxene	Thomson+ 1985	82-72	alkali basalt	bronzite	Aoki 1968
9	Mexico	74-87	hb. andesite	pyroxene	Luhr+ 1980	31	Niijima, Japan	orthopyroxene	Koyaguchi 1986a
10	Chile	>82	(bas)andesite	plag. opx	O'Callaghan+ 1986	31	Japan	thol basalt	Kuno 1960
11	St. Kitts	WI	basalt	clinopyroxene <sup>8</sup>	Baker 1968	31	Hakone, Japan	hypersthene, mt	Kuno 1950
11	Mt Pelée	WI 77-71	intermediate	opx (en <sub>69-82</sub> )	Bourdier+ 1985	83-57	andesite	hypersthene, pig	Sakuyama 1981
11	Soufrière	WI	andesite	hypersthene	Flett 1908	31	Myoko, Japan	hypersthene	Uchimizu 1966
11	Soufrière	WI 76-74	bas. andesite	orthopyroxene	Graham+ 1981	31	Ok, Japan	trachyandesite	Uchimizu 1966
11	Mt Pelé	WI	"dacite"	hy or augite	MacGregor 1938	fa	rhyolite	(corroded)	Komatsu 1980
12	Kialineq,	GR fa	syenite	pyroxene, amph, bi	Brown+ 1986	92	bonin. andesite	bronzite	Bloomer+ 1987
12	Ilfmausaq	GR fa	(alkaline) <sup>9</sup>	mica or amphibole	Larsen 1976	90-80	bas. andesite	rare opx rims	Dixon+ 1979
13	Iceland		basalt	pig "rxn relation"	Carmichael 1964	80-75	alkali basalt	orthopyroxene	Arculus+ 1983
14	Arran		pitchstone	orthopyroxene <sup>10</sup>	Carmichael 1960	Mg-ol	monzonite	orthopyroxene	Irving 1980
14	Derbyshire	90	basalt	clinopyroxene <sup>10</sup>	Hamad 1963	NZ 80	basalt	resorption	Smith+ 1988
						NZ	andesite	augite	Cole 1973
						NZ 94-74	"hybrid"	hypersthene	Eichelberger 1975
						NZ 83	dacite	orthopyroxene	Graham+ 1987
						NZ	basalt	aug. ores, (ol)	Lewis 1968
						NZ	alkali basalt	augite	Searle 1961
						NZ	hybrid <sup>4</sup>	hypersthene	Searle 1962b
						NZ	andesite	hypersthene	Searle 1962b
						40	basalt	pigeonite, cpx	Steiner 1958
									Brothers+ 1970

# refers to the map location on figure 7.1.  
Abbreviations are given in table 7.5.

- 11 Formed by partial melting of biotite gneiss xenoliths.
- 12 The direct reaction to opx + mt was not observed.
- 13 Groundmass pyroxene is aegirine-augite.
- 14 Alkali olivine basalt which now contains hypersthene, as a result of contamination with argillaceous sediments.

- 1 Olivine composition (% forsterite component).
- 2 This pigeonite is Fe-rich and Ca-poor compared to the groundmass pigeonite. Augite is present in basalt, but not in rim.
- 3 Phenocryst composition. Fo<sub>90</sub> xenocrysts do not have reaction rims.
- 4 Composition of olivine rim formed by prior olivine-liquid reaction.
- 5 Inclusions in rhyolites and dacites
- 6 Olivine impinged onto glass around dissolving quartz.
- 7 Olivines with hypersthene rims and with augite rims may be seen in same section.
- 8 This feature is more common in basalts with a crystalline matrix than in those with a glassy matrix.
- 9 pulaskite - naujaite, derivatives of augite syenite magma.
- 10 Not mentioned by Donaldson 1978.

Figure 7.1  
Referenced localities



Approximate localities of rocks containing incongruent reaction textures referred to in tables 7.1, 7.3-7.5.

---

the magma (eg Muir and Long, 1965) and, by this, type a2 reactions are distinguishable from type a1.

In some liquids, reactions may involve a two-pyroxene cotectic, crystallizing two distinct pyroxene compositions simultaneously (MacGregor, 1938; Brothers and Searle, 1970; Nicholls, 1971).

Local variations in melt chemistry resulting from dissolution may lead to limited regions of stability for neocrystic minerals. For example, Uchimizu (1966) documents an example of olivine dissolving to produce hypersthene whilst elsewhere in the same rock hypersthene is dissolving to form pigeonite. Similarly, Le Maitre (1965) describes orthopyroxene in an ultramafic inclusion reacted to form olivine, while at the edge of the inclusion this olivine has dissolved to form a compositionally distinct orthopyroxene.

The reaction of olivine with alkali basalt usually leads to

the crystallization of granular augite around olivine, but the assimilation of both aluminous and siliceous material may allow the development of hypersthene and initiation of the olivine-hypersthene reaction rather than the olivine-clinopyroxene reaction (Searle, 1962b).

These reactions may proceed down-temperature beyond pyroxene to amphibole (eg Pe, 1974; Conrad *et al.*, 1983) or mica (Larsen, 1976; Brown and Becker, 1986), and for some samples there is no evidence of pyroxene having participated in the reaction at all (eg Arculus *et al.*, 1983; Conrad and Kay, 1984). This may be due to lower temperature and higher H<sub>2</sub>O content of the magma.

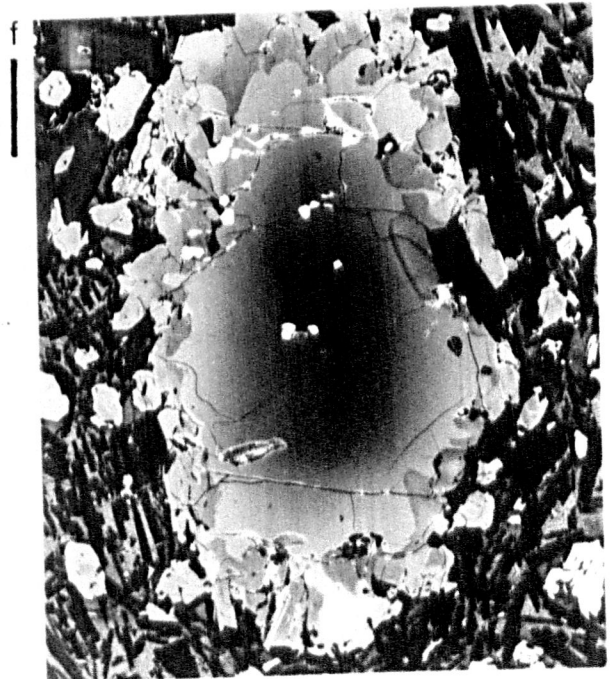
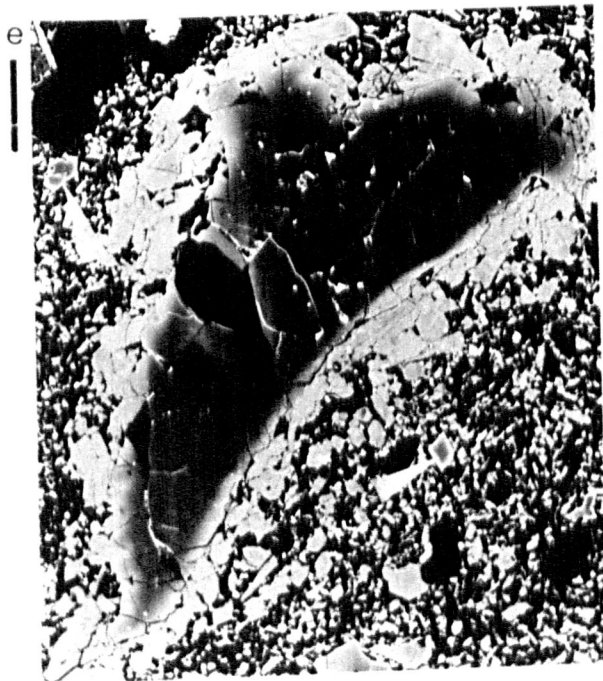
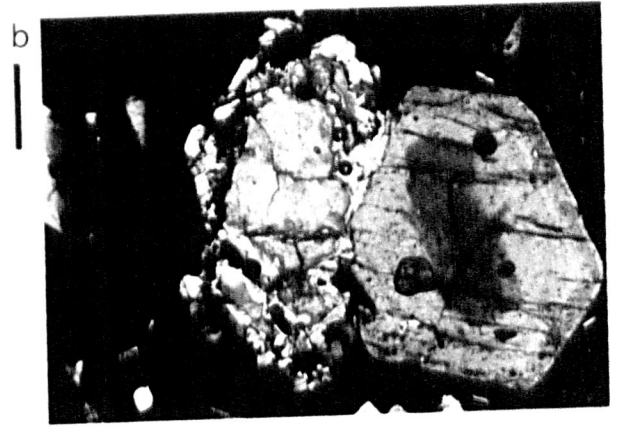
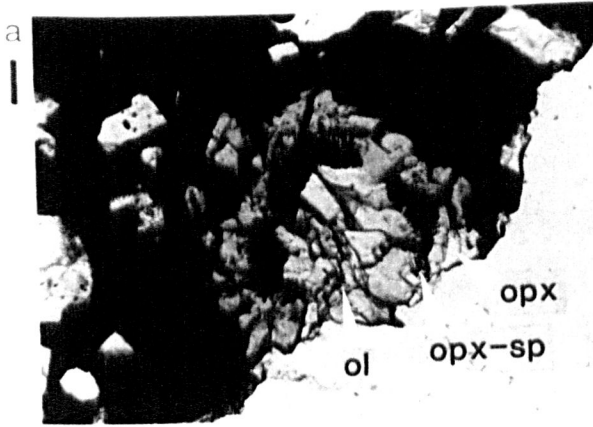
#### 7.1.1 Examples of rimmed olivine

Three different olivine reaction textures are presented in plate 7.1. Olivine and melt may react to form a continuous rim of orthopyroxene (RC417; plate 7.1d,f), a magnetite-orthopyroxene symplectite rimmed by granular orthopyroxene (H57273; plate 7.1a,b), or a rim of granular, zoned clinopyroxene (RF10; plate 7.1c,e). Experimental investigation of the reactions of olivine and melt has shown that granular rims of orthopyroxene may be reproduced if the olivine xenocryst is more magnesian than the equilibrium olivine composition, and opaque zones consisting of orthopyroxene, magnetite and melt may be reproduced by the reaction of more fayalitic olivine with melt (Tsuchiyama, 1986b). Reaction of olivine with siliceous basalt just above the liquidus may also lead to the crystallization of a rim of granular orthopyroxene (Thornber and Huebner, 1985; §1.2.4c).

Plate 7.1  
**Olivine reaction textures.**  
Scale bars are 100 $\mu$ m.

- a) H52723 Olivine grain with a fringe of orthopyroxene and magnetite in symplectic intergrowth.
- b) H52723 (crossed polars) Euhedral zoned clinopyroxene with rounded corners (right) and olivine with orthopyroxene-magnetite reaction rim (left).
- c) RF10 (crossed polars) Olivine, at extinction, with reaction rim of clinopyroxene.
- d) RC417 (crossed polars) Olivine, at extinction, with reaction rim of orthopyroxene.
- e) RF10 (As (c)). Olivine, zoned outward to more Fe-rich compositions, surrounded by complexly zoned clinopyroxene. Small, zoned, euhedral, unrimmed olivines are present throughout the groundmass (arrowed).
- f) RC417 (As (d)). Embayed olivine (medium grey) with included spinel (white) with a continuous overgrowth of orthopyroxene (slightly darker) (see also plate A2c).

Plate 7.1  
Olivine reaction textures.



### 7.1.2 Chemistry of olivine and rim phases

Olivines in RC417 (plates 7.1d,f, A2a) are zoned ( $fo_{89-82}$ ; table 7.2#1) and overgrown by orthopyroxene ( $wo_3en_{81}fs_{16}$ ; table 7.2#2) that is less aluminous than the groundmass orthopyroxene composition (table 7.2#3).

Olivines in RF10 (plate 7.1c,e) are zoned ( $fo_{88-80}$ ; table 7.2#4,5) and rimmed by augite (table 7.2#7), which is Mg-rich and Ti-, Al-poor compared to groundmass pyroxenes (table 7.2#8). Smaller, euhedral crystals of olivine (cores  $fo_{85}$ ; table 7.2#6) show no reaction with the basalt. The pyroxenes display oscillatory zoning, which shows that pyroxene growth was away from the olivine as well as towards it.

For RC417 it is difficult to distinguish between (a1) and (a2) varieties of incongruent dissolution on the basis of chemistry, but since most olivine crystals in this rock are euhedral and unrimmed (see appendix), those with rims are assumed to be xenocrystal. For RF10, the Mg-rich, Al-poor composition of the rim pyroxenes suggests that rim growth preceded pyroxene crystallization in the groundmass, arguing against reaction at peritectic condition (type a1). The presence of small euhedral olivine microphenocrysts (plate 7.1e) also precludes type (a1).

### 7.2 Clinopyroxene

Spongy textures of clinopyroxene (with rims full of melt inclusions or other crystalline phases eg plate 7.2c,e) have been frequently described in the literature (eg White, 1966; Donaldson, 1978; Brearley *et al.* 1984; Canil *et al.* 1987). This has been interpreted as disequilibrium melting (Donaldson, 1978) since in some rocks it can be found inside xenoliths, distant from host melt. It is strongly reminiscent of the partial melting

Table 7.2  
Analysed mineral compositions.

# Rock	Sample	Number	SiO <sub>2</sub>	TiO <sub>2</sub>	Al <sub>2</sub> O <sub>3</sub>	FeO*	MnO	MgO	CaO	Na <sub>2</sub> O	K <sub>2</sub> O	Total	
<b>Olivine reactions</b>													
1	RC417	ol core	239/8	39.78	-	-	10.60	0.12	48.66	0.17	-	-	99.93
2	RC417	opx	239/12	54.45	0.38	0.94	15.07	0.37	27.46	2.08	-	-	100.75
3	RC417	gm opx	239/13	54.61	0.22	2.33	12.65	0.34	28.39	1.67	-	-	100.21
4	RF10	ol core	264/14	39.75	-	-	12.23	0.17	47.39	0.18	-	-	99.72
5	RF10	ol rim	264/19	39.04	-	-	19.36	0.41	42.20	0.38	-	-	101.39
6	RF10	gm ol	264/18	39.85	-	-	14.25	0.24	46.10	0.29	-	-	100.73
7	RF10	fr cpx	264/17	48.74	1.97	4.33	6.31	0.17	14.64	22.54	0.34	-	99.04
8	RF10	gm cpx	264/20	47.04	2.90	6.14	7.97	0.11	12.38	22.46	0.72	-	99.72
<b>Clinopyroxene</b>													
9	RF11	M-cryst	248/1	50.20	0.76	7.14	5.61	0.10	16.29	17.86	1.11	-	99.07
10	RF11	spng px	248/5	50.22	1.09	4.02	5.30	0.13	15.71	21.80	0.42	-	98.69
11	RF11	over px	248/3	42.97	4.39	8.97	8.41	0.11	11.52	22.21	0.53	-	99.11
12	RC417	ph px	245/1	50.42	0.53	4.25	6.86	0.20	15.45	20.83	0.46	-	99.00
13	RC417	fr cpx	245/7	51.77	0.36	1.71	8.82	0.31	16.70	19.09	0.27	-	99.03
14	RC417	fr opx	245/9	54.30	0.31	0.88	14.68	0.37	26.59	1.98	-	-	99.11
<b>Amphibole reactions</b>													
15	RF9	kr core	235/23	38.84	5.28	13.48	13.74	0.26	10.42	11.62	3.01	1.29	97.94
16	RF9	kr rim	235/24	40.06	4.00	11.20	17.86	0.77	8.56	11.15	2.95	1.67	98.22
17	RF9	fr px	235/18	50.97	0.85	2.05	13.70	1.57	8.35	20.20	2.10	-	99.79
18	RF9	incl hb	235/30	48.13	2.95	5.02	11.52	0.78	15.20	8.90	4.84	1.43	98.77
19	RC409	hb	233/1	43.49	2.61	11.05	13.84	0.34	13.34	10.95	2.11	0.42	98.15
20	RC409	fr cpx	233/6	51.55	0.54	1.73	9.59	0.48	15.95	19.38	0.27	-	99.49
21	RC409	fr opx	233/2	52.95	0.32	1.73	17.27	0.55	25.72	1.68	-	-	100.22
22	RC404	hb	228/46	49.69	0.93	5.91	11.54	0.59	16.55	11.19	1.17	0.34	97.91
23	RC404	fr cpx	228/36	50.42	1.24	2.92	10.83	0.48	16.68	17.31	0.33	-	100.22
24	RC404	fr opx	228/37	54.28	0.37	1.37	14.81	0.50	27.54	1.75	-	-	100.62
25	RC404	gm cpx	228/50	53.20	0.29	1.27	9.42	0.34	17.68	18.24	0.21	-	100.65
26	RC404	gm opx	228/52	54.24	0.21	1.36	15.84	0.42	27.40	1.54	-	-	101.01
<b>Biotite reactions</b>													
27	RC404	biotite	227/6	37.27	4.08	13.65	14.13	0.21	15.99	-	0.83	8.27	94.43
28	RC404	fr opx	227/9	51.64	0.57	4.19	13.87	0.36	28.40	1.04	-	-	100.07

**Abbreviations:**

cpx - clinopyroxene  
fr - fringe  
gm - groundmass  
hb - hornblende  
incl - included  
kr - kaersutite

M - megacryst  
ol - olivine  
opx - orthopyroxene  
over - overgrowth  
ph - phenocryst  
spng - sponge-textured

and dissolution textures of albitic plagioclase (Tsuchiyama and Takahashi, 1983; Tsuchiyama, 1985).

In one sample (RF11, plate 7.2b), partial dissolution of the aluminous clinopyroxene megacryst (table 7.2#9) has led to the formation of a sponge-textured zone of clinopyroxene (richer in Ca and poorer in Al, table 7.2#10). The whole is overgrown by a Si-poor, Ti, Al-rich augite (table 7.2#11). Partial dissolution of aluminous clinopyroxene is also seen in BM16, where these pyroxenes impinge on the reaction rims around dissolving quartz (plate A4b,d).

Another texture observed (plate 7.2c), which apparently has not been reported in the literature, is the formation of granular rims of Al-poor clinopyroxene (table 7.2#13) and orthopyroxene (table 7.2#14) around aluminous clinopyroxene phenocrysts (table 7.2#12). Orthopyroxene of the rim is compositionally different from the groundmass orthopyroxene

---

Table 7.2 (facing page)

**Descriptions:**

**Olivine:**

- RC417 "ol" is rimmed by "opx". "opx rim" is the composition of the outer edge of the overgrowth layer and "gm opx" is the composition of orthopyroxene in the host.
- RF10 The reacted olivine has a core composition of "ol core", a rim composition of "ol rim" and is surrounded by clinopyroxene of composition "fr cpx". "gm ol" and "gm cpx" are the compositions of olivine and clinopyroxene in the host.

**Clinopyroxene:**

- RF11 The clinopyroxene "M-cryst" is rimmed by "spng px", and these are overgrown by "over px".
- RC417 The clinopyroxene "ph px" is rimmed by granular "fr cpx" and "fr opx".

**Amphibole:**

- RF9 The reacted kaersutite "kr" is rimmed by aegirine-augite "fr cpx". "hb" is the composition of a distinct amphibole phase within a hollow kaersutite grain.
- RC409/404 "hb" is rimmed by "fr cpx" and "fr opx".

**Biotite:**

- RC404 "biotite" is rimmed by granular "fr opx".

# Rock

Olivine

1 RC41  
2 RC41  
3 RC41

4 RF10  
5 RF10  
6 RF10  
7 RF1C  
8 RF1C

Clinopy

9 RF11  
10 RF11  
11 RF11

12 RC4:  
13 RC4:  
14 RC4:

Amphib

15 RF9  
16 RF9  
17 RF9  
18 RF9

19 RC4  
20 RC4  
21 RC4

22 RC4  
23 RC4  
24 RC4  
25 RC4  
26 RC4

Bioti

27 RC  
28 RC

Abbre  
cpx  
fr  
gm  
hb  
incl  
kr

Plate 7.2

Spinel and clinopyroxene reaction textures.

Scale bars are 100 $\mu$ m.

- a) RF11 Green spinel (black) with spongy magnetite overgrowth (white) in basalt.
- b) RF11 Clinopyroxene megacryst (with cracks), is surrounded by an inclusion-rich spongy zone, all overgrown by zoned, aluminous clinopyroxene with many re-entrants, indicative of rapid growth.
- c) RC417 Aluminous clinopyroxene phenocrysts, surrounded by granular rims of aluminium-poor orthopyroxene and clinopyroxene.

# Plate 7.2

Spinel and clinopyroxene reaction textures.

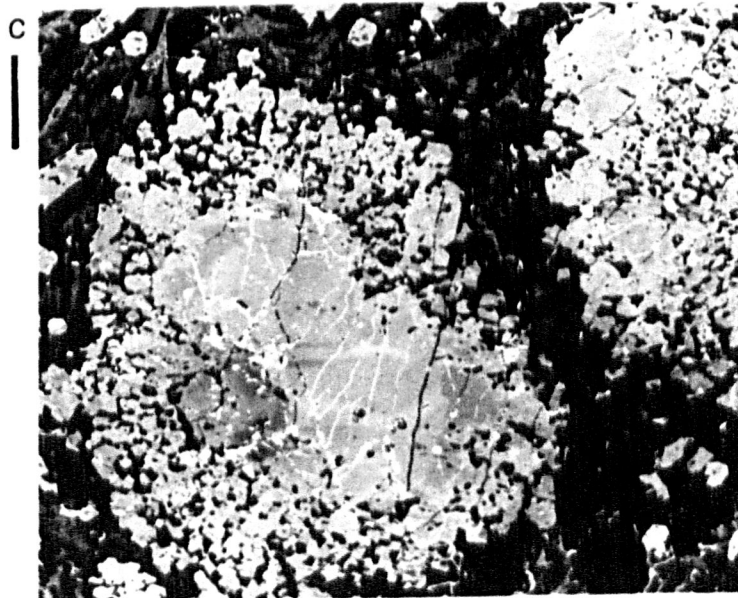
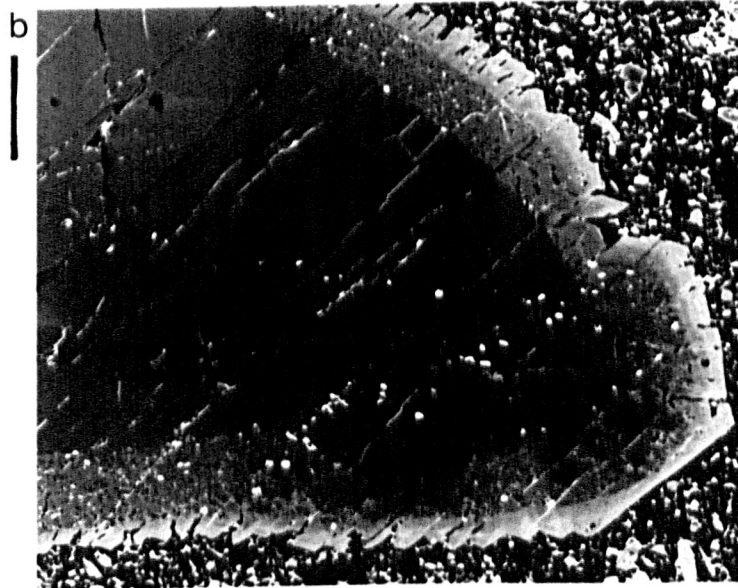
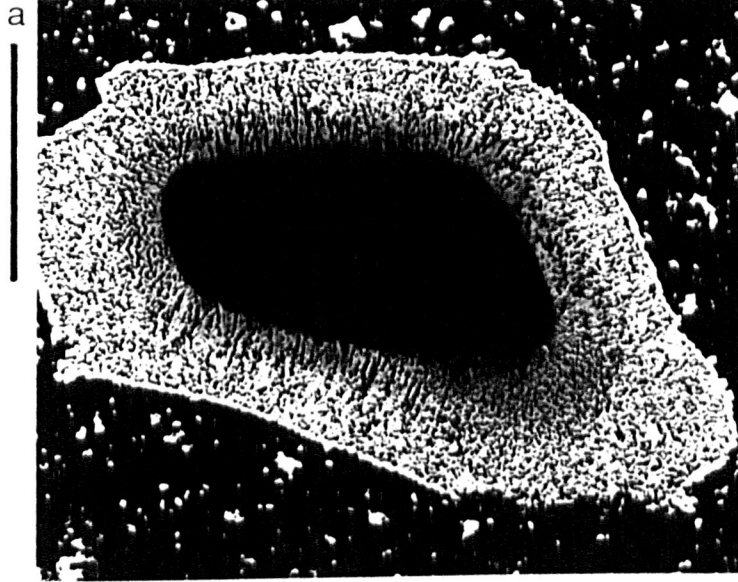


(table 7.2#4). It probably resulted from the incongruent dissolution of the aluminous phenocryst into the basalt. The presence of orthopyroxene in the reaction rim suggests an "up-temperature" reaction (type b), since orthopyroxene usually crystallizes before clinopyroxene during normal cooling.

### 7.3 Spinel

Translucent brown, blue and green spinel grains exposed at the margins of spinel lherzolite xenoliths are replaced by sponge-textured mixtures of magnetite and spinel (plate 7.2a) such that frequently only larger grains retain spinel cores (Wilshire and Binns, 1961; Donaldson, 1978). These textures have been interpreted as the result of oxidation reactions and not of dissolution, even when the spinel grain is rounded and rimmed by granular magnetite (Mokhtari and Velde, 1988). This is interpreted here to be the result of incongruent dissolution (type a2). Such textures are often seen in magmas where spinel xenocrysts result from the disaggregation of spinel lherzolite xenoliths (table 7.3).

#### B: Hydrous minerals

The dissolution of hydrous minerals in a melt may well be complicated by the possibility of dehydration and redox reactions resulting from physical instability, and/or changes in  $fH_2O$  and  $fO_2$ . The initial loss of water and alkalis from biotite is complicated by oxidation of  $Fe^{2+}$  through dehydrogenation, and results in the formation of iron oxide and the development of opacite (Grapes, 1986).

Table 7.3  
Spinel-melt reactions

#	Area	Spinel	Host	Phases in rim	Reference
4	BC	Cr-sp	alkali basalt	(reaction rims)	Brearley+ 1984
7	Leucite Hills	chr	orendite	phlogopite	Carmichael 1967
8	Arizona USA	green	alkali basalt	FeTi oxides	Evans+ 1979
14	Calton Hill	Cr-sp	ankaramite	magnetite	Donaldson 1978
15	Massif Central		basalt	olivine, ores	Hutchison+ 1975
18	Morocco	Al-sp	camptonite	Ti magnetite	Mokhtari+ 1988
23	W.Ethiopia	Cr-sp	alkali basalt	magnetite	Augustithis 1978
27	Kerguelen	gr/br	basalt	opaques	Talbot+ 1963
37	NSW Australia	pico	alkali basalt	opaques	Binns+ 1970
37	NSW Australia	brown	basalt(analc)	opaques	Wilshire 1961
37	NSW Australia	<sup>15</sup>	basalt	opaques	Wilshire+ 1961
38	Tasmania		basalt	opaques (Ti-mt)	Varne 1977

# refers to the map location on figure 7.1.  
Abbreviations are given in table 7.5.

<sup>15</sup> Translucent brown, blue and green spinels.

## 7.4 Amphibole

The maximum temperature stability of amphibole in andesite is  $950 \pm 20^\circ\text{C}$  (at 210MPa, with 4wt%  $\text{H}_2\text{O}$ ; Egger 1972). The upper temperature stability limit may represent either an incongruent reaction with melt or a dehydration reaction, depending on the total pressure and composition of the fluid phase in equilibrium with melt (Egger, 1972). Hornblende phenocrysts in volcanic rocks commonly show breakdown textures (table 7.4). Three distinct types of reaction products and textures are seen:

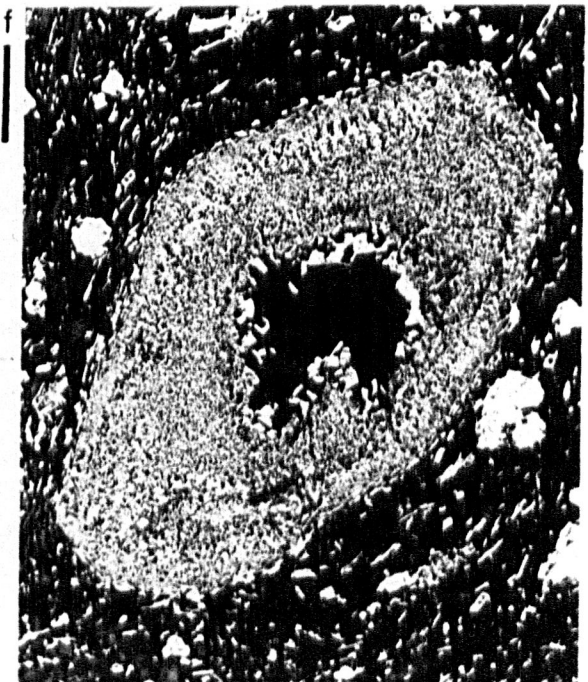
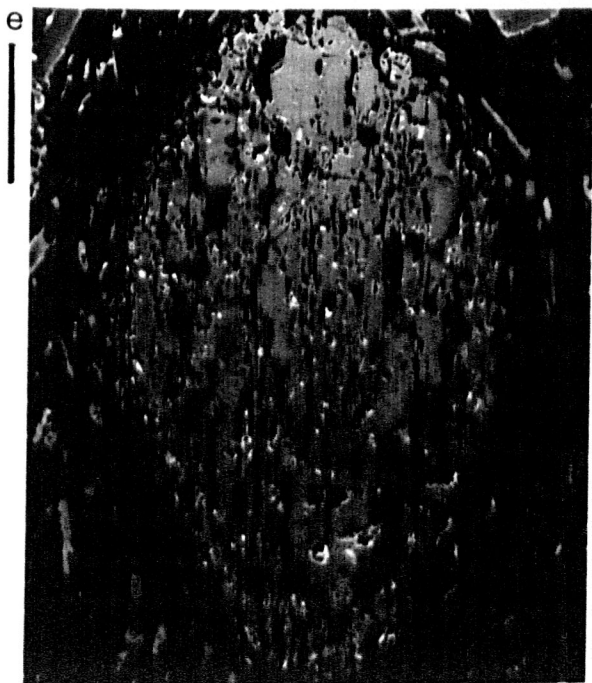
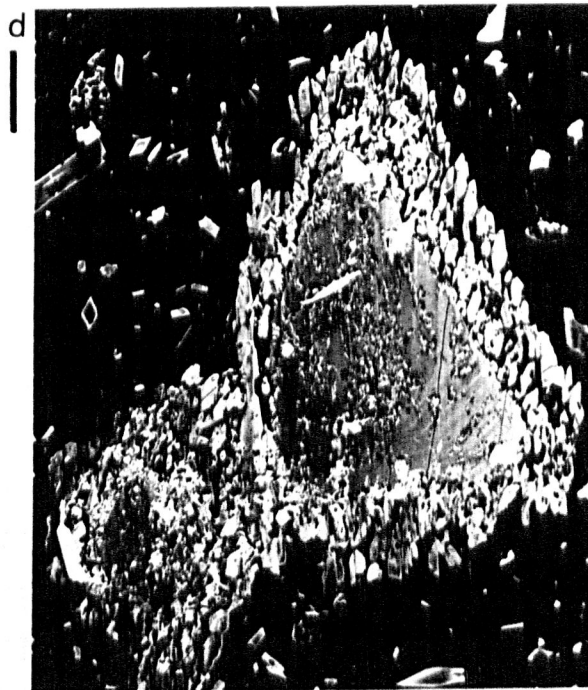
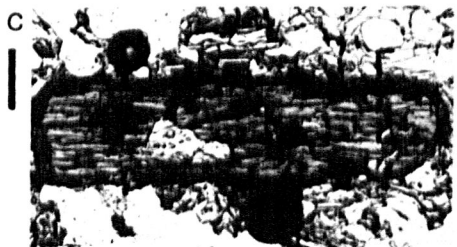
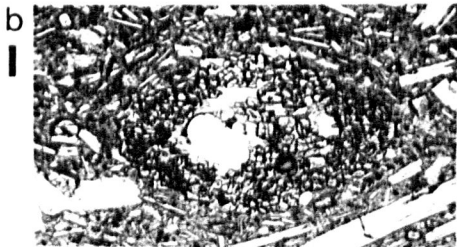
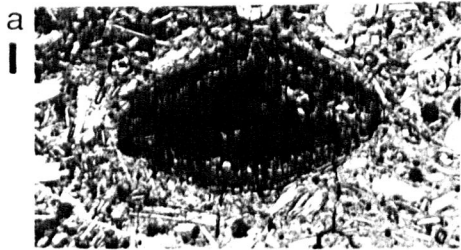
- (a) a "black" type (plate 7.3a,f) in which the amphibole is wholly or predominantly replaced by a very fine aggregate of minute iron ore and pyroxenes (opacite);
- (b) a "granular" type in which the amphibole is wholly (plate 7.3c) or partly (plate 7.3b,c,d) replaced by a fine-medium-grained aggregate of anhedral orthopyroxene, clinopyroxene, plagioclase and magnetite;
- (c) a sponge-texture (plate 7.3e), apparently not described in the literature.

Reaction (a) is caused by dehydrogenation and oxidation (Kuno, 1950) or dehydration (Mazzone *et al.*, 1987), occurring at shallow depths during magma ascent or at the Earth's surface, as indicated by the frequent presence of opacite rims in rocks with crystalline groundmass but their absence in coexisting rocks with glassy groundmass (eg Larsen *et al.*, 1937a). It has been suggested that (b) is caused by dehydration in the magma chamber (Garcia and Jacobsen, 1979), but the textures are very similar to the granular rim textures experimentally reproduced for quartz (chapter three) and orthopyroxene (chapter five). Kaersutite

**Plate 7.3**  
**Amphibole reaction textures.**  
Scale bars are 100 $\mu$ m.

- a) RC412 Rounded amphibole, partly replaced by opacite, with a rim of granular pyroxene.
- b) RC412 Clot of granular pyroxenes, probably pseudomorphing amphibole (compare with (a)).
- c) RC409 Hornblende in dacite with fine reaction rim of pyroxene.
- d) RC404 Hornblende suffering internal breakdown to opacite (speckled areas) as well as incongruent dissolution to form a rim of zoned clinopyroxene and orthopyroxene. Pyroxenes exhibit strong zoning towards hornblende. Note that pyroxenes are smaller near the hornblende and larger and connected further away.
- e) H121594 Inclusion-rich (sponge-textured) hornblende crystal surrounded by a rim of very fine-grained pyroxene.
- f) H121594 Opacite pseudomorph after hollow hornblende, composed of magnetite (white), pyroxene (medium grey) and plagioclase (black). The core of the hollow crystal contains coarse groundmass material originally included in the hornblende precursor.

Plate 7.3  
Amphibole reaction textures.



grains undergo similar reactions (see plate A6c).

Single crystals may display multiple reaction textures, in the form of granular coronas surrounding opacite (eg plate 7.3a,d). In these examples, the formation of the granular reaction product precedes the opacite, since incongruent reactions proceed from the outside of a crystal inwards, indicating that resorption also occurs within magma reservoirs. The rounded forms of the amphiboles suggest that they had been dissolving into melt and crystallizing granular pyroxene rims, despite being thermally stable. The opacite formed during subsequent eruption of the magma. Since neocryst phases often nucleate on a dissolving host, epitaxial nucleation leading to preferred orientation of neocrysts is possible (§5.1.2, §5.2.2), and subsolidus conditions do not need to be invoked to explain uniform crystallographic orientation of neocrysts (eg Mazzone *et al.* 1987).

#### 7.4.1 Chemistry of amphibole and rim phases

Hornblende crystals in RC404 are rimmed by complexly zoned pyroxene crystals. This intricate zoning comprises alternate layers of orthopyroxene ( $\text{wo}_{39}\text{en}_{76}\text{fs}_{21}$ ; table 7.2#26) and clinopyroxene ( $\text{wo}_{39}\text{en}_{46}\text{fs}_{14}$ ; table 7.2#25), and is well developed towards the central hornblende (plate 7.3d), suggesting that most pyroxene growth was in this direction and simultaneous with hornblende dissolution. Orthopyroxenes in the reaction rim are compositionally similar to those in the groundmass (table 7.2#27), but clinopyroxenes of the rim (table 7.2#23) are quite different from those in the groundmass (table 7.2#25).

Two-pyroxene thermometry (§2.7) can be applied to coexisting clinopyroxene and orthopyroxene compositions resulting from

Table 7.4  
Described amphibole reactions.

#	Area	Amph	Host	Phases in rim	Reference	#	Area	Amph	Host	Phases in rim	Reference
2	Aleutians	hb	andesite	aug ± mt	Coats 1952	18	Morocco	kaer	Camptonite	mica <sup>17</sup> or cpx <sup>18</sup>	Mokhtari+ 1988
2	Aleutians	parg hb	andesite	opaques	Conrad+ 1983	19	Teneriffe	kaer (nod)	alkali basalt	px, Fe-oxides	Borley+ 1971
5	Mt. St. Helens	hb	dacite	pl, op, opx	Kuntz+ 1981	19	Teneriffe	kaer (gm)	phonolite	px, Fe oxides	Borley+ 1971
5	Mt. Hood	OR hb	andesite	mt, hy, pl	Wise 1969	19	Canary Is	kaer	alkali basalt	cpx, bi, ore	Frisch+ 1970
6	Sierra Nevada	CA hb	bas. andesite	ores	Al Rawi+ 1967	21	Tristan da C.	kaer	trachybasalt	pl, ti-aug, ore, rh <sup>19</sup>	Le Maitre 1969
6	Lassen	CA hb	dacite	magnetite	Macdonald+ 1965	24	Yemen	kaer	basalt	opaques	Cox+ 1977
6	Modoc	CA hb	dacite	clinopyroxene, mt	Powers 1932	25	Funk Seamount	kaer	alkali basalt	pyroxene, mt	Reid+ 1988
7	Arkansas	USA	carbonatite	magnetite	McCormick+ 1987	26	Rodriguez Is.	kaer	basalt	clinopyroxene, mt	Baxter+ 1985
8	Taos	NM hb	ol. tholeiite	magnetite	Aoki 1967	27	Kerguelen	kaer	basalt	opaques+	Talbot+ 1963
8	Utah	USA kaer	basalt	glass (melt)	Hausei+ 1977	28	Antarctica	kaer	basanite	ol, px, pl, mt, rh?	Kyle 1981
8	San Juan	CO bas hb	and-dac-rhy	mt, hm?, di(hy), fsp	Larsen+ 1937a	29	Indonesia	parg	andesite	opacite	Morrice+ 1986
8	Colorado	trachy-dacite	trachy-dacite	Fel1 oxides	Leat+ 1988	31	Oki Is. Japan	kaer	trachybasalt	magnetite	Uchimizu 1966
8	New Mexico	USA Ti-hb	andesite	px, fsp, oxides	Stormer 1972	31	Iki Is. Japan	kaer	alkali basalt	ol, pl, cpx, ore <sup>20</sup>	Aoki 1970
8	Colorado	USA hb	bas/andesite	hy, aug, mt	Waters 1955	31	Iki Is. Japan	kaer	alkali basalt	hb, ore, cpx, fsp <sup>21</sup>	Aoki 1970
9	Mexico	hb	hb, andesite	opacite <sup>16</sup>	Luhr+ 1980	31	Japan	oxyhb	andesite	magnetite, px	Kawano+ 1961
10	Chile	hb	andesite	pl, px, oxides	O'Callaghan+ 1986	31	Hakone, Japan	hb	basalt	opacite	Kuno 1950
11	Saba	WI	andesite	opaque corona	Baker+ 1980	34	Papua	kaer	shoshonite	aug, mt, pl	MacKenzie+ 1972
11	St. Kitts	WI	andesite	opaque corona	Baker 1968	37	NSW Australia	kaer	basanite	opaques (few)	Binns 1969
11	Martinique	WI hb	andesite	opaques	Eichelberger 1978a	37	NSW Australia	kaer	basalt (analc)	opaques (cpx)	Wilkinson 1962
11	Soufriere	WI hb	andesite	hy, bi, fsp	Flett 1908	37	NSW Australia	hb	basalt	salite, ore (pl, ap)	Wilshire+ 1961
15	France	hb	basalt	augite, magnetite	Lacroix 1893	39	Taupo	hb	dacite	px, pl, mt	Lewis 1968
16	Greece	hb	dacite	magnetite	Di Paola 1974						
16	Santorini	hb	dacite	oxides	Nicholls 1971						
16	Santorini	hb	basalt x1	pigeonite	Nicholls 1971						
16	Santorini	hb	andesite	hy, aug, pl, mt	Nicholls 1971						
16	Aegina	hb	bas. andesite	bi or pl, aug, mt	Pe 1973						
17	Algeria	hb	basanite	magnetite, rhönite	Dantria+ 1987						

# refers to the map location on figure 7.1.

Abbreviations are given in table 7.5.

16 Or a granular reaction corona of pyroxene, plagioclase and magnetite. Both types present in same section, although opacite reaction restricted to microphenocrysts and phenocryst rim, suggesting that it preceded formation of the reaction corona.

17 Polycrystalline rim.

18 Overgrowth.

19 Plus olivine, biotite, ilmenite and alkali amphibole.

20 Marginal reaction.

21 Along cracks.

hornblende breakdown. Estimated temperatures are 1140-1100°C (RC409) and 1120-1050°C (RC404), using the atmospheric pressure isotherms of Davidson and Lindsley (1985). A two-pyroxene temperature of 1050 ± 50°C for an opacite assemblage was obtained by Mazzone *et al.* (1987).

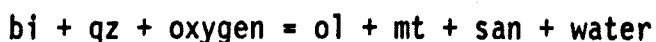
Dissolution of zoned kaersutite (RF9; plate A6c; table 7.2#15,16) leads to the crystallization of aegirine-augite (table 7.2#17). This pyroxene is too rich in the aegirine component to permit application of pyroxene thermometry. Hollow kaersutite grains (plate A6c) also contains hornblende (table 7.2#18), pyroxene, titanite and feldspar.

Granular pyroxene rims around amphibole are interpreted to form by "up-temperature" (type b) incongruent dissolution reactions. In cases where the compositions of pyroxenes in the rim are significantly different from those in the groundmass the reaction is probably of type (b2).

### 7.5 Biotite

The substitution of Mg-Fe<sup>2+</sup> has a pronounced effect on mica stability. This effect is demonstrated by comparing the temperatures at 210 MPa for phlogopite decomposition (1100°C; Yoder and Eugster, 1954) and annite decomposition (400-825°C depending on fO<sub>2</sub><sup>1</sup>; Eugster and Wones, 1962). As a consequence, micas of volcanic rocks tend to be magnesian biotites.

The stability of biotite decreases with increasing fO<sub>2</sub> and silica activity, as illustrated by the breakdown reaction (Eugster and Wones, 1962)



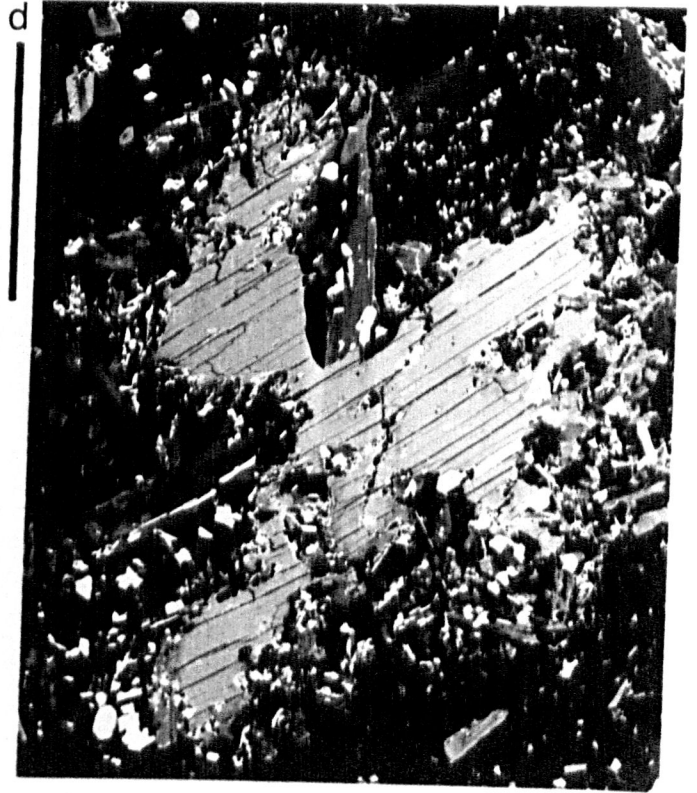
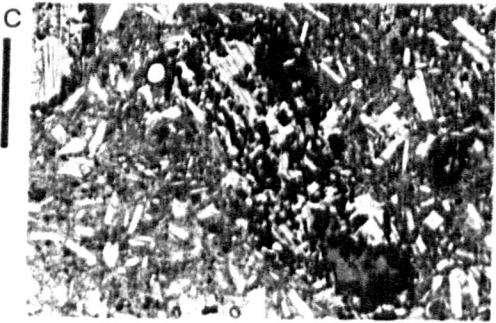
---

<sup>1</sup> At typical basalt-andesite oxygen fugacities (equivalent to QFM and NNO buffers; Gill, 1981) annite decomposes at about 700°C.

**Plate 7.4**  
**Biotite reaction textures.**  
Scale bars are 500 $\mu$ m.

- a-c) RC404 (Transmitted light). Biotite xenocrysts with reaction rims of magnetite and acicular orthopyroxene.
- d) RC404 (Backscattered electron image). (As (a)). Biotite (light grey) with associated hornblende (medium grey), rimmed by zoned, acicular orthopyroxenes (medium grey) and granular magnetite (white).

Plate 7.4  
Biotite reaction textures.



so that biotite is stable at higher temperatures in Si-poor magmas.

The breakdown products of biotite described in the literature are similar to those of amphibole (§7.4), ie either replacement by opacite, or the formation of a granular rim of pyroxene, magnetite and plagioclase (table 7.5).

#### 7.5.1 Examples of rimmed biotite

In the samples studied, biotite may be completely replaced by black opacite, but it is difficult to distinguish between opacite pseudomorphs after amphibole and after biotite. Biotites may be associated with some hornblende, and are surrounded by fine-medium-grained rims of magnetite and acicular, often skeletal orthopyroxene (plate 7.4). In these examples there is no development of opacite within the biotites after formation of granular reaction rims (eg Larsen *et al.*, 1937b), as was the case for the amphiboles (above).

#### 7.5.2 Chemistry of biotite and rim phases

Dissolution of biotite (RC404; table 7.2#27) leads to the crystallization of orthopyroxene ( $wo_2en_{80}fs_{18}$ ; table 7.2#28). The lack of clinopyroxene in the reaction rim prevents the application of pyroxene thermometers. The orthopyroxenes are Mg-rich and Ca-poor compared to those crystallized around dissolving hornblende in the same rock, despite the fact that the biotite has a lower Mg/(Mg+Fe) ratio than the hornblende. These orthopyroxenes are also Al-rich compared to the groundmass pyroxenes (table 7.2#26), consistent with their formation at the expense of biotite.

Table 7.5  
Biotite-melt reactions

#	Area	Host	Phases in rim	Reference
2	Adak	AK andesite	magnetite	Coats 1952
6	Chaos Crags	CA dacite	hb, pl, mt, gl	Heiken+ 1980
6	Owens Valley	CA basalt	magnetite	Knopf 1938
6	Lassen	CA dacite	magnetite	Macdonald+ 1965
7	Montana <sup>22</sup>	USA mafic phonolite	biotite	O'Brien+ 1988
8	Colorado	USA trachy-dacite	FeTi oxides	Leat+ 1988
8	Colorado	USA basalt	oxides, silicates	Thomson+ 1985
8	Colorado	USA bas/andesite	hypersthene, aug, mt	Waters 1955
10	Chile	andesite	pl, px, oxides, amph	O'Callaghan+ 1986
11	Martinique	WI hb.andesite	hornblende, pl, mt	Eichelberger 1978a
11	Soufrière	WI px.andesite	magnetite, px, pl	Eichelberger 1978a
16	Greece	ne-t-basalt	opaques	Wyers+ 1986
21	Gough Island	trachyte	magnetite	Le Maitre 1962
27	Kerguelen	basalt	opaques	Talbot+ 1963
37	NSW Australia	pyroxenite	salite, ore, (pl, ap)	Wilshire+ 1961
39	Taupo	NZ dacite	opacite	Lewis 1968

# refers to the map location on figure 7.1.

Abbreviations for tables 7.1 and 7.3-7.5 are as for table 6.1, except for:

Area:	CO - Colorado, USA		
	GR - Greenland		
	WI - West Indies		
Host:	bas. = basaltic	bonin. = boninitic	
	c-a = calc-alkaline	incl. = inclusion	
	ne-t- = nepheline-trachy-	ophiol = ophiolitic	
	rhyo = rhyolitic	sil. = siliceous	
Phases:	amph = amphibole	ap = apatite	
	di = diopside	en = enstatite	
	gl = glass	hm = haematite	
	hy = hypersthene	opx = orthopyroxene	
	ol = olivine	pig = pigeonite	
	pl = plagioclase	rh = rhönite	
	rxn = reaction	wo = wollastonite	
Amph:	gm = groundmass	kaer = kaersutite	

<sup>22</sup> This example is of the reaction of phlogopite with magma.

## 7.6 Summary

The textures of granular reaction rims around olivine, spinel, clinopyroxene, amphibole and biotite are very similar to those formed by the incongruent dissolution of quartz and orthopyroxene, and are interpreted here to result from incongruent dissolution. In contrast to the experimentally investigated systems, some of the natural textures (those around olivine and spinel) resulted from "down-temperature" (type a) reactions, forming rims of minerals lower in Bowen's reaction series. The compositions of the crystallizing phases may be different from the original phases and from the groundmass phases, arguing against reaction occurring at peritectic condition, and the presence of additional phases favours incongruent dissolution over partial dissolution as the process responsible for these textures.

## Chapter eight

### Applications

Mineral dissolution data acquired by previous workers has been applied in one of two ways:

- 1) Modelling the dissolution of xenoliths into (assumed superheated) magmas (eg Watson, 1982; Brearley and Scarfe, 1986) in order to estimate the time required for complete destruction of the xenolith. Brearley and Scarfe's (1986) simple model for ultramafic xenoliths suggests that dissolution will only be significant if the magma is superheated to a large degree (in excess of 50°C) or the xenoliths are small.
- 2) Estimating ascent velocities of peridotite-bearing basalts. Kuo and Kirkpatrick (1985b) suggested that adiabatic ascent of an alkali basalt from depths equivalent to 1.4MPa will cause the magma to become superheated by about 30°C at the surface, and on this basis apply superliquidus data to ascertain the duration of the dissolution reactions. They argued that, during the reaction process, latent heat required for dissolution must be absorbed from the host magma, but since the volume of xenoliths is usually small compared to the volume of magma, the heat absorbed from the magma will be negligible and should have little effect on the path of adiabatic ascent.

For each application, the dissolution data applied were acquired in superheated melts, and superheated conditions have been a primary assumption of each model.

At source, a magma will be in equilibrium with local solid

### 8.1 Xenocryst digestion in a crystallizing magma.

Complete digestion of xenocrysts is rarely observed in systems involving subliquidus dissolution of quartz. More normally a quartz xenocryst or quartzose xenolith may be surrounded by a sealed reaction rim, implying that dissolution has been halted by cessation of melt transport across the rim. This abrupt change in dissolution behaviour has been observed for longer duration experiments under isothermal conditions (§3.2), where the increasing tortuosity of the pyroxene fringe was held responsible for disabling melt transport. The high viscosity of the siliceous interface melt is also partly responsible. By contrast, in orthopyroxene experiments, complete replacement of orthopyroxenes by the granular olivine reaction product of incongruent dissolution has been observed both in experiments and in natural samples.

For examples where dissolution is not complete, the pre-dissolution size of both quartz and orthopyroxene xenocrysts may be obtained by locating the locus of highest neocryst density in the reaction rim. This marks where initial nucleation of neocrysts takes place on the surface of the dissolving crystal (§3.1, §5.1, §5.2). Subsequently, the neocryst density immediately adjacent to the dissolving phase decreases, because growth occurs preferentially on existing neocrysts (discontinuous grain growth; §5.5.3). For example:

Sample BM16 contains about 0.5% quartz grains by volume, of average radius 500 $\mu\text{m}$ , with pyroxene reaction rims about 50 $\mu\text{m}$  wide. Hence, the volume change per grain is about  $1.7 \times 10^{-10}\text{m}^3$  and the original (incorporated) quartz content was actually about 0.7%.

## **8.2 Residence times.**

The widths of rims produced by incongruent dissolution provide a means to estimate the duration of the reaction (equal to a minimum residence time, if it can be shown that the dissolution reaction did not cease before eruption of the magma). These reaction durations (residence times) may be estimated for both incorporated xenocrysts from country rock encountered by the magma during its passage, or phenocrysts of another magma which has mixed with the first.

### **8.2.1 Reacted quartz.**

The residence time for quartz can be interpreted in one of two ways, depending on the texture of the pyroxene fringe. If the fringe is porous, and melt transport across the fringe was possible until eruption caused the system to be quenched, the residence time estimates the duration between incorporation of the quartz and eruption. If the fringe is sealed and impermeable, the residence time estimates the duration between incorporation of the quartz and halting of the dissolution reaction. The estimates are minima, because:

- 1) Dissolution of quartz following incorporation may have started at temperatures above the pyroxene liquidus, and such reaction would not be recorded by the pyroxene fringe. No information can be obtained about superliquidus dissolution unless there is alternative evidence of the original xenocryst grain sizes.
- 2) There may be no evidence of the abrasion of previous reaction rims.

- 3) Hybridization will not be instantaneous, and some time may elapse before particular quartz crystals find themselves in an undersaturated magma. During magma mixing this hybridization may first result in superheating of the magma carrying quartz, leading to simple dissolution and rounding, before complete mixing results in incongruent dissolution.
- 4) The estimated residence time for fringes which have become sealed is only that taken for growth of the pyroxene fringe to halt dissolution. When melt transport through the fringe is no longer possible, pyroxene growth continues at the outer edge of the fringe with material derived from the host, until the fringe is sealed. Such textures could remain at magmatic temperatures for unknown durations after sealing of the fringe prevents further quartz dissolution .

Residence times for reacted crystals have been estimated by assuming that:

- a) the reaction occurs under isothermal subliquidus conditions (ie the dissolution rate is constant), and
- b) the reaction is quenched (eg by eruption) while dissolution is still time-independent (ie while melt still has access through the reaction rim).

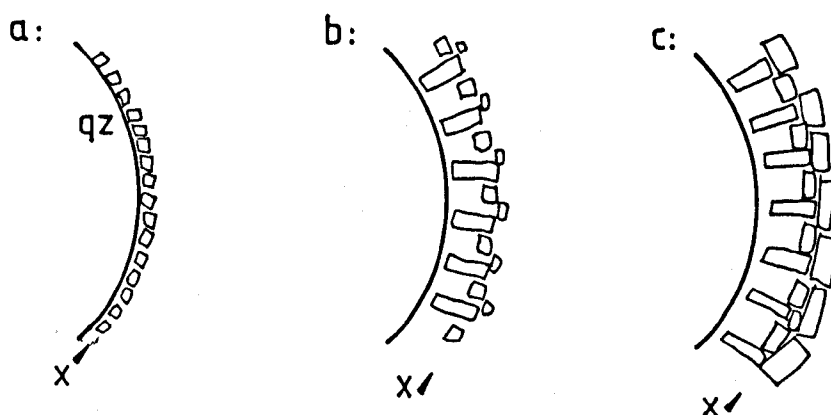
The constant temperature assumption is reasonable because most of the dissolution in a cooling system will occur while temperatures are still close to the initial conditions (because of the exponential dependence of dissolution rate on temperature). The quenching assumption is only valid for porous (unsealed) fringes, for which the estimates are most accurate. If the fringe is not porous, the computed residence times will be too low because the model only estimates the time taken to

develop a fringe of that width.

The widths of pyroxene fringes around quartz in natural samples were measured (from backscattered electron images) from the surface of the quartz to the outer edge of the band of highest pyroxene density (inferred location of first pyroxene nucleation; figure 8.1). In order to correct for oblique sectioning across the fringe, the minimum width was used, whilst ensuring that this did not result from abrasion of the fringe or from the presence of large crystals visible in the plane of the section. For samples where the pyroxene fringe has been analysed in some detail, the pyroxene compositions may reveal the location of the first pyroxene nucleation (highest recorded temperature) to be within the fringe, rather than at the edge. This information, where known, is given in table 4.5 as the fraction  $x$ , and may be used to correct the measured fringe width for

---

Figure 8.1  
Textural evolution of a pyroxene fringe.



Sketch to show the textural evolution of a pyroxene fringe around a quartz grain.

- Initial nucleation of pyroxene on the surface of the quartz.
- After some dissolution, the quartz has retreated. Some of the pyroxenes grow in towards the quartz, while others nucleate at the outer edge of the rim.
- Growth of pyroxene at and outside the locus of first pyroxene nucleation (X) isolates the dissolving quartz from the host magma. Dissolution ceases and pyroxene growth continues only at outside of fringe.

additional pyroxene growth outwards from the original edge of the reaction rim (see figure 8.1). This has not been done here, because the error corrected by this method is much smaller than that resulting from temperature uncertainty (see below).

For the purpose of isothermal modelling of the reaction, the highest pyroxene temperatures (§4.5.3) were used to estimate a fringe growth rate (§3.2) from figure 3.5. In Nature, the magma will cool, decreasing the reaction rate and thus increasing the duration of the dissolution reaction. The lower end of each estimated temperature range is regarded as resulting from subsolidus re-equilibration of pyroxene compositions and is ignored. The duration of the dissolution reactions were simply obtained by dividing the fringe width by the computed growth rate.

Computed residence times for reacted quartz with pyroxene rims are presented in table 8.1, and range from less than a day

Table 8.1  
Calculated residence times from rims around reacted quartz.

Rock	type	x ( $\mu\text{m}$ )	t	Temp ( $^{\circ}\text{C}$ )	Rate $\ast 10^{-12}\text{ms}^{-1}$	Residence time $\ast 10^4\text{s}$	days
H100428	basalt	163	sealed	1160	300	54	6
H121372	basalt	36	porous	1180	600	6	0.7
H121592	andesite	69	sealed	1100	60	120	14
LP14	basalt	75	sealed	1140	300	25	3
RC404	dacite	36	porous	1000	2	1800	208
RC417	basalt	69	sealed	1150	300	23	2.7
BM16	basanite	35	sealed	1100?	60	58	7
H74389	basalt	73	porous	1050	14	520	60
H100426	basalt	89	sealed	1120	100	89	10
H100429	bas.and	137	sealed	1130	100	140	16
H106444	basalt	51	sealed	1120	100	51	6
H121594	andesite	42	sealed	1100?	60	70	8
RCACD	hybrid	65	sealed	1100?	60	110	13
RC394	basalt?	232	porous	1100?	60	390	45
RC420	basalt	100	sealed	1120	100	100	11.6

x = minimum measured width of pyroxene fringe.  
t = textural type of pyroxene fringe (§4.3.1).  
? = temperature guessed.

to about seven months. The simplest interpretation of this timespan is that it represents the period between introduction of the quartz into a magma and final quenching (eruption).

To test whether this method gives reasonable results, estimated reaction durations for quartz are compared with estimated reaction durations for plagioclase xenocrysts, assuming that both plagioclase and quartz were incorporated together. Reaction durations for sponge-textured rims on plagioclase crystals may be estimated by comparison with the experimental textures reproduced by Tsuchiyama (1985), using the pyroxene temperature estimates. Plagioclase in H121372 has sponge-textured rims about 60 $\mu$ m wide, corresponding to reaction lasting about two days at 1200°C, in comparison to the quartz residence time of 0.7 days. Sponge-textures in RC417 would form in 2-3 days at 1200°C, while the quartz texture is estimated to form in about three days at 1150°C. This good agreement confirms the applicability of estimated residence times for quartz in mafic magmas.

The largest single source of error in estimates of quartz residence times is the computed temperature at which the reaction takes place, as the maximum error attached to the thermometry corresponds to an order of magnitude variation in the estimated fringe growth rate, and hence the calculated reaction duration. If sealing of the pyroxene fringe occurs by sintering or subsolidus recrystallization (Kingery *et al.*, 1976; Lorand and Cottin, 1987), rather than by continued growth of the outermost pyroxenes, some care must be attached to the pyroxene compositions used in thermometry, since these may have changed during recrystallization, whether entirely solid-state or aided by a liquid phase. This lack of precision could be improved by conducting quartz dissolution experiments on each individual

sample until the textures and pyroxene compositions had been reproduced, but would be extremely tedious. Nonetheless, if precise information is required on the mixing behaviour of magmas in an individual volcano, or indeed individual mixing events, experiments of the kind used here offer a precise means of attaining the information.

The majority of reaction rims around quartz studied in chapter four became sealed and halted dissolution before quenching of the magma. Subsequent to rim formation, quartz crystals may have split (H121372) or their reaction rims may have been partly abraded (eg H100429, RC404 (figure 4.2a,b)), presumably by movement within the magma. In these examples, there has been no crystallization of pyroxene near the newly exposed quartz surfaces. If splitting and abrasion occurred during eruption, the reaction rims may record the period of time between xenocryst incorporation and eruption, especially if the rims are still porous and dissolution was not halted by growth of the rim before quenching. The time elapsed between fracture or abrasion and quenching of the magma must be very short to prevent pyroxene growth (of the order of a few hours at 1140°C), and is probably the time interval over which the fraction of magma involved erupts and cools.

Several of the rocks examined are clearly hybrids, the preserved heterogeneity indicating incomplete blending of two mingled liquids (eg H121372, H121592, RC404, RC409, RC420). Resorbed and reacted quartz grains with pyroxene rims may be present in both liquids before mingling, and the rims are often abraded at boundaries between the two liquids. Quartz grains with fully sealed reaction rims, which have subsequently split or been abraded, may indicate a prior mixing event which introduced

quartz into a mafic liquid. These quartz grains may be the only remaining evidence of this earlier mixing event, which had sufficient time to fully homogenize and obscure other evidence of hybridization.

Some mafic liquids contain both angular quartz fragments with reaction rims, as well as rounded grains without reaction rims (H121594; figure 4.3k,l,m). Such textures must result from the mixing of two magmas with quite distinct populations of quartz crystals just before or during eruption. The rounding of grains probably results from simple dissolution in a superheated melt before mixing, possibly at the start of the hybridization process. The lack of pyroxene growth on the rounded grains suggest that the timescale of mixing and eruption was just a few hours.

Estimated residence times of hours to days are calculated by this method for porous reaction fringes around quartz, and are in good agreement with estimated residence times for sponge-textured plagioclase. For cases of quartz xenocrysts incorporated from country rock, the residence time again measures the period from incorporation to quenching or sealing, whichever is shorter. If the incorporation of quartz in a hybrid magma results from magma mixing, the formation of reaction textures about quartz in such short times suggests that the interval between mixing and eruption may be very short on a geologic timescale, implying in turn that magma chamber replenishment may trigger eruption (Sparks *et al.*, 1977; Eichelberger, 1980; Huppert *et al.*, 1982).

It should be possible to apply this data to the products of a volcanic eruption for which there is detailed seismological data suggesting movement of magma under the volcano (eg the 1980 eruption of Mount St. Helens; Decker and Decker, 1981) as an

independent measure of residence time. The residence time may be related to a period between magma movement and eruption.

### 8.2.2 Reacted orthopyroxene.

Residence times for reacted orthopyroxene crystal may be estimated in similar fashion to those of quartz crystals.

Measurements were taken from the current orthopyroxene surface to the original surface (ie where the density of olivine grains changes abruptly; §5.3.1). In cases where such a boundary is indistinct (eg plate 6.2c) measurements were taken from the surface of the orthopyroxene to the outer limit of the olivine rim.

The maximum computed temperature (§6.4.3) was used to estimate dissolution rates from figure 5.2, using the composition of the reacted orthopyroxene to decide whether to employ the data for enstatite or bronzite dissolution. Durations of dissolution reactions are estimated from the computed dissolution rates and the measured widths of the fringe and are given in table 8.2. The estimates are minimum values, since:

- 1) the highest temperature estimated has been used to model the dissolution reaction, and no attempt has been made to model the effects of cooling on the rate of dissolution;
- 2) orthopyroxene dissolution may have started at temperatures above the olivine liquidus;
- 3) growth of the reaction rim might prevent melt access and halt further dissolution, although there is no evidence that this occurs, either in experiments or in Nature.

Computed residence times range from 0.6 to 462 days and are

Table 8.2  
**Pyroxene temperatures and estimates of reaction durations  
 for reacted orthopyroxenes.**

Rock	Pyroxene temperature (°C)	fringe width ( $\mu\text{m}$ )	pyroxene composition	estimated rate $\ast 10^{-12} \text{ms}^{-1}$	computed duration $\ast 10^4 \text{s}$	reaction duration days
CHD	1250-1100	330	en <sub>93</sub> (en)	6000	5.5	0.6
RAW860	1100-900	295	en <sub>73</sub> (brz)	30	1000	116
RF10	1100-1000	160	en <sub>93</sub> (en)	4	4000	462
RF11	(1100-1000)	36-40	en <sub>91</sub> (en)	4	900	104
RF12	1180-1030	240	(en)	400	60	7
RF15	1150-950	67-75	en <sub>91</sub> (en)	80	84	10
RF16	1250-1070	680	en <sub>90</sub> (en)	6000	11	1.3

Where there is insufficient data for a temperature estimate, the inferred temperature (from similar samples) is indicated in parentheses.

The column "pyroxene composition" indicates (in parentheses) which set of pyroxene dissolution data was used to estimate the dissolution rate for a particular sample.

---

given in table 8.2. Estimated residence times for orthopyroxene in basalts may reflect the time period of orthopyroxene instability before quenching, if instability postdates xenocryst incorporation. The most significant variable in the estimation of reaction durations is the estimated temperature, because the rate of orthopyroxene dissolution increases tenfold for a temperature increase of 50°C, which is similar to the range of error inherent in the thermometer. Using this method for calculating residence times, the reaction rims shown by the range of samples in Kuo and Kirkpatrick (1985b) suggest dissolution reactions lasting from 2.5 - 5 days (assuming a constant temperature of 1200°C), whereas their method calculated values of 3 - 12 hours. The fact that values calculated by this method for similar rocks, and indeed for some of their examples, are very much larger, is consistent with the possibility that the ascent of a partially crystalline magma is much slower, because xenoliths are unable to settle if they fail to exceed the yield strength of the magma (Sparks *et al.*, 1977a).

### 8.3 Estimation of cooling rates.

If the dissolving crystal becomes isolated from the host magma, or approximately isothermal conditions are not maintained, a different set of assumptions from those used in §8.2 allows a cooling rate for the magma to be estimated. If the cooling rate is known and constant, the progress of fringe growth may be related to the degree of cooling that the system has undergone from the temperature at which dissolution commenced. If the cooling rate is not known, knowledge of the width of the reaction rim and the temperature range over which cooling has occurred allow the cooling rate to be estimated.

Model cooling rates can be calculated for a magma containing quartz with pyroxene reaction rims, or orthopyroxene with olivine rims, if the temperature interval over which the dissolution reaction occurred can be estimated, assuming that:

- a) cooling starts with or before dissolution;
- b) the cooling rate is constant;
- c) there has been negligible crystal growth (either pyroxene or olivine) at the outer edge of the reaction rim;
- d) the lowest temperatures recorded in the rim represent eruption and quenching of the magma.

If the cooling rate is  $k$ , the time taken for the temperature to decrease by  $1^\circ\text{C}$  is  $1/k$  and therefore the width of quartz dissolved in this time is  $r/k$ , where  $r (= A \exp\{-E_A/RT\})$ ; §3.2.3) is the dissolution rate. Summing over the measured temperature interval  $(T_1 - T_2)$  gives

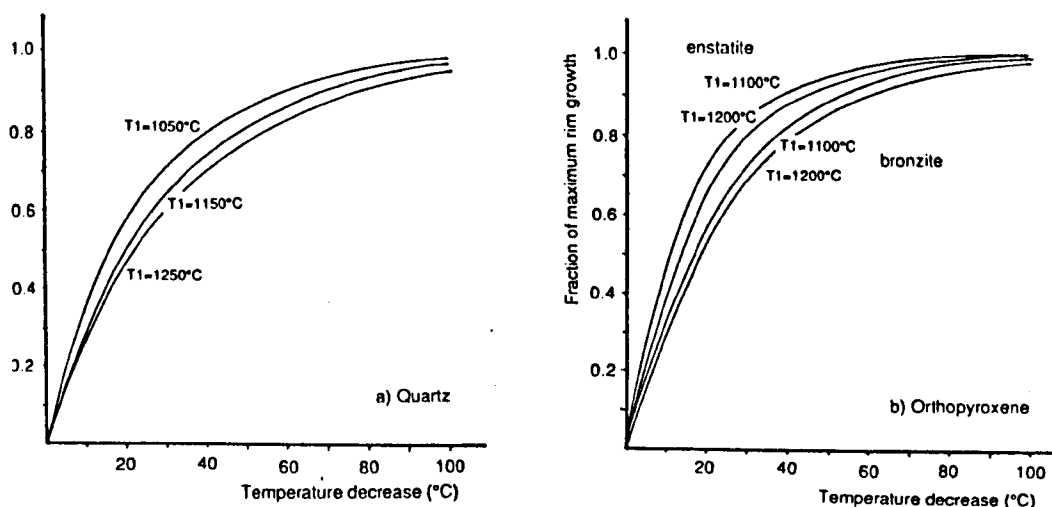
$$\begin{aligned}
 x &= \int_{T_1}^{T_2} \frac{r}{k} dT \\
 &= \int_{T_1}^{T_2} \frac{A}{k} \exp(-E_A/RT) dT \quad (8.1)
 \end{aligned}$$

where  $x$  is the measured width of the rim. Since  $k$  is being assumed constant, it may be placed outside the integral, which may then be evaluated separately. The cooling rate,  $k$ , is then equal to the evaluated integral divided by the rim width.

The integral was approximated over the estimated temperature range by a simple iterative procedure, using  $E_A = 530 \text{ kJmol}^{-1}$  and  $A = 6.7 \cdot 10^9 \text{ ms}^{-1}$  for quartz (§3.2.3). For enstatite the constants are  $E_A = 920 \text{ kJmol}^{-1}$  and  $A = 7.7 \cdot 10^{23} \text{ ms}^{-1}$ , and for bronzite they are  $E_A = 640 \text{ kJmol}^{-1}$  and  $A = 7.8 \cdot 10^{13} \text{ ms}^{-1}$  (§5.3.2). If the temperature decrease over which cooling occurs exceeds  $50^\circ\text{C}$ , the actual extent of the temperature decrease is insignificant, since, after a temperature decrease of  $50^\circ\text{C}$ , the model predicts that reaction rims around quartz will have attained 77-86% of their maximum width (depending on initial temperature) (figure 8.2a). For orthopyroxene the higher activation energies imply faster decrease of dissolution rates with decreasing temperature, such that 81-95% of dissolution will have occurred after the system has cooled by  $50^\circ\text{C}$  (figure 8.2b).

Estimated cooling rates for magmas developing a fringe on quartz (table 8.3) range from  $0.07$  to  $50^\circ\text{Cday}^{-1}$ , and for orthopyroxene (table 8.4) from  $0.07$  to  $120^\circ\text{Cday}^{-1}$ . As with the estimates of reaction duration (§8.2), the error in maximum computed temperature introduces the largest error into these cooling-rate estimates.

Figure 8.2  
Progress of fringe growth during cooling.



Graphs to show the fraction of rim growth during constant cooling as a function of the temperature decrease that the system has undergone. (a) Quartz. (b) Orthopyroxene.

Table 8.3  
Calculated cooling rates from rims around reacted quartz.

Rock	T range (°C)	integral ( $\times 10^{-11} \text{m}^2 \text{C}^{-1} \text{S}^{-1}$ )	rim width ( $\mu\text{m}$ )	cooling rate ( $\times 10^{-7} \text{C s}^{-1}$ ) ( $^{\circ}\text{C day}^{-1}$ )	
LP14	1140-900	520	75	690	6
H121372	1180-1000	1900	36	5300	50
H121592	1100-1000	130	69	190	2
H100428	1600-900	1000	163	610	5
RC404	1000-900	2.9	36	8	0.07
RC417	1150-1020	710	69	1000	9
BM16	1100-900?	130	35	370	3
H74389	1050-950	21	73	29	0.2
H100426	1120-1000	260	89	290	2.5
H100429	1130-900	370	137	250	2
H106444	1120-950	260	51	510	4
H121594	1100?-1000?	130	42	300	3
RCACD	1100?-900?	130	65	200	2
RC394	1100?-900?	130	232	56	0.5
RC420	1120-900	260	100	260	2

Temperature range from table 4.5.  
Fringe width from table 8.1.

Table 8.4  
**Calculated cooling rates for rims around reacted orthopyroxene.**

Rock	Integral (*10 <sup>-11</sup> m°C <sup>-1</sup> S <sup>-1</sup> )	Cooling rate (*10 <sup>-7</sup> °Cs <sup>-1</sup> ) (°Cday <sup>-1</sup> )	
CHD	4500	14000	120
RAW860	8.4	28	0.25
RF10	1.3	8	0.07
RF11	1.3	36	0.31
RF12	120	500	4.3
RF15	24	360	3.1
RF16	4500	6600	57

### 8.3.1 Size estimates of cooling magma bodies.

The size of a magma body in which incongruent dissolution has occurred can be estimated from knowledge of the cooling rate of the magma.

Simple, one-dimensional, thermal models to mimic the conductive cooling history and to estimate the thermal regime both inside and outside a tabular magma body (eg a lava flow, dyke or sill) have been developed by Jaeger (1957, 1968) and Long and Wood (1986). These models numerically simulate the cooling histories of:

- i) a dyke emplaced beneath deep cover (where the temperature of both contacts are free to vary) (Jaeger, 1957) ;
- ii) a lava flow erupted at the surface (where the top contact is maintained at 0°C) (Long and Wood, 1986).

The models assume that:

- a) the magma is completely static and crystallizes in place, without undergoing movement or differentiation;
- b) the range of crystallization and the way in which latent heat is emitted are known;

- c) magma and country rock have the same thermal properties and there are no changes in these properties with temperature;
- d) the magma is intruded at its liquidus, since it is unlikely to be superheated (see above).

From these simulations it is possible to estimate cooling rates over the crystallization interval for the centre and margins of a magma body, in relation to its size. Both simulations assume a magma emplacement temperature of 1100°C. For the dyke model, the average cooling-rates at the centre of the intrusion is  $6.8 \cdot 10^{-4}/d^2$  ( $^{\circ}\text{Cs}^{-1}$ ) and near the margins the cooling-rate is  $7 \cdot 10^{-3}/d^2$  ( $^{\circ}\text{Cs}^{-1}$ ) (Jaeger, 1957). For the subaerial flow, the cooling-rates are  $2.6 \cdot 10^{-4}/d^2$  ( $^{\circ}\text{Cs}^{-1}$ ) at the centre and  $6 \cdot 10^{-3}/d^2$  ( $^{\circ}\text{Cs}^{-1}$ ) near the margins (Long and Wood, 1986). In each case,  $d$  is the thickness of the magma body in metres. The values for centre and margins set a range which may span the actual value.

Given  $k$  (the cooling-rate), the thickness of the magma body undergoing conductive cooling may be estimated (table 8.5). Four values are presented, one for the centre and one for the margins of each model situation. The values for the centres of intrusions agree well with each other, as do the estimates for margins, but there is a sizeable difference between the two sets. If it is assumed that the estimated cooling-rate for a sample refers to the centre of the magma, when it actually represents cooling near the margin, the size of the magma body could be underestimated by a factor of five. The calculated values range from 0.4 - 18m, assuming that the samples represent the centre of the magma body, and from 2.2 - 94m, assuming that they represent the margins. For comparison, the dyke from which RC394 was collected is about 8m wide (Harker, 1904; p351), comparing favourably with estimates of

Table 8.5  
Estimated magma body thicknesses.

Rock	$T_0$ °C	k (*10 <sup>-7</sup> m°Cs <sup>-1</sup> )	thickness (m)			
			(a)	(b)	(c)	(d)
LP14	1140	690	3.1	10	1.9	9.3
H121372	1180	5300	1.1	3.6	0.7	3.7
H121592	1100	190	6.0	19	3.7	18
H100428	1160	610	3.3	11	2.1	9.9
RC404	1000	8	29	94	18	87
RC417	1150	1000	2.6	8.4	1.6	7.7
BM16	1100?	370	4.3	14	2.7	13
H74389	1050	29	15	49	9.5	46
H100426	1120	290	4.8	16	3.0	14
H100429	1130	250	5.2	17	3.2	16
H106444	1120	510	3.7	12	2.3	11
H121592	1100?	300	4.8	15	2.9	14
RCACD	1100?	200	5.8	19	3.6	17
RC394	1100?	56	11	35	6.8	33
RC420	1120	260	5.1	16	3.2	15
CHD	1250	14000	0.7	2.2	0.4	2.1
RAW860	1100	28	16	50	9.6	46
RF10	1100	8	29	94	18	87
RF11	1100	36	14	44	8.5	41
RF12	1150	500	3.7	13	2.3	11
RF15	1150	360	4.3	14	2.7	13
RF16	1250	6600	1.0	3.3	0.63	3.0

- a) Assuming centre of dyke.      b) Assuming margin of dyke.  
c) Assuming centre of lava.      d) Assuming margin of lava.

11m, 6.8m for dyke centres. The dyke from which RAW860 originated was 2m wide (Wiebe, 1986), significantly narrower than the estimates of 9.6 - 50m. This probably indicates that the dyke in which the sample was located is not where the reaction occurred.

The effect of convection within the magma is to even out any temperature variations and to effectively increase the rate of heat conduction away from the magma, but the timescale of cooling will still be controlled by the rate of removal of heat through the country rock.

An alternative situation to be considered is the incomplete mingling of two magmas of contrasting compositions and rheological properties, which may be co-erupted as banded pumices (eg sample RC409; Macdonald and Katsura, 1965). Consider the

situation where the forceful intrusion of a basic magma forms a fountain in a chamber of more acidic magma (Campbell and Turner, 1986; Turner and Campbell, 1986). Since the viscosity contrast between the two magmas will be high, and since acid and basic magmas are frequently seen to coexist in close proximity without significant mixing (eg Blake *et al.*, 1965; Taylor *et al.*, 1980), it will be assumed that little mixing occurs, but also that some quartz phenocrysts from the acidic magma may become entrained in the basic magma by mechanical effects along the interface (Kouchi and Sunagawa, 1985, 1983).

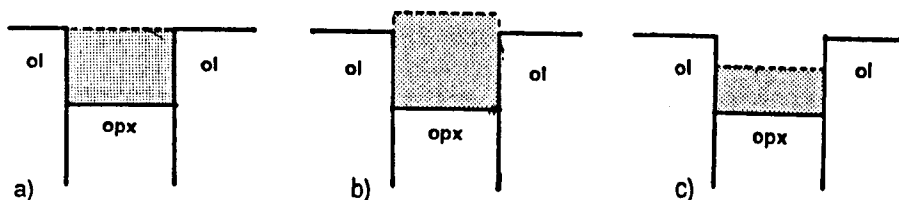
Assuming that the initial temperature of the basic member is 1200°C and that it is at least 100°C hotter than the acid magma, the cooling rate of the mingled basic magma may be estimated so that no significant dissolution of quartz occurs (as seen in the banded pumice sample RC409). The minimum cooling rate required to restrict growth of the rim to 1µm is  $2 \cdot 10^{-2} \text{ } ^\circ\text{Cs}^{-1}$  (§8.3) ( $\approx 1730^\circ\text{Cday}^{-1}$ ), implying that the maximum width of the basic layers should be of the order of 10-50cm. If the initial temperature of the basic magma were 1100°C, the minimum cooling-rate required is  $1.3 \cdot 10^{-3} \text{ } ^\circ\text{Cs}^{-1}$ , implying that the layers should be less than 45-230cm across. The banded pumice (RC409) is composed of alternating layers of andesite and dacite 5-10mm thick, which are within the maximum size permitted. If the layers were wider, significant pyroxene growth might occur around entrained quartz grains. If the fountain remained coherent without breaking up upon entering the magma chamber, the estimated width would be approximately the diameter of the fountain.

## 8.4 Magma ascent velocities.

Dissolution data for mafic minerals have been applied by several investigators to the problem of xenolith assimilation and rates of magma ascent. Kuo and Kirkpatrick assumed that indentations on xenolith surfaces (eg Wilshire and Binns, 1961) are due to the faster dissolution of orthopyroxene than olivine, and that the fine-grained olivine within these indentations postdates dissolution and grew during cooling.

The study of incongruent dissolution of orthopyroxene (chapter five) suggests an alternative interpretation. Since the outer surface of the olivine and clinopyroxene reaction zone is continuous with the xenolithic olivine surface (figure 8.3a) in most of the examples shown here (chapter six) and by Kuo and Kirkpatrick (1985b), it is quite possible that these textures were formed by incongruent dissolution of the orthopyroxene with simultaneous olivine crystallization, and that the magma was not

Figure 8.3  
Surface indents on lherzolite xenoliths.



Schematic diagram to indicate differences in height at the surface of a xenolith, of olivine (ol) and the products of incongruent orthopyroxene dissolution (shaded).

- Reaction products level with the surface of the xenolith, implying either abrasion of the reaction rim, or no dissolution of xenolithic olivine.
- Reaction products standing proud of xenolith surface, indicating that dissolution of xenolithic olivine has occurred, but that it is slower than the incongruent dissolution of olivine.
- Reaction products retaining slight surface indent, at xenolith surface, indicating some simple dissolution of orthopyroxene before incongruent dissolution began.

always or ever superheated. If this is the case, it is likely (although not necessary) that the bulk liquid will be saturated with olivine, and dissolution of xenolithic olivine will be unlikely. If dissolution of xenolithic olivine occurred in addition to orthopyroxene, the reaction products of incongruent dissolution might stand proud of the xenolith surface (figure 8.3b), unless dissolved or abraded by the magma. If some superliquidus dissolution occurred, indentation as described by Kuo and Kirkpatrick (1985b) would result and subsequent incongruent dissolution of orthopyroxene below the liquidus would retain the surface indent, if there was no further dissolution of xenolithic olivine (figure 8.3c).

This model, which is also based on the indentations on xenolith surfaces, assumes:

- a) a constant magma ascent velocity and constant cooling rate;
- b) the temperature of the magma at segregation from its source region is its liquidus temperature at that depth;
- c) the magma rises slowly enough to equilibrate thermally with its surroundings and thus avoids becoming superheated; its temperature stays within its crystallization interval as it ascends;
- d) the depth of last ascent of the magma is the point at which it picks up accidental lherzolite xenoliths and orthopyroxene dissolution begins immediately;
- e) the dissolution rates have negligible pressure dependence;
- f) the xenolithic olivines are unchanged upon exposure to the magma, undergoing no growth or dissolution;

g) the magma is erupted immediately upon reaching the surface and does not halt *en route* to the surface.

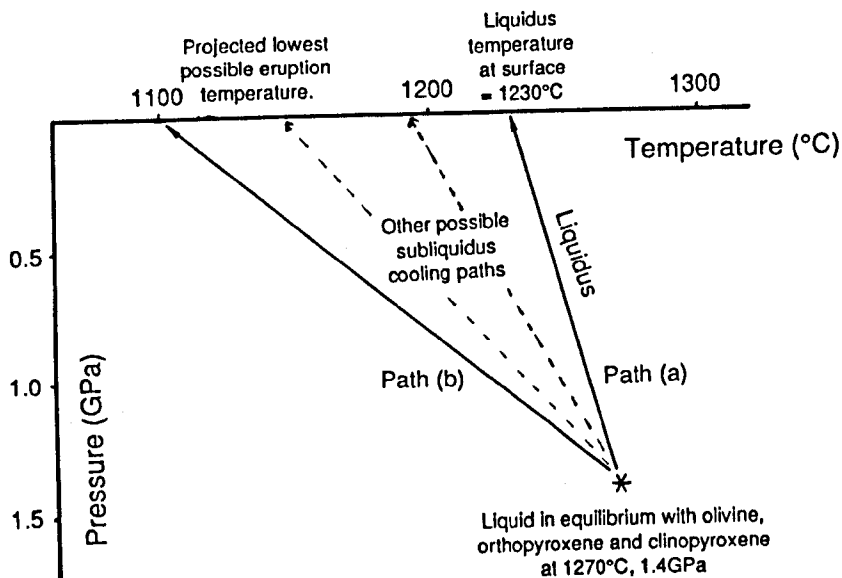
The depth of generation of alkali basalt magmas is likely to be variable (Yoder, 1976; Takahashi, 1980). As an example an alkali olivine basalt from Japan has been chosen, whose phase relations are known to 3GPa (Takahashi, 1980). The melt is multiply saturated with olivine, clinopyroxene and orthopyroxene at about 1270°C and 1.4GPa, and is assumed to separate from its source region under these conditions.

Ultramafic xenoliths included in alkali basalts appear to have equilibrated at much lower temperatures than would be expected of the basalt source region (eg Kuo and Essene, 1986) and thus are not thought to be derived from the magma source region. However, since the estimated pressure at which they last equilibrated is also around 1.5GPa, it is assumed here that xenolith incorporation occurred soon after magma segregation.

If the magma is to be erupted at the surface within its crystallization interval, its temperature must decrease to between 1230°C (the liquidus temperature at atmospheric pressure) and 1100°C. (The solidus temperature of this magma was not reported, but at this temperature some liquid is still present. In any case, above 60% crystallinity a magma will be too viscous to move (Marsh, 1981)). As a result, the magma must ascend along a path between (a) and (b) on figure 8.4.

The width of the reaction rim ( $x$ ) will be given by equation 8.1. The cooling rate,  $k$  ( $= -dT/dt$ ), is related to the ascent

Figure 8.4  
Cooling paths of ascending magma.



Possible cooling paths of a magma ascending from 1.4GPa at 1270°C, so that it erupts within the range 1100-1230°C. Data from Takahashi (1980).

time ( $t_A$ ) for the xenolith by  $k = (T_2 - T_1)/t_A$ . Hence

$$x = \frac{t_A}{(T_2 - T_1)} \int_{T_1}^{T_2} r \, dT \quad (8.2)$$

and, from this

$$t_A = \frac{x(T_2 - T_1)}{\int_{T_1}^{T_2} r \, dT} \quad (8.3)$$

Using the data for incongruent dissolution of enstatite (§5.3), the values of the integral evaluated between 1270 and 1230°C, and 1270 and 1100°C, are  $1.0 \cdot 10^{-6} \text{ m}^\circ\text{Cs}^{-1}$  and  $1.2 \cdot 10^{-6} \text{ m}^\circ\text{Cs}^{-1}$ , respectively. A typical indentation of 300 $\mu\text{m}$  (table 8.2) implies ascent times of between 3.3 and 11.8 hours, and ascent velocities of between 12 and 3.4 $\text{kmhr}^{-1}$ .

The depth at which dissolution is initiated is highly critical to estimates of magma ascent velocities. If orthopyroxene dissolution is assumed to start at a depth of 30km ( $\approx 1\text{GPa}$ ) and a typical indent is still 300 $\mu\text{m}$ , then, if the magma is following path (a) (figure 8.5) the temperature interval over which dissolution occurs is 1260 - 1230°C, the value of the

integral is  $5.6 \cdot 10^{-7} \text{m}^\circ\text{Cs}^{-1}$ , the ascent time is 4.5 hours and the ascent velocity is  $9 \text{kmhr}^{-1}$ . If the magma is following path (b) (figure 8.5), the temperature interval is  $1220 - 1100^\circ\text{C}$ , the value of the integral is  $1.0 \cdot 10^{-7} \text{m}^\circ\text{Cs}^{-1}$ , the ascent time is 100 hours and the ascent velocity is now only  $400 \text{mhr}^{-1}$ .

Kuo and Kirkpatrick (1985b) computed ascent times and velocities for a number of samples, ranging from 3 - 12 hours and  $14 - 4 \text{kmhr}^{-1}$ . Fortuitously, the values obtained here correspond well with theirs, if dissolution of the orthopyroxene started immediately. If dissolution started later, for example, as a result of xenolith incorporation at shallower depths, the estimated ascent velocities are much lower, consistent with the Bingham plastic model of a partly crystalline magma (Sparks *et al.*, 1977a).

If the magma comes from greater depths and higher temperatures of segregation from its source, and orthopyroxene dissolution starts deeper, the model developed here will predict unrealistically high ascent velocities, because of the rapid increase in orthopyroxene dissolution rate with temperature. For such situations, refinement of this model by the use of subliquidus dissolution data at high pressures is required.

### 8.5 Summary

In summary, estimating ascent times and velocities from models of natural situations requires numerous assumptions. Existing models include the assumption of dissolution under superheated conditions. The data obtained in this study indicate that this assumption is unnecessary and may be removed to be consistent with the observations that most basalts are erupted with some crystal content and a measurable yield strength.

The accuracy of the estimated temperatures used in these models is very important, because of the large variation in dissolution rates caused by small differences in temperature.

## Chapter nine

### Recapitulation and suggestions for further work

Review of previous work in chapter one highlighted the need to investigate dissolution processes within a crystallizing magma. This study has followed up reconnaissance work to find out whether such dissolution was responsible for pyroxene rims around quartz and olivine rims around orthopyroxene in basalts by Donaldson (1985b, unpublished work).

Chapter three investigated silica dissolution into a basalt, both above and below the pyroxene liquidus. The petrography of the charges was examined, and the textures of pyroxene and silica documented. The effect of controlled cooling on the dissolution system results in strong compositional zonation of the pyroxenes and liquid immiscibility in the groundmass.

The kinetics of silica dissolution and pyroxene fringe growth were studied, so that the duration of the dissolution reaction in natural samples could be assessed. Constant dissolution rates and compositional gradients around silica suggest that diffusion and convection in the melt both have important rate-controlling effects on the dissolution processes. The presence of a silica-rich layer of melt around the surface of higher temperature charges suggests instead that convection is driven by compositionally-induced variations in melt surface tension.

The pyroxenes crystallizing around dissolving silica in the tholeiite (this study) and slightly alkaline basalts (Donaldson, unpublished data) are pigeonitic, whereas pyroxenes found around reacted quartz in natural samples are exclusively augitic. Investigation of the chemical relationships between pyroxenes and coexisting melts reveals that the most likely control on the type

of pyroxene crystallizing is the composition of the interface melt between quartz and basalt. There is probably only a limited range of compositions that crystallize pigeonite, and fortuitously, both basalt compositions studied produce interface melts within this narrow range.

Chapter four reported the textures around reacted quartz in natural samples and the chemistry of phases involved with these reactions. The possible origins of quartz in mafic magmas were discussed, and the possibility that it might be a high pressure phenocrystic phase was rejected. The petrography of natural samples is very similar to that of the experimental charges, showing that the conditions imposed during the experiments were comparable to those experienced by natural samples. Quartzose xenoliths and xenocrysts rimmed by neocrystic pyroxene or amphibole are interpreted as having suffered incongruent dissolution, rather than simply acting as sites for the nucleation of crystallizing phases. The variety of quartz grain shapes seen in mafic rocks was discussed, and the importance of fluid inclusions and gas vesicles in determining final grain shapes was stressed.

Chapter five investigated the dissolution of orthopyroxene into alkali olivine basalt below its liquidus temperature. Reaction of both orthopyroxene compositions with melt is sometimes complicated by the reactions of their included phases (in lamellae), which may melt independently of the enclosing basalt. The more magnesian enstatite dissolves at constant rates except at the lowest run temperature, whereas dissolution of the bronzite appears to be time-dependent at all temperatures investigated. The reason for the difference is not apparent, as melt compositions and apparent viscosities across the reaction

rims are similar for both compositions. Time-dependent dissolution is controlled solely by diffusion across the boundary layer. Time-independent dissolution is controlled by a combination of diffusion across a boundary layer, and convection of melt outside this boundary layer. The driving force for convection is unlikely to be buoyancy differences, and is inferred to be compositionally induced variations in surface or interfacial tension between melts.

The chemistry of olivines formed from the reaction melt adjacent to dissolving orthopyroxene, as well as from breakdown reactions in the absence of melt, showed that such olivines are not in equilibrium with the bulk system, and olivine-melt thermometers may not be applied to reaction textures to estimate temperatures of formation. These olivines equilibrate chemically upon prolonged exposure to external melt more rapidly than would be expected by solid-state diffusion. Progress in chemical equilibration may be related to textural equilibration, which takes place by a variety of processes, mostly involving solution and re-precipitation of material via the melt.

In chapter six, natural examples of mafic rocks containing partly or completely reacted orthopyroxenes were examined and compared to experimental runs. The natural textures are similar to those developed experimentally but are often complicated by extensive crystallization of clinopyroxene during cooling. Textural and chemical equilibration were observed for some but not all specimens examined. The crystallization of clinopyroxene with or shortly after olivine crystallization allows pyroxene thermometry to be applied and estimates of reaction temperatures to be obtained.

Chapter seven examines the formation of visually similar

textures around a variety of other common rock-forming minerals, and tries to overcome the difficulties in distinguishing between reactions at peritectic conditions from those at other temperatures, on the basis of differences between neocryst and groundmass crystal compositions. In most of the examples examined, the variation in neocryst chemistry from that of groundmass phases suggests that the incongruent reactions occurred away from peritectic conditions, probably as a result of xenocryst incorporation.

The most common incongruent dissolution reaction products of olivine are orthopyroxene and clinopyroxene, which may form monocrystalline overgrowths or granular rims. A previously undescribed reaction texture around clinopyroxene is attributed to incongruent dissolution. The hydrous minerals amphibole and biotite appear to undergo dissolution reactions forming granular rims under conditions within their stability fields, as these reaction textures are quite distinct from the fine-grained decomposition products attributed to physical instability.

In chapter eight the dissolution data acquired for the two systems investigated were applied to some problems tackled by previous workers, as well as two new problems.

Residence times may be estimated for reacted quartz and orthopyroxene in mafic rocks, if the temperature can be accurately estimated. The dissolution rates are strongly temperature-dependent, and the error range attributed to the mineral thermometers is equivalent to an order of magnitude variation in dissolution rate. Digestion of xenoliths may be modelled using the dissolution data obtained and residence times estimated, but it must be remembered that the growth of the reaction rim hinders melt transport around the dissolving phase

and may halt dissolution altogether, preserving part of the original xenolith.

Cooling rates have been estimated for both orthopyroxene and quartz dissolution systems, and these were, in turn, used to estimate the size of the igneous body in which the dissolution reaction occurred, even if this magma is incompletely mingled within another magma.

Ascent rates for alkali basalts bearing ultramafic xenoliths were estimated by modelling the rate of olivine fringe growth around orthopyroxene during magma cooling upon ascent. Values obtained are fortuitously similar to previous estimates if orthopyroxene dissolution is assumed to start soon after xenolith incorporation. If the onset of dissolution is delayed, magma ascent velocities are very much lower than previously estimated, consistent with the possibility that a partially crystalline magma may be able to ascend slowly to the surface, but will still be able to transport xenoliths without settling occurring, because of its yield strength.

In all of the models it was necessary to make simplifying assumptions, some of which have been made by previous workers, and some of which result from this study. In order to use the predictions of these models, care must be taken to justify the assumptions made.

#### Suggestions for further work

In general it is necessary to see how variations in magmatic conditions (pressure, temperature, oxygen fugacity, water content and melt composition) affect the stability of minerals with magma present, when under the same conditions the minerals would be stable in the absence of melt. Whereas the stability

relationships of most minerals in the absence of melt are known quite well, their stabilities with melt present are poorly known, and much more knowledge is required before accurate assessment of the processes of assimilation can be made.

Further work investigating the dissolution kinetics of quartz and orthopyroxene at higher pressures, varying water contents and differing melt compositions, is required. This would allow better understanding of

- a) the controls on the chemistry of the pyroxene phase around quartz, and
- b) variation in the dissolution rate of orthopyroxene during ascent in alkali basalts, enabling better constraint of the thermal model used to calculate ascent velocities.

Dissolution experiments involving amphibole and biotite into andesite, for example, should be attempted under conditions within the physical stability fields of these minerals, to check whether the formation of granular pyroxene rims and opacite form at different stages and under differing conditions of a magma's history. The incongruent reaction textures around olivine, spinel and clinopyroxene reported here also require experimental reproduction.

A study of a single volcano should be undertaken to test the models developed here against seismological evidence of a recent eruption (eg Mount St. Helens, May 1980: Decker and Decker 1981; plate 9a). Study of previously erupted rocks may also give some indication of the period between incorporation of the xenocrysts (during magma movement) and eruption, enabling prediction of volcanic events.

### Plate 9

- a) Mount St. Helens seen from the north, eight years after the cataclysmic landslide and eruption.
- b) Crater Lake, looking north from Garfield Peak across to Wizard Island and Llao rock. Crater Lake is the caldera formed during the eruption of Mt. Mazama about 6000 years ago, and is still regarded as dangerous. Wizard Island was erupted only 1000 years ago.



Appendix to chapters four, six and seven.

Sample descriptions.

<u>Sample</u>	<u>Location</u>	<u>Host description</u>	<u>Xenocrysts</u>	<u>Source</u>
RC404	Lassen Peak	mingled dacite	ol,hb,bi,qz	5
RC409	Lassen Peak (summit)	banded pumice	pl,bi,hb,ol,qz	5
RC412	Lassen Peak (summit)	dacite	pl,bi,hb	5
H106444	Cinder Cone, Lassen	basalt	} ol,opx	2
LP14	Cinder Cone, Lassen	basalt	} pl	1
RC417	Cinder Cone, Lassen	basalt	} qz	5
RC420	Cinder Cone, Lassen	basalt	} cpx	5
H74389	Gardiner River, Yellowstone	basalt	pl,qz	2
RAW860	Nain, Labrador	basalt	opx	3
CHD	Calton Hill, Derbyshire	ankaramite	ol,opx,cpx,sp	4
RC324	Glamaig, Skye	marscoite	qz	5
RC394	Bla Bheinn, Skye	basalt	qz	5
RCACD	Arran	composite dyke	qz	6
BM16	Massif Central	leucite basanite	qz,fsp	1
RF9	Massif Central	phonolite	kaersutite	5
RF10	Massif Central	basalt	} ol,opx,cpx	5
RF11	Massif Central	basalt	} qz,pl,bi,sp	5
RF12	Massif Central	basalt	} qz	5
RF15	Massif Central	basalt	} opx	5
RF16	Massif Central	basalt	} qz	5
H59909	Trégastrel, Brittany	norite	qz	2
H100426	Omori Jama, Izu, Japan	basalt	pl,ol,qz	2
H100428	Omori Jama, Izu, Japan	basalt	pl,qz	2
H100429	Omori Jama, Izu, Japan	basaltic andesite	pl,qz	2
H121372	Iki island, Japan	basalt	opx,qz	2
H121592	Togitsu, Japan	olivine basalt	pl,qz	2
H121594	Togitsu, Japan	andesite	pl,hb,qz	2
H52723	Ngauruhoe, Taupo Zone, NZ	basaltic andesite	ol,qz-fsp xl	2

**Source:**

- 1 University of St.Andrews.
- 2 Harker Collection, University of Cambridge.
- 3 Dr R A Wiebe, Franklin and Marshall College, Lancaster PA.
- 4 Dr C H Donaldson, University of St.Andrews.
- 5 Richard Curry, University of St.Andrews
- 6 Mark Errington, University of St.Andrews.

These sections are curated for inspection in the Department of Geology, University of St.Andrews.

## Area one: Lassen.

Lassen Peak is a large, late Pleistocene dacite dome which rose within the caldera of the andesitic Brokeoff volcano (Mt. Tehama). The last eruption of basalt in the area took place in 1851 at Cinder Cone, 10 miles north east of Lassen Peak. The most recent eruptions of dacite occurred during the summit eruptions of 1914-1917. As a consequence, magmas ranging in composition from basalt to dacite are regarded as present and eruptible in the region around Lassen (Macdonald and Katsura, 1965).

Sample RC409 is a banded pumice, and RC412 is a loose fragment of dacite, both erupted in 1915 from the summit crater of Lassen Peak. RC404 is a mingled dacite found as a block in a lahar, 2 miles north of the main cone at the edge of the Devastated Area, a region of forest destroyed by a mud flow formed when dacite spilled over the eastern edge of the crater into snow. The resultant melt water, mixed with debris from previous eruptions and blocks of dacite, formed a mud flow down Lassen's north flank (Harris, 1976). Both the summit dacite and banded pumice are described by Macdonald and Katsura (1965). The eruptions of quartz basalt from Cinder Cone are represented by samples H106444, RC417, RC420, and LP14 (Finch and Anderson, 1930; Eichelberger, 1975).

### RC404

Dacite block in lahar, from Devastated Area 2 miles north of Lassen Peak. Probably erupted in 1915. Contains reacted olivine, hornblende, biotite and quartz.

The rock is composed of dacite and andesite mingled on a thin section scale. In the dacite, rare olivine microphenocrysts, euhedral with some skeletal terminations, show slight reaction to orthopyroxene, but little rounding. Hornblende is surrounded by rims of oriented elongate pyroxene and some magnetite (plate 7.3d). Biotite has reaction rims of magnetite and orthopyroxene (plate 7.4). Some biotites and hornblendes are pseudomorphed by opacite.

Quartz grains in the dacite are well rounded and either surrounded by reaction rims of glass and pyroxene (plate A1a), or unrimmed (figure 4.2). The pyroxenes are radially oriented, acicular, skeletal, and occasionally embayed by quartz. The porous nature of the fringe and the presence of tiny pyroxene crystals close to the quartz suggests that quartz dissolution and consequent pyroxene growth continued until eruption caused the system to be quenched. The coexistence of quartz grains with and without reaction rims shows that the development of rims preceded a final mixing event which juxtaposed two different generations of quartz xenocrysts, both of which had undergone dissolution, as evidenced by rounded shapes with or without pyroxene rims.

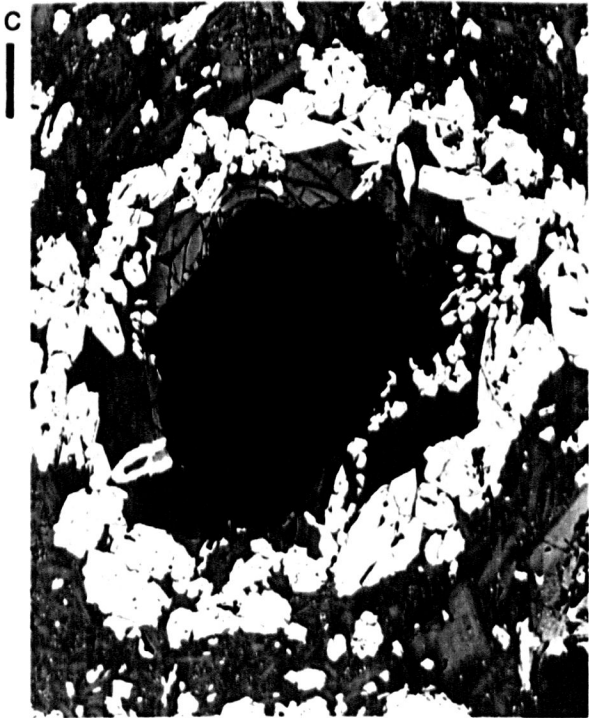
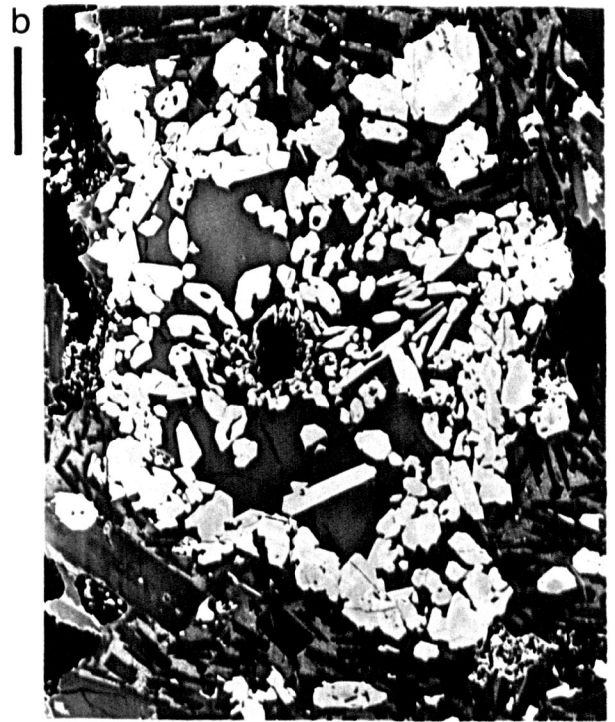
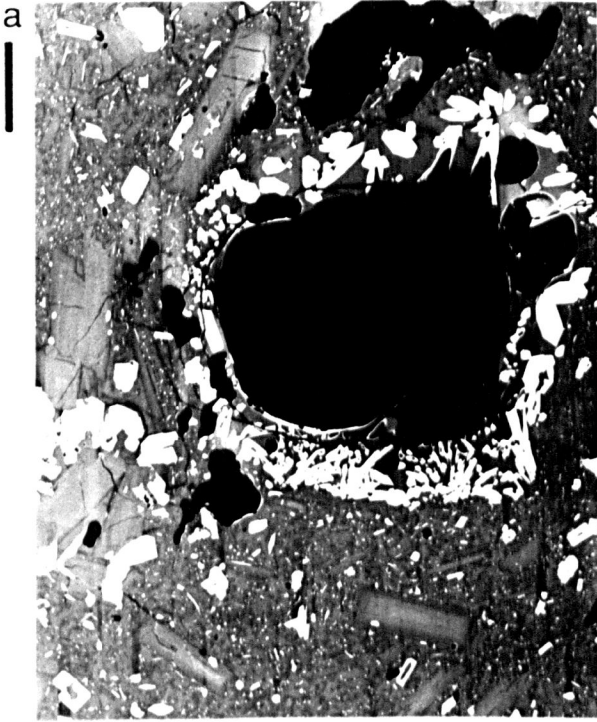
One andesite clot within the dacite contains a basal section of hornblende without any sign of reaction, along with a pseudomorph after skeletal olivine composed of parallel needles of orthopyroxene and some magnetite, while another contains a large reacted hornblende (plate A2a).

Plate A1  
Quartz reaction textures from Lassen.  
Scale bars are 100 $\mu$ m.

- a) RC404 Round quartz grain surrounded by a porous reaction rim of glass and radially oriented pyroxene. Close to the quartz are many small skeletal pyroxenes, some embayed by the quartz.
- b) RC417 Tiny remnant of quartz surrounded by pyroxene and glass. Pyroxenes at the edge of the reaction rim show compositional zones developed as chevrons pointing towards the quartz, indicating that most of the pyroxene growth was towards the quartz. In the centre, small highly skeletal pyroxene crystals are overgrowing and sheltering cusps on the quartz surface.
- c) LP14 Angular quartz fragment with a reaction rim of pyroxene and glass. On close inspection it can be seen that the faces of the quartz are not straight, but slightly concave, and there are accumulations of pyroxene crystals near the corners. This texture is similar to cusps formed on the surface of the silica rod (§3.1.4).
- d) LP14 Enlargement of the right hand side of the pyroxene reaction rim (of (c)), with the gain control of the back-scattered electron detector increased to detect boundaries between contacting pyroxene grains. These grain boundaries show up as bright lines, which may be due to a compositional difference, or to an edge effect at grain boundaries if they have not polished flat.

# Plate A1

Quartz reaction textures from Lassen.



## RC409

Banded pumice (1915) containing reacted plagioclase, biotite and hornblende, summit crater, Lassen Peak.

This pumice is composed of interlayered andesite and dacite (Macdonald and Katsura, 1965). Plagioclase is present in the andesite either as euhedral, zoned crystals with slightly spongy margins, or as crystals with spongy cores and clear euhedral margins. Xenocrysts of biotite and amphibole with thin (<50 $\mu$ m) rims of opacite or orthopyroxene needles are common, as are rounded, cracked grains of quartz (1.5mm) without reaction rims.

Streaked through the andesite are wisps of colourless, highly vesicular dacite, containing olivine with orthopyroxene reaction rims, biotite with opacite reaction rims and rounded quartz grains without pyroxene fringes.

## RC412

1915 dacite containing reacted plagioclase, biotite and hornblende, west lip of crater, Lassen Peak.

Plagioclase is present as xenocrysts with clear cores, spongy mantles and clear rims, or as clear rounded crystals with slightly corroded margins. Biotite is rimmed by either granular orthopyroxene and magnetite, or opacite (plate 7.4d), while hornblende has been pseudomorphed either by prismatic orthopyroxene and clinopyroxene (plate 7.3c), or by opacite rimmed by prisms of orthopyroxene and clinopyroxene (plate 7.3b). Rounded quartz grains without pyroxene fringes are also common in this rock.

## H106444, LP14, RC417, RC420

Quartz basalts containing reacted olivine, orthopyroxene, plagioclase, quartz and clinopyroxene, Cinder Cone, Lassen Volcanic National Park, CA.

These are fine-grained vesicular andesites, containing euhedral olivine phenocrysts, some of which are skeletal and some overgrown by orthopyroxene (plates 7.1d,f; A2c), rare orthopyroxene phenocrysts, often elongate and embayed with ragged edges (absent in RC420) and round spongy plagioclase xenocrysts (riddled with glass inclusions) with clear euhedral rims that have grown since partial dissolution formed the spongy core (Tsuchiyama, 1985).

The basalts have picked up occasional quartz-feldspar xenoliths, which have undergone partial melting ( $\approx 40\%$ ) and are now highly porous. Feldspar fragments have developed spongy margins or have been completely replaced by tiny round plagioclase "grains" in glass, while quartz has simply become rounded. At the boundary between the partially melted xenolith and its host there has been little mixing, and the zone of hybridization is less than 50 $\mu$ m wide. Quartz from the xenolith abutting onto the host basalt exhibits no reaction, and similarly, olivine phenocrysts from the basalt are not affected when adjacent to this hybridization zone, presumably because diffusive exchange of components from the viscous silica-rich partial melt in the xenolith will be slow. The limited disaggregation of the xenolith suggest that it was not a source

Plate A2  
Other reaction textures from Lassen.

- a) RC404 Contact between host dacite (top) and a vitrophyric andesite inclusion containing acicular plagioclase and prismatic orthopyroxene and clinopyroxene. An hornblende xenocryst within the vitrophyric andesite inclusion has a reaction rim of epitaxial acicular pyroxene, but has also partially decomposed to fine-grained opacite. Associated with the hornblende is a rounded, partially dissolved plagioclase crystal with a clear rim. Scale bar is 1mm.
- b) RC417 Sponge-textured plagioclase xenocryst with clear rim and round embayment now filled by groundmass material. Scale bar is 1mm.
- c) RC417 Skeletal olivine phenocryst partially replaced by orthopyroxene. Scale bar is 100 $\mu$ m.
- d) H106444 Olivine phenocryst, with skeletal overgrowth of more Fe-rich olivine. Scale bar is 100 $\mu$ m.

# Plate A2

Other reaction textures from Lassen.

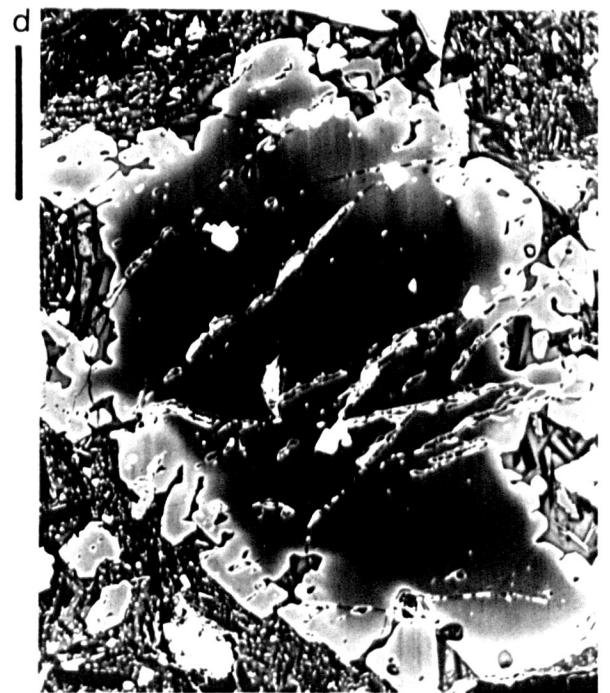
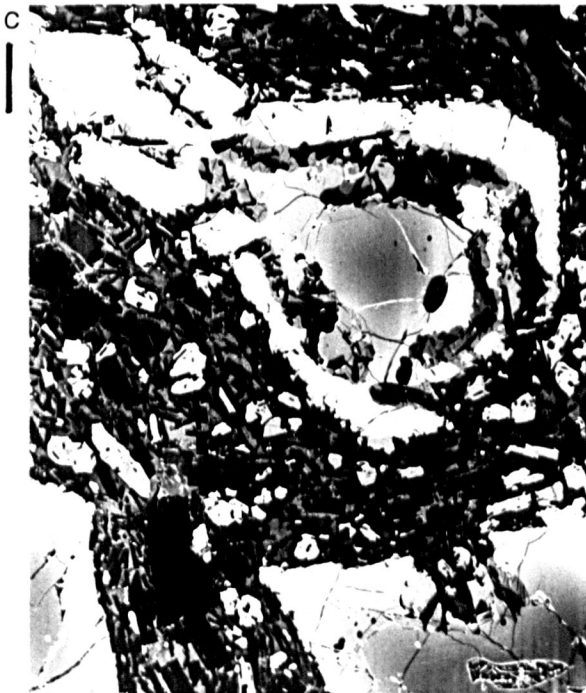
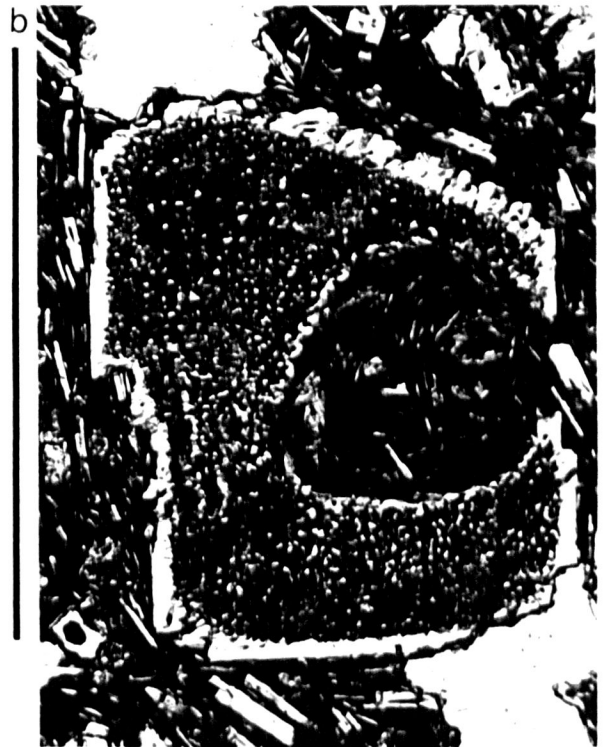
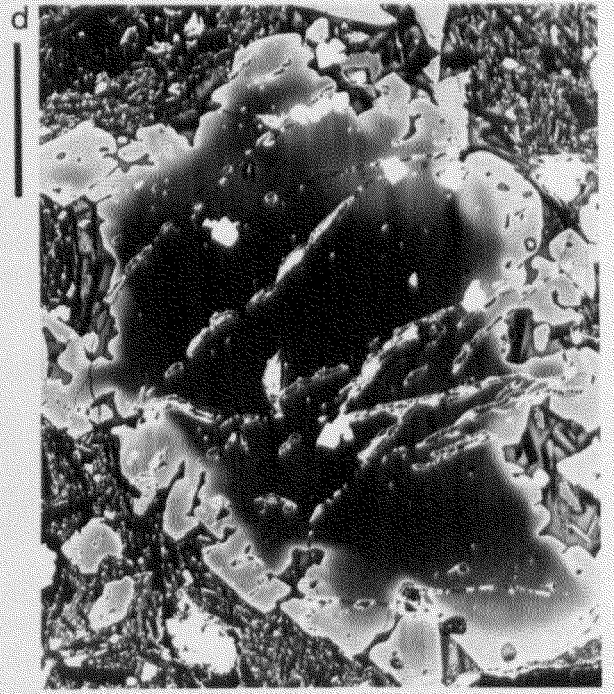
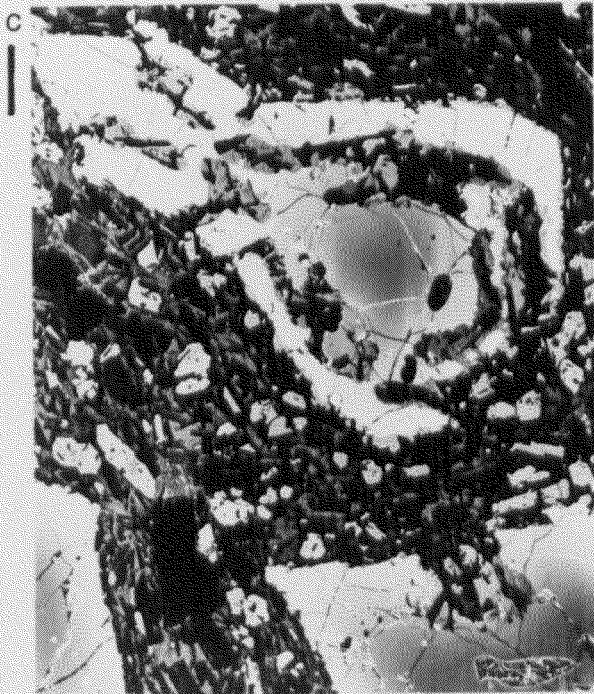
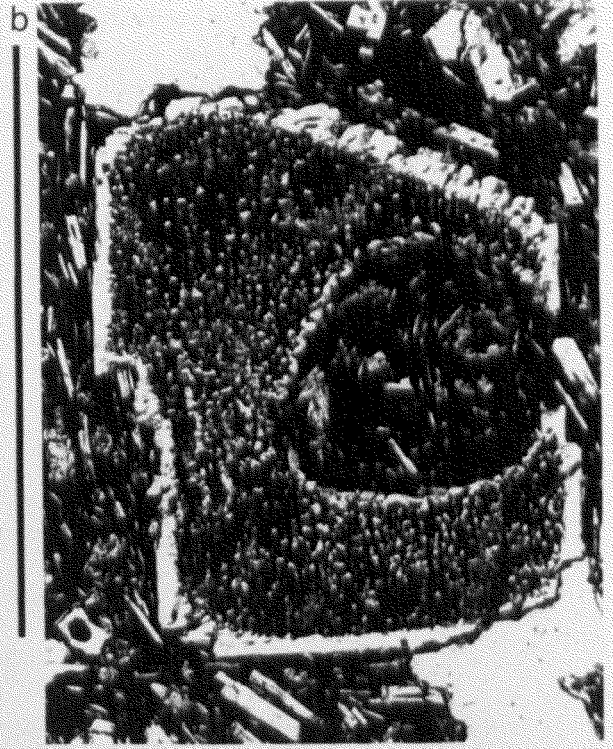


Plate A2  
Other reaction textures from Lassen.

- a) RC404 Contact between host dacite (top) and a vitrophyric andesite inclusion containing acicular plagioclase and prismatic orthopyroxene and clinopyroxene. An hornblende xenocryst within the vitrophyric andesite inclusion has a reaction rim of epitaxial acicular pyroxene, but has also partially decomposed to fine-grained opacite. Associated with the hornblende is a rounded, partially dissolved plagioclase crystal with a clear rim. Scale bar is 1mm.
- b) RC417 Sponge-textured plagioclase xenocryst with clear rim and round embayment now filled by groundmass material. Scale bar is 1mm.
- c) RC417 Skeletal olivine phenocryst partially replaced by orthopyroxene. Scale bar is 100 $\mu$ m.
- d) H106444 Olivine phenocryst, with skeletal overgrowth of more Fe-rich olivine. Scale bar is 100 $\mu$ m.

# Plate A2

Other reaction textures from Lassen.



for the quartz and feldspar xenocrysts found within the basalt.

Rounded quartz xenocrysts, some with included pyroxene and glass, are surrounded by reaction rims of brown glass and a solid interlocking network of clinopyroxene crystals (plates 4.2a,b,d; Alb,c,d). At the outer edge of the rim the pyroxenes are equant, but close to the quartz they are prismatic, and may be arranged parallel to the surface of the quartz rather than perpendicular. Projecting from the quartz there may be many needles of tridymite (plate 4.2d). There are many similar structures without a central quartz. Close to the quartz are small skeletal pyroxenes, while at the edge of the rim the pyroxenes have formed a solid band. Some pyroxenes contain quartz inclusions and pyroxenes close to the quartz may overgrow cusps on the quartz surface, formed by pyroxene overgrowing and sheltering regions of quartz from dissolution (plates 4.2a,b; Alb; §3.1.4).

Partially dissolved pyroxene xenocrysts with spongy margins full of small granular pyroxenes are also present in RC417 (plate 7.2d,f).

RC420 is heterogeneous, containing mingled patches of a second basalt, which was also carrying quartz xenocrysts with clinopyroxene reaction rims. Where this texture is at the boundary between the two basalts, the rim is missing, presumably because of abrasion upon mingling. This suggests that growth of the pyroxene rims preceded mingling, and that both magmas were reasonably crystalline at the time of mixing.

#### **Area two: Yellowstone.**

##### H74389

Contaminated basalt containing reacted plagioclase and quartz, First Cataract, Gardiner River, Yellowstone National Park, (Wilcox, 1944)

The host basalt is fine-grained, with plagioclase crystals with spongy cores riddled with melt inclusions overgrown by clear euhedral rims.

Small ( $\approx 0.5\text{mm}$ ), rounded and embayed quartz grains are surrounded by reaction rims of pyroxene and glass. The reaction rim is predominantly glass with radial, columnar pyroxenes in contact with and embayed by the quartz, surrounded by a porous band of granular pyroxene.

#### **Area three: Labrador.**

##### RAW860

Proterozoic alkali basalt dyke containing reacted orthopyroxene, Nain complex, Labrador (Wiebe, 1986).

Basalt contains megacrysts of orthopyroxene ( $\leq 20\text{mm}$ ) with reaction rims of olivine, clinopyroxene, magnetite (plate 6.2a).

The orthopyroxene is rimmed by clinopyroxene crystals with orthopyroxene cores, and elongate, skeletal olivine crystals, aligned more or less perpendicular to the surface of the orthopyroxene. Further out clinopyroxene is interstitial to olivine crystals. The inferred order of crystallization in these reaction rims is olivine, followed by olivine and clinopyroxene, and finally clinopyroxene.

## Area four: Great Britain.

### CHD

Ankaramite with reacted olivine, orthopyroxene, clinopyroxene and spinel, Calton Hill, Derbyshire, England, (Donaldson, 1978).

Included within the basalt are xenoliths of harzburgite and spinel lherzolite. Where orthopyroxene is exposed to the basalt it has reacted to form rims of rounded olivine grains embedded in clinopyroxene (plate 6.2b). Olivines at the xenolith margin have slightly ragged margins; greenish clinopyroxene has undergone partial melting, and brown spinel has reaction rims of opaque magnetite.

### RC324

Marscoite sill containing reacted quartz, Allt Daraich, south west of Glamaig, near Sligachan, Skye, (Harker, 1904; p187).

Rounded quartz grains are rimmed by crystals of green hornblende, or of augite in the process of transformation to hornblende (plates 4.1d; A3b). Hornblende and augite are often overgrown by the quartz (plate A3a), proving that the rim of the latter postdates the formation of the ferromagnesian minerals. Some of these quartz grains possess quite distinct growth pyramids (plate A3b).

### RC394

Basaltic dyke containing reacted quartzose xenoliths, Bla Bheinn, Skye (Harker, 1904; p351).

Quartzose xenoliths are surrounded by rims of pyroxene, which are skeletal and approximately radially oriented close to the xenolith, and show peripheral alteration to hornblende (plate A3c).

### RCACD

Composite dyke containing reacted quartz, An Cumhann, Arran, Scotland, (Kanaris-Sotirion and Gibb, 1985).

Rounded quartz grains are surrounded by a reaction rim of pyroxene and devitrified glass (plate A3d). The outer part of the pyroxene rim is composed of equant pyroxene crystals which have become interconnected. Close to the quartz the pyroxenes are acicular, skeletal and radially oriented.

## Area five: France.

### BM16

Leucite basanite containing reacted quartz and feldspar, Massif Central, France.

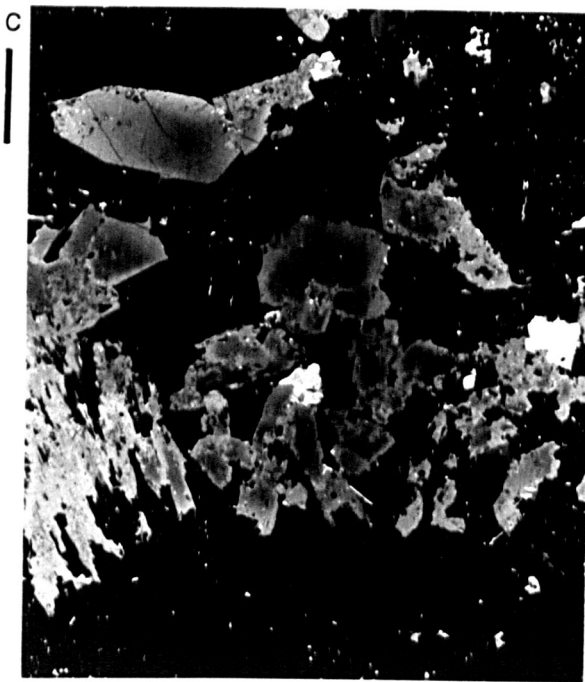
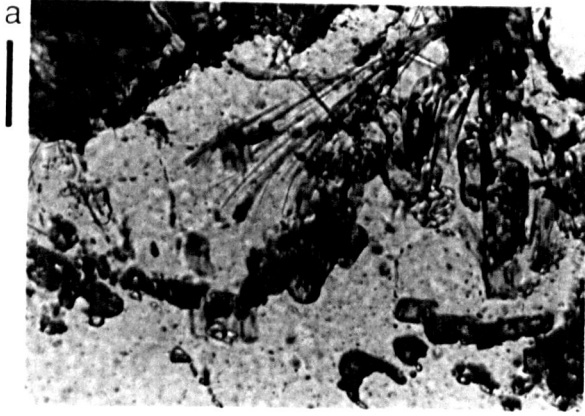
The rock contains abundant rounded quartz xenocrysts rimmed by pyroxene and feldspathic glass (plate A4a,b), and ocelli (plates A4c,d; A5a,b), most of which are also composed of pyroxene and glass. The similarity between the structures of

Plate A3  
Quartz reaction textures from Britain.  
Scale bars are 100 $\mu$ m.

- a) RC324 Detail of prismatic and acicular augites enclosed by quartz.
- b) RC324 Quartz crystal rimmed by hornblende, showing the line of melt inclusions at the base of the quartz growth pyramids.
- c) RC394 Part of quartzose xenolith (black, bottom) in altered basalt, with reaction rim of augite, partly altered to amphibole.
- d) RCACD Round quartz with a reaction rim of pyroxene and devitrified glass in an altered matrix containing plagioclase laths (dark grey), and microphenocrysts of pyroxene (light grey)

# Plate A3

Quartz reaction textures from Britain.



ocelli and reaction rims around quartz suggests that ocelli are either the result of sectioning through the edge of a quartz reaction rim, or of complete dissolution of the quartz.

Other types of ocelli are present in this rock. One example shows fine pyroxene needles radiating into glassy feldspar (plate A5b). The paucity of pyroxene in this case suggests little exchange of material between ocellus and host, and the ocellus probably resulted from the fusion of a feldspar xenocryst. More coarsely crystalline clots, composed mostly of plagioclase with some pyroxene and glass, are probably inclusions of a different magma composition, resulting from the mixing of two liquids.

Quartz grains (plate A4a,b) have a maximum size of 2mm, are well rounded and sometimes consist of more than one crystal. They are usually cracked, the cracks containing tiny glass inclusions. At its margin the quartz may exhibit pyramidal facets, indicating that regrowth of the quartz may have followed dissolution (§4.3.2). They are, without exception, rimmed by clinopyroxene and glass. The innermost part of the rim consists of equant euhedral pyroxenes (10%) and silica-rich glass (90%), sometimes partly devitrified with small box-shaped feldspars (plate A4a,c). The pyroxenes close to the quartz have colourless cores with bright green rims which are thickest on faces towards the quartz. Around this zone is a band of colourless, equant, stubby euhedral pyroxenes with some interstitial glass. Separating these pyroxenes from the groundmass is a zone composed of small, randomly orientated, colourless pyroxenes in a matrix of feldspathic glass. Some of these latter pyroxenes are well rounded and associated with partially dissolved pyroxene phenocrysts at the edge of the glassy zone (plate A4b,d), whereas others are subhedral and associated with the pyroxene band.

#### RF9

Borée phonolite with reacted kaersutite, near Mézenc, Velay, Massif Central, France.

Brown kaersutite grains are always surrounded by reaction rims of green clinopyroxene (without well-formed crystal faces), and titanomagnetite (plate A6c). Some kaersutites are hollow, and the central inclusions contain brown hornblende, titanite, titanomagnetite, green clinopyroxene and feldspar.

#### RF10-11

Xenolithic basalt with reacted olivine, spinel, orthopyroxene, clinopyroxene, quartz, biotite and plagioclase, from maar, 1km E of Borée, near Mézenc, Velay, Massif Central, France.

Most olivines show no reaction, but some are surrounded by reaction rims of clinopyroxene prisms (plate 7.1c,e).

A second vesicular basalt is mingled with the host, appearing as wisps and clots. It contains euhedral phenocrysts and skeletal microphenocrysts of olivine, but no clinopyroxene or plagioclase and is opaque in thin section due to lots of tiny black particles (magnetite or liquid immiscibility glass droplets) in the groundmass. The boundary between the two basalts is lobate, indicating that they were both liquid during mingling.

The basalt contains numerous xenoliths and xenocrysts:

Plate A4  
Compositional images of quartz reaction textures.  
Scale bars are 100 $\mu$ m.

- a) BM16 Rounded quartz grain surrounded by a reaction rim of aegirine-augite and glass. Note devitrification product intergrowth next to quartz, zoning of pyroxenes in rim and partially dissolved pyroxene phenocrysts in feldspathic region outside. Small pyramids (20 $\mu$ m high and 100 $\mu$ m across) can be seen on the quartz surface.
- b) BM16 Rounded quartz grain, surrounded by a reaction rim of aegirine-augite and devitrified glass. A large rectangular pyroxene phenocryst has impinged on a glassy feldspathic region (top right), developing a spongy texture towards the quartz and leaving small rounded pyroxenes in the glassy matrix.
- c) BM16 (As plate A5a). Ocellus, with inner zone of equant, euhedral pyroxenes and tiny skeletal plagioclases in a devitrified glassy matrix. Outer zone composed of feldspar.
- d) BM16 Ocellus, composed of central glassy zone with pyroxenes, surrounded by a continuous solid band of pyroxene, which completely isolates the interior of the ocellus from the exterior. Around this is a feldspathic region containing some rounded and partially dissolved groundmass pyroxenes. Note that the highest nucleation density of pyroxenes is at the outer edge of the solid pyroxene band, where there are numerous small, equant pyroxenes.

# Plate A4

Quartz reaction textures from the Massif Central.



- a) Websterite and harzburgite xenoliths with rounded margins, showing reaction of orthopyroxene forming granular olivine plus clinopyroxene (§6.3; eg plate 6.1b).
- b) Orthopyroxene xenocrysts with olivine and clinopyroxene rims (§6.3; plates 6.1a,b; 6.2c; A6d,e,f).
- c) Angular quartz fragments (1-1.5mm) without fringes, and ocelli of clinopyroxene and glass without quartz (plate A5d, left).
- d) A trachytoidal plagioclase xenolith with a little quartz and magnetite, but displaying no evidence of reaction with the host magma.
- e) Some plagioclase crystals with annealed inclusion-riddled cores and clear rims, while others are fragmental.
- f) Biotites mostly replaced by strongly pleochroic orthopyroxene.
- g) Green spinels that have reacted with melt to form magnetite (plate 7.2a).
- h) Clots of clinopyroxene, possibly remnant from olivine dissolution (plate A6a; compare with plate 7.1e).
- j) Clinopyroxene megacryst, with spongy mantle and irregular rim dominated by re-entrants (plate 7.2b).

#### RF12-16

Xenolithic basalt containing reacted orthopyroxene and quartz, from basalt lake in maar, 12km SSW of Yssingaux, Velay, Massif Central, France.

Orthopyroxene, both as xenocrysts and at the margins of spinel lherzolite xenoliths, is partly replaced by rounded, irregular, elongate olivine grains, clinopyroxene and some devitrified glass (plates 6.1c-f; A5c). The clinopyroxene poikilitically encloses the olivine rods and shows sector twinning (plate 6.1e). These reaction zones are often overgrown by optically continuous, twinned, euhedral clinopyroxene (plate 6.2d,e).

Similar clots comprise rounded skeletal olivines enclosed in a mass of pyroxene, all surrounded by a band of equant olivine grains, which are faceted only where they are in direct contact with the groundmass (plates 6.1f; 6.2f). Remnant olivine ( $f_{0.80}$ ) with ragged outlines are embayed by small pockets of orthopyroxene, suggesting that such clots were originally ultrabasic xenoliths containing both olivine and orthopyroxene. The orthopyroxene dissolved to produce olivine and clinopyroxene, whilst the xenolithic olivine developed ragged edges.

Rounded quartz grains are surrounded by a reaction rim of prismatic pyroxene and brown glass. There are also numerous clinopyroxene ocelli without quartz (plate A5c). These comprise a central area of prismatic pyroxene and brown glass surrounded by a band of granular pyroxene, separated from the groundmass by numerous small pyroxenes in brown glass.

#### H59909

Olivine norite hybrid containing reacted quartz, in augite dolerite dyke, Trégastel, France, (Thomas and Smith, 1932).

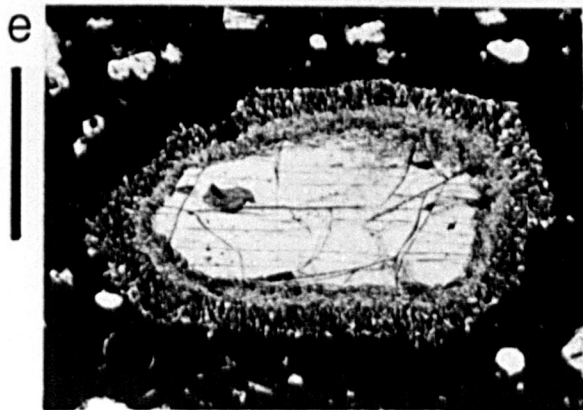
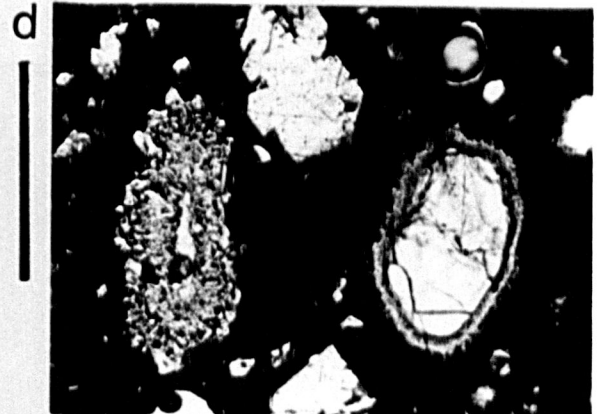
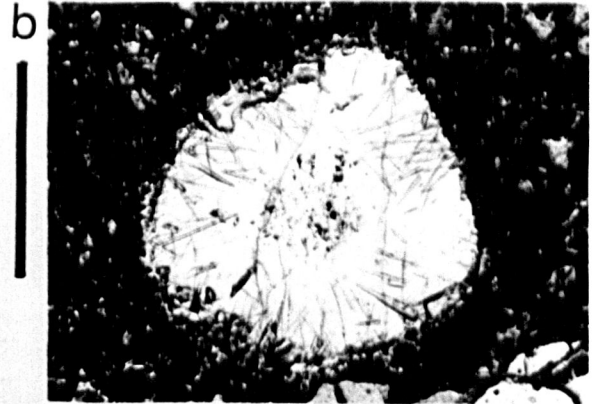
The dominant textural feature is the presence of oval patches of yellowish quartz and feldspar, up to 8mm across. These consist of perthitic orthoclase and quartz, sometimes graphically

Plate A5  
Other reaction textures from France.  
I. Transmitted light.  
Scale bars are 500 $\mu$ m.

- a) BM16 (As plate A4c) Ocellus composed of a central opaque glassy zone with some pyroxene, a pyroxene band and an enclosing clear feldspathic zone with some pyroxene.
- b) BM16 Ocellus, composed of fine pyroxene needles radiating into a mass of feldspathic glass.
- c) RF12 Clinopyroxene-glass ocellus (left) remnant from dissolution of quartz into the basalt. At the right is a complex clinopyroxene phenocryst riddled with inclusions of melt and other crystalline phases.
- d) RF11 To the left, a quartz xenocryst with a reaction rim of clinopyroxene and glass; to the right, an orthopyroxene xenocryst with a reaction rim of olivine.
- e) RF11 Orthopyroxene xenocryst, surrounded by fine-grained olivine and clinopyroxene reaction products, in turn enclosed by a band of granular olivine.
- f) RF11 Orthopyroxene and olivine xenocrysts, the orthopyroxene surrounded by a reaction rim of granular olivine.

# Plate A5

Other reaction textures from France. I.



intergrown or arranged concentrically. They are usually fringed by a complete ring of a pale-green monoclinic pyroxene, of which individual crystals project inwards and are euhedral towards the quartz. Some biotite and hornblende may be present (plates 4.1b; A6b).

Thomas and Smith (1932) proposed that these pyroxene-rimmed quartzose patches are neither xenocrysts nor phenocrystic quartz overgrown by later augite, but that the pyroxene lined a hollow cavity that was subsequently filled by feldspar and quartz, either in succession or as a micro-pegmatite (also Augustithis, 1978).

The preferred explanation of this study is that the quartz crystals are xenocrysts, which dissolved and were surrounded by reaction rims of clinopyroxene after introduction into the magma. Continued growth of the pyroxenes sealed off the quartz and adjacent melt, which subsequently precipitated alkali feldspar, biotite, hornblende and quartz during cooling, so that no glass remained. Some of the pyroxenes are partly overgrown by quartz, and the intergrowth (hence co-crystallization) of quartz and feldspar suggests some regrowth of quartz after dissolution ceased.

#### Area six: Japan.

##### H100426

Basalt with reacted plagioclase, olivine and quartz, Omori Yama crater, Izu, Japan.

Host basalt contains partially resorbed plagioclase xenocrysts with unaltered cores, spongy mantles and clear overgrowth rims. Euhedral olivine phenocrysts are present, sometimes with skeletal terminations, sometimes with spinel inclusions and reaction rims of pyroxene and spinel.

Quartz xenocrysts are well rounded, traversed by melt-filled cracks, and are rimmed by dark brown glass and pale-green pyroxene prisms, radial and elongate close to the quartz, forming a continuous band of equant crystals against the groundmass.

##### H100428

Basalt containing reacted plagioclase and quartz, Omori Yama crater, Izu, Japan.

This rock is composed of two basalts mingled on a thin section scale. The groundmass of the host is dark grey, and the inclusions of the other basalt are brown. The difference in colour is due to the presence of immiscible glass droplets in the host, but not in the inclusions. Plagioclase crystals have clear unaltered cores, spongy mantles and clear overgrowth rims. The groundmass comprises plagioclase laths, with grains of pyroxene and olivine in a fine-grained matrix.

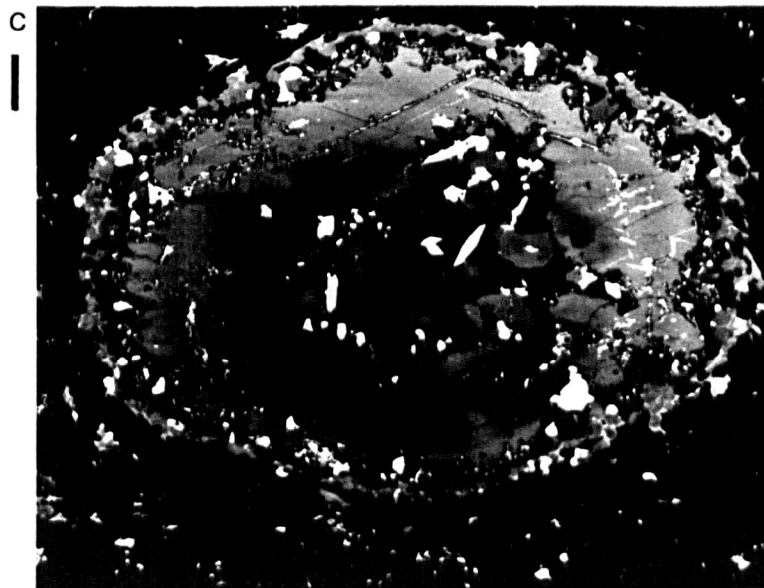
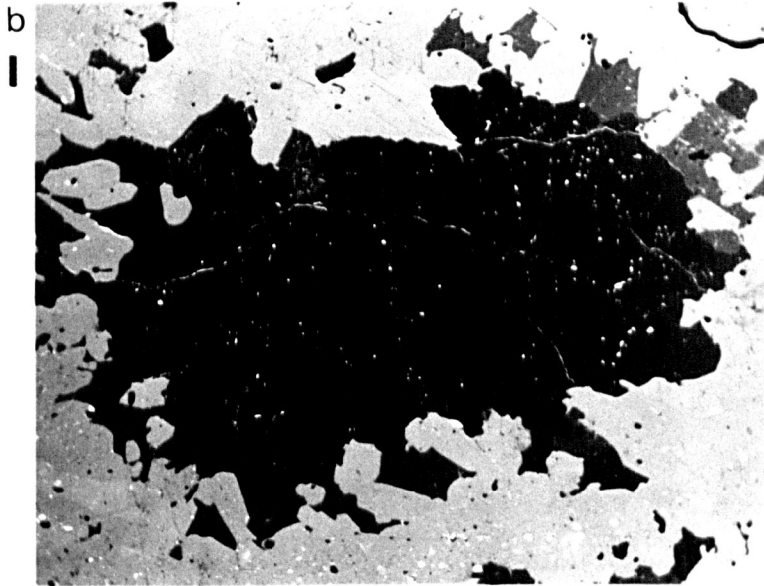
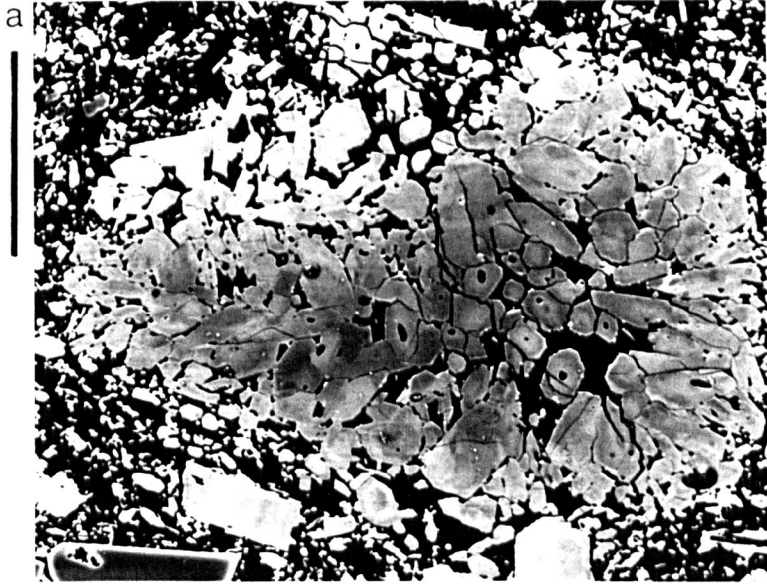
Rounded quartz grains with hemispherical glass-filled embayments are surrounded by a glassy zone containing acicular, skeletal and unzoned pyroxenes (plate A7a). This grades outwards into a continuous band of pyroxene, where the crystals form a solid interlocking network. Embayments in the quartz contain crystallites of tridymite, some pyroxene and immiscible droplets of iron-rich glass, and may retain original gas bubbles.

Plate A6  
Other reaction textures from France.  
II. Compositional images.  
Scale bars are 100 $\mu$ m.

- a) RF10 Clot of zoned clinopyroxene, possibly representing a completely dissolved olivine (cf plate 7.1c,e).
- b) H59909 (Also plate 4.1b). Quartz (black), surrounded by pyroxene (light grey) and feldspar (dark grey) reaction rim. The quartz is quite irregular in shape, in places intergrown with feldspar and partly encloses several pyroxenes, suggesting some regrowth of the quartz after dissolution ceased.
- c) RF9 Hollow kaersutite crystal with reaction rim of aegirine-augite. (The white speckled material is opacite, a decomposition product of the kaersutite). Within the hollow centre of this kaersutite are hornblende (dark grey), feldspar (black), calcite (white), titanite (white acicular crystals) and aegirine-augite (medium grey).

# Plate A6

Other reaction textures from France. II.



### H100429

Basaltic andesite with reacted plagioclase and quartz, Omori Yama crater, Izu, Japan.

Well-rounded, spongy plagioclase xenocrysts (often in clusters) are overgrown by clear rims.

Quartz xenocrysts are well rounded, embayed, full of holes and surrounded by reaction rims of pyroxene and glass, either completely or only partly (plate 4.1g; 7mm away). Pyroxenes of these rims are prismatic and radial in orientation close to quartz, but at the outer edge of the fringe they are equant and may form a continuous solid band, physically isolating the quartz from the andesite. The tubes or holes in the quartz are filled mostly by glass, with 5-10% pyroxene and occasional tridymite crystals, and are probably connected to the host. The opaque aspect of the fringe (plate 4.1g) is due to the presence of lots of small glass droplets, resulting from liquid immiscibility.

Such a large variation in reaction textures precludes *in situ* formation of the complete reaction rim texture, because the abraded version would then have developed to the same extent. One explanation is that development of the reaction texture followed one mixing event. Subsequently, movement within this partly crystalline magma abrasively removed most of the pyroxene fringe of the latter before allowing it to come to rest close to the former. The former retained a complete reaction rim either because it had a smooth ride, or because the pyroxenes of its reaction rim were more interconnected, forming a stronger, more rigid skeleton which survived whatever removed the rim from the latter.

### H121372

Olivine-hypersthene-clinopyroxene basalt, with reacted orthopyroxene and quartz, Iki Islands, Japan.

Orthopyroxene phenocrysts may be rimmed by clinopyroxene, or may have clinopyroxene jackets on certain faces {100} only. Some phenocrysts show the clinopyroxene on only one side, while others show clinopyroxene exsolution parallel to the jackets. These {100} "jackets" may result from pyroxene phenocrysts splitting or separating along exsolution planes. This basalt also carries clots of bronzite crystals surrounding zoned carbonates (plate A7c), and complex clinopyroxene crystals with spongy cores of clinopyroxene, orthopyroxene, feldspar and carbonate (plate A7d).

Quartz grains (up to 3mm across) are usually well rounded with glass-filled cracks, and surrounded by a reaction rim of pyroxene prisms and brown glass (plates 4.1c; A7b). Some have both rounded and irregular faces, and appear to be fragments resulting from separation of a grain along a crack. Separation has, in some examples, occurred after growth of the pyroxene reaction rim. Some crystals contain large round embayments, or circular melt inclusions connected to the melt of the reaction rim by cracks. Pyroxene prisms in the fringe are typically radially oriented, except in some cases where they are parallel to the quartz surface, forming a thinner rim which appears to have been flattened. Pyroxenes are equant towards the host and skeletal close to the quartz.

Plate A7

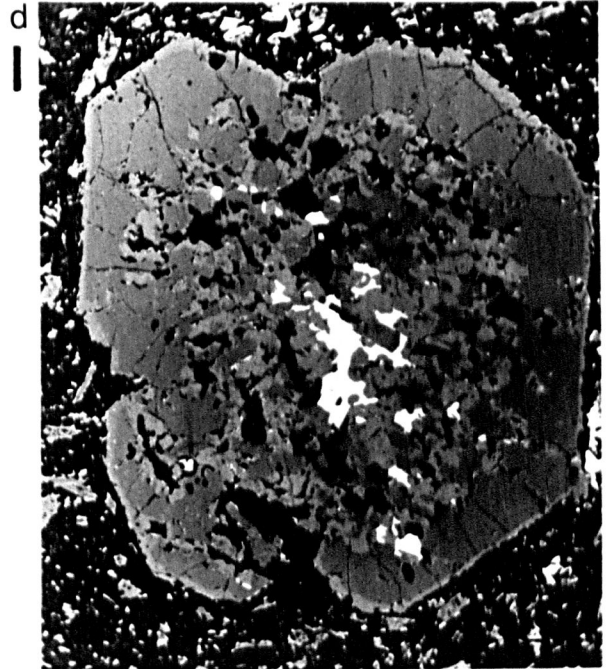
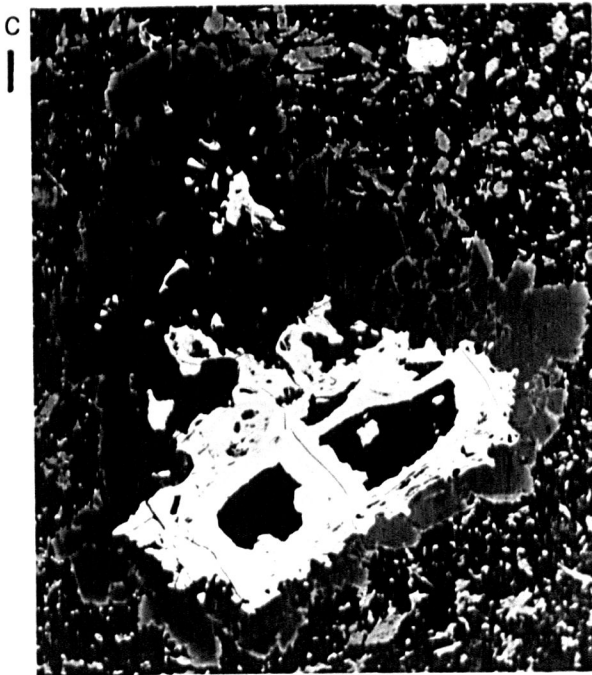
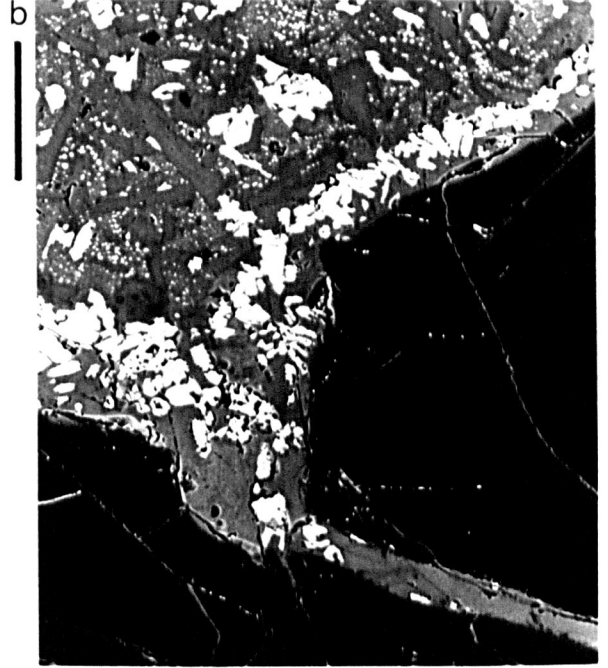
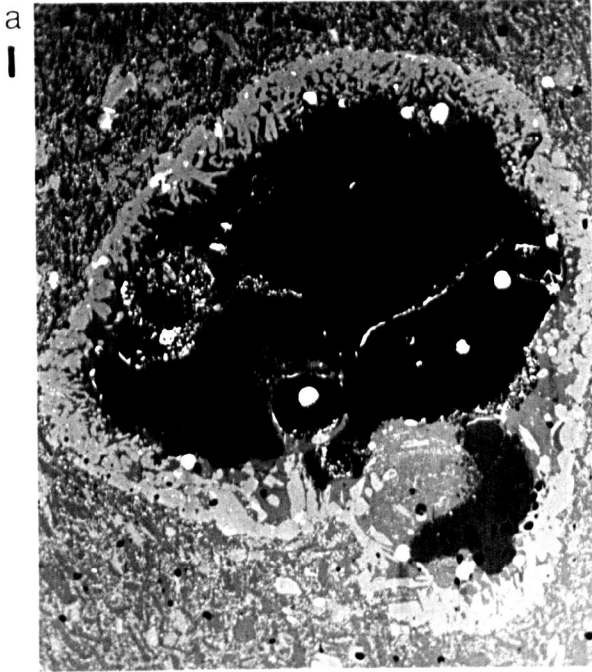
Compositional images of reaction textures from Japan.

Scale bars are 100 $\mu$ m.

- a) H100428 Rounded quartz grain with large glass-filled embayments, surrounded by a reaction rim of pyroxenes and glass. The central embayment contains a vesicle and lots of small dark crystallites (tridymite). The groundmass comprises plagioclase laths, pyroxene and olivine microphenocrysts. The tiny white dots are iron-rich glass droplets resulting from late-stage liquid immiscibility. Larger white patches are SnO<sub>2</sub> from polishing the section.
- b) H121372 (As plate 4.1c). Part of a quartz crystal (bottom) with a reaction rim of pyroxene and glass against basalt (top). The quartz is cracked and the crack filled by melt, with a few skeletal pyroxenes and tiny tridymite needles.
- c) H121372 Clot of aluminous bronzite crystals (wo<sub>5</sub>en<sub>80</sub>fs<sub>15</sub>, 4.5wt% Al<sub>2</sub>O<sub>3</sub>) enclosing siderite (white; 43wt% FeO) and a glassy Fe-rich material. Around the margin is a narrow overgrowth of clinopyroxene.
- d) H121372 Clinopyroxene phenocryst (wo<sub>37</sub>en<sub>48</sub>fs<sub>15</sub>, 10% others) overgrowing core region of granular clinopyroxene (light grey; wo<sub>34</sub>en<sub>50</sub>fs<sub>16</sub>, 8% others) and orthopyroxene (darker grey; wo<sub>4</sub>en<sub>73</sub>fs<sub>23</sub>, 3% others), with interstitial carbonate (white), plagioclase (an<sub>58</sub>, black). The clinopyroxene overgrowth has crystallized with the same orientation as the clinopyroxene grains in the centre. The texture is possibly the result of hornblende breakdown to clinopyroxene, orthopyroxene and plagioclase, followed by clinopyroxene overgrowth.

# Plate A7

Reaction textures from Japan.



## H121592

Olivine-plagioclase basalt with reacted plagioclase and quartz, Iki, south of Mt. Togitsu, near Kinkai, Nagasaki, Japan.

Partially dissolved plagioclase xenocrysts, with spongy cores and clear narrow overgrowth rims, are rare. Elongate orthopyroxene phenocrysts are often found in the groundmass, in direct contact with the outer edges of reaction rims around quartz.

Quartz xenocrysts are common, ranging in size from 1 to 4mm. They are usually well rounded (eg plate 4.1e), but some show almost euhedral outlines. All are traversed by cracks filled by brown glass, which may connect with glass-filled cavities within the quartz. Some of these cavities also contain pyroxene and/or tridymite. One quartz (plate 4.2c) has an irregular shape with several large embayments, of which one has a carbonate-filled vesicle at the blind end, suggesting that the embayment was caused by "upward drilling" of the vesicle into the quartz (Donaldson and Henderson, 1988).

Quartz grains are surrounded by reaction rims of pyroxene and brown glass, the pyroxenes tending to be elongate and radially oriented next to the quartz, and equant adjacent to the groundmass. Some of the skeletal pyroxene crystals may enclose inclusions of quartz, or cusps on the quartz surface (§3.1.4; plate A12f,h). Pyroxenes in the glass-filled embayments are fewer and larger; the locally enhanced dissolution which created the embayments favoured growth of pyroxene over nucleation in these regions. Fine needles of tridymite have crystallized along the margins of embayments and cracks of the quartz (plate 4.2c). This is not visible along the exterior of the quartz where pyroxene growth is extensive, but not sufficient to isolate the melt adjacent to the quartz.

## H121594

Andesite with reacted plagioclase, hornblende and quartz, Iki, south of Mt. Togitsu, near Kinkai, Nagasaki, Japan.

Plagioclase phenocrysts have either spongy margins and no rims, or spongy cores and clear euhedral rims which, in turn, show slightly ragged edges. There are also aggregates of three or four plagioclase crystals with rounded corners, clear rims over inclusion-rich cores and slight fritting of the rims. The inclusion-rich cores appear to result from annealing of sponge texture so that the tiny plagioclase grains resulting from partial dissolution (Tsuchiyama, 1985) reconnect with one another. I consider that these are recycled spongy plagioclases that have undergone one complete cycle of partial dissolution, followed by overgrowth and annealing, and are just starting out on their second.

Small brown, pleochroic, inclusion-rich, diamond-shaped hornblendes are surrounded by reaction rims of dark brown material (plate 7.3e). There are also small black clots composed of finely divided opaque material pseudomorphing amphibole (some showing a 56° angle on basal section; eg plate 7.3f). These opacite pseudomorphs may contain some orthopyroxene.

Quartz xenocrysts are traversed by glass-filled cracks and contain melt inclusions. They may be well rounded without a pyroxene fringe (figure 4.3k), or highly angular with thin rims

of equant reddish brown pyroxene prisms and clear glass, which may (figure 4.31) or may not (figure 4.3m) be continuous around the quartz. Close to the quartz the pyroxenes are more prismatic than against the groundmass, with occasional fan-shaped clusters. The pyroxenes are, on the whole, randomly oriented, with some elongate parallel to the quartz surface. The irregular outlines of the quartz are due to round embayments (§4.4.2). Round "tunnels" are filled with feldspathic glass and occasional tridymite needles.

#### Area Seven: New Zealand.

##### Ngauruhoe

Ngauruhoe is one of the volcanoes in the Tongariro volcanic centre, which itself is one of the five major centres of the Taupo Volcanic Zone (TVZ), New Zealand. The TVZ is a volcanic arc and marginal basin of the Taupo-Hikurangi subduction system, and is a southward extension of the Tonga-Kermadec arc into the continental crustal environment of North Island, New Zealand. The lavas of the Tongariro volcanic centre are calc-alkaline andesites and dacites. Ngauruhoe is a composite cone which last erupted a basic andesitic lava between June and September 1954 in thirteen separate flows. Metaquartzites occur widely throughout the Tongariro centre and are found as xenoliths in most lava types. Some are surrounded by a corona of Si-K-rich glass with a zone rich in clinopyroxene (Graham and Hackett, 1987).

##### H52723

1954 andesite containing reacted olivine, plagioclase, quartz-rich and feldspar-rich xenoliths, Ngauruhoe, Taupo volcanic zone, New Zealand (Steiner, 1954).

Euhedral phenocrysts of clinopyroxene, orthopyroxene and plagioclase are set in a glassy to cryptocrystalline groundmass, with rare olivine crystals rimmed by magnetite and orthopyroxene (plate 7.1a,b). Some plagioclase crystals have inclusion-rich cores and clear, inclusion-free margins. Feldspathic xenoliths, with rare elongate clinopyroxene and brown glass, and quartzose xenoliths have not interacted noticeably with the host andesite.

Appendix 2: microprobe data

Silica dissolution experiments

	dist	SiO2	TiO2	Al2O3	FeO	MnO	MgO	CaO	Na2O	K2O	Total
1120 °C experimental charges:											
R61											
PX 1	40	54.15	0.21	0.52	16.37	0.28	24.34	3.78	nd	nd	99.65
PX 2	30	53.77	0.31	0.67	15.42	0.33	23.88	4.26	0.10	nd	98.76
PX 3	70	52.75	0.51	0.94	19.15	0.38	21.80	4.38	nd	nd	99.91
PX 4	40	53.08	0.39	0.54	19.27	0.38	22.04	4.13	0.12	nd	99.95
PX 7	15	54.33	0.27	0.32	16.47	0.32	24.10	4.03	nd	nd	99.92
PX 10	50	53.59	0.33	0.55	18.08	0.38	22.76	3.82	nd	nd	99.59
PX 11	60	51.31	0.84	2.20	9.63	0.17	16.50	18.60	0.24	nd	99.50
PX 12	30	53.99	0.25	0.42	16.46	0.28	24.74	3.31	nd	nd	99.55
PX 13	20	54.10	0.21	0.34	16.34	0.31	24.70	3.85	nd	nd	99.86
PX 16	70	53.60	0.35	0.78	16.29	0.34	23.24	5.16	nd	nd	99.80
PX 19	80	52.82	0.61	0.83	18.92	0.43	22.32	4.24	nd	nd	100.27
PX 22	80	53.27	0.40	0.81	15.99	0.38	23.15	4.72	0.11	nd	98.83
PX 25	40	53.75	0.32	0.73	17.12	0.36	23.89	4.20	nd	nd	100.50
PX 28	30	53.72	0.25	0.42	16.35	0.36	24.22	3.76	nd	nd	99.12
PX 29	40	54.13	0.22	0.51	16.48	0.39	24.00	4.08	0.12	nd	99.94
PX 30	35	53.36	0.30	0.51	16.52	0.25	23.37	4.87	nd	nd	99.24
PX 31	GM	51.55	0.65	1.80	11.09	0.26	17.35	16.79	0.21	nd	99.71
PX 34	GM	52.30	0.68	1.02	18.62	0.47	20.27	6.63	0.11	nd	100.10
PX 35	GM	51.67	0.78	1.73	13.59	0.24	17.26	14.64	0.20	nd	100.11
PX 37	140	52.02	0.57	2.14	8.59	0.16	16.94	18.79	0.21	nd	99.42
GL 38	5	73.34	1.04	10.82	4.39	nd	1.52	2.52	1.20	2.62	97.52
GL 40	40	61.05	1.67	13.62	8.79	0.17	3.09	6.17	2.24	1.80	98.60
GL 42	35	63.23	1.45	13.32	7.83	nd	2.72	5.54	0.81	2.04	97.03
GL 43	120	59.03	1.87	13.77	8.75	0.16	3.25	6.71	2.24	1.71	97.49
GL 44	120	59.12	1.78	13.80	9.57	nd	3.47	9.74	2.12	1.73	101.33
GL 45	GM	54.77	1.84	17.76	9.66	0.14	2.85	8.63	3.41	1.05	100.11
GL 47	GM	54.52	1.60	19.38	8.70	nd	2.38	9.23	3.15	1.00	100.00
R62											
PX 1	70	53.73	0.38	0.50	16.38	0.36	23.64	4.88	0.12	nd	100.00
PX 2	30	54.13	0.36	0.42	16.64	0.40	23.79	4.41	nd	nd	100.19
PX 4	50	53.46	0.35	0.56	16.43	0.30	22.82	5.57	nd	nd	99.56
PX 5	60	53.25	0.34	0.57	16.90	0.40	23.36	4.64	0.13	nd	99.59
PX 7	100	53.16	0.42	0.69	17.13	0.40	23.68	3.98	nd	nd	99.52
PX 12	110	51.19	0.82	2.37	9.85	0.26	16.12	18.30	0.26	nd	99.17
PX 16	130	51.17	0.91	2.15	11.68	0.23	16.20	17.61	0.22	nd	100.17
PX 17	70	53.11	0.33	0.59	16.44	0.39	23.67	4.42	nd	nd	99.02
PX 18	40	53.65	0.31	0.46	16.73	0.35	23.80	4.38	nd	nd	99.70
PX 19	40	53.40	0.37	0.49	16.37	0.29	23.57	4.67	nd	nd	99.17
PX 20	30	54.29	0.24	0.50	16.46	0.35	23.97	4.22	0.15	0.18	100.36
PX 24	160	51.05	0.87	2.12	10.12	0.23	15.79	18.47	0.24	nd	98.90
PX 25	160	50.77	0.79	2.22	10.50	0.23	15.65	18.39	0.24	nd	98.80
PX 26	180	52.68	0.57	0.94	18.63	0.42	21.56	5.11	0.17	nd	100.08
PX 27	120	51.07	0.89	1.71	12.85	0.32	16.16	16.09	0.21	nd	99.30
PX 30	25	54.08	0.20	0.28	16.75	0.36	23.90	4.19	nd	nd	99.80
PX 31	90	53.25	0.32	0.70	16.37	0.35	23.12	5.20	0.11	nd	99.42
PX 32	35	54.19	0.31	0.41	16.30	0.38	23.70	4.48	nd	nd	99.87
PX 33	10	54.14	0.23	0.26	15.97	0.36	24.40	3.96	nd	nd	99.38
PX 37	90	54.33	0.25	0.42	16.91	0.36	23.83	4.53	nd	nd	100.67
PX 38	200	51.83	0.85	1.71	10.74	0.37	16.16	18.70	0.23	nd	100.61
PX 41	110	53.73	0.26	0.63	17.45	0.44	23.86	3.97	nd	nd	100.35
PX 44	50	54.14	0.30	0.40	16.35	0.40	23.58	5.04	nd	nd	100.32
PX 45	70	53.91	0.27	0.63	16.74	0.38	23.33	4.53	nd	nd	100.66
PX 46	50	54.25	0.27	0.33	16.91	0.32	24.20	4.31	nd	nd	100.62
PX 47	90	54.17	0.28	0.43	17.26	0.37	24.25	3.86	nd	nd	100.68
PX 48	GM	51.26	0.99	2.37	9.53	0.26	16.10	18.54	0.24	nd	99.31
PX 49	GM	51.50	0.97	2.04	10.76	0.16	15.72	18.91	0.25	nd	100.34
PX 51	GM	52.88	0.37	1.10	16.04	0.37	23.07	5.61	0.12	nd	99.55
PX 54	GM	53.48	0.37	0.76	16.23	0.29	23.97	4.33	0.14	nd	99.62
PX 55	GM	51.54	0.76	2.40	8.56	0.24	15.75	19.86	0.33	nd	99.43
PX 56	GM	54.18	0.38	0.64	15.58	0.39	24.59	3.78	0.13	nd	99.68
GL 57	GM	54.58	2.35	12.68	10.93	0.16	4.06	7.57	3.27	1.01	96.65
GL 58	GM	53.00	2.70	12.61	11.70	nd	4.33	7.95	3.26	0.83	96.53
R70											
PX 2	GM	51.26	1.08	1.68	15.18	0.36	16.58	13.58	0.22	nd	99.99
OL 4	GM	38.66	nd	nd	26.58	0.31	36.08	0.46	nd	nd	102.49
OL 5	GM	38.76	nd	0.15	25.72	0.35	35.00	0.66	nd	nd	100.79
PX 6	GM	51.14	0.92	2.66	9.30	0.24	16.06	18.31	0.27	nd	98.89
PX 8	GM	52.45	0.37	1.05	14.90	0.27	24.07	4.90	0.11	nd	98.11

core to pig xtal

"

"

	dist	SiO2	TiO2	Al2O3	FeO	MnO	MgO	CaO	Na2O	K2O	Total
1140 °C experimental charges:											
R30											
PX 1		55.84	0.20	0.78	13.02	0.31	26.96	4.04	nd	nd	101.16
PX 6		55.87	0.10	0.49	12.38	0.40	28.36	3.14	nd	nd	100.76
GL 8	F	58.80	1.33	14.39	7.53	0.11	4.41	7.94	2.34	1.14	97.99
GL 9	X	57.98	1.37	14.76	9.17	0.15	4.85	8.20	2.85	1.05	100.38
GL 10	I	67.28	0.92	13.12	5.84	nd	2.77	5.31	1.56	1.74	98.61
GL 11	GM	55.80	1.72	14.51	10.57	0.12	4.93	8.59	2.58	0.93	99.75
PX 5		55.47	0.20	0.77	13.49	0.37	27.01	3.85	nd	nd	101.18
OL 16		39.05	nd	nd	20.64	0.39	39.99	0.34	nd	nd	100.46
R31											
PX 2		55.22	0.23	0.95	12.65	0.28	26.04	5.50	nd	nd	100.87
PX 6		56.20	0.16	0.69	13.06	0.44	27.18	3.74	nd	nd	101.55
GL 8	I	70.76	0.92	11.98	5.22	nd	2.42	4.39	1.50	1.86	99.14
GL 9	F	60.05	1.29	14.24	8.22	0.10	4.18	7.40	2.34	1.31	99.13
GL 10	X	58.55	1.40	14.51	8.76	0.21	4.60	8.02	2.31	1.18	99.54
GL 12	GM	56.58	1.82	14.43	10.16	0.24	5.02	8.54	2.85	0.99	100.63
R32											
PX 2		54.92	0.28	0.91	12.75	0.35	26.80	4.24	nd	nd	100.26
GL 3	I	74.35	0.70	10.93	4.32	nd	1.84	2.90	1.42	1.92	98.41
GL 4	F	62.69	1.24	14.87	6.78	0.11	2.49	6.56	2.02	1.56	98.32
GL 5	X	57.37	1.55	14.24	9.93	0.19	4.64	8.50	2.65	1.05	100.12
GL 6	GM	55.78	1.91	14.32	10.76	0.23	4.67	9.14	2.42	0.91	100.14
OL 1		39.26	nd	0.11	21.09	0.28	37.43	0.34	nd	nd	98.55
R33											
PX 1		54.46	0.44	0.73	17.42	0.41	23.35	4.43	nd	nd	101.25
OL 2		38.72	nd	nd	22.26	0.26	39.30	0.39	nd	nd	100.98
R36											
PX 1	30	53.91	0.29	0.70	13.31	0.21	26.26	3.89	nd	nd	98.62
PX 4	50	54.75	0.21	0.57	13.14	0.34	26.72	3.61	nd	nd	99.38
PX 5	35	54.08	0.21	0.44	12.66	0.28	27.14	3.30	nd	nd	98.21
PX 6	230	53.29	0.29	1.70	13.04	0.29	28.13	2.20	nd	nd	98.99
PX 8	105	52.95	0.33	1.33	12.46	0.22	25.98	4.50	nd	nd	97.83
PX 10	120	54.80	0.15	0.62	12.42	0.22	27.71	3.32	nd	nd	99.29
PX 12	60	53.89	0.29	0.90	12.73	0.37	26.65	4.29	0.11	nd	99.26
PX 13	65	54.45	0.25	0.53	12.32	0.28	27.02	3.91	nd	nd	98.81
PX 14	65	54.08	0.17	0.79	12.08	0.25	26.37	4.67	0.10	nd	98.53
PX 16	110	54.75	0.16	0.60	12.64	0.35	27.45	3.27	nd	nd	99.34
PX 17	60	54.14	0.26	0.64	13.11	0.25	27.25	2.92	nd	nd	98.58
PX 18	70	54.40	0.20	0.69	13.03	0.31	27.17	3.32	nd	nd	99.14
PX 19	35	54.84	0.18	0.45	12.62	0.35	27.59	3.16	nd	nd	99.19
PX 20	GM	53.88	0.24	1.05	13.03	0.31	26.96	3.62	nd	nd	99.16
PX 23	55	54.24	0.24	0.75	13.27	0.32	26.29	4.18	nd	nd	99.38
PX 24	15	54.47	0.18	0.50	12.84	0.24	27.15	3.34	nd	nd	98.84
PX 25	15	54.56	0.12	0.33	12.90	0.32	26.91	3.63	nd	nd	98.83
PX 26	GM	53.69	0.28	1.25	12.84	0.24	26.32	4.34	nd	nd	99.02
GL 7	F	57.86	1.29	13.78	8.28	0.13	4.71	7.83	2.84	0.93	97.65
GL 8	F	59.73	1.30	13.73	7.92	nd	4.34	7.45	2.79	1.12	98.46
GL 9	I	71.03	0.73	11.79	4.54	nd	2.39	3.97	1.34	1.68	97.52
GL 10	I	72.42	0.69	11.26	4.24	nd	2.02	3.48	1.02	1.81	97.01
GL 11	GM	56.83	1.43	13.99	8.62	nd	4.97	8.00	2.44	1.00	97.37
GL 12	GM	55.60	1.50	13.64	9.90	0.20	5.16	8.64	2.82	0.79	98.25
GL 13	X	58.07	1.23	13.51	8.78	0.14	4.55	7.71	2.44	1.10	97.53
GL 14	X	59.13	1.27	13.89	8.53	0.16	4.42	7.55	2.48	1.11	98.54
R37											
PX 1		52.80	0.22	0.59	13.75	0.31	25.61	3.98	0.11	nd	97.44
PX 11		53.59	0.24	0.91	11.49	0.32	25.50	3.73	nd	nd	95.88
GL 12	I	72.76	0.73	11.13	3.96	nd	1.76	3.34	0.98	1.71	96.39
GL 13	F	60.01	1.28	14.32	8.22	nd	4.04	7.32	1.89	1.18	98.35
GL 14	X	59.46	1.42	14.55	7.27	0.12	4.36	7.66	2.19	1.07	98.10
GL 15	GM	55.79	1.69	14.26	9.59	0.16	5.19	8.46	2.32	0.91	98.37
R38											
PX 1		55.09	0.22	0.59	12.98	0.34	27.23	3.17	nd	nd	99.67
PX 6		54.62	0.20	0.76	12.04	0.29	26.57	3.99	nd	nd	98.58
PX 7		53.69	0.27	1.30	11.60	0.25	24.88	5.79	nd	nd	97.87
GL 8	I	71.12	0.69	11.30	4.83	nd	2.11	3.68	1.15	1.61	96.56
GL 9	I	72.68	0.68	10.86	4.30	nd	1.89	3.34	1.08	1.82	96.68
GL 10	F	57.66	1.34	13.75	8.25	0.21	4.52	7.75	2.31	1.00	96.79
GL 11	F	58.33	1.30	14.06	8.17	0.13	4.57	7.63	2.70	1.09	97.98
GL 12	X	59.21	1.25	13.78	8.14	0.16	4.34	7.23	2.92	1.23	98.26
GL 13	X	56.53	1.48	13.74	9.62	nd	5.03	7.96	3.02	0.82	98.23

	dist	SiO2	TiO2	Al2O3	FeO	MnO	MgO	CaO	Na2O	K2O	Total
GL 14	GM	55.84	1.41	13.73	10.23	0.21	5.34	8.80	2.98	0.85	99.39
GL 15	GM	55.23	1.58	13.72	9.85	0.16	5.28	8.65	3.03	0.82	98.32
GL 16	GM	54.90	1.62	13.78	10.30	0.18	5.36	8.29	2.83	0.83	98.09
R49											
PX 1	320	53.95	0.25	1.22	13.79	0.32	27.23	2.05	nd	nd	98.86
PX 2	210	53.54	0.32	1.19	14.26	0.34	26.26	3.93	nd	nd	99.86
PX 4	200	53.70	0.29	1.02	14.14	0.26	26.26	3.32	nd	nd	99.10
PX 6	180	53.77	0.27	0.88	13.96	0.35	26.49	3.53	nd	nd	99.32
PX 8	105	54.19	0.26	0.48	13.82	0.36	26.72	3.14	nd	nd	99.03
PX 9	10	54.74	0.16	0.32	14.03	0.28	27.22	2.71	nd	nd	99.46
PX 13	120	54.57	0.23	0.55	14.02	0.32	26.33	3.67	nd	nd	99.72
PX 15	110	54.99	0.19	0.42	14.25	0.37	26.53	3.13	nd	nd	99.93
PX 18	65	54.45	0.21	0.39	14.62	0.37	26.71	3.08	nd	nd	99.88
PX 19	280	54.45	0.19	0.75	13.59	0.26	27.97	1.95	nd	nd	99.20
PX 22	15	54.63	0.18	0.50	14.24	0.27	27.11	2.99	nd	nd	99.92
PX 23r	15	54.86	0.16	0.33	14.12	0.33	26.81	2.71	nd	nd	99.33
PX 24	120	54.34	0.20	0.57	13.71	0.32	26.11	3.61	nd	nd	98.87
PX 27	170	54.59	0.19	0.52	14.18	0.33	26.50	3.31	nd	nd	99.69
PX 28	400	53.52	0.35	1.28	14.24	0.29	25.77	4.22	nd	nd	99.72
PX 29	600	54.27	0.20	0.71	13.87	0.31	27.14	2.91	nd	nd	99.42
PX 31	GM	54.20	0.20	0.79	13.89	0.27	26.90	2.95	nd	nd	99.25

1160 C experimental charges:

R43											
PX 1		55.69	0.21	0.81	11.46	0.34	29.16	2.51	nd	nd	100.21
PX 2		55.58	0.18	0.66	10.68	0.29	29.16	2.28	nd	nd	98.90
GL 5	10	67.93	0.67	12.63	5.61	0.12	3.49	5.02	1.82	1.45	98.74
GL 6	5	72.53	0.48	11.53	4.27	0.11	2.58	3.60	1.50	1.57	98.17
GL 7	F	57.83	0.97	14.75	8.94	0.11	5.67	7.82	3.09	0.80	99.98
GL 8	F	57.78	0.95	14.43	8.27	0.17	5.77	7.85	3.13	0.83	99.18
GL 9	X	56.60	0.98	15.11	9.07	0.11	6.02	8.12	3.10	0.84	99.95
GL 10	X	56.02	1.04	15.08	8.94	0.12	6.02	8.26	3.08	0.81	99.37
GL 11	GM	55.26	1.22	14.88	9.55	0.11	6.16	8.62	2.93	0.74	99.47
GL 12	GM	54.49	1.22	14.87	8.81	0.19	6.09	8.61	3.00	0.75	98.03

R44											
PX 2		56.86	nd	0.42	10.78	0.21	30.40	2.13	nd	nd	100.90
GL 5	I	75.98	0.54	9.49	3.46	nd	2.01	2.60	1.25	1.49	96.84
GL 6	I	67.17	0.67	13.13	5.65	nd	3.71	5.30	1.98	1.34	99.00
GL 7	F	58.10	1.02	14.82	8.18	0.17	5.69	7.65	2.90	0.76	99.29
GL 8	F	57.88	1.07	14.59	8.29	nd	5.73	7.90	3.02	0.83	99.38
GL 9	G	56.72	1.11	15.06	8.60	0.18	5.76	8.25	3.02	0.81	99.51
GL 10	G	56.28	1.30	15.02	9.11	0.10	6.16	8.24	2.76	0.76	99.73

R56											
PX 4	20	55.00	0.15	0.72	12.86	0.26	28.19	2.86	nd	nd	100.08
PX 6	20	55.47	0.19	0.81	12.61	0.29	27.64	2.96	nd	nd	100.01
PX 7	50	55.42	0.20	0.80	12.60	0.31	28.06	2.98	nd	nd	100.44

R57											
PX 1	30	56.22	0.16	0.49	11.07	0.20	29.52	2.55	nd	nd	100.23
PX 2	105	54.94	0.19	0.76	11.80	0.31	28.18	2.73	nd	nd	98.94
PX 4	20	55.41	0.11	0.42	12.03	0.24	28.82	2.30	nd	nd	99.41
PX 5	110	55.40	0.19	0.56	12.56	0.29	28.09	2.98	nd	nd	100.08
PX 6r	110	55.52	0.20	0.61	12.18	0.16	28.52	2.79	nd	nd	99.98
PX 8	135	55.67	0.11	0.49	12.26	0.29	28.69	2.40	nd	nd	99.98
PX 9	110	55.44	0.11	0.50	11.71	0.32	28.85	2.56	nd	nd	99.55
PX 10r	110	55.43	0.12	0.57	11.77	0.26	28.57	2.68	nd	nd	99.46
PX 11	65	55.40	0.15	0.56	11.68	0.32	28.71	2.94	nd	nd	99.79
PX 12r	65	54.93	0.25	0.90	11.88	0.28	28.08	2.64	nd	nd	99.03
PX 14	80	55.60	0.16	0.60	11.42	0.18	29.07	2.41	nd	nd	99.51
PX 15	70	55.65	0.16	0.66	11.15	0.36	28.77	2.74	nd	nd	99.58
PX 16r	70	55.41	0.15	0.46	12.02	0.30	28.27	3.18	nd	nd	99.80
PX 20	60	55.30	0.16	0.69	11.78	0.24	28.67	2.74	nd	nd	99.63
PX 21	30	55.72	0.18	0.47	12.15	0.28	28.76	2.54	nd	nd	100.10
PX 22r	30	55.34	0.17	0.38	11.77	0.31	28.69	2.49	nd	nd	99.22
PX 23	20	55.08	0.18	0.64	12.09	0.23	28.46	2.37	nd	nd	99.11
PX 24r	20	55.49	0.14	0.60	12.62	0.22	28.59	2.41	nd	nd	100.10
PX 25	100	55.19	0.20	0.86	12.51	0.27	28.05	2.68	nd	nd	99.77
PX 27	60	55.69	0.13	0.37	12.29	0.33	28.71	2.40	nd	nd	99.95
PX 28	75	55.54	0.15	0.86	12.16	0.18	28.18	2.79	nd	nd	99.87
PX 29	130	55.44	0.18	0.63	11.98	0.23	28.21	2.87	nd	nd	99.54
PX 30r	130	55.49	0.16	0.63	12.46	0.25	28.35	3.00	nd	nd	100.37
PX 31	40	55.55	0.15	0.50	12.41	0.27	27.93	3.50	nd	nd	100.39
PX 33	90	55.02	0.22	0.90	12.59	0.28	28.10	2.48	nd	nd	99.59
PX 34r	90	54.92	0.18	0.77	12.42	0.25	28.47	2.69	nd	nd	99.77

	dist	SiO2	TiO2	Al2O3	FeO	MnO	MgO	CaO	Na2O	K2O	Total	
Cooling-rate experiments:												
R50												
PX 1	70	54.32	0.18	0.60	12.11	0.40	25.28	5.23	nd	nd	98.12	
PX 2	70r	55.00	0.19	0.47	12.44	0.22	26.57	4.64	nd	nd	99.53	
PX 15	GM	52.47	0.73	1.52	11.80	0.23	18.62	13.24	0.25	nd	98.86	
PX 16	GM	52.43	0.66	1.42	11.76	0.23	18.62	13.49	0.15	nd	98.76	
PX 19	GM	51.97	0.61	1.36	12.26	0.34	18.07	13.37	0.24	nd	98.22	
PX 20	GM	51.96	0.63	1.43	12.28	0.33	17.98	13.57	0.15	nd	98.33	
PX 21	GM	51.43	0.91	1.63	11.45	0.23	14.29	18.83	0.35	nd	99.12	
PX 22	GM	51.60	0.92	1.63	11.35	0.25	14.51	18.61	0.32	nd	99.19	
PX 26	GM	51.13	0.80	1.15	15.66	0.30	15.84	13.28	0.28	nd	98.44	
PX	50	56.68	0.16	0.83	13.19	0.29	25.89	3.69	0.26	nd	100.99	
PX 25	GM	51.38	0.72	1.36	15.52	0.36	15.57	13.55	0.24	nd	98.70	
R51												
PX 4	25	54.69	0.18	0.22	15.52	0.24	24.75	3.85	nd	nd	99.45	
PX 8	50	55.01	0.27	0.43	12.33	0.35	25.89	5.10	0.14	nd	99.52	
PX 16	150	51.83	0.72	1.26	13.66	0.27	16.10	14.87	0.21	nd	98.92	
PX 20	280	51.71	0.87	1.32	15.00	0.28	15.03	14.26	0.13	nd	98.60	rim
PX 17	280	53.40	0.37	0.94	13.40	0.28	22.92	6.88	nd	nd	98.19	core
PX 23	GM	52.52	0.62	1.16	13.67	0.40	20.79	8.57	0.15	nd	97.88	
PX 24	GMr	52.73	0.64	1.22	14.11	0.17	21.06	8.75	0.26	nd	98.94	

r designates replicate analyses.

For glass analyses, I, F, X and GM denote interface, fringe limit, crystal limit and groundmass compositions, respectively, as defined in table 3.1

## Enstatite dissolution experiments

	SiO2	TiO2	Al2O3	FeO	MnO	MgO	CaO	Na2O	K2O	Total	
Starting enstatite:											
ENSTATIT	57.38	nd	0.83	4.56	0.10	36.18	0.25	nd	nd	99.30	
PYROPE	42.24	nd	22.24	7.05	0.35	20.18	5.05	nd	nd	97.11	
DIOPSIDE	55.44	nd	1.86	1.62	0.07	19.26	18.69	1.31	nd	98.25	
CHROMITE	0.34	nd	15.72	16.47	0.21	13.02	0.08	nd	nd	45.84	
•											
1130 °C charges											
R88											
OL 190/1	37.36	0.27	0.17	23.37	0.37	36.98	0.44	nd	nd	98.97	
OL 190/2	38.07	nd	nd	22.92	0.44	37.24	0.43	nd	nd	99.22	
OL 190/3	38.38	nd	nd	22.76	0.40	37.75	0.38	nd	nd	99.77	
OL 190/4	38.02	nd	nd	22.68	0.32	37.47	0.47	nd	nd	99.03	
OL 190/5	38.13	0.12	nd	22.13	0.40	37.54	0.46	nd	nd	98.87	
OL 190/6	38.75	0.10	0.13	22.86	0.39	37.95	0.42	nd	nd	100.64	
OL 190/7	38.68	nd	0.19	22.38	0.33	37.54	0.53	nd	nd	99.77	
OL 190/8	38.23	nd	nd	22.67	0.33	38.04	0.43	nd	nd	99.82	
OL 190/9	38.62	nd	nd	22.64	0.35	37.53	0.40	nd	nd	99.73	
OL 190/10	38.36	nd	nd	22.39	0.40	37.64	0.43	nd	nd	99.26	
OL 190/11	38.49	nd	nd	21.83	0.31	37.55	0.51	nd	nd	98.91	
OL 190/13	39.25	nd	nd	17.18	0.27	42.14	0.35	nd	nd	99.22	
OL 190/14	38.20	nd	nd	22.96	0.39	37.32	0.46	nd	nd	99.47	
GL 190/16	50.81	2.84	13.74	12.08	0.21	4.91	8.80	3.22	0.92	97.53	
PX 190 A	57.17	nd	0.81	4.60	nd	36.33	0.28	nd	nd	99.26	enstatite
PX 190 B	57.54	nd	0.86	4.41	0.15	35.40	0.95	nd	nd	99.31	enstatite
R91											
PX 212/5	57.41	nd	1.10	4.13	0.15	33.79	3.73	0.27	nd	100.62	enstatite
PX 212/13	58.03	nd	1.23	5.60	nd	35.07	0.43	0.11	nd	100.64	"
PX 212/6	52.21	0.58	1.45	6.53	0.20	18.58	17.47	0.35	nd	97.38	cpx sheath
PX 212/7	52.27	0.57	1.51	6.66	0.20	18.91	17.65	0.34	nd	98.11	"
PX 212/8	51.55	0.94	2.37	7.16	0.15	16.72	19.67	0.46	nd	99.02	"
PX 212/10	52.15	0.84	2.03	7.11	0.21	17.19	18.96	0.50	nd	99.00	"
PX 212/14	51.08	0.78	2.11	7.15	0.23	17.56	19.29	0.43	nd	98.63	"
PX 212/16	52.61	0.70	1.71	6.14	0.13	17.95	19.10	0.52	nd	98.88	"
PX 212/17	52.32	0.70	1.82	7.23	0.27	17.16	19.09	0.47	nd	99.06	"
PX 212/18	51.08	1.10	2.64	7.22	0.19	15.92	20.42	0.46	nd	99.04	"
PX 212/19	52.84	0.63	1.55	6.78	0.26	17.39	18.71	0.45	nd	98.62	"
PX 212/22	50.76	1.27	2.55	7.75	0.30	16.06	20.16	0.38	nd	99.24	"
PX 211/26	52.79	0.58	1.76	6.74	0.28	18.71	17.80	0.52	nd	99.20	"
PX 211/27	53.38	0.56	1.43	7.00	0.24	19.12	17.76	0.44	nd	99.94	"
OL 212/11	38.75	nd	nd	21.31	0.38	40.14	0.42	nd	nd	101.10	
GL 211/23	52.19	3.60	13.72	11.15	0.25	5.00	8.45	3.09	1.10	98.55	fringe
GL 211/24	52.04	3.48	13.78	11.45	0.24	4.81	8.52	3.11	1.04	98.47	fringe
GL 211/25	52.28	3.49	13.66	11.59	0.27	4.85	8.46	3.12	1.04	98.76	groundmass
GL 212/9	55.74	2.68	14.25	8.95	0.13	4.34	7.41	3.53	1.38	98.41	internal glass
GL 212/12	55.20	2.95	14.25	9.85	0.20	4.37	7.49	2.96	1.42	98.69	"
GL 212/15	55.06	2.86	14.14	9.66	0.24	4.67	7.58	3.09	1.29	98.59	"
GL 212/20	54.48	2.95	14.23	9.69	0.15	4.59	7.82	3.15	1.25	98.31	"
GL 211/21	52.57	3.47	13.78	10.71	0.16	5.04	8.39	3.27	1.07	98.46	"
GL 211/28	61.19	1.80	14.89	6.58	0.19	4.19	5.28	2.59	1.92	98.63	"
GL 211/29	61.84	1.73	15.29	6.42	0.13	3.90	5.45	2.47	1.83	99.06	"
OL 211/11	38.89	nd	nd	17.39	0.30	42.95	0.42	nd	nd	99.97	
•											
1150 °C charges											
R74											
OL 152/2	38.78	nd	nd	18.65	0.40	42.36	0.35	nd	nd	100.56	15
OL 152/3	38.47	nd	nd	19.09	0.40	41.74	0.32	nd	nd	100.17	10
OL 152/4	38.36	nd	nd	19.52	0.39	41.67	0.33	nd	nd	100.36	5
PX 152/6	52.64	0.72	1.72	6.77	0.28	18.83	17.88	0.34	nd	99.20	cpx sheath
OL 152/12	38.52	nd	0.15	17.76	0.30	42.90	0.40	nd	nd	100.19	
PX 152/13	51.58	0.47	1.47	6.78	0.26	20.87	14.88	0.32	nd	96.65	cpx sheath
PX 152/14	55.29	nd	1.19	4.24	0.13	33.86	2.69	0.14	nd	97.59	enstatite
PX 152/16	57.45	nd	0.82	4.78	0.17	36.55	0.22	nd	nd	100.02	enstatite
PX 152/25	53.01	0.42	1.00	7.23	0.19	20.77	14.53	0.25	nd	97.40	cpx sheath
PX 152/26	51.87	0.57	1.43	6.55	0.21	18.97	17.19	0.39	nd	97.19	cpx sheath
PX 152/28	53.44	0.46	1.05	6.71	0.24	20.61	16.10	0.24	nd	98.86	cpx sheath
GL 152/29	59.18	1.99	14.27	6.96	0.10	4.04	6.61	2.69	1.49	97.33	fringe glass
GL 152/30	55.20	2.20	14.63	8.61	0.23	4.48	6.13	3.12	1.19	95.79	"
GL 152/31	52.05	2.26	14.73	7.73	0.20	4.41	7.18	3.00	1.28	92.84	"
GL 152/32	56.02	1.62	14.87	8.38	0.14	4.69	7.10	2.96	0.87	96.65	gm glass
OL 152/21	39.17	nd	nd	18.82	0.27	41.00	0.35	nd	nd	99.69	
OL 152/22	39.55	nd	nd	19.48	0.25	41.20	0.35	nd	nd	100.99	
OL 152/23	39.25	nd	nd	19.61	0.28	41.05	0.30	nd	nd	100.58	
OL 152/24	39.23	nd	nd	19.38	0.25	41.31	0.29	nd	nd	100.54	
OL 192/25	40.08	nd	nd	18.46	0.30	41.66	0.33	nd	nd	100.91	

	SiO2	TiO2	Al2O3	FeO	MnO	MgO	CaO	Na2O	K2O	Total
OL 152/27	39.81	nd	nd	17.94	0.27	42.17	0.32	nd	nd	100.64
OL 152/28	39.65	nd	nd	17.69	0.42	42.15	0.37	nd	nd	100.32
OL 152/29	39.78	nd	nd	18.26	0.26	41.90	0.34	nd	nd	100.55
OL 152/30	39.53	nd	nd	16.57	0.31	43.22	0.29	nd	nd	99.96
OL 152/31	40.02	nd	nd	16.17	0.24	43.25	0.26	nd	nd	99.97
OL 152/32	39.55	nd	nd	16.81	0.35	42.47	0.32	nd	nd	99.55
OL 152/34	39.96	nd	nd	17.63	0.30	42.40	0.42	nd	nd	100.80
OL 152/35	40.05	nd	0.11	17.97	0.26	42.11	0.45	nd	nd	101.03
OL 152/36	39.05	nd	nd	18.07	0.36	41.46	0.33	nd	nd	99.39
OL 152/38	38.54	0.16	0.33	18.84	0.31	40.83	0.37	nd	nd	99.40
OL 152/39	39.46	nd	nd	18.47	0.38	41.77	0.30	nd	nd	100.44
OL 152/40	39.98	nd	nd	18.65	0.22	41.42	0.64	nd	nd	101.08
OL 152/41	39.93	nd	nd	18.64	0.22	41.61	0.43	nd	nd	100.97
OL 152/42	39.57	nd	0.11	18.84	0.27	41.58	0.34	nd	nd	100.79
OL 152/43	39.59	nd	nd	18.75	0.40	41.48	0.28	nd	nd	100.53

R80										
OL 266/1	39.29	nd	nd	18.46	0.30	42.73	0.36	nd	nd	101.14
OL 266/2	39.45	nd	0.23	18.17	0.42	42.03	0.48	nd	nd	100.85
OL 266/5	38.69	nd	nd	20.09	0.34	41.56	0.43	nd	nd	101.16
OL 266/6	38.28	nd	nd	20.41	0.31	41.29	0.40	nd	nd	100.77
OL 266/7	38.41	nd	nd	20.78	0.36	41.01	0.40	nd	nd	101.02
OL 266/8	38.54	0.11	0.20	20.45	0.32	40.83	0.46	nd	nd	100.91
OL 266/9	38.94	0.12	0.63	20.24	0.33	39.72	0.62	0.15	nd	100.75
OL 266/10	38.39	nd	nd	21.49	0.36	40.62	0.36	nd	nd	101.27
OL 266/14	38.87	nd	0.14	20.36	0.27	41.27	0.51	nd	nd	101.51
OL 266/15	38.58	nd	nd	20.12	0.32	41.46	0.37	nd	nd	100.85
OL 266/16	38.92	nd	nd	19.61	0.26	42.13	0.43	nd	nd	101.35
OL 266/17	39.15	nd	nd	18.23	0.32	42.10	0.38	nd	nd	100.22
OL 266/18	38.49	nd	nd	19.14	0.36	41.45	0.37	nd	nd	99.81

1170 °C charges

R110										
GL 282/16	59.40	1.02	14.27	7.68	nd	5.37	5.84	4.00	1.00	98.66
GL 282/17	54.77	1.33	15.37	8.97	0.16	5.45	6.92	4.16	0.82	97.95
GL 282/18	51.00	1.68	15.86	10.04	0.22	6.23	7.56	4.17	0.68	97.44
GL 282/19	49.32	1.89	15.36	11.30	0.18	6.29	8.05	4.10	0.62	97.11
OL 282/1	40.28	nd	nd	14.90	0.24	44.03	0.27	nd	nd	99.72
OL 282/5	40.11	nd	nd	14.24	0.26	44.34	0.26	nd	nd	99.21
OL 282/6	39.79	nd	nd	14.73	0.26	44.10	0.26	nd	nd	99.14
OL 282/7	39.85	nd	nd	15.29	0.24	43.93	0.27	nd	nd	99.58
OL 282/13	39.45	nd	nd	16.25	0.26	43.36	0.32	nd	nd	99.64
OL 282/10	39.76	nd	nd	16.14	0.24	42.52	0.26	nd	nd	98.92
OL 282/4	39.81	nd	nd	14.99	0.33	43.21	0.26	nd	nd	98.60
OL 282/2	39.52	nd	nd	14.73	0.28	43.51	0.23	nd	nd	98.27

R85										
PX 198/1	57.36	nd	0.84	4.58	0.14	36.84	0.24	nd	nd	100.09
GL 198/2	58.57	1.42	14.01	8.62	0.22	4.72	6.90	3.39	1.20	99.05
GL 198/3	56.46	1.57	14.76	9.08	0.16	5.23	7.52	3.38	1.05	99.21
GL 198/4	53.17	1.89	15.17	9.87	0.21	5.67	8.38	3.84	0.92	99.12
GL 198/5	52.56	1.99	15.15	10.05	0.15	5.66	8.57	3.75	0.80	98.68
GL 198/6	52.14	1.93	15.40	10.48	0.18	5.91	8.63	3.85	0.84	99.36
GL 198/7	51.59	2.04	15.34	10.47	0.26	5.68	8.80	3.86	0.86	98.90
GL 198/8	51.66	2.09	15.66	10.90	0.26	6.02	8.71	3.84	0.81	99.95
GL 198/9	51.37	1.98	15.40	11.05	0.19	5.81	8.81	4.04	0.79	99.44
OL 221/10	38.63	nd	nd	17.66	0.31	43.15	0.35	nd	nd	100.10
OL 211/12	38.76	nd	nd	18.89	0.30	42.70	0.32	nd	nd	101.02
OL 211/13	38.77	nd	nd	18.53	0.36	42.54	0.34	nd	nd	100.54
OL 211/14	38.87	nd	nd	18.96	0.22	42.45	0.33	nd	nd	100.83
OL 211/15	38.35	nd	nd	19.22	0.23	41.79	0.34	nd	nd	99.93
OL 211/16	38.85	nd	nd	18.97	0.21	41.92	0.32	nd	nd	100.27
OL 211/17	38.72	nd	nd	19.68	0.34	42.16	0.36	nd	nd	101.35
OL 211/18	38.63	nd	nd	19.20	0.31	42.28	0.34	nd	nd	100.81
OL 211/19	38.08	nd	0.29	20.03	0.25	41.64	0.36	nd	nd	100.70
OL 211/20	38.53	nd	nd	19.80	0.27	41.96	0.46	nd	nd	101.07
OL 211/21	39.18	nd	nd	16.37	0.21	44.35	0.30	nd	nd	100.45
OL 211/22	39.73	nd	nd	14.43	0.26	45.12	0.25	nd	nd	99.79

enstatite  
10  
22 Distance (µm)  
40 from enstatite  
55 surface.  
65  
80  
100  
115

	S102	TiO2	Al2O3	FeO	MnO	MgO	CaO	Na2O	K2O	Total	
1190 °C charges											
R82											
PX 202/1	57.62	nd	0.85	4.58	nd	36.50	0.27	nd	nd	99.92	enstatite
PX 202/4	56.14	nd	0.62	8.06	0.31	32.72	1.64	nd	nd	99.62	"new" opx
PX 202/5	56.29	0.11	0.55	8.44	0.31	32.05	1.54	nd	nd	99.33	"
GL 202/3	50.50	0.36	7.24	10.67	0.24	28.63	2.42	1.49	0.38	101.93	internal glass
GL 202/6	60.08	1.13	14.33	6.66	0.11	5.49	6.40	3.28	1.03	98.51	11
GL 202/7	56.15	1.49	15.28	8.02	0.17	6.19	7.46	3.93	0.77	99.46	48
GL 202/8	54.95	1.48	15.57	8.04	0.20	6.24	7.97	3.85	0.74	99.04	79 Distance (µm)
GL 202/9	52.94	1.58	16.03	8.85	0.12	6.49	8.21	3.84	0.66	98.72	120 from opx
GL 202/10	52.45	1.72	16.20	8.30	0.16	6.74	8.39	3.82	0.63	98.41	150 surface.
GL 202/11	51.49	1.90	16.23	9.00	0.19	6.79	8.70	3.82	0.61	98.73	190
GL 202/12	51.48	1.79	16.30	8.91	0.19	6.75	8.56	3.80	0.63	98.39	215
GL 13	50.80	1.81	16.02	9.29	0.16	6.82	8.94	3.72	0.62	98.18	groundmass
GL 14	50.00	2.05	16.38	9.59	0.18	6.96	9.01	3.47	0.57	98.21	"
GL 15	48.82	2.22	16.27	9.57	0.12	7.03	9.12	3.50	0.58	97.23	"
OL 202/13	39.73	nd	nd	14.99	0.28	44.57	0.27	nd	nd	99.84	
OL 202/14	39.80	nd	nd	14.84	0.26	44.46	0.27	nd	nd	99.63	
OL 202/15	39.72	nd	nd	15.35	0.27	44.38	0.26	nd	nd	99.98	
OL 202/16	39.78	nd	nd	15.32	0.27	43.87	0.28	nd	nd	99.52	
OL 202/17	39.65	nd	nd	15.90	0.24	43.85	0.31	nd	nd	99.95	
OL 202/18	39.49	nd	nd	15.96	0.24	43.89	0.28	nd	nd	99.86	
OL 202/19	39.78	nd	nd	16.07	0.35	43.25	0.41	nd	nd	99.86	
OL 202/20	39.69	nd	nd	16.18	0.21	44.07	0.26	nd	nd	100.41	
OL 202/21	39.33	nd	nd	16.20	0.30	43.38	0.32	nd	nd	99.53	
OL 201/23	39.03	nd	nd	17.57	0.26	42.66	0.32	nd	nd	99.84	
OL 201/24	38.96	nd	nd	17.90	0.20	42.21	0.31	nd	nd	99.58	
R84											
PX 200/2	57.33	nd	0.83	4.52	nd	35.70	0.25	nd	nd	98.75	enstatite
PX 200/3	57.18	nd	0.81	4.47	nd	36.57	0.24	nd	nd	99.42	"
GL 200/4	58.64	1.30	13.64	7.57	0.14	5.19	6.93	3.23	0.95	97.59	6
GL 200/5	57.39	1.40	14.41	8.22	0.12	6.01	7.39	3.48	0.84	99.26	30
GL 200/6	53.73	1.75	15.13	8.97	0.15	6.31	8.19	3.56	0.73	98.52	52 Distance (µm)
GL 200/7	54.38	1.63	14.87	8.44	0.18	6.11	7.92	3.72	0.72	97.97	53 from opx
GL 200/8	51.45	1.90	15.66	9.62	0.18	6.60	8.61	3.67	0.60	98.29	110 surface.
GL 200/9	50.65	2.05	16.00	9.85	0.12	6.75	8.96	3.48	0.58	98.44	155
GL 200/10	50.28	1.98	16.24	10.24	0.13	6.60	9.08	3.57	0.55	98.67	240
OL 200/11	38.62	nd	nd	18.25	0.34	41.73	0.34	nd	nd	99.28	
OL 200/12	38.67	nd	nd	17.75	0.18	41.98	0.30	nd	nd	98.88	
OL 200/13	38.76	nd	0.23	17.62	0.29	41.84	0.37	nd	nd	99.17	
OL 200/14	38.66	0.14	0.60	17.62	0.19	41.96	0.32	nd	nd	99.49	
OL 200/15	39.11	nd	nd	16.37	0.28	42.67	0.29	nd	nd	98.72	
OL 200/16	39.06	nd	nd	16.41	0.27	42.45	0.27	nd	nd	98.46	
OL 200/17	38.87	nd	nd	16.76	0.32	42.73	0.26	nd	nd	98.94	
OL 200/18	39.03	nd	nd	16.86	0.28	42.72	0.30	nd	nd	99.19	
OL 200/19	39.33	nd	nd	16.80	0.25	42.80	0.28	nd	nd	99.52	
OL 200/20	39.16	nd	nd	16.60	0.20	42.70	0.30	nd	nd	98.96	
OL 200/21	38.80	nd	nd	16.50	0.29	43.76	0.27	nd	nd	99.62	
OL 200/22	38.96	nd	nd	15.88	0.22	43.70	0.25	nd	nd	99.01	
OL 200/23	39.18	nd	nd	15.80	0.30	43.84	0.28	nd	nd	99.46	
OL 200/24	38.68	nd	nd	15.09	0.25	43.97	0.26	nd	nd	98.30	
OL 200/25	39.20	nd	nd	16.02	0.32	42.83	0.31	nd	nd	98.68	
OL 200/26	39.44	nd	0.29	16.38	0.20	42.73	0.45	nd	nd	99.58	
OL 200/27	39.37	nd	0.19	16.35	0.14	42.92	0.34	nd	nd	99.31	
OL 200/28	38.73	nd	nd	17.10	0.25	42.81	0.37	nd	nd	99.26	

## Bronzite dissolution experiments

	SiO <sub>2</sub>	TiO <sub>2</sub>	Al <sub>2</sub> O <sub>3</sub>	FeO	MnO	MgO	CaO	Na <sub>2</sub> O	K <sub>2</sub> O	Total	
Starting bronzite:											
BRZ	52.58	0.27	4.64	13.70	0.24	27.67	0.80	nd	nd	99.90	
CPX	48.37	1.62	6.31	4.62	nd	14.23	23.63	0.23	nd	99.10	included phase
AMPH	44.74	1.70	12.19	6.52	nd	18.65	10.15	2.55	nd	96.55	"
SP	nd	nd	58.03	20.40	0.14	13.85	nd	nd	nd	92.42	"
1130 °C charges											
R128											
PX 310/ 2	53.09	0.24	4.80	13.59	0.25	27.34	0.61	nd	nd	99.92	bronzite
PX 310/ 1	55.35	0.27	1.23	11.34	0.21	28.91	2.14	nd	nd	99.49	low-Al bronzite
PX 310/ 3	55.22	0.30	1.46	11.34	0.26	28.76	1.86	nd	nd	99.25	"
PX 310/ 4	53.58	0.48	1.68	8.40	0.27	19.01	15.88	0.36	nd	99.66	new clinopyroxene
PX 310/ 5	53.10	0.62	1.90	7.96	0.23	17.82	17.91	0.37	nd	99.91	"
PX 310/ 6	53.16	0.59	1.75	7.96	0.30	17.71	18.48	0.39	nd	100.34	"
OL 310/20	39.59	nd	nd	18.74	0.35	41.92	0.24	nd	nd	100.84	internal olivine
OL 310/21	39.55	nd	nd	18.34	0.24	41.52	0.25	nd	nd	99.90	"
OL 310/19	39.35	0.12	nd	19.36	0.27	40.05	0.31	nd	nd	99.46	fringe olivine
OL 310/14	39.46	nd	nd	20.20	0.28	40.25	0.34	nd	nd	100.53	"
OL 310/15	39.12	nd	nd	20.75	0.33	39.93	0.31	nd	nd	100.44	"
OL 310/16	39.16	nd	nd	21.96	0.37	39.12	0.33	nd	nd	100.94	"
OL 310/17	38.85	nd	nd	20.79	0.29	38.41	0.38	nd	nd	98.72	"
OL 310/18	38.62	0.10	nd	21.66	0.42	38.54	0.42	nd	nd	99.76	groundmass olivine
GL 310/22	61.98	1.40	14.09	6.86	nd	3.48	5.56	3.64	1.69	98.70	
GL 310/13	61.21	1.48	13.72	6.58	0.14	4.06	5.94	4.37	1.63	99.13	
GL 310/23	58.58	1.80	14.09	8.34	0.15	4.09	6.56	4.10	1.41	99.12	
GL 310/12	56.31	2.03	13.12	8.86	0.15	5.45	7.87	3.96	1.29	99.04	
GL 310/24	54.33	2.41	13.23	9.91	0.15	5.07	7.46	3.80	1.12	97.48	
GL 310/11	53.88	2.30	13.17	10.26	0.19	5.81	7.55	4.23	1.06	98.45	
GL 310/10	52.28	2.26	12.53	9.95	0.21	8.53	6.75	4.06	1.00	97.57	
GL 310/ 9	53.97	2.65	13.49	10.02	0.14	4.66	8.02	4.17	1.14	98.26	
GL 310/ 7	53.14	2.57	13.76	10.38	0.21	4.73	8.08	4.14	1.08	98.09	
GL 310/ 8	52.88	2.72	13.99	10.07	0.14	4.33	8.14	4.21	1.04	97.52	groundmass glass
1150 °C charges											
R112											
GL 288/25	52.98	1.51	15.77	10.85	0.17	5.40	6.71	3.96	0.72	98.07	
GL 288/16	59.03	1.36	13.63	8.69	nd	4.32	5.41	4.25	1.16	97.94	
GL 288/18	55.74	1.63	14.30	10.12	0.16	4.79	6.28	4.53	0.97	98.52	
GL 288/19	53.39	1.91	14.52	10.76	0.15	5.06	7.17	4.33	0.88	98.17	
GL 288/20	52.58	2.07	14.80	11.12	0.18	5.22	7.31	4.28	0.83	98.39	
GL 288/21	62.49	0.98	14.19	6.80	0.10	4.56	4.57	3.46	1.37	98.52	
GL 288/22	62.61	0.93	14.76	6.77	0.12	3.68	4.41	3.73	1.36	98.37	
OL 288/2	39.16	nd	nd	19.29	0.30	40.81	0.25	nd	nd	99.81	
OL 288/3	39.13	nd	nd	20.49	0.37	40.59	0.28	nd	nd	100.86	
OL 288/5	38.81	nd	nd	21.66	0.32	39.21	0.29	nd	nd	100.29	
OL 288/6	38.73	nd	nd	21.92	0.35	39.15	0.32	nd	nd	100.47	
OL 288/7	38.78	nd	nd	21.87	0.39	38.99	0.35	nd	nd	100.38	
OL 288/8	38.56	nd	nd	22.50	0.45	38.80	0.33	nd	nd	100.64	
OL 288/9	38.87	nd	nd	22.43	0.33	38.87	0.38	nd	nd	100.88	
OL 288/10	38.76	nd	nd	21.88	0.34	38.90	0.34	nd	nd	100.22	
OL 288/11	38.59	nd	nd	22.31	0.31	38.70	0.41	nd	nd	100.32	
OL 288/12	38.71	nd	nd	22.10	0.29	38.62	0.36	nd	nd	100.08	
OL 288/13	38.84	nd	nd	22.55	0.38	38.77	0.37	nd	nd	100.91	
OL 288/14	38.57	nd	nd	22.25	0.32	38.67	0.39	nd	nd	100.20	
PX 288/15	52.84	0.26	4.38	13.97	0.25	27.85	0.87	nd	nd	100.43	bronzite
PX 288/23	55.33	0.25	2.00	11.78	0.31	28.89	1.95	0.17	nd	100.72	low-Al bronzite
PX 288/24	54.92	0.24	1.71	11.97	0.22	29.61	1.66	nd	nd	100.39	"
R77											
GL 165/15	57.14	1.66	13.99	9.00	0.16	4.32	5.93	4.34	1.02	97.56	
GL 165/16	56.97	1.65	14.09	9.17	0.20	4.40	5.85	4.50	0.98	97.81	
GL 165/17	53.74	1.96	14.79	10.09	0.15	4.77	6.75	4.20	0.81	97.26	
GL 165/18	53.28	2.08	14.83	10.16	0.17	5.04	6.62	4.57	0.83	97.58	
GL 165/19	50.41	2.78	14.36	11.12	0.23	5.43	7.35	5.16	0.68	97.52	groundmass glass
OL 165/1	38.31	nd	nd	19.24	0.30	41.75	0.27	nd	nd	99.87	
OL 165/2	38.77	nd	nd	19.48	0.32	41.45	0.27	nd	nd	100.29	
OL 165/4	38.46	nd	nd	20.29	0.36	39.85	0.28	nd	nd	99.24	
OL 165/5	38.59	nd	nd	21.11	0.35	39.75	0.34	nd	nd	100.14	
OL 165/6	38.33	nd	nd	21.18	0.35	39.55	0.33	nd	nd	99.74	
OL 165/7	38.44	nd	nd	21.18	0.31	39.76	0.28	nd	nd	99.97	
OL 165/8	38.38	nd	nd	21.00	0.37	39.48	0.35	nd	nd	99.58	
OL 165/9	38.55	nd	nd	21.11	0.32	39.27	0.34	nd	nd	99.59	
OL 165/11	38.37	nd	nd	21.09	0.29	39.43	0.32	nd	nd	99.5	
OL 165/13	38.30	nd	nd	22.80	0.40	38.73	0.43	nd	nd	100.66	
OL 164/12	37.95	nd	nd	21.61	0.34	39.27	0.37	nd	nd	99.54	
OL 164/14	38.24	nd	nd	20.94	0.34	39.44	0.38	nd	nd	99.34	

	SiO2	TiO2	Al2O3	FeO	MnO	MgO	CaO	Na2O	K2O	Total	
R111											
OL 283/1	39.60	nd	nd	17.55	0.25	43.07	0.26	nd	nd	100.73	
OL 283/2	39.34	nd	nd	16.75	0.17	43.18	0.31	nd	nd	99.75	
OL 283/3	39.50	nd	nd	16.98	0.23	42.45	0.42	nd	nd	99.58	
OL 283/4	39.44	nd	nd	18.49	0.24	42.04	0.27	nd	nd	100.48	
OL 283/5	39.11	nd	nd	19.60	0.27	40.80	0.29	nd	nd	100.07	
OL 283/6	39.66	nd	nd	20.28	0.21	41.63	0.29	nd	nd	102.07	
1170 °C charges											
R86											
GL 196/4	63.07	1.03	13.78	7.37	0.10	4.22	5.09	2.78	1.29	98.73	internal glass
GL 196/5	62.15	0.95	13.72	8.19	0.11	4.48	5.84	2.64	1.27	99.35	"
GL 196/7	59.33	1.31	13.66	8.49	0.19	4.86	6.35	3.05	1.14	98.38	fringe glass
GL 196/8	58.57	1.41	13.88	8.99	0.13	4.95	6.70	3.18	1.10	98.91	"
GL 192/9	58.66	1.35	13.86	9.48	0.22	4.88	6.82	3.04	1.08	99.39	10
GL 192/10	58.78	1.36	13.84	9.06	0.17	4.90	6.68	3.26	1.12	99.17	10 distance (µm)
GL 192/11	55.90	1.60	14.72	9.67	0.18	5.32	7.41	3.64	0.93	99.37	75 from bronzite
GL 192/13	52.78	1.84	15.39	10.71	0.23	5.53	8.08	3.82	0.86	99.24	120 surface.
GL 192/14	53.95	1.76	15.32	10.15	0.20	5.39	8.14	3.96	0.84	99.71	155
GL 192/15	52.58	1.74	15.87	11.03	0.19	5.52	8.41	4.07	0.86	100.27	200
GL 192/16	51.83	1.96	15.74	10.52	0.21	5.66	8.51	4.08	0.77	99.28	220
GL 192/17	51.13	2.05	15.91	10.48	0.16	5.73	8.51	4.03	0.80	98.80	255 groundmass
GL 192/20	51.15	1.94	16.14	10.79	0.31	5.17	8.76	3.86	0.76	98.88	265
GL 192/21	51.11	1.94	15.89	11.00	0.12	5.59	8.74	3.79	0.78	98.96	265
PL 192/18	50.75	0.12	30.68	0.89	nd	0.14	13.85	3.52	0.13	100.08	
PL 192/19	51.56	0.10	30.76	0.88	nd	0.12	13.40	3.69	0.10	100.62	
OL 192/21	38.96	nd	nd	19.83	0.34	40.53	0.30	nd	nd	99.96	
OL 192/22	38.71	nd	nd	20.20	0.30	40.19	0.31	nd	nd	99.76	
OL 192/23	38.57	nd	nd	20.23	0.32	39.98	0.30	nd	nd	99.40	
OL 192/24	38.26	nd	nd	20.20	0.31	39.93	0.30	nd	nd	99.00	
OL 192/25	38.49	nd	nd	20.39	0.34	40.22	0.29	nd	nd	99.73	
OL 192/26	38.43	nd	nd	20.92	0.34	39.43	0.31	nd	nd	99.43	
OL 192/27	38.79	nd	nd	20.43	0.26	39.66	0.29	nd	nd	99.43	
OL 192/30	38.43	nd	nd	20.72	0.35	39.60	0.38	nd	nd	99.48	
OL 192/28	38.53	nd	nd	21.23	0.29	39.50	0.31	nd	nd	99.86	
OL 192/29	37.96	0.12	0.55	20.85	0.31	38.99	0.36	nd	nd	99.14	
OL 192/31	38.42	nd	nd	20.63	0.35	39.31	0.35	nd	nd	99.06	
OL 192/32	38.26	nd	nd	20.63	0.36	39.40	0.40	nd	nd	99.11	
OL 192/33	38.55	nd	nd	20.66	0.34	39.15	0.32	nd	nd	99.07	
OL 192/34	37.91	nd	nd	21.59	0.39	38.38	0.38	nd	nd	98.65	
OL 192/35	38.19	nd	nd	21.46	0.29	38.10	0.42	nd	nd	98.46	
PX 196/2	52.74	0.28	4.87	14.06	0.33	27.79	0.67	nd	nd	100.74	bronzite
PX 196/1	54.86	0.21	1.47	11.43	0.20	29.57	2.01	nd	nd	99.79	low-Al bronzite
PX 196/6	55.27	0.23	1.45	10.97	0.21	29.84	2.06	nd	nd	100.08	"
PX 196/3	49.14	1.35	5.18	4.61	nd	15.24	23.06	0.20	nd	98.84	exsolved cpx
R96											
PX 208/2	52.06	0.39	4.52	13.27	0.25	27.16	1.83	nd	nd	99.48	bronzite
PX 208/12	52.72	0.26	4.57	13.52	0.24	27.79	0.64	nd	nd	99.76	"
PX 208/1	55.35	0.23	1.14	10.18	0.16	29.98	1.97	nd	nd	99.06	low-Al bronzite
PX 208/11	56.11	0.14	0.73	10.94	0.22	30.18	1.91	nd	nd	100.29	"
GL 208/8	63.46	1.01	14.29	7.24	0.12	4.58	5.50	2.91	1.03	100.14	internal glass
GL 208/9	62.30	1.07	14.15	7.10	nd	4.77	5.68	2.93	0.91	98.98	"
GL 208/10	62.85	1.04	14.32	6.90	nd	4.43	5.62	2.96	1.00	99.21	"
GL 208/3	59.91	1.22	14.22	8.09	0.13	4.83	6.64	3.32	1.13	99.49	
GL 208/4	55.53	1.46	15.38	9.31	0.20	5.36	7.73	3.79	0.88	99.64	
GL 208/5	52.73	1.83	15.86	9.65	0.13	5.76	8.34	3.96	0.72	98.98	
GL 208/6	52.86	1.72	16.08	10.00	0.13	5.62	8.24	3.86	0.76	99.27	
GL 208/7	51.43	1.98	16.40	10.68	0.14	6.00	8.83	3.82	0.74	100.02	groundmass glass
OL 208/13	39.46	nd	nd	17.76	0.29	42.70	0.25	nd	nd	100.46	
OL 208/14	38.85	nd	nd	18.22	0.24	41.65	0.26	nd	nd	99.22	
OL 208/15	38.73	nd	nd	19.87	0.32	41.13	0.31	nd	nd	100.36	
OL 208/16	39.14	nd	nd	19.42	0.30	40.91	0.30	nd	nd	100.07	
OL 208/17	38.51	nd	nd	19.72	0.25	40.65	0.29	nd	nd	99.42	
OL 208/18	37.98	nd	nd	20.09	0.24	39.66	0.33	nd	nd	98.30	
OL 208/19	38.32	nd	0.12	19.58	0.28	40.31	0.32	nd	nd	98.98	
OL 208/20	38.38	nd	0.11	19.82	0.27	40.29	0.37	nd	nd	99.29	
OL 208/21	38.32	nd	nd	20.27	0.37	39.30	0.40	nd	nd	98.72	
OL 208/23	38.34	nd	nd	20.63	0.37	39.69	0.41	nd	nd	99.49	
OL 208/24	38.35	nd	nd	20.04	0.27	39.86	0.47	nd	nd	99.07	
OL 208/25	38.22	nd	0.12	21.04	0.34	38.90	0.42	nd	nd	99.12	
OL 208/26	38.03	nd	nd	20.93	0.35	38.83	0.42	nd	nd	98.56	
OL 208/27	38.03	nd	nd	20.87	0.35	38.59	0.43	nd	nd	98.34	
OL 208/28	38.88	nd	nd	17.79	0.22	41.66	0.31	nd	nd	98.86	
OL 208/29	39.47	nd	nd	18.16	0.28	42.02	0.29	nd	nd	100.22	

	SiO2	TiO2	Al2O3	FeO	MnO	MgO	CaO	Na2O	K2O	Total	
1190 °C charges											
GL 254/16	63.52	0.87	13.09	7.35	0.12	5.41	5.58	3.30	1.21	100.45	internal glass
GL 254/17	59.79	1.14	13.08	8.43	0.10	5.60	6.54	4.12	1.04	99.84	fringe glass
GL 254/18	58.89	1.21	13.86	8.56	0.18	6.44	6.71	4.27	0.99	101.11	"
GL 254/19	54.40	1.50	15.01	9.49	0.15	6.15	7.81	4.46	0.83	99.80	"
GL 254/20	52.72	1.69	15.40	9.58	0.14	6.00	8.41	3.85	0.72	98.51	"
GL 254/21	51.01	1.79	16.07	10.25	0.16	6.53	8.86	4.14	0.70	99.51	groundmass glass
GL 254/22	49.54	2.10	16.56	10.20	0.20	6.67	9.06	3.87	0.61	98.81	"
GL 254/23	49.04	1.96	16.66	10.54	0.24	6.74	9.13	3.28	0.59	98.18	"
PX 256/12	52.84	0.28	4.76	13.76	0.22	27.57	1.15	nd	nd	100.58	bronzite
PX 256/14	56.35	0.15	0.69	11.01	0.22	30.06	1.81	nd	nd	100.34	low-Al bronzite
OL 254/1	40.80	nd	nd	18.24	0.24	43.23	0.26	nd	nd	102.77	internal olivine
OL 254/2	39.70	nd	nd	18.50	0.24	42.09	0.22	nd	nd	100.75	"
OL 254/3	39.15	nd	nd	18.49	0.23	41.52	0.21	nd	nd	99.60	"
OL 254/4	39.74	nd	nd	18.15	0.18	41.94	0.25	nd	nd	100.26	"
OL 254/5	39.81	nd	nd	18.25	0.24	42.12	0.25	nd	nd	100.67	22
OL 254/6	39.90	nd	nd	18.63	0.27	41.88	0.27	nd	nd	101.01	76
OL 254/7	39.35	nd	nd	18.66	0.25	41.37	0.25	nd	nd	99.88	163
OL 254/8	39.10	nd	nd	18.51	0.30	41.82	0.28	nd	nd	100.01	250
OL 254/10	39.28	nd	nd	18.97	0.28	41.25	0.41	nd	nd	100.26	387
OL 254/11	39.44	nd	nd	18.43	0.26	41.76	0.34	nd	nd	100.23	493
R94											
PX 207/4	52.81	0.25	4.39	12.96	0.29	27.89	0.57	nd	nd	99.16	bronzite
PX 207/5	55.80	0.17	0.74	10.82	0.29	30.48	1.49	nd	nd	99.87	low-Al bronzite
PX 207/6	56.10	0.18	0.63	9.36	0.15	30.79	2.36	nd	nd	99.61	"
GL 207/7	62.97	0.96	13.81	7.04	0.15	4.95	5.33	2.54	1.06	98.81	internal olivine
OL 207/8	39.76	nd	nd	17.68	0.15	43.14	0.25	nd	nd	101.05	"
PX 207/9	53.44	0.25	4.31	13.30	0.22	28.32	0.61	nd	nd	100.47	bronzite
OL 207/18	38.65	nd	nd	17.24	0.33	42.83	0.30	nd	nd	99.44	internal olivine
OL 207/19	38.43	nd	nd	17.57	0.32	42.81	0.28	nd	nd	99.47	"
OL 207/20	38.53	nd	nd	17.56	0.24	43.01	0.27	nd	nd	99.72	"
OL 207/21	38.67	nd	nd	17.37	0.20	43.15	0.31	nd	nd	99.81	18
OL 207/22	38.44	nd	nd	17.54	0.25	42.74	0.33	nd	nd	99.38	41
OL 207/23	39.30	nd	nd	17.93	0.26	43.19	0.26	nd	nd	101.00	68
OL 207/24	38.89	nd	nd	17.38	0.32	42.79	0.29	nd	nd	99.78	106 distance
OL 207/25	38.80	nd	nd	17.33	0.27	42.80	0.29	nd	nd	99.57	68 from bronzite
OL 207/26	38.84	nd	nd	18.08	0.19	42.72	0.25	nd	nd	100.17	247 surface.
OL 207/27	38.39	nd	nd	17.99	0.29	42.59	0.31	nd	nd	99.63	306
OL 207/28	38.85	nd	nd	17.50	0.25	42.37	0.32	nd	nd	99.43	353
OL 207/29	38.48	nd	nd	17.96	0.27	42.03	0.40	nd	nd	99.26	415
OL 207/30	38.13	nd	nd	21.17	0.39	39.07	0.45	nd	nd	99.32	465 (core)
OL 207/31	39.01	nd	nd	18.00	0.31	42.49	0.41	nd	nd	100.31	(rim of #30)
OL 207/32	39.21	nd	nd	17.34	0.25	43.53	0.28	nd	nd	100.70	182
OL 207/33	39.31	nd	nd	17.01	0.19	43.62	0.33	nd	nd	100.54	15
GL 207/34	61.81	0.94	14.10	7.60	0.12	5.03	5.42	2.51	0.94	98.47	internal glass
GL 207/40	59.23	1.14	13.81	8.27	0.17	5.57	6.72	3.56	0.92	99.39	15
GL 207/43	58.00	1.32	14.31	8.65	0.13	6.03	6.98	3.05	0.87	99.34	50
GL 207/44	54.50	1.44	15.26	9.37	0.13	6.17	7.66	3.87	0.66	99.06	80 distance (µm)
GL 207/45	51.43	1.67	16.26	10.43	0.15	6.85	8.51	3.80	0.59	99.69	180 from bronzite
GL 207/49	50.10	1.81	16.75	10.94	0.18	6.77	8.97	3.79	0.56	99.87	280 surface.
GL 207/47	49.98	1.90	16.80	10.87	0.16	6.87	8.87	3.60	0.55	99.60	350
GL 207/48	49.63	1.99	16.97	10.32	0.17	6.81	9.14	3.68	0.51	99.22	420
GL 207/50	49.81	1.99	16.86	10.81	0.22	6.94	9.13	3.77	0.54	100.07	500
PX 207/36	52.19	0.29	4.50	13.81	0.20	27.69	0.95	nd	nd	99.68	bronzite
PX 207/41	51.86	0.28	4.76	13.55	0.22	27.41	1.04	nd	nd	99.12	"
PX 207/42	52.16	0.28	4.70	14.11	0.20	27.67	0.69	nd	nd	99.84	"
PX 207/35	55.19	0.19	0.71	10.06	0.18	30.44	2.18	nd	nd	99.01	low-Al bronzite
PX 207/37	55.05	0.17	0.70	10.35	0.17	30.09	1.90	nd	nd	98.47	"
PX 207/38	54.72	0.20	0.85	11.47	0.25	29.91	1.57	nd	nd	99.04	"
PX 207/39	55.44	0.19	0.78	11.11	0.31	29.97	1.68	nd	nd	99.53	"

## Natural samples

#	SiO2	TiO2	Al2O3	FeO	MnO	MgO	CaO	Na2O	K2O	Total
BM16, fringe pyroxenes (1 = close to quartz, 3 = close to groundmass)										
PX1 13	53.21	0.23	nd	10.27	0.29	11.70	23.49	0.61	nd	99.84
PX1 14	53.53	0.49	0.53	15.97	0.43	8.16	19.65	2.31	0.48	101.55
PX1 22	52.87	0.34	nd	11.58	0.32	10.88	22.88	0.96	nd	99.93
PX1 23	52.51	0.71	0.20	16.80	0.47	7.21	18.07	3.85	0.10	99.92
PX1 24	52.70	0.25	nd	11.83	0.48	10.28	22.87	0.96	nd	99.43
PX1 25	53.61	0.20	nd	7.98	0.41	13.21	24.31	0.45	nd	100.20
PX1 26	53.51	0.27	nd	8.87	0.33	13.15	23.65	0.54	nd	100.35
PX1 30	53.36	0.17	nd	8.44	0.17	13.08	23.69	0.56	nd	99.57
PX1 31	52.29	0.32	nd	13.15	0.40	9.49	22.05	1.59	nd	99.41
PX1 34	52.53	0.31	nd	10.66	0.44	11.65	22.95	0.81	nd	99.45
PX1 42	53.17	0.24	0.12	8.74	0.19	13.15	23.62	0.61	nd	99.90
PX1 43	53.26	0.27	nd	8.98	0.18	12.84	23.90	0.49	nd	99.95
PX1 52	53.43	0.38	0.11	8.66	0.29	12.47	23.27	0.44	nd	99.13
PX1 61	53.54	0.16	nd	8.24	0.31	13.42	22.93	0.29	nd	98.92
PX2 15	52.89	0.35	0.60	9.34	0.30	12.76	22.46	0.73	0.14	99.57
PX2 16	53.45	0.17	nd	9.72	0.40	12.13	23.56	0.73	nd	100.23
PX2 17	53.64	0.22	nd	8.16	0.24	13.45	23.76	0.43	nd	99.94
PX2 28	53.41	0.20	nd	9.02	0.22	13.34	23.73	0.59	nd	100.58
PX2 29	53.59	0.30	nd	9.00	0.39	12.85	23.53	0.45	nd	100.21
PX2 32	52.31	0.30	0.11	12.60	0.49	10.08	22.11	1.03	nd	99.11
PX2 45	53.48	0.24	nd	8.70	0.25	13.23	24.05	0.52	nd	100.55
PX2 46	53.43	0.22	nd	8.73	0.29	12.99	24.02	0.40	nd	100.13
PX2 47	53.50	0.28	0.28	8.44	0.26	13.11	23.48	0.60	nd	99.97
PX2 48	53.65	0.27	0.10	9.44	0.28	12.95	23.91	0.61	nd	101.23
PX2 54	53.14	0.27	0.13	9.55	0.23	12.99	23.64	0.44	nd	100.41
PX2 58	53.19	0.20	0.12	8.80	0.37	13.25	23.40	0.41	nd	99.76
PX2 59	53.57	0.27	0.22	8.81	0.26	13.42	23.31	0.46	nd	100.36
PX3 7	51.23	1.55	2.23	6.29	0.22	14.17	23.18	0.63	nd	99.57
PX3 8	52.42	1.23	1.44	6.12	0.32	14.62	23.49	0.56	nd	100.29
PX3 9	52.59	0.12	1.23	10.34	0.41	11.57	22.79	0.75	0.12	99.92
PX3 10	52.01	0.17	1.68	11.20	0.33	11.05	22.79	0.95	0.17	100.35
PX3 11	53.19	0.13	1.42	7.70	0.34	12.45	23.20	0.80	0.10	99.33
PX3 21	51.62	1.28	1.74	6.28	0.14	13.30	23.65	0.71	nd	98.79
PX3 35	50.37	0.55	0.63	6.99	0.20	12.73	25.41	0.54	0.13	97.55
PX3 36	47.35	3.80	4.16	7.93	0.11	12.37	22.73	0.88	nd	99.39
PX3 49	53.18	0.83	0.97	7.05	0.26	14.12	23.89	0.69	0.10	101.09
PX3 50	52.85	0.77	1.08	6.52	0.22	13.97	23.98	0.62	nd	100.08
PX3 62	52.19	0.92	1.35	6.18	0.23	14.12	23.40	0.40	nd	98.88
PX1 CORE	52.48	0.17	nd	9.68	0.23	12.55	23.22	0.65	nd	99.04
PX1 RIM	52.97	0.21	nd	8.61	0.28	13.30	23.57	0.51	nd	99.50
Groundmass pyroxene analyses:										
PX 1	47.69	2.00	5.83	6.26	nd	13.46	23.41	0.20	nd	98.97
PX 2	43.66	3.68	9.33	7.89	nd	11.52	23.67	0.38	nd	100.21
PX 3	40.60	4.81	12.51	8.43	0.16	10.00	23.08	0.61	nd	100.23
PX 4	39.68	5.03	11.84	8.04	0.11	10.15	23.38	0.38	nd	98.61
PX 5	47.83	2.30	6.08	6.14	0.17	13.37	23.24	0.29	nd	99.46
PX 6	42.95	4.02	9.93	7.70	nd	11.28	23.62	0.34	nd	99.89
PX 7	41.96	3.94	11.01	7.84	nd	10.83	23.54	0.30	nd	99.49
PX 8	40.22	4.78	11.96	7.59	nd	9.99	23.59	0.34	nd	98.60
PX 9	40.01	4.88	12.23	8.26	nd	10.14	23.77	0.31	nd	99.70
PX 10	48.13	2.13	5.37	6.04	nd	13.68	23.85	0.29	nd	99.54
PX 11	46.30	2.83	7.32	7.01	0.13	12.75	23.54	0.34	nd	100.22
PX 12	45.81	3.24	7.33	7.73	0.15	12.44	23.97	0.17	nd	100.85
PX 13	46.68	2.67	6.74	7.59	nd	12.83	23.68	0.34	nd	100.62
PX 14	42.02	4.72	11.14	7.85	0.11	10.34	23.69	0.41	nd	100.28
PX 15	41.00	4.70	11.69	8.47	0.10	10.67	23.74	0.30	nd	100.67
PX 16	42.14	4.42	10.58	8.02	0.16	10.59	23.86	0.38	nd	100.19
PX 17	39.61	5.48	12.80	9.30	0.10	9.45	23.33	0.52	nd	100.64
PX 65	47.50	2.23	5.97	6.13	nd	13.61	23.33	0.23	nd	99.04

	t	dist	SiO2	TiO2	Al2O3	FeO	MnO	MgO	CaO	Na2O	K2O	Total
H74389												
PX	A	10	52.85	0.59	0.44	11.20	0.13	14.48	19.41	0.27	nd	99.40
PX	B	10	52.71	0.49	0.37	12.51	0.30	14.92	17.11	0.21	nd	98.65
PX	C	10	52.91	0.46	0.39	11.50	0.30	14.81	18.83	0.36	nd	99.60
PX	A	30	52.40	0.58	0.40	11.24	0.28	14.40	19.25	0.36	nd	98.94
PX	A	20	53.46	0.49	0.57	11.86	0.35	14.90	18.33	0.13	nd	100.09
PX	A	40	53.38	0.49	0.42	12.93	0.31	15.72	16.67	0.18	nd	100.11
PX	B	40	53.10	0.54	0.44	12.49	0.24	15.42	18.03	0.15	nd	100.43
PX	B	30	52.78	0.52	0.36	12.56	0.19	15.17	17.63	0.12	nd	99.37
PX	D	10	52.98	0.48	0.45	11.40	0.29	14.23	18.95	0.44	nd	99.26
PX	B	20	52.64	0.50	0.45	11.61	0.27	14.59	18.68	0.25	nd	99.01
PX	A	GM	52.87	0.39	0.56	21.65	0.40	19.95	3.52	nd	nd	99.43
PX	B	GM	52.00	0.88	1.20	11.49	0.28	14.57	18.10	0.26	nd	98.85
PX	C	GM	52.69	0.54	0.50	21.44	0.49	19.59	4.26	nd	nd	99.57
PX	D	GM	50.18	1.34	2.32	13.08	0.25	14.00	17.55	0.44	nd	99.20
PX	E	GM	51.32	0.75	1.19	11.99	0.24	14.28	18.20	0.90	nd	98.90
PX	F	GM	52.54	0.78	1.40	12.13	0.28	14.44	17.67	0.37	nd	99.65
PX	1	XC	51.70	0.66	3.19	7.25	0.20	17.06	19.36	0.32	nd	99.74
PX	2	XC	52.13	0.53	2.84	6.88	0.24	17.49	18.83	0.21	nd	99.17
PX	3	XC	52.47	0.45	2.42	7.20	0.18	17.52	18.91	0.22	nd	99.37
PX	4	XC	51.84	0.56	2.80	8.64	0.27	17.70	17.79	0.24	nd	99.85
H100426												
PX	A	20	54.74	0.11	0.27	8.83	0.31	16.16	20.36	0.23	nd	101.04
PX	B	20	53.21	0.14	0.48	8.40	0.22	15.45	20.20	0.17	nd	98.29
PX	A	70	51.98	0.45	2.46	8.31	0.25	15.79	19.65	0.31	nd	99.20
PX	B	70	51.83	0.35	2.79	7.43	0.29	15.94	20.03	0.21	nd	98.88
PX	A	50	53.27	0.35	0.85	11.53	0.33	15.01	18.51	0.30	nd	100.17
PX	B	50	53.17	0.35	1.09	11.10	0.26	14.75	18.37	0.11	nd	99.22
PX	A	15	53.08	0.40	0.64	12.84	0.44	17.97	13.83	0.23	nd	99.43
PX	A	80	52.41	0.52	1.37	11.07	0.30	15.55	17.97	0.23	nd	99.42
PX	A	60	52.87	0.18	0.75	9.03	0.23	16.13	19.14	0.15	nd	98.53
PX	A	30	52.76	0.51	0.82	10.84	0.29	15.38	18.44	0.26	0.10	99.40
PX	A	GM	53.29	0.31	0.59	18.44	0.50	21.77	4.34	nd	nd	99.25
PX	B	GM	53.31	0.35	0.69	19.43	0.59	20.45	4.01	nd	nd	98.89
PX	C	GM	54.52	0.37	0.89	18.84	0.61	21.47	4.08	nd	nd	100.91
PX	D	GM	54.76	0.32	0.64	19.37	0.51	21.15	4.32	nd	nd	101.16
PX	E	GM	52.18	0.38	3.25	20.57	0.47	18.51	2.79	0.24	nd	98.43
PX	F	GM	53.70	0.36	0.80	17.94	0.47	21.70	4.04	0.11	nd	99.14
PX	G	GM	53.60	0.38	0.83	18.43	0.36	21.57	3.88	0.10	nd	99.15
PX	H	GM	53.14	0.46	0.61	19.26	0.45	20.51	4.53	nd	nd	98.98
H100428												
PX	A	70	53.86	0.22	0.57	6.65	0.24	17.81	19.74	0.20	nd	99.29
PX	A	20	54.40	0.11	0.20	6.70	0.24	16.41	21.49	0.19	nd	99.77
PX	A	100	53.56	0.12	0.58	6.63	0.18	18.06	19.59	0.21	nd	98.93
PX	B	100	52.25	0.30	2.00	6.37	0.30	17.05	19.97	0.29	nd	98.53
PX	A	25	53.29	0.22	0.58	8.68	0.33	16.76	19.41	0.10	nd	99.37
PX	A	80	53.95	0.14	0.31	6.81	0.16	16.82	20.55	0.22	nd	98.99
PX	B	80	53.89	0.14	0.40	6.86	0.29	17.21	20.55	0.27	nd	99.64
PX	C	100	53.86	nd	0.28	7.11	0.17	19.28	18.18	0.12	nd	99.09
PX	A	160	54.05	0.10	0.13	6.22	0.17	16.48	22.23	0.15	nd	99.56
PX	A	180	52.74	0.26	1.15	6.49	0.19	16.37	20.97	0.23	nd	98.42
PX	B	80	53.80	nd	0.22	6.13	nd	16.68	21.30	0.20	nd	98.48
PX	B	150	53.46	0.10	0.48	6.71	0.20	17.36	19.92	0.10	nd	98.36
PX	C	150	53.41	nd	0.50	6.17	0.25	17.35	20.54	0.25	nd	98.54
PX	A	110	54.10	0.20	0.27	7.20	0.26	18.28	19.06	0.29	nd	99.67
PX	A	GM	53.31	0.25	1.59	13.55	0.42	27.54	2.15	nd	nd	98.85
PX	B	GM	48.38	1.05	5.12	7.73	0.20	15.47	19.86	0.32	nd	98.16
PX	C	GM	54.78	0.16	1.16	12.20	0.33	28.53	1.68	nd	nd	98.84
PX	D	GM	55.17	0.21	0.67	13.23	0.29	28.37	1.88	nd	nd	99.85
PX	E	GM	54.22	0.35	0.66	16.19	0.40	24.64	2.31	nd	nd	98.88
H100429												
PX	A	50	53.17	0.32	0.47	9.22	0.33	16.18	18.12	0.27	nd	98.17
GL	A	GM	51.37	nd	27.42	1.00	nd	0.18	11.83	4.27	nd	96.18
PX	A	60	53.59	0.16	0.36	8.23	0.20	16.66	18.84	0.21	nd	98.27
PX	A	150	52.83	0.32	1.47	8.60	0.26	18.41	17.06	0.14	nd	99.11
PX	B	150	52.96	0.28	1.40	8.41	0.35	18.41	17.22	nd	nd	99.15
PX	C	150	52.40	0.27	1.55	8.65	0.30	18.39	16.87	0.26	nd	98.69
PX	D	150	52.79	0.36	1.50	8.37	0.30	18.36	16.68	0.19	nd	98.55
PX	A	25	53.82	0.18	0.27	8.69	0.22	16.91	19.42	0.17	nd	99.70
PX	B	50	53.99	0.28	1.27	9.61	0.34	15.40	17.27	0.38	0.32	98.86
PX	A	130	51.68	0.54	1.69	11.72	0.22	16.38	15.96	0.33	nd	98.55
PX	A	140	50.81	0.61	3.20	8.42	0.22	16.16	18.88	0.20	nd	98.50
PX	A	90	53.01	0.25	0.53	7.97	0.27	16.94	19.26	0.12	nd	98.39
PX	B	130	51.67	0.52	1.43	10.90	0.35	17.08	16.83	0.23	nd	99.02
PX	C	130	51.55	0.43	1.47	10.97	0.35	17.20	16.83	0.22	nd	99.03

glass

	t	dist	SiO2	TiO2	Al2O3	FeO	MnO	MgO	CaO	Na2O	K2O	Total
PX A	80		52.89	0.26	0.51	7.93	0.38	16.78	18.81	0.23	nd	97.84
PX C	50		53.15	0.15	0.27	8.33	0.22	16.01	20.45	0.25	nd	98.89
PX A	100		51.10	0.57	2.76	10.28	0.27	16.18	17.41	0.19	nd	98.78
PX B	100		50.85	0.61	2.92	10.34	0.20	15.90	17.27	0.19	nd	98.29
PX 36			52.06	0.39	1.53	9.84	0.27	16.79	17.82	0.20	nd	98.90
PX 37			51.98	0.41	1.66	9.71	0.41	16.83	17.77	0.31	nd	99.10
PX C	GM		51.37	0.41	1.84	9.89	0.26	16.17	17.64	0.25	nd	97.86
H106444												
PX 1			53.46	0.21	0.67	7.68	0.20	15.90	20.62	0.28	nd	99.02
PX 2			53.93	0.24	1.05	6.68	0.22	17.04	20.57	0.28	nd	100.01
PX 3			51.82	0.51	3.90	5.85	0.12	16.64	20.39	0.29	nd	99.52
GL 4			83.48	0.24	6.54	1.82	nd	0.45	0.76	2.26	2.58	98.16
GL 5			83.73	0.22	6.81	1.82	nd	0.45	0.80	2.50	2.69	99.02
OL 6			39.56	nd	nd	18.42	0.28	42.37	0.25	nd	nd	100.88
PX 7			51.20	0.65	4.23	6.38	0.16	17.25	19.01	0.31	nd	99.19
H121372												
PX A	60		53.06	0.44	0.45	10.11	0.31	15.39	18.98	0.33	nd	99.09
PX B	60		53.19	0.34	0.58	10.65	0.24	14.37	18.09	0.25	nd	97.76
PX C	60		53.34	0.34	0.57	10.49	0.26	14.23	18.69	0.25	nd	98.24
CAR A			0.87	nd	nd	46.49	3.48	0.36	3.58	0.10	nd	55.00
CAR B			0.80	nd	nd	46.13	3.56	0.37	3.58	nd	nd	54.57
PX A	45		52.94	0.51	2.55	14.70	0.31	25.60	2.05	nd	nd	98.73
PX B	45		53.49	0.53	2.43	14.68	0.34	26.17	1.86	nd	nd	99.54
PX A	GM		50.58	1.18	3.72	7.95	0.13	15.59	19.07	0.20	nd	98.42
PX B	GM		51.98	0.90	2.85	8.32	0.20	17.02	17.65	0.31	nd	99.24
PX C	50		52.06	1.02	2.92	8.69	0.27	17.42	17.22	0.25	nd	99.87
PX O	50		53.55	0.55	2.60	14.55	0.32	25.88	2.11	nd	nd	99.65
PX 30			51.65	0.40	0.75	11.55	0.32	16.07	16.38	0.18	nd	97.37
PX 35			52.17	0.64	1.75	9.89	0.27	16.82	16.65	0.29	nd	98.54
GL 20			74.57	1.21	12.38	1.91	nd	nd	0.28	1.29	6.17	97.84
PX C	GM		50.58	1.62	1.83	13.94	0.27	12.22	18.13	0.35	nd	99.00
PX D	GM		50.88	0.99	2.83	7.77	0.19	16.06	19.78	0.30	nd	98.81
PX E	GM		51.54	1.01	3.66	7.52	0.23	16.42	19.10	0.42	nd	99.93
PX 9	GM		51.97	0.77	2.72	7.93	0.24	17.53	17.88	0.30	nd	99.34
PX G	GM		50.74	1.29	2.85	9.36	0.21	16.14	17.99	0.25	nd	98.86
PX H	GM		51.45	0.93	3.12	7.53	0.20	17.08	18.84	0.26	nd	99.43
PX 182/6			54.85	0.19	1.73	10.24	0.16	29.87	1.90	nd	nd	98.99
PX 182/7			53.93	0.23	2.29	10.45	0.17	29.20	2.02	nd	nd	98.35
PX 182/8			54.21	0.30	2.39	10.71	0.18	29.35	2.05	nd	nd	99.28
PX 182/11			51.06	0.90	3.25	9.15	0.23	18.84	15.02	0.33	nd	98.78
PX 182/9			48.52	1.88	6.33	9.79	0.24	16.00	16.83	0.32	nd	99.91
PX 182/10			48.80	2.37	2.39	17.56	0.39	11.70	16.26	0.36	nd	99.85
PX 182/12			53.14	0.52	0.95	17.33	0.38	24.50	2.07	nd	nd	98.93
PX 182/13			53.02	0.49	0.74	18.80	0.39	24.03	2.18	nd	nd	99.77
PX 184/18			50.65	1.26	2.00	11.86	0.29	15.50	16.64	0.17	nd	98.41
PX 183/20			50.19	1.04	3.16	8.92	0.29	16.04	17.13	0.31	nd	97.11
PX 183/21			51.46	1.06	1.87	10.61	0.21	17.34	16.11	0.25	nd	98.93
PX 183/23			54.83	0.46	0.65	15.54	0.31	27.21	2.05	nd	nd	101.08
PX 180/15			51.49	0.44	4.47	10.85	0.15	27.80	2.36	nd	nd	97.60
H121592												
PX 100			51.97	0.18	1.57	24.91	0.91	20.41	1.25	nd	nd	101.24
PX A	20		52.46	0.44	0.51	10.44	0.29	15.83	18.61	0.23	nd	98.81
PX A	80		51.42	0.24	1.97	24.53	0.78	19.91	1.47	0.13	nd	100.46
PX A	130		52.72	0.42	0.51	10.79	0.26	15.83	18.46	0.30	nd	99.33
PX A	160		51.17	0.35	2.04	19.79	0.60	22.96	1.62	0.16	nd	98.70
PX B	160		53.94	0.28	1.77	20.00	0.71	21.54	1.59	0.26	nd	100.11
PX A	200		51.85	0.26	1.99	21.50	0.68	22.52	1.44	nd	nd	100.29
PX B	200		52.37	0.19	2.08	21.05	0.65	23.09	1.58	0.10	nd	101.12
PX A	90		51.36	0.32	2.63	23.49	0.95	19.79	1.18	0.11	nd	99.85
PX B	90		50.66	0.25	3.15	24.56	0.96	19.34	1.18	nd	nd	100.12
PX A	30		53.11	0.53	0.48	10.41	0.33	15.79	18.25	0.28	nd	99.19
PX B	30		52.90	0.60	0.57	10.14	0.40	15.48	18.34	0.21	nd	98.68
PX C	30		53.01	0.51	0.34	11.55	0.28	16.27	15.94	0.29	nd	98.20
PX B	20		53.10	0.44	0.43	10.27	0.21	15.66	17.86	0.28	nd	98.28
PX A	150		53.55	0.24	1.11	18.59	0.40	24.21	1.79	0.20	nd	100.09
PX A	230		52.63	0.47	2.17	20.68	0.65	22.93	1.12	0.16	0.17	100.98
PX A	GM		52.30	0.81	1.44	10.11	0.32	15.40	17.38	0.34	0.16	98.26
GL GM			57.85	nd	25.57	0.92	nd	nd	8.55	6.17	0.35	99.52
PX A	GM		53.25	0.37	2.29	16.19	0.37	25.37	1.78	0.10	nd	99.72
PX A	170		52.42	0.26	2.48	21.67	0.60	21.34	1.56	nd	nd	100.42
PX D	30		52.98	0.53	0.40	10.61	0.29	15.66	18.18	0.28	nd	98.93
PX A	35		52.88	0.53	0.49	11.11	0.46	15.82	17.88	0.23	nd	99.45
PX E	30		53.56	0.63	0.53	9.72	0.37	15.30	19.42	0.35	nd	99.89
PX A	25		53.29	0.56	0.34	10.46	0.25	15.88	18.61	0.26	nd	99.68
PX A	40		53.11	0.47	0.41	10.75	0.32	15.42	18.22	0.33	nd	99.05

	t	dist	SiO2	TiO2	Al2O3	FeO	MnO	MgO	CaO	Na2O	K2O	Total
PX	B	170	54.23	0.53	0.57	18.75	0.53	24.36	2.13	nd	nd	101.12
PX	C	170	54.38	0.49	0.66	18.37	0.58	24.19	2.09	0.10	nd	100.86
PX	D	170	53.44	0.49	1.11	19.17	0.53	24.13	2.09	nd	nd	101.01
PX	D	150	54.51	0.46	0.59	17.84	0.58	24.35	1.95	nd	nd	100.30
PX	E	150	53.85	0.29	1.22	18.09	0.40	24.47	1.68	0.11	nd	100.11
PX	H	30	53.15	0.55	0.44	9.92	0.38	15.16	18.95	0.21	nd	98.77
PX	C	35	52.93	0.49	0.38	10.94	0.28	15.66	18.00	0.26	nd	98.96
PX	A	150	54.29	0.40	0.65	16.86	0.42	23.92	2.03	nd	nd	98.65
PX	A	20	53.25	0.44	0.51	10.93	0.41	16.74	16.30	0.24	nd	98.86
PX	A	15	53.62	0.54	0.61	9.13	0.35	15.38	18.35	0.32	nd	98.31
PX	J	30	53.06	0.50	0.41	10.58	0.36	15.70	18.44	0.19	nd	99.26
PX	D	20	52.77	0.53	0.45	10.01	0.47	15.76	19.06	0.34	nd	99.39
PX	F	80	50.72	0.28	2.96	23.25	0.91	19.49	1.33	nd	nd	98.94
PX	G	80	50.67	0.22	2.82	22.60	0.84	19.53	1.33	nd	nd	98.08
PX	H	80	50.88	0.28	2.79	23.72	0.82	19.64	1.32	0.15	nd	99.61
PX	J	80	50.91	0.18	2.84	23.24	0.94	19.58	1.26	0.17	nd	99.14
PX	K	80	52.96	0.52	0.40	10.65	0.37	15.83	18.35	0.30	nd	99.38
PX	L	80	51.43	0.24	1.85	24.86	0.77	19.72	1.26	nd	nd	100.15
PX	M	80	51.54	0.19	1.71	24.72	1.11	19.47	1.34	nd	nd	100.08
PX	N	80	51.96	0.22	1.89	24.66	0.90	19.52	1.20	nd	nd	100.35
PX	P	80	51.70	0.25	1.80	24.89	0.93	19.33	1.31	0.13	nd	100.34
PX	R	80	51.13	0.16	1.88	24.67	0.86	19.56	1.26	nd	nd	99.55
PX	K	30	52.40	0.54	0.44	10.21	0.30	16.01	18.28	0.30	nd	98.48
PX	L	30	53.20	0.50	0.45	10.49	0.26	15.87	18.29	0.29	nd	99.36
PX	M	30	52.81	0.53	0.46	10.91	0.19	15.85	18.12	0.24	nd	99.13
PX	N	30	52.52	0.55	0.52	10.77	0.32	15.72	18.09	0.18	nd	98.67
OL	1		39.49	nd	nd	17.56	0.19	44.08	0.16	nd	nd	101.49
PX	1		53.76	0.52	0.69	18.54	0.48	24.00	2.08	nd	nd	100.13
OL	3		38.45	nd	nd	23.06	0.30	39.57	0.20	nd	nd	101.62
PX	5		53.49	0.62	1.05	16.65	0.50	25.70	1.81	nd	nd	99.84
PX	4		52.94	0.62	0.70	18.37	0.46	24.78	2.19	nd	nd	100.14

	SiO2	TiO2	Al2O3	FeO	MnO	MgO	CaO	Na2O	K2O	Total	
LP14											
GL 3	79.58	0.62	11.35	0.94	nd	nd	0.30	1.18	3.28	97.40	interface glass
GL 4	78.70	0.76	10.88	1.35	nd	nd	0.26	0.93	2.79	95.69	interface glass
PX 5	53.95	0.25	0.93	7.38	0.14	16.38	21.48	nd	nd	100.58	
GL 7	64.06	0.61	7.29	5.84	0.21	6.88	11.26	0.87	1.75	98.77	
PX 9	53.99	0.14	0.41	8.18	0.18	16.69	20.66	0.28	nd	100.56	
PX 11	53.07	0.31	0.42	8.75	0.20	16.38	19.89	nd	nd	99.02	
PX 13	51.71	0.55	4.35	5.20	0.10	16.94	20.24	0.10	nd	99.19	
GL 14	77.09	0.75	12.32	1.06	nd	nd	0.27	1.53	3.46	96.50	interface glass
GL 15	69.79	0.83	9.21	3.68	nd	2.60	6.08	1.16	3.44	96.87	
PX 12	51.39	0.54	4.41	5.10	nd	16.81	20.77	0.12	nd	99.25	
PX 18	54.64	0.19	0.52	7.01	0.25	18.08	20.05	0.28	nd	101.03	
PX A GM	54.49	0.27	1.08	7.48	0.28	18.31	18.51	0.28	nd	100.70	
PX B GM	52.64	0.52	1.21	9.90	0.32	16.90	18.47	0.20	nd	100.20	
PX C GM	52.80	0.78	2.15	10.77	0.35	15.41	18.08	0.50	nd	100.89	
PX D GM	52.05	0.62	1.41	9.45	0.27	16.30	18.50	0.20	nd	98.80	
PX E GM	50.94	0.68	4.51	6.16	0.20	15.42	20.71	0.28	nd	98.91	
PX G GM	53.19	0.37	2.19	5.42	0.23	17.70	20.14	0.21	nd	99.45	
PX H GM	51.07	0.60	4.12	8.50	0.27	16.62	18.53	0.36	nd	100.08	
PX J GM	52.05	0.76	1.57	10.56	0.42	16.03	18.08	0.42	nd	99.90	
PX K GM	51.54	0.52	3.85	7.82	0.19	16.00	19.60	0.32	nd	99.85	
PX L GM	54.41	0.27	0.93	6.13	0.17	18.15	19.77	0.30	nd	100.15	
PX 1 GM	54.22	0.22	0.56	2.74	nd	16.92	24.55	0.14	nd	99.36	
PX 2 GM	53.56	0.22	0.53	2.83	0.13	16.90	24.41	0.21	nd	98.79	
PX 3 GM	53.80	0.24	0.63	2.66	nd	16.85	24.46	0.25	nd	98.97	
PX 4 GM	53.17	0.29	0.52	2.98	0.13	16.70	24.25	0.24	nd	98.28	
PX 5 GM	53.05	0.27	0.59	2.96	nd	16.65	24.44	0.17	nd	98.13	
PX 11/4	53.35	0.13	0.36	7.53	0.14	16.75	20.99	0.23	nd	99.53	
PX 11/21	54.18	0.11	0.35	7.27	0.22	16.72	21.09	0.27	nd	100.28	
PX 11/13	54.06	0.11	0.25	7.38	0.25	16.94	20.36	0.28	nd	99.68	
PX 11/5	54.31	0.16	0.33	7.29	0.22	17.42	20.46	0.33	nd	100.55	
PX 11/14	54.43	0.11	0.27	6.80	0.23	17.52	20.12	0.25	nd	99.78	
PX 11/1	53.42	0.17	0.47	6.75	0.25	17.50	20.49	0.25	nd	99.34	
PX 11/7	53.76	0.19	0.64	6.39	0.16	17.01	20.82	0.25	nd	99.26	
PX 11/15	53.92	0.24	0.88	6.29	0.21	17.78	20.29	0.30	nd	99.93	
PX 11/16	53.89	0.20	1.46	6.22	0.11	17.50	20.41	0.30	nd	100.09	
PX 11/8	54.00	0.17	0.84	6.72	0.21	17.65	19.58	0.30	nd	99.47	
PX 11/3	53.13	0.23	1.09	6.46	0.18	18.42	19.56	0.22	nd	99.30	
PX 11/19	54.37	0.17	0.72	7.36	0.28	18.13	18.67	0.28	nd	99.99	
PX 11/17	54.30	0.16	0.33	7.89	0.34	17.39	19.29	0.23	nd	99.95	
PX 11/11	51.98	0.57	1.83	8.26	0.21	16.44	19.56	0.27	nd	99.13	
PX 11/18	53.31	0.43	1.16	18.21	0.39	24.16	2.32	nd	nd	100.02	
PX 11/9	54.08	0.26	1.92	13.87	0.30	27.83	2.05	nd	nd	100.31	
PX 11/10	51.00	0.70	1.26	15.40	0.32	18.59	10.96	0.18	nd	98.42	
RAW860											
OL 215/1	37.02	nd	nd	28.46	0.46	34.15	0.35	nd	nd	100.49	
OL 215/2	36.93	nd	nd	29.53	0.44	32.98	0.30	nd	nd	100.28	
PX 215/3	50.57	1.18	2.72	9.78	0.25	16.64	17.00	0.62	0.16	98.92	
OL215/12	36.59	nd	nd	31.78	0.52	31.62	0.32	nd	nd	100.96	
OL 215/6	36.42	nd	nd	32.01	0.41	30.48	0.31	nd	nd	99.72	
OL 215/7	36.55	0.10	nd	31.32	0.43	30.18	0.45	nd	nd	99.08	
OL 215/9	36.29	0.10	nd	32.36	0.47	29.77	0.37	nd	nd	99.39	
OL215/10	36.51	nd	nd	32.39	0.48	30.08	0.31	nd	nd	99.82	
PX215/13	50.46	0.53	6.01	15.39	0.27	24.53	1.74	0.13	nd	99.06	
PX215/23	50.69	0.55	6.17	15.79	0.22	24.95	1.74	nd	nd	100.23	
PX215/24	50.75	0.54	5.98	15.58	0.28	24.79	1.73	0.14	nd	99.79	
PX215/25	51.07	0.56	6.04	15.98	0.20	25.05	1.92	nd	nd	100.90	
PX215/15	50.40	1.79	2.78	8.67	0.11	14.23	20.79	0.51	nd	99.30	
PX215/14	51.45	1.24	2.25	9.50	0.29	15.44	18.79	0.55	nd	99.53	
PX215/16	50.59	0.51	5.99	16.10	0.28	24.97	1.85	0.13	nd	100.42	
PX215/17	50.85	1.30	2.38	8.31	0.20	15.08	20.33	0.56	nd	99.01	
PX215/18	51.31	1.07	1.88	9.39	0.21	15.38	19.62	0.46	nd	99.34	
PX215/19	49.01	2.18	3.75	9.69	0.23	13.65	20.55	0.53	nd	99.59	
PX215/20	50.29	0.57	6.07	15.84	0.36	24.34	2.01	0.13	nd	99.63	
PX215/21	50.81	1.33	2.44	8.55	0.25	15.22	19.97	0.51	nd	99.09	
PX215/22	49.61	2.03	3.57	9.23	0.19	14.16	20.74	0.52	nd	100.06	
PX215/26	48.09	2.82	4.57	10.17	0.14	12.90	20.26	0.58	nd	99.54	
PX215/27	49.00	2.30	4.06	9.71	0.22	13.38	20.39	0.62	nd	99.69	
OL215/4	36.49	nd	nd	31.11	0.39	32.76	0.29	nd	nd	101.11	
OL215/4r	36.36	0.15	nd	31.09	0.46	30.61	0.28	nd	nd	98.99	
OL215/5	36.90	0.18	nd	31.95	0.38	31.87	0.25	nd	nd	101.56	
OL215/5r	36.66	nd	nd	29.73	0.48	31.49	0.25	nd	nd	98.67	
OL215/5r	36.93	nd	nd	30.91	0.42	32.89	0.29	nd	nd	101.51	

	SiO2	TiO2	Al2O3	FeO	MnO	MgO	CaO	Na2O	K2O	Total	
RC324											
PX 1	51.91	0.26	0.25	20.35	0.73	8.47	19.31	0.18	nd	101.47	
PX 1	50.81	0.24	0.34	24.41	0.68	8.95	13.90	nd	nd	99.37	
PX 29	51.24	0.28	0.32	22.33	0.76	8.76	17.09	0.20	nd	100.98	
PX 31	51.53	0.20	0.44	19.97	0.55	8.80	18.71	0.17	nd	100.38	
AM 33	49.81	0.49	2.66	25.41	0.40	9.40	9.89	0.95	0.31	99.32	
PX 34	51.18	0.26	0.21	21.84	0.98	8.98	17.61	0.16	nd	101.23	
PX 35	51.08	0.40	0.29	21.02	0.70	9.48	17.73	0.22	nd	100.92	
AM 38	48.81	0.38	2.92	24.93	0.60	8.31	8.98	1.13	0.34	96.40	
PX 39	51.15	0.22	0.28	19.22	0.68	8.69	18.05	0.14	nd	98.43	
RC404											
CC 225/1	0.37	nd	nd	0.75	0.18	0.66	49.60	0.26	0.22	52.07	225 = Biotite with pyroxene rim.
GL 225/2	73.14	0.58	15.45	1.56	nd	0.47	0.45	2.56	5.20	99.49	
PX 225/3	54.07	0.36	1.31	16.68	0.73	26.86	0.98	nd	nd	101.06	
PX 225/4	54.15	0.50	1.70	13.83	0.69	29.09	0.86	nd	nd	100.83	
PX 225/5	52.58	0.70	3.69	17.04	0.51	23.08	2.03	0.19	0.20	100.02	
BI 227/6	37.27	4.08	13.65	14.13	0.21	15.99	nd	0.83	8.27	94.45	227 = Biotite with pyroxene rim.
PX 227/7	51.40	0.71	4.06	13.70	0.37	27.93	1.11	nd	nd	99.30	
AM 227/8	40.45	4.01	13.06	9.91	0.15	15.82	10.15	2.39	0.40	96.34	
PX 227/9	51.64	0.57	4.19	13.87	0.36	28.40	1.04	nd	nd	100.09	
PX 227/10	51.52	0.68	3.62	13.80	0.36	28.13	1.37	nd	nd	99.49	
CC 227/11	0.22	nd	nd	0.62	0.26	0.17	50.57	nd	nd	51.96	
OP 227/12	0.20	11.90	2.83	75.27	0.31	1.47	nd	nd	nd	92.03	
CC 227/13	0.20	nd	nd	0.56	0.20	0.23	50.20	0.10	nd	51.55	
PX 227/14	51.90	0.45	3.87	14.02	0.34	28.56	1.20	nd	nd	100.37	
PX 227/15	51.78	0.47	2.97	13.51	0.28	28.46	1.47	nd	nd	98.96	
PX 227/18	52.32	0.92	2.89	14.70	0.41	27.31	1.41	nd	nd	100.01	
PX 227/17	51.90	0.59	3.76	13.41	0.38	28.36	1.22	nd	nd	99.64	
PX 227/19	52.01	0.51	3.52	13.77	0.28	28.65	1.17	nd	nd	99.92	
PX 227/20	54.69	0.29	1.92	13.66	0.40	27.25	1.09	0.10	0.30	99.70	
PX 227/21	54.16	0.24	1.16	12.57	0.43	30.31	1.20	nd	nd	100.08	
PX 227/22	51.33	0.92	4.50	14.26	0.33	28.28	0.77	nd	nd	100.41	
PX 228/23	53.32	0.28	2.58	12.49	0.35	28.50	2.03	nd	nd	99.57	228 = Hornblende with pyroxene rim.
PX 228/24	52.83	0.27	1.82	16.35	0.39	26.11	1.52	nd	nd	99.35	
PX 228/25	51.45	0.40	2.11	8.91	0.27	16.01	19.66	0.34	nd	99.18	
PX 228/26	55.06	0.27	1.69	12.66	0.74	23.83	4.90	0.11	0.26	99.52	
PX 228/29	53.01	0.35	1.24	15.60	0.89	26.53	1.55	nd	nd	99.20	
PX 228/30	54.18	0.44	1.10	14.77	0.81	27.48	1.61	nd	nd	100.40	
PX 228/31	51.61	0.71	1.90	8.25	0.31	15.59	19.78	0.28	nd	98.45	
PX 228/32	54.07	0.43	1.36	15.55	0.64	26.46	1.51	nd	nd	100.07	
PX 228/33	50.72	1.31	2.73	10.46	0.45	17.28	16.92	0.28	nd	100.15	
PX 228/34	50.48	0.98	3.19	10.81	0.52	16.02	17.45	0.32	nd	99.82	
AM 228/35	49.65	1.02	5.59	11.63	0.51	16.63	11.33	1.21	0.34	97.91	
PX 228/36	50.42	1.24	2.92	10.83	0.48	16.68	17.31	0.33	nd	100.24	
PX 228/37	54.28	0.37	1.37	14.81	0.50	27.54	1.75	nd	nd	100.66	
PX 228/38	52.87	0.90	2.08	10.51	0.63	20.18	13.82	0.18	nd	101.21	
PX 228/39	52.16	1.00	2.19	10.77	0.55	20.17	13.80	0.18	nd	100.84	
PX 228/40	54.93	0.29	0.83	15.82	0.58	27.00	1.85	nd	nd	101.34	
PX 228/41	50.93	1.00	2.51	9.65	0.21	15.45	19.57	0.39	nd	99.71	
PX 228/42	54.02	0.40	1.01	15.88	0.62	26.33	2.33	nd	nd	100.63	
PX 228/43	54.64	0.45	1.13	13.36	0.81	28.11	1.61	nd	nd	100.14	
PX 228/44	54.97	0.34	1.77	14.47	0.79	27.13	1.26	0.12	nd	100.89	
AM 228/45	54.10	0.56	1.35	15.39	1.00	26.95	1.79	nd	nd	101.17	
AM 228/46	49.69	0.93	5.91	11.54	0.59	16.55	11.19	1.17	0.34	97.91	
PX 228/47	54.76	0.29	0.85	15.26	0.47	27.34	2.15	nd	nd	101.16	
PX 228/48	52.11	0.63	1.81	8.67	0.49	16.79	19.63	0.26	nd	100.41	
PX 228/49	55.64	0.16	0.48	15.19	0.78	28.13	1.30	nd	nd	101.68	
PX 228/50	53.20	0.29	1.27	9.42	0.34	17.68	18.24	0.21	nd	100.66	
PX 228/52	54.24	0.21	1.36	15.84	0.42	27.40	1.54	nd	nd	101.05	
PX 228/51	55.58	0.15	1.00	12.55	0.29	29.19	1.66	nd	nd	100.46	
PX 228/57	52.81	0.24	2.46	15.82	0.44	25.94	1.33	nd	nd	99.06	
PX 228/53	54.73	0.27	0.84	14.87	0.98	28.28	1.07	nd	nd	100.85	
PX 228/54	53.56	0.30	1.00	9.03	0.34	17.68	18.42	0.20	nd	100.54	
PX 228/55	53.97	0.51	1.45	14.54	0.78	27.15	1.60	nd	nd	100.06	
PX 228/56	54.42	0.31	1.12	14.61	0.68	27.92	2.01	nd	nd	101.09	
GL 229/1	74.85	0.58	13.59	1.96	nd	0.18	0.83	1.45	4.33	97.80	229 = Quartz with pyroxene rim.
GL 229/2	79.21	0.37	10.87	1.61	nd	0.11	0.48	1.28	4.23	98.16	
PX 229/3	53.43	0.17	0.41	9.91	0.36	15.42	19.94	0.25	nd	99.93	
PX 229/5	53.73	0.21	0.76	9.75	0.39	14.55	19.91	0.31	0.14	99.75	
PX 229/7	52.72	0.27	0.99	8.72	0.28	15.20	21.15	0.34	nd	99.72	
PX 229/8	53.57	0.18	0.61	8.52	0.30	15.41	21.25	0.28	nd	100.15	
PX 229/9	52.98	0.38	0.94	9.93	0.36	15.01	19.64	0.33	nd	99.62	
PX 229/6	53.14	0.24	0.60	8.70	0.31	15.27	21.31	0.38	nd	100.00	
PX 229/10	53.56	0.18	0.26	10.16	0.33	14.73	20.65	0.23	nd	100.17	
PX 229/11	53.03	0.17	0.31	9.46	0.26	15.40	20.07	0.26	nd	98.98	

	SiO2	TiO2	Al2O3	FeO	MnO	MgO	CaO	Na2O	K2O	Total	
PX 229/12	54.17	0.29	1.44	15.55	0.33	27.20	1.38	nd	nd	100.41	
PX 229/13	54.12	0.26	2.70	12.70	0.28	28.94	1.48	nd	nd	100.52	
PX 229/14	54.00	0.29	1.52	16.19	0.46	26.14	1.47	nd	nd	100.12	
PX 229/15	54.34	0.11	0.62	18.60	1.04	24.98	0.63	nd	nd	100.35	
PX 229/16	53.70	0.37	2.43	14.25	0.30	26.76	2.30	nd	nd	100.15	
PX 229/17	53.63	0.34	0.93	10.35	0.37	16.92	17.46	0.19	nd	100.21	
PX 229/58	52.84	0.29	0.57	10.74	0.32	15.24	19.21	0.33	nd	99.61	
PX 229/59	53.48	0.22	0.60	9.26	0.24	15.75	20.28	0.32	nd	100.20	
PX 229/60	53.18	0.19	0.51	9.99	0.34	15.80	19.45	0.26	nd	99.76	
PX 232/18	55.00	0.20	2.25	11.11	0.31	29.71	1.82	nd	nd	100.45	232 = Hornblende with pyroxene rim.
PX 232/19	53.29	0.30	2.42	15.50	0.44	26.58	1.69	nd	nd	100.24	
PX 232/21	55.01	0.24	0.78	13.96	0.76	27.98	1.18	nd	nd	99.95	
PX 232/20	55.11	0.19	0.82	14.43	0.73	28.04	1.17	nd	nd	100.52	
PX 232/23	54.06	0.39	1.34	14.08	0.66	27.47	1.51	nd	nd	99.52	
PX 232/26	50.45	0.97	3.19	8.87	0.24	14.82	20.42	0.30	nd	99.29	
?? 232/25	30.29	0.75	1.45	7.26	0.36	7.10	14.03	nd	nd	61.33	
PX 232/27	48.39	1.22	4.77	11.16	0.54	14.76	15.51	0.98	0.21	97.54	
PX 232/28	50.51	1.10	3.04	11.61	0.44	16.74	15.61	0.27	nd	99.36	
PL 232/29	58.17	nd	25.71	0.80	0.40	nd	8.23	6.20	0.46	100.14	
GL 232/30	70.50	1.16	13.26	3.06	0.14	2.79	2.15	1.48	3.98	98.52	
AM 232/31	49.59	1.01	5.23	11.08	0.62	15.98	10.87	1.11	0.31	95.80	
RC409											
AM 233/1	43.49	2.61	11.05	13.84	0.34	13.34	10.95	2.11	0.42	98.15	233 = Hornblende with pyroxene rim.
AM 233/10	45.21	1.93	9.68	12.80	0.32	14.54	10.87	2.09	0.35	97.79	
PX 233/2	52.95	0.32	1.73	17.27	0.55	25.72	1.68	nd	nd	100.23	
PX 233/3	52.92	0.39	2.19	16.43	0.62	26.57	1.57	nd	nd	100.69	
PX 233/4	50.53	0.71	2.63	10.14	0.45	15.82	18.89	0.27	nd	99.44	
PX 233/5	52.17	0.27	1.97	17.88	0.73	25.20	1.60	nd	nd	99.84	
PX 233/6	51.55	0.54	1.73	9.59	0.48	15.95	19.38	0.27	nd	99.50	
PX 233/7	52.89	0.38	1.68	17.63	0.60	25.31	1.73	nd	nd	100.27	
PX 233/8	52.52	0.37	2.08	16.54	0.56	24.54	3.12	nd	nd	99.82	
PX 233/9	49.66	1.12	3.44	10.29	0.40	15.10	19.56	0.32	nd	99.90	
RC417											
PX 245/4	53.82	0.19	1.21	15.84	0.43	26.12	1.63	nd	nd	99.29	245 = Pyroxene with 2-pyroxene rim.
PX 245/5	53.04	0.30	1.44	15.93	0.37	26.65	2.16	nd	nd	99.94	
PX 245/7	51.77	0.36	1.71	8.82	0.31	16.70	19.09	0.27	nd	99.05	
PX 245/9	54.30	0.31	0.88	14.68	0.37	26.59	1.98	nd	nd	99.20	
PX 245/10	53.59	0.28	0.90	14.84	0.46	26.78	2.23	nd	nd	99.10	
PX 245/1	50.42	0.53	4.25	6.86	0.20	15.45	20.83	0.46	nd	99.00	
PX 245/2	50.02	0.27	3.35	5.85	0.21	16.88	20.88	0.37	nd	97.83	
OL 239/8	39.78	nd	nd	10.60	0.12	48.66	0.17	nd	nd	99.38	239 = Olivine with pyroxene rim.
OL 239/9	39.91	nd	nd	11.25	0.17	48.91	0.20	nd	nd	100.49	
OL 239/10	39.02	nd	nd	17.18	0.32	43.64	0.21	nd	nd	100.41	
OL 239/11	38.89	nd	nd	17.39	0.31	42.95	0.19	nd	nd	99.75	
OL 239/12	40.66	nd	nd	8.11	0.10	50.40	nd	nd	nd	99.30	
PX 239/11	54.65	0.22	2.54	11.75	0.27	29.71	1.45	nd	nd	100.61	
PX 239/12	54.45	0.38	0.94	15.07	0.37	27.46	2.08	nd	nd	100.83	
PX 239/13	54.61	0.22	2.33	12.65	0.34	28.39	1.67	nd	nd	100.24	
OL 239/1	40.71	nd	nd	10.72	0.22	49.26	0.16	nd	nd	101.12	
PX 239/2	54.22	0.28	3.28	11.90	0.21	29.74	1.56	nd	nd	101.26	
PX 239/3	53.88	0.25	2.40	13.17	0.30	27.94	1.78	nd	nd	99.76	
PX 239/4	55.39	0.19	2.01	11.90	0.24	29.93	1.55	nd	nd	101.25	
PX 239/5	54.83	0.35	1.07	13.62	0.34	27.53	1.96	nd	nd	99.77	
PX 239/6	53.72	0.31	3.50	11.52	0.20	29.34	1.55	nd	nd	100.14	
OL 239/7	39.63	nd	nd	17.36	0.32	44.59	0.19	nd	nd	102.15	
PX 239/8	52.89	0.30	4.78	13.20	0.30	27.72	1.50	nd	nd	100.74	
PX 239/9	54.96	0.26	2.64	11.71	0.21	29.87	1.42	nd	nd	101.12	
PX 239/10	54.93	0.40	0.91	14.83	0.39	27.56	1.97	nd	nd	101.06	
PX 243/14	50.57	0.63	5.06	6.78	0.18	16.25	19.43	0.33	nd	99.24	243 = Quartz with pyroxene rim.
PX 243/15	55.30	0.32	0.63	15.06	0.32	27.54	2.15	nd	nd	101.39	
PX 243/16	51.68	0.67	2.81	8.23	0.30	16.53	19.12	0.27	nd	99.63	
PX 243/18	54.38	0.35	0.79	14.89	0.40	26.70	2.13	nd	nd	99.65	
PX 243/19	52.99	0.48	1.06	8.82	0.26	17.15	18.32	0.25	nd	99.37	
PX 243/21	53.57	0.37	0.58	9.43	0.25	17.04	18.50	0.19	nd	99.96	
PX 243/22	54.29	0.15	0.46	6.88	0.16	17.37	20.68	0.22	nd	100.26	
PX 243/23	53.71	0.36	0.37	8.66	0.24	17.15	18.97	0.22	nd	99.70	
PX 243/24	53.73	0.40	0.55	8.09	0.21	17.43	19.48	0.21	nd	100.12	
GL 243/26	73.87	0.67	12.00	3.12	nd	0.37	1.01	1.62	4.94	97.66	
GL 243/27	68.98	0.86	13.83	3.51	nd	0.26	1.20	1.71	5.09	95.53	
PX 243/28	54.16	0.22	0.47	8.84	0.31	18.03	17.81	0.20	nd	100.06	
PX 243/29	54.09	0.24	0.47	8.37	0.22	17.60	19.19	0.16	nd	100.38	
PX 243/31	54.64	0.36	0.95	14.93	0.33	27.03	1.94	nd	nd	100.21	
PX 243/34	54.41	0.31	0.77	14.80	0.38	27.31	2.03	nd	nd	100.08	
GL 243/33	78.10	0.48	10.92	2.78	nd	0.36	0.75	1.02	3.94	98.38	

	SiO2	TiO2	Al2O3	FeO	MnO	MgO	CaO	Na2O	K2O	Total	
RC420											
PX 224/ 1	53.82	0.10	0.25	7.17	0.22	16.33	21.03	0.20	nd	99.12	224 = Quartz with pyroxene rim.
PX 224/ 2	53.65	0.13	0.32	7.39	0.15	16.22	21.08	0.28	nd	99.22	
PX 224/ 3	53.57	0.14	0.49	7.03	0.20	16.57	20.95	0.26	nd	99.21	
PX 224/ 4	53.70	0.20	0.58	7.86	0.27	16.82	19.72	0.26	nd	99.41	
PX 224/ 5	53.17	0.21	0.95	8.96	0.22	16.01	19.39	0.35	nd	99.26	
PX 224/ 6	52.83	0.25	0.67	10.08	0.35	15.03	19.64	0.39	nd	99.24	
PX 224/ 7	53.26	0.22	1.10	6.77	0.23	16.91	20.56	0.30	nd	99.35	
PX 224/ 8	51.82	0.42	3.42	6.04	0.15	16.95	20.14	0.28	nd	99.22	
PX 224/10	52.57	0.34	2.45	5.26	0.17	17.81	20.08	0.22	nd	98.90	
PX 224/ 9	51.71	0.48	3.48	5.66	0.21	16.66	20.58	0.28	nd	99.06	
GL 224/11	80.97	0.23	7.56	2.03	nd	0.56	0.88	2.53	3.34	98.15	
GL 224/12	79.90	0.25	8.46	2.25	nd	0.50	1.09	2.66	3.05	98.22	
GL 224/13	73.26	0.47	12.24	3.03	nd	0.42	1.11	3.22	5.00	98.77	
GL 224/14	80.64	0.22	7.68	2.07	nd	0.53	1.05	2.51	3.33	98.07	
GL 224/15	79.99	0.24	8.31	2.13	nd	0.41	0.92	2.68	3.07	97.78	
CHD											
PX 169/1	55.29	nd	3.91	5.32	0.13	34.04	0.79	0.14	nd	99.67	
PX 169/2	54.36	0.17	0.80	4.08	0.16	20.09	18.83	0.53	nd	99.02	
PX 169/4	53.85	0.27	1.32	4.05	0.10	19.15	18.96	0.74	nd	98.44	
PX 169/6	53.10	0.36	1.47	4.37	0.14	18.87	20.41	0.46	nd	99.18	
PX 169/7	50.63	1.77	5.44	5.49	0.11	14.24	22.28	0.39	nd	100.35	
PX 169/3	55.84	0.10	3.74	5.11	0.12	34.29	0.84	0.14	nd	100.18	
PX 169/12	54.57	0.17	0.82	4.44	0.21	20.89	17.59	0.56	nd	99.25	
PX 169/13	55.05	nd	3.89	5.27	0.15	34.08	0.69	0.13	nd	99.35	

Analysis	SiO2	TiO2	Al2O3	FeO	MnO	MgO	CaO	Na2O	K2O	Total	
RF9											
AM 234/1	39.50	5.20	12.39	14.04	0.35	10.21	11.32	2.87	1.41	97.29	
PX 234/2	51.80	0.91	0.96	12.70	1.41	9.49	19.53	2.54	nd	99.36	
PX 234/3	50.27	1.06	1.75	14.04	1.46	8.46	19.76	2.12	nd	98.93	
PX 234/4	49.75	0.96	1.70	14.65	1.82	7.67	20.40	1.65	nd	98.64	
PX 234/8	51.01	0.93	0.94	12.11	1.21	10.11	20.18	2.53	nd	99.02	
PX 234/9	50.25	1.73	1.61	13.26	1.45	8.95	18.55	3.12	nd	98.92	
PX 234/10	49.25	2.61	2.11	12.87	1.16	8.82	18.65	3.25	nd	98.74	
PX 234/12	48.25	1.84	3.04	15.39	1.67	7.25	20.17	2.23	nd	99.85	
CC 234/13	0.32	nd	nd	0.88	nd	0.10	53.56	nd	nd	54.99	
OP 234/14	0.16	13.29	0.27	74.89	3.79	0.23	0.38	nd	nd	93.02	
AM 234/15	39.26	5.34	12.60	13.61	0.40	10.80	11.63	3.12	1.28	98.04	
PX 234/16	48.49	2.20	2.70	14.31	1.39	7.94	19.62	2.46	nd	99.12	
PX 234/17	50.36	2.02	1.46	13.87	1.54	8.32	18.61	3.10	nd	99.28	
PX 235/18	50.97	0.85	2.05	13.70	1.57	8.35	20.20	2.10	0.10	99.89	
PX 235/19	50.00	0.93	1.53	14.74	2.11	7.50	20.86	1.78	nd	99.46	
PX 235/20	49.68	1.80	2.27	13.40	1.54	7.85	20.14	2.55	nd	99.23	
PX 235/21	51.05	1.02	1.05	12.13	1.36	9.44	19.41	2.66	nd	98.13	
AM 235/22	38.87	5.00	12.86	15.42	0.55	9.31	11.34	3.31	1.33	97.99	
AM 325/23	38.84	5.28	13.48	13.74	0.26	10.42	11.62	3.01	1.29	97.94	
AM 235/24	40.06	4.00	11.20	17.86	0.77	8.56	11.15	2.95	1.67	98.22	
PX 235/25	51.44	1.55	1.52	12.75	1.18	9.31	18.94	3.19	nd	99.88	
PX 235/26	51.09	1.89	1.58	12.87	0.99	9.33	18.85	3.18	nd	99.79	
SP 235/27	30.03	33.35	1.20	2.38	0.16	nd	27.83	nd	nd	94.98	
SP 235/28	29.28	33.83	0.64	2.16	0.11	nd	25.33	nd	nd	91.53	
AM 235/29	49.22	2.74	4.41	11.05	0.63	15.03	8.30	5.54	1.33	98.25	
AM 235/30	48.13	2.95	5.02	11.52	0.78	15.20	8.90	4.84	1.43	98.77	
PX 235/31	52.19	1.11	0.89	12.42	0.98	10.48	20.11	2.39	nd	100.57	
FS 235/32	49.56	nd	33.24	1.48	nd	nd	nd	16.16	3.49	104.08	
PX 235/33	50.90	1.48	1.39	13.10	1.11	9.28	19.39	3.02	nd	99.67	
PX 235/34	50.98	1.40	1.47	12.84	1.03	9.45	18.90	3.16	nd	99.23	
FS 235/41	54.12	nd	32.52	1.23	nd	nd	nd	14.02	2.40	104.54	
AM 235/35	39.18	3.96	10.93	19.10	0.93	8.09	10.89	2.91	1.68	97.67	
PX 235/36	51.17	1.13	0.99	12.43	1.31	9.88	20.08	2.42	nd	99.42	
AM? 235/38	39.11	4.86	9.04	20.13	1.41	6.54	11.32	6.09	1.23	99.73	
PX 235/39	50.29	2.06	1.92	12.87	1.16	9.19	18.79	3.34	nd	99.62	
AM? 235/40	40.73	3.35	11.71	17.43	0.77	6.75	10.74	5.91	1.35	98.74	
RF10											
PX 262/ 1	55.47	nd	3.07	5.21	0.11	34.47	0.67	nd	nd	99.16	
PX 262/ 2	55.63	nd	2.95	5.31	0.16	34.33	0.75	0.11	nd	99.29	
PX 262/ 5	54.73	0.17	0.40	3.70	0.16	18.43	20.57	0.69	nd	98.85	31
PX 262/ 7	54.09	0.19	0.60	3.83	0.22	18.32	20.90	0.81	nd	98.96	50 distance
PX 262/10	51.09	1.32	2.87	6.47	0.13	15.62	22.01	0.66	nd	100.17	92 (µm)
OL 262/ 4	39.01	nd	nd	17.45	0.41	43.38	0.30	nd	nd	100.55	27 from opx
OL 262/ 6	39.25	nd	nd	17.16	0.35	43.67	0.42	nd	nd	100.85	42 surface
OL 262/ 8	38.66	nd	0.31	20.23	0.46	40.48	0.59	nd	nd	100.79	77 (#1,2)
OL 262/11	38.49	nd	nd	21.95	0.54	38.85	0.41	nd	nd	100.39	108
OL 262/12	37.97	nd	nd	21.50	0.50	39.17	0.44	nd	nd	99.66	154
OL 262/13	39.39	nd	nd	14.88	0.18	45.52	0.21	nd	nd	100.18	
OL 264/14	39.75	nd	nd	12.23	0.17	47.39	0.18	nd	nd	99.72	
PX 264/17	48.74	1.97	4.33	6.31	0.17	14.64	22.54	0.34	nd	99.04	
OL 264/18	39.85	nd	nd	14.25	0.24	46.10	0.29	nd	nd	100.73	
PX 264/20	47.04	2.90	6.14	7.97	0.11	12.38	22.46	0.72	nd	99.72	
PX 264/21	43.07	4.25	8.78	8.07	0.18	11.15	22.26	0.77	nd	98.59	
PX 264/23	47.64	2.36	5.65	7.26	0.14	13.65	22.26	0.48	nd	99.44	
RF11											
PX 248/ 1	50.20	0.76	7.14	5.61	0.10	16.29	17.86	1.11	nd	99.07	Sponge-textured
PX 248/ 2	50.01	1.33	4.49	5.52	nd	15.07	21.54	0.45	nd	98.50	pyroxene
PX 248/ 4	50.93	0.99	2.99	5.21	0.10	16.06	22.39	0.34	nd	99.01	megacryst.
PX 248/ 5	50.22	1.09	4.02	5.30	0.13	15.71	21.80	0.42	nd	98.69	Core #1
PX 248/ 7	50.24	0.84	4.82	4.89	0.14	15.97	21.16	0.45	nd	98.51	Sponge #2,4,5,7
PX 248/ 3	42.97	4.39	8.97	8.41	0.11	11.52	22.21	0.53	nd	99.11	Rim #3,8,9
PX 248/ 8	46.17	2.45	6.82	6.55	nd	13.09	22.44	0.45	nd	98.06	
PX 248/ 9	41.44	4.93	10.48	8.87	0.16	10.12	22.23	0.66	nd	98.89	
OL 249/ 1	40.49	nd	nd	11.03	0.20	47.85	0.18	nd	nd	99.75	Orthopyroxene
OL 249/ 2	39.84	nd	nd	16.65	0.35	44.26	0.38	nd	nd	101.48	xenocryst (#10,
OL 249/ 3	39.68	nd	nd	14.34	0.27	44.78	0.22	nd	nd	99.29	12) with
OL 249/ 4	39.54	nd	nd	14.56	0.32	44.01	0.30	nd	nd	98.73	olivine rim.
OL 249/ 5	39.71	nd	nd	15.87	0.28	43.49	0.24	nd	nd	99.59	
OL 249/ 6	39.30	nd	nd	17.34	0.37	42.60	0.30	nd	nd	99.91	
OL 249/ 7	40.69	nd	nd	14.58	0.21	45.05	0.31	nd	nd	100.84	
PX 249/10	55.88	nd	4.07	6.24	0.16	33.73	0.66	nd	nd	100.88	
OL 249/11	40.18	nd	nd	13.57	0.33	46.35	0.30	nd	nd	100.73	
PX 249/12	55.94	nd	4.07	6.16	0.11	33.59	0.67	nd	nd	100.60	

Analysis	SiO2	TiO2	Al2O3	FeO	MnO	MgO	CaO	Na2O	K2O	Total	
RF12											
PX 268/ 2	54.70	0.15	0.62	5.19	0.21	16.87	21.34	0.60	nd	99.68	8 Distance
PX 268/ 4	54.83	0.20	0.58	4.77	0.14	17.82	20.83	0.59	nd	99.76	50 (µm) of
PX 268/ 5	55.44	0.15	0.62	4.42	0.20	18.93	19.67	0.49	nd	99.92	97 analyses
PX 268/ 7	54.24	0.24	0.68	4.93	0.20	17.63	21.36	0.60	nd	99.88	159 from
PX 268/ 8	47.62	2.80	5.29	6.60	0.17	13.25	22.25	0.67	nd	98.65	186 olivine
PX 268/ 9	49.99	1.68	3.78	6.06	0.16	14.17	22.42	0.54	nd.	98.80	200 xenocryst.
PX 268/ 6	48.27	2.40	5.22	6.62	0.11	13.44	22.14	0.70	nd	98.90	206
PX 268/11	49.00	1.53	3.92	6.46	0.14	14.34	22.44	0.42	nd	98.25	GM
PX 268/12	45.97	3.16	7.40	7.30	0.13	12.48	22.22	0.66	nd	99.32	GM
OL 268/ 1	39.82	nd	nd	18.96	0.47	41.56	0.29	nd	nd	101.10	Olivine xenocryst
OL 268/10	38.55	nd	nd	20.94	0.56	38.50	0.43	nd	nd	98.98	Rim olivine
RF15											
PX 247/ 1	49.01	1.71	4.34	6.60	0.12	14.10	22.45	0.44	nd	98.77	(overgrowth)
OL 247/ 2	40.28	nd	nd	14.23	0.34	44.67	0.24	nd	nd	99.76	63 Distance (µm)
OL 247/ 4	40.30	nd	nd	13.96	0.37	45.41	0.25	nd	nd	100.29	46
OL 247/ 6	40.88	nd	nd	12.32	0.28	46.18	0.23	nd	nd	99.89	33
PX 247/10	55.11	0.14	0.66	3.54	0.18	19.15	20.51	0.49	nd	99.78	28
PX 247/11	54.60	0.22	0.74	3.79	0.11	17.75	21.60	0.50	nd	99.31	63
PX 247/12	53.37	0.77	1.57	5.08	0.15	16.23	22.32	0.54	nd	100.03	85
PX 247/13	53.53	0.64	2.33	4.54	0.11	17.79	19.59	0.67	nd	99.20	107
PX 247/14	49.67	1.82	4.19	6.63	0.16	14.48	22.60	0.40	nd	99.95	144 (overgrowth)
PX 247/15	49.56	1.87	4.26	6.53	0.12	14.41	23.05	0.39	nd	100.19	GM
PX 247/16	47.60	2.36	5.95	7.16	0.12	14.16	22.45	0.57	nd	100.37	GM
RF16											
PX 1	51.86	0.82	7.12	2.52	nd	14.37	21.15	1.60	nd	99.49	-205 Distance
PX 2	54.96	0.11	4.62	5.95	0.14	33.35	0.41	nd	nd	99.54	-130 from opx
PX 3	55.17	0.12	4.65	5.91	0.13	33.16	0.35	nd	nd	99.49	-17 surface to
OL 4	41.13	nd	nd	9.48	0.18	49.64	0.13	nd	nd	100.56	8 analysis
PX 5	55.30	0.16	0.63	3.37	0.15	19.91	18.87	0.66	nd	99.05	25 (µm)
PX 7	55.26	0.19	0.59	3.09	nd	19.37	20.03	0.69	nd	99.31	154 (- implies
PX 8	55.06	0.20	0.64	3.18	0.16	18.07	21.70	0.58	nd	99.59	167 within opx).
PX 9	55.33	0.22	0.71	3.42	0.12	18.27	20.97	0.57	nd	99.61	375
PX 10	51.55	1.38	2.74	5.23	0.15	15.34	22.58	0.63	nd	99.60	529
PX 11	53.83	0.55	1.49	4.07	0.13	16.89	22.35	0.70	nd	100.01	641
PX 13	52.29	1.00	2.23	6.00	0.26	15.82	21.64	0.80	nd	100.04	710
PX 15	49.73	1.37	4.35	6.28	0.11	14.62	22.32	0.64	nd	99.42	775
PX 17	44.27	3.77	8.59	7.52	0.17	11.69	22.59	0.61	nd	99.21	GM
PX 18	50.79	0.61	5.06	4.04	0.10	15.09	23.09	0.52	nd	99.30	GM
OL 19	40.42	nd	nd	9.27	0.17	49.16	0.14	nd	nd	99.16	21
OL 20	39.89	nd	nd	10.03	0.25	48.55	0.13	nd	nd	98.85	79
OL 21	40.30	nd	nd	10.12	0.22	47.78	0.15	nd	nd	98.57	117
OL 22	39.97	nd	nd	11.50	0.25	47.19	0.19	nd	nd	99.10	192
OL 23	40.47	nd	nd	12.70	0.25	46.57	0.22	nd	nd	100.21	250
OL 24	39.75	nd	nd	13.47	0.33	45.62	0.22	nd	nd	99.39	296
OL 25	39.68	nd	nd	14.40	0.37	44.81	0.22	nd	nd	99.46	358
OL 26	39.47	nd	nd	16.02	0.30	43.31	0.23	nd	nd	99.33	417

# References cited

- Adams GE, Bishop FC. 1986. The olivine-clinopyroxene geobarometer: experimental results in the CaO-FeO-MgO-SiO<sub>2</sub> system. *Contributions to Mineralogy and Petrology* 94:230-237
- Ainslie NG, MacKensie JD, Turnbull D. 1961. Melting kinetics of quartz and cristobalite. *Journal of Physical Chemistry* 65:1718-1724
- Al-Rawi Y, Carmichael ISE. 1967. A note on the natural fusion of granite. *American Mineralogist* 52:1806-1814
- Anderson CA. 1968. Metamorphosed Precambrian silicic volcanic rocks in central Arizona. *Geological Society of America Memoir* 116:9-44
- Anderson AT. 1976. Magma mixing: petrological process and volcanological tool. *Journal of Volcanology and Geothermal research* 1:3-33
- Aoki K-I. 1967. Petrography and petrochemistry of latest Pliocene olivine-tholeiites of Taos area, northern New Mexico, USA. *Contributions to Mineralogy and Petrology* 14:190-203
- Aoki K-I. 1968. Petrogenesis of ultrabasic and basic inclusions in alkali basalts, Iki Island, Japan. *American Mineralogist* 53:241-256
- Aoki K-I. 1970. Petrology of kaersutite-bearing ultramafic and mafic inclusions in Iki Island, Japan. *Contributions to Mineralogy and Petrology* 25:270-283
- Aoki K-I, Fujimaki H. 1982. Petrology and geochemistry of calc-alkaline andesite of presumed upper mantle origin from Itinome-gata, Japan. *American Mineralogist* 67:1-13
- Arculus RJ, Johnson RW, McKee CD, Chappell BW, Sakai H. 1983. Ophiolite-contaminated andesites, trachybasalts and cognate inclusions of Mount Lamington, Papua New Guinea: anhydrite-amphibole-bearing lavas and the 1951 cumuldrome. *Journal of Volcanology and Geothermal Research* 18:215-247
- Augustithis SS. 1978. Atlas of the textural patterns of basalts and their genetic significance. Elsevier.
- Baker DR, Eggler DH. 1987. Compositions of anhydrous and hydrous melts coexisting with plagioclase, augite and olivine or low-Ca pyroxene from 1atm to 8kbar: application to the Aleutian volcanic centre of Atka. *American Mineralogist* 72:12-28
- Baker, I. 1969. Petrology of the volcanic rocks of St. Helena Island, South Atlantic. *Geological Society of America Bulletin* 80:1283-1310
- Baker MB, Grove TL. 1985. Kinetic controls on pyroxene nucleation and metastable liquid lines of descent in basaltic andesite. *American Mineralogist* 70:279-287
- Baker PE. 1968. Petrology of Mt. Misery volcano, St. Kitts, West Indies. *Lithos* 1:124-150
- Baker PE, Buckley F, Padfield T. 1980. Petrology of the volcanic rocks of Saba, West Indies. *Bulletin Volcanologique* 43:337-346
- Barbarin, B. 1988. Field evidence for successive mixing and mingling between the Piolard diorite and the Saint-Julien-la-Verte monzogranite (Nord-Forez, Massif Central, France). *Canadian Journal of Earth Sciences* 25:49-59
- Barton H, Huijsmans JJP. 1986. Post-caldera dacites from the Santorini volcanic complex, Aegean Sea, Greece: an example of the eruption of lavas of near constant chemical composition over a 2200 year period. *Contributions to Mineralogy and Petrology* 94:472-495
- Basaltic Volcanism Study Project. 1981. *Basaltic Volcanism on the Terrestrial Planets*. Pergamon Press, New York. 1286pp.
- Baxter AN, Upton BJG, White WM. 1985. Petrology and geochemistry of Rodriguez Island, Indian Ocean. *Contributions to Mineralogy and Petrology* 89:90-101
- Bence AE, Papike JJ. 1972. Pyroxene as recorders of lunar basalt petrogenesis: chemical trends due to crystal-liquid interaction. *Proceedings of the 3rd Lunar Science Conference* 1:431-469
- Bevan JC. 1982. Reaction rims of orthopyroxene and plagioclase around chrome spinels in olivine from Skye and Rhum (NW Scotland). *Contributions to Mineralogy and Petrology* 79:124-129
- Binns RA. 1969. High pressure megacrysts in basaltic lavas near Armidale, New South Wales. *American Journal of Science (Schairer volume)* 267A:33-49
- Binns RA, Duggan MB, Wilkinson JFG. 1970. High pressure megacrysts in alkaline lavas from northeastern New South Wales. *American Journal of Science* 269:132-168
- Black PM, Brothers RN. 1965. Olivine nodules in olivine nephelinite from Tokatoka, Northland. *New Zealand Journal of Geology and Geophysics* 8:62-80
- Blake DH, Elwell RWD, Gibson IL, Skelhorn RR, Walker GPL. 1965. Some relationships resulting from the intimate association of acid and basic magmas. *Quarterly Journal of the Geological Society of London* 121:31-49
- Blake S, Hamilton DL. 1988. Silica diffusivity and rates of quartz dissolution in rhyolitic liquids. *Abstracts, Seventh Meeting, Geological Societies of the British Isles*.
- Bloomer SH, Hawkins JW. 1987. Petrology and geochemistry of boninite series volcanic rocks from the Marianas Trench. *Contributions to Mineralogy and Petrology* 97:361-377
- Bogoyavlenskaya GE. 1972. Melted xenoliths of intrusive rocks in the deposits of the Uzon and Semyatchinskaya ring structures (Kamchatka). *Bulletin Volcanologique* 36:443-445
- Borley GD, Suddaby P, Scott P. 1971. Some xenoliths from the alkalic rocks of Tenerife, Canary Islands. *Contributions to Mineralogy and Petrology* 31:102-114
- Bottinga Y, Weill D. 1970. Densities of liquid silicate systems calculated from partial molar volumes of oxide components. *American Journal of Science* 269:169-182

- Bottinga Y, Weill D, Richet P. 1982. Density calculations for silicate liquids. I: Revised method for aluminosilicate compositions. *Geochimica et Cosmochimica Acta* 46:909-920
- Bourdier JL, Gourgaud A, Vincent PM. 1985. Magma mixing in a main stage of formation of Montagne Peleé: the Saint Vincent-type scoria flow sequence (Martinique, FWI). *Journal of Volcanology and Geothermal Research* 25:309-332
- Bowen NL. 1928. The evolution of the igneous rocks. Princeton University Press. 332pp.
- Bowen NL, Schairer JF. 1935. The system MgO - FeO - SiO<sub>2</sub>. *American Journal of Science* 5th series 29:151-217
- Brady JB, McCallister RH. 1983. Diffusion data for clinopyroxene from homogenization and self-diffusion experiments. *American Mineralogist* 68:95-108
- Breareley M, Scarfe CM. 1986. Dissolution rates of upper mantle minerals in an alkali basalt melt at high pressure: an experimental study and implications for ultramafic xenolith survival. *Journal of Petrology* 27:1157-1182
- Breareley M, Scarfe CM, Fujii T. 1984. The petrology of ultramafic xenoliths from Summit Lake, near Prince George, British Columbia. *Contributions to Mineralogy and Petrology* 88:53-63
- Brophy JG. 1987. The Cold Bay volcanic centre, Aleutian volcanic arc. II. Implications for fractionation and mixing mechanism in calc-alkaline andesite genesis. *Contributions to Mineralogy and Petrology* 97:378-388
- Brothers RN, Searle EJ. 1970. The geology of Raoul Island, Kermadec Group, SW Pacific. *Bulletin Volcanologique* 34:7-37
- Brown PE, Becker SM. 1986. Fractionation, hybridisation and magma mixing in the Kialineq centre, East Greenland. *Contributions to Mineralogy and Petrology* 92:57-70
- Brückner, R. 1961. Zur Kinetik des Stoffaustausches an den Grenzflächen zwischen Silikatglas- und Salz-schmelzen und des Stofftransportes in Silikatglasschmelzen unter besonderer Berücksichtigung des Verhaltens von Na<sub>2</sub>SO<sub>4</sub> und seinen Zersetzungsprodukten. *Glastechnisches Berichte* 34:438-456
- Bryan WB, Stice GD, Ewart A. 1972. Geology, petrology and geochemistry of the volcanic islands of Tonga. *Journal of Geophysical Research* 77:1566-1585
- Bulau JR, Waff HS, Tyburczy JA. 1979. Mechanical and thermodynamic constraints on fluid distribution in partial melts. *Journal of Geophysical Research* 84:6102-6108
- Byers FM. 1961. Petrology of three volcanic suites, Umnak and Bogoslov Islands, Aleutian Islands, Alaska. *Geological Society of America Bulletin* 72:93-128
- Campbell IH, Turner JS. 1986. The influence of viscosity in fountains in magma chambers. *Journal of Petrology* 27:1-30
- Canil D, Breareley M, Scarfe CM. 1987. Petrology of ultramafic xenoliths from Rayfield River, south central British Columbia. *Canadian Journal of Earth Sciences* 24:1679-1687
- Carmichael ISE, Turner FJ, Verhoogen J. 1974. Igneous petrology. McGraw Hill, 739pp.
- Carmichael ISE. 1960. The pyroxenes and olivines from some Tertiary acid glasses. *Journal of Petrology* 1: 309-336
- Carmichael ISE. 1962. A note on the composition of some natural acid glasses. *Geological Magazine* 99:253-264
- Carmichael ISE. 1964. The petrology of Thingmuli, a Tertiary volcano in eastern Iceland. *Journal of Petrology* 5:435-460
- Carmichael ISE. 1967. Mineralogy and petrology of the volcanic rocks from the Leucite Hills, Wyoming. *Contributions to Mineralogy and Petrology* 15:24-66
- Cheadle MJ, McKenzie DP. 1988. Theoretical determination of three-dimensional geometries of texturally equilibrated partially molten rocks. Abstracts, Seventh Meeting, Geological Societies of the British Isles.
- Cigolini C, Kudo AM. 1987. Basalt-andesite relationship, Poas volcano, Costa Rica: geochemical evidence for crustal contamination. *EOS* 68(44)
- Coats RR. 1952. Magmatic differentiation in Tertiary and Quaternary volcanic rocks from Adak and Kanaga Islands, Aleutian Islands, Alaska. *Geological Society of America Bulletin* 63:485-514
- Coats RR. 1968. The Circle Creek Rhyolite, a volcanic complex in Northern Elko County, Nevada. *Geological Society of America Memoir* 116:69-106
- Cole JW. 1973. High alumina basalts of Taupo Volcanic Zone, New Zealand. *Lithos* 6:53-64
- Conrad WK. 1984. The mineralogy and petrology of compositionally zoned ashflow tuffs, and related silicic volcanic rocks, from the McDermitt caldera, Nevada-Oregon. *Journal of Geophysical Research* 89:8639-8664
- Conrad WK, Kay RW. 1984. Ultramafic and mafic inclusions from Adak Island: crystallization history and implications for the nature of primary magmas and crustal evolution in the Aleutian island arc. *Journal of Petrology* 25:88-125
- Conrad WK, Kay SM, Kay RW. 1983. Magma mixing in the Aleutian arc: evidence from cognate inclusions and composite xenoliths. *Journal of Volcanology and Geothermal Research* 18:279-295
- Coriell SR, Cordes MR, Böttlinger WJ, Sekerka RF. 1980. Convective and interfacial instabilities during unidirectional solidification of a binary alloy. *Journal of Crystal Growth* 49:13-28
- Coriell SR, Sekerka RF. 1981. Effect of convective flow on morphological stability. *PhysicoChemical Hydrodynamics* 2:281-293
- Cox KG, Gass IG, Mallick DIJ. 1977. The western part of the Shuqra volcanic field, South Yemen. *Lithos* 10:185-191

- Crank J. 1975. The mathematics of diffusion. Clarendon Press.
- Dantria JM, Liotard JM, Cabanes M, Girod M, Briquieu L. 1987. Amphibole-rich xenoliths and host alkali basalts: petrogenetic constraints and implications on the recent evolution of the upper mantle beneath Ahaggar (Central Sahara, Southern Algeria). *Contributions to Mineralogy and Petrology* 95:133-144
- Davidson PM. 1985. Thermodynamic analysis of quadrilateral pyroxenes. I: Derivation of the ternary non-convergent site-disorder model. *Contributions to Mineralogy and Petrology* 91:383-389
- Davidson PM, Lindsley DH. 1985. Thermodynamic analysis of quadrilateral pyroxenes. II: Model calibration from experiments and applications to geothermometry. *Contributions to Mineralogy and Petrology* 91:390-404
- Dawson JB, Stephens WE. 1975. Statistical classification of garnets from kimberlite and associated xenoliths. *Journal of Geology* 83:589-607
- Dawson JB, Stephens WE. 1976. Statistical classification of garnets from kimberlite and associated xenoliths - addendum. *Journal of Geology* 84:495-496
- Decker R, Decker B. 1981. The eruptions of Mount St. Helens. *Scientific American* 244(3):52-64
- Deer WA, Howie RA, Zussman J. 1978. Rock forming minerals. Volume 2A (second edition): Single-chain silicates. Longman 668pp.
- Di Paola GM. 1974. Volcanology and petrology of Nisyros Island (Dodecanese, Greece). *Bulletin Volcanologique* 38:944-987
- Dixon TH, Batiza R. 1979. Petrology and chemistry of recent lavas in the Northern Marianas: implications for the origin of island arc basalts. *Contributions to Mineralogy and Petrology* 70:167-181
- Doe BR, Lipman PW, Hedge CE, Kurawawa H. 1969. Primitive and contaminated basalts from the Southern Rocky Mountains, USA. *Contributions to Mineralogy and Petrology* 21:142-156
- Donaldson CH. 1975. Calculated diffusion coefficients and the growth rate of olivine in basaltic magma. *Lithos* 8:163-174
- Donaldson CH. 1976. An experimental investigation of olivine morphology. *Contributions to Mineralogy and Petrology* 57:187-213
- Donaldson CH. 1978. Petrology of the uppermost upper mantle deduced from spinel hercynite and harzburgite nodules at Calton Hill, Derbyshire. *Contributions to Mineralogy and Petrology* 65:363-377
- Donaldson CH. 1979. Compositional changes in a basalt melt contained in a wire loop of Pt<sub>90</sub>Rh<sub>10</sub>: effects of temperature, time and oxygen fugacity. *Mineralogical Magazine* 43:115-119
- Donaldson CH. 1984. Kinetics of pyrope megacryst reactions in ascending basaltic magma - relevance to high-pressure magmatic crystallization at Elie Ness, East Fife. *Geological Magazine* 121:615-620
- Donaldson CH. 1985a. A comment on crystal shapes resulting from dissolution in magmas. *Mineralogical Magazine* 49:129-132
- Donaldson CH. 1985b. The rates of dissolution of olivine, plagioclase and quartz in a basalt melt. *Mineralogical Magazine* 49:683-693
- Donaldson CH, Hamilton DL. 1987. Compositional convection and layering in a rock melt. *Nature* 327:413-415
- Donaldson CH, Henderson CMB. 1988. A new interpretation of round embayments in quartz crystals. *Mineralogical Magazine* 52:27-34
- Donaldson CH, Usselman TM, Williams RJ, Lofgren GE. 1975a. Experimental modelling of the cooling history of Apollo 12 olivine basalts. *Proceedings of the 6th Lunar Science Conference* p843-869
- Donaldson CH, Williams RJ, Lofgren GE. 1975b. A sample holding technique for study of crystal growth in silicate melts. *American Mineralogist* 60:324-326
- Dowty E. 1980. Crystal growth and nucleation theory and the numerical simulation of igneous crystallization. In "Physics of magmatic processes", ed. Hargraves RB, p419-479
- Duggan MB, Wilkinson JFG. 1973. Tholeiitic andesite of high pressure origin from the Tweed Shield Volcano, northeastern New South Wales. *Contributions to Mineralogy and Petrology* 39:267-276
- Eggler DH. 1972. Amphibole stability in H<sub>2</sub>O-undersaturated calc-alkaline melts. *Earth and Planetary Science Letters* 15:28-34
- Eiché GE, Francis DM, Ludden JN. 1987. Primary alkaline magmas associated with the Quaternary Alligator Lake complex, Yukon Territory, Canada. *Contributions to Mineralogy and Petrology* 95:191-207
- Eichelberger JC. 1975. Origin of andesite and dacite: evidence of mixing at Glass Mountain in California and other circum-Pacific volcanoes. *Geological Society of America Bulletin* 86:1381-1391
- Eichelberger JC. 1978a. Andesites in island arcs and continental margins: relationship to crustal evolution. *Bulletin Volcanologique* 41:480-500
- Eichelberger JC. 1978b. Andesitic volcanism and crustal evolution. *Nature* 275:21-27
- Eichelberger JC. 1980. Vesiculation of mafic magma during replenishment of silicic magma reservoirs. *Nature* 288:446-450
- Eitel W. 1965. Silicate science. Volume II: "Glasses, enamels and slags". Academic Press, Chicago. 707pp.
- Eugster HP, Wones DR. 1962. Stability relations of the ferruginous biotite, annite. *Journal of Petrology* 3:82-125

- Evans SH Jr, Nash WP. 1979. Petrogenesis of xenolith bearing basalts from southeastern Arizona. *American Mineralogist* 64:249-267
- Finch RH, Anderson CA. 1930. The quartz-basalt eruptions of Cinder Cone, Lassen Volcanic National Park, California. *University of California, Department of Geological Sciences, Bulletin* 19:245-278
- Fleet ME. 1975. Growth habits of clinopyroxene. *Canadian Mineralogist* 13:336-341
- Flett JS. 1908. Petrographical notes on the products of the eruptions of May, 1902, at the Soufrière in St. Vincent. *Philosophical Transactions of the Royal Society of London* A208:305-332
- Fodor V. 1978. Ultramafic and mafic inclusions and megacrysts in Pliocene basalt, Black Range, New Mexico. *Geological Society of America Bulletin* 89:451-459
- Fournelle J, Marsh BD. 1987. Diopsidic clinopyroxene produced by assimilation of Fe-rich olivine by magmas at Shishaldin volcano: implications for Alaskan layered complexes. *EOS* 68(44).
- Garcia MO, Jacobsen SS. 1979. Crystal clots, amphibole fractionation, and the evolution of calc-alkaline magmas. *Contributions to Mineralogy and Petrology* 69:319-327
- Gerlach DC, Grove TL. 1982. Petrology of Medicine Lake Highland volcanics: characterization of the end members of magma mixing. *Contributions to Mineralogy and Petrology* 80:147-159
- German RM. 1985. Liquid phase sintering. *Plenum, New York.*
- Gill JB. 1981. Orogenic andesites and plate tectonics. *Springer Verlag, Berlin, 390pp.*
- Graham IJ, Hackett WR. 1987. Petrology of calc-alkaline lavas from Ruapehu volcano and related vents, Taupo Volcanic Zone, New Zealand. *Journal of Petrology* 28:531-567
- Graham AM, Thirlwall MF. 1981. Petrology of the 1979 eruption of Soufrière volcano, St. Vincent, Lesser Antilles. *Contributions to Mineralogy and Petrology* 76:336-342
- Grapes RH. 1986. Melting and thermal reconstruction of pelitic xenoliths, Wehr volcano, east Eifel, West Germany. *Journal of Petrology* 27:343-396
- Green TH, Ringwood AE. 1968. Genesis of the calc-alkaline igneous rock suite. *Contributions to Mineralogy and Petrology* 18:105-162
- Griffin WL. 1973. Lherzolite nodules from the Fen alkaline complex, Norway. *Contributions to Mineralogy and Petrology* 38:135-146
- Grove TL, Juster TC. 1987. Orthopyroxene and pigeonite stability relations at 1-atmosphere in natural andesite and basalt liquids. *Geological Society of America Abstracts* 19:685
- Grove TL, Donnelly-Nolan JM. 1986. The evolution of young silicic lavas at Medicine Lake Volcano, CA: implications for the origin of compositional gaps in calc-alkaline series lavas. *Contributions to Mineralogy and Petrology* 92:281-302
- Grove TL, Baker MB. 1984. Phase equilibrium controls on the tholeiitic vs calc-alkaline differentiation trends. *Journal of Geophysical Research* 89:2253-2274
- Grove TL, Bryan WB. 1983. Fractionation of pyroxene-phyric MORB at low pressure: an experimental study. *Contributions to Mineralogy and Petrology* 84:293-309
- Grove TL, Gerlach DC, Sando TW, Baker MB. 1983. Origin of calc-alkaline series lavas at Medicine Lake Volcano by fractionation, assimilation and mixing: corrections and clarifications. *Contributions to Mineralogy and Petrology* 82:407-408
- Grove TL, Gerlach DC, Sando TW. 1982. Origin of calc-alkaline series lavas at Medicine Lake Volcano by fractionation, assimilation and mixing. *Contributions to Mineralogy and Petrology* 80:160-182
- Grove TL, Bence AE. 1979. Crystallization kinetics in a multiply saturated basalt magma: An experimental study of Luna 24 ferrobasalt. *Proceedings of the 10th Lunar and Planetary Science Conference* 439-478
- Hamad S el D. 1963. The chemistry and mineralogy of olivine nodules of Calton Hill, Derbyshire. *Mineralogical Magazine* 33:483-497
- Harker. 1904. The Tertiary igneous rocks of Skye. *HMSO Glasgow*
- Harris SL. 1976. Fire and Ice. *Pacific Search Press, 316pp.*
- Harrison TM, Watson EB. 1983. Kinetics of zircon dissolution and zirconium diffusion in granitic melts of variable water content. *Contributions to Mineralogy and Petrology* 84:66-72
- Harrison TM, Watson EB. 1984. The behaviour of apatite during crustal anatexis: equilibrium and kinetic considerations. *Geochimica et Cosmochimica Acta* 48:1467-1478
- Hausel WD, Nash WP. 1977. Petrology of Tertiary and Quaternary volcanic rocks, Washington County, southwestern Utah. *Geological Society of America Bulletin* 88:1831-1842
- Heiken G, Eichelberger JC. 1980. Eruptions at Chaos Crags, Lassen Volcanic National Park California. *Journal of Volcanology and Geothermal Research* 7:443-481
- Helgeson HC, Murphy WM, Aagaard P. 1984. Thermodynamic and kinetic constraints on reaction rates among minerals and aqueous solutions. II. Rate constants, effective surface area, and the hydrolysis of feldspar. *Geochimica et Cosmochimica Acta* 33:455-481
- Heming RF, Carmichael ISE. 1973. High temperature pumice flows from the Rabaul caldera, Papua New Guinea. *Contributions to Mineralogy and Petrology* 38:1-20

- Higgins MW. 1973. Petrology of Newberry volcano, Central Oregon. *Geological Society of America Bulletin* 84:455-488
- Hofmann AH. 1980 Diffusion in silicate melts: a critical review. In "Physics of magmatic processes", ed Hargraves RB, Princeton University Press.
- Holmes A. 1936. Transfusion of quartz xenoliths in alkali basic and ultrabasic lavas, southwest Uganda. *Mineralogical Magazine* 24:408-421
- Holmes A. 1921. Petrographic methods. Murby, London. 515pp.
- Huppert HE, Sparks RSJ, Turner JS. 1982. Effects of mixing in calc-alkaline magma systems. *Nature* 297:554-557
- Hunter RH. 1986. Textural equilibrium in layered igneous rocks. In "Origins of igneous layering", ed. Parsons I. (Reider; NATO ASI Series C) p473-503.
- Hutchison R, Chambers AC, Paul DK, Harris DG. 1975. Chemical variation among French ultramafic xenoliths - evidence for a heterogeneous upper mantle. *Mineralogical Magazine* 40:153-170
- Hutchison R, Gass IG. 1971. Mafic and ultramafic inclusions associated with undersaturated basalt on Kod All island, southern Red Sea. *Contributions to Mineralogy and Petrology* 31:94-101
- Irving AJ. 1980. Petrology and geochemistry of composite ultramafic xenoliths in alkalic basalts and the implications for magmatic processes within the mantle. *American Journal of Science (Jackson volume)* 280A:389-426
- Jaeger JC. 1968. Cooling and solidification of igneous rocks. Basalts ed. Poldervaart.
- Jaeger JC. 1957. The temperature in the neighbourhood of a cooling intrusive sheet. *American Journal of Science* 255:306-318
- Jebsen-Marwedel H. 1956. "Fäden" im Glas - eine Folge "dynactiven" Verhaltens von Schlieren. (Threads in glass - a consequence of the dynactive behaviour of schlieren). *Glastechnische Berichte* 29:269 - 275
- Jezek PA, Hutchison CS. 1978. Banda arc of Eastern Indonesia: petrology and geochemistry of the volcanic rocks. *Bulletin Volcanologique* 41:586-608
- Joesten R. 1986. The role of magmatic reaction, diffusion and annealing in the evolution of coronitic microstructure in troctolitic gabbro from Risør, Norway. *Mineralogical Magazine* 50:441-468
- Johnstone AD, Wyllie PJ. 1988. Interaction of granitic and basic magmas: experimental observations on contamination processes at 10kbar with H<sub>2</sub>O. *Contributions to Mineralogy and Petrology* 98:352-362
- Jurewicz AJG, Watson EB. 1988a. Cations in olivine, Part I: Calcium partitioning and calcium-magnesium distribution between olivine and coexisting melts, with petrologic applications. *Contributions to Mineralogy and Petrology* 99:176-185
- Jurewicz AJG, Watson EB. 1988b. Cations in olivine, Part 2: Diffusion in olivine xenocrysts, with applications to petrology and mineral physics. *Contributions to Mineralogy and Petrology* 99:186-201
- Jurewicz SR, Watson EB. 1985. The distribution of partial melt in a granitic system: the application of liquid phase sintering theory. *Geochimica et Cosmochimica Acta* 49:1109-1121
- Kanaris-Sotirion R, Gibb FGF. 1985. Hybridization and petrogenesis of composite intrusions: the dyke at An Cumhann, Isle of Arran. *Journal of Geology* 122:361-372
- Kawano Y, Yagi K, Aoki K-I. 1961. Petrography and petrochemistry of the volcanic rocks of Quaternary volcanoes of northeastern Japan. *Science Reports of Tohoku University, Series 3*, 7:1-46
- Keller J. 1974a. Quaternary maar volcanism near Karapinar in Central Anatolia. *Bulletin Volcanologique* 38:378-396
- Keller J. 1974b. Petrology of some volcanic rock series of the Aeolian arc, southern Tyrrhenian Sea: calc-alkaline and shoshonitic associations. *Contributions to Mineralogy and Petrology* 46:29-47
- Kingery WD, Bowen HK, Uhlmann DR. 1976. Introduction to ceramics. Second edition, John Wiley and sons, NY.
- Kinzler, Grove TL. 1985. Crystallization and differentiation of Archaean komatiite lavas from NE Ontario: phase equilibrium and kinetic studies. *American Mineralogist* 70:40-51
- Kirkpatrick RJ. 1975. Crystal growth from the melt: a review. *American Mineralogist* 60:798-814
- Kirkpatrick RJ. 1983. Theory of nucleation in silicate melts. *American Mineralogist* 68:66-77
- Kirkpatrick RJ, Kuo LC, Melchior J. 1981. Crystal growth in incongruently melting compositions: programmed cooling experiments with diopside. *American Mineralogist* 66:223-241
- Knopf A. 1938. Partial fusion of granodiorite by intrusive basalt, Owens Valley, California. *American Journal of Science* 34:373-376
- Kouchi A, Sunagawa I. 1985. A model for mixing basaltic and dacitic magmas by forced convection. *Contributions to Mineralogy and Petrology* 89:17-23
- Kouchi A, Sunagawa I. 1983. Mixing basaltic and dacitic magmas by forced convection. *Nature* 304:527-528
- Kovach, Marsh BD. 1981 Magma flow rate and partial fusion of wall rock: Huntingdon Lake, CA. *Geological Society of America Abstracts and Program* 14:490
- Koyaguchi T. 1986a. Evidence for two stage mixing in magmatic inclusions and rhyolitic lava domes on Niijima Island, Japan. *Journal of Volcanology and Geothermal Research* 29:71-98

- Koyaguchi T. 1986b. Textural evidence for magma mixing and its mechanism, Abu volcanic group, SW Japan. *Contributions to Mineralogy and Petrology* 93:33-45
- Koyaguchi T. 1986c. Lifetime of a stratified magma chamber recorded in ultramafic xenoliths from Ichinomegata volcano, NE Japan. *Bulletin of Volcanology* 48:313-324
- Kuno H. 1960. High alumina basalt. *Journal of Petrology* 1:121-145
- Kuno H. 1950. Petrology of Hakone volcano and adjacent area, Japan. *Geological Society of America Bulletin* 61:957-1020
- Kuntz MA, Rowley PD, MacLeod NS, Reynolds RL, McBroome LA, Kaplan AM, Lidke DJ. 1981. Petrography and particle-size distribution of pyroclastic-flow, ash cloud and surge deposits. *United States Geological Survey Professional Paper* 1250:525-539
- Kuo L-C, Essene EJ. 1986. Petrology of spinel Thersolite xenoliths from the Kishb plateau, Saudi Arabia. *Contributions to Mineralogy and Petrology* 93:335-346
- Kuo LC, Kirkpatrick RJ. 1985a. Kinetics of crystal dissolution in the system, diopside-forsterite-silica. *American Journal of Science* 285:51-90
- Kuo LC, Kirkpatrick RJ. 1985b. Dissolution of mafic minerals and its implication for the ascent velocities of peridotite bearing basaltic magmas. *Journal of Geology* 93:691-700
- Kuroda N, Shiraki K, Urano H. 1988. Ferropigeonite quartz dacites from Chichi-jima, Bonin Islands: latest differentiates from boninite-bearing magma. *Contributions to Mineralogy and Petrology* 100:129-138
- Kushiro I. 1960. Si-Al relation in clinopyroxenes from igneous rocks. *American Journal of Science* 258:548-554
- Kushiro I. 1972. Determination of liquidus relations in synthetic silicate systems with electron probe analysis: the system forsterite-diopside-silica at 1 atmosphere. *American Mineralogist* 57:1260-1271
- Kutolin VA, Rolova VM. 1970. Petrology of ultramafic inclusions from basalts of Minusa and Transbaikalian regions (Siberia, USSR). *Contributions to Mineralogy and Petrology* 29:163-179
- Kyle PR. 1981. Mineralogy and geochemistry of a Basanite to phonolite sequence at Hut Point peninsula, Antarctica, based on core from Dry Valley Drilling Project drillholes 1,2 and 3. *Journal of Petrology* 22:451-500
- Lacroix A. 1893. Les enclaves des roches volcaniques. *Masson, Paris*.
- Larsen ES, Irving J, Gonyer FA, Larsen ES III. 1936. Petrologic results of a study of the minerals from the Tertiary volcanic rocks of San Juan, Colorado. 2. The silica minerals. *American Mineralogist* 21:679-701
- Larsen ES, Irving J, Gonyer FA, Larsen ES III. 1937a. Petrologic results of a study of the minerals from the Tertiary volcanic rocks of the San Juan region, Colorado. 5. The amphiboles. *American Mineralogist* 22:889-898
- Larsen ES, Irving J, Gonyer FA, Larsen ES III. 1937b. Petrologic results of a study of the minerals from the Tertiary volcanic rocks of the San Juan region, Colorado. 6. Biotite. *American Mineralogist* 22:898-905
- Larsen LM. 1976. Clinopyroxenes and coexisting mafic minerals from the alkaline Ilmaussaq intrusion, South Greenland. *Journal of Petrology* 17:258-290
- Lasaga AC. 1982. Towards a master equation in crystal growth. *American Journal of Science* 282:1264-1288
- Leat PT, Thompson RN, Morrison MA, Hendry GL, Dickin AP. 1988. Silicic magmas derived by fractional crystallization from Miocene minette, Elkhead Mountains, Colorado. *Mineralogical Magazine* 52:577-585
- Le Bas. 1962. The role of aluminum in igneous clinopyroxenes with relation to their parentage. *American Journal of Science* 260:267-288
- Le Maitre RW. 1962. Petrology of volcanic rocks, Gough Island, South Atlantic. *Geological Society of America Bulletin* 73:1309-1340
- Le Maitre RW. 1965. The significance of the gabbroic xenoliths from Gough Island, South Atlantic. *Mineralogical Magazine* 34:303-317
- Le Maitre RW. 1969. Kaersutite-bearing plutonic xenoliths from Tristan da Cunha; South Atlantic. *Mineralogical Magazine* 37:185-197
- Lewis JF. 1968. Tauhara volcano, Taupo Zone. Part 2 - mineralogy and petrology. *New Zealand Journal of Geology and Geophysics* 11:651-684
- Lindsley DH. 1983. Pyroxene thermometry. *American Mineralogist* 68:477-493
- Löffler, J. 1958. Diffusionsvorgänge um das Sandkorn II. (Diffusion phenomena around a sandgrain). *Glastechnisches Berichte* 31:268 - 269
- Lofgren GE. 1974. An experimental study of plagioclase crystal morphology: isothermal crystallization. *American Journal of Science* 274:243-273
- Lofgren GE. 1980. Experimental studies on the dynamic crystallization of silicate melts. In "Physics of magmatic processes", ed Hargraves RB. *Princeton University Press*, p487-551.
- Lofgren GE. 1983. Effect of heterogeneous nucleation on basaltic textures: a dynamic crystallization study. *Journal of Petrology* 24:229-255
- Lofgren GE, Norris. 1981. Experimental duplication of plagioclase sieve and overgrowth textures. *Geological Society of America Abstracts*

- Koyaguchi T. 1986b. Textural evidence for magma mixing and its mechanism, Abu volcanic group, SW Japan. *Contributions to Mineralogy and Petrology* 93:33-45
- Koyaguchi T. 1986c. Lifetime of a stratified magma chamber recorded in ultramafic xenoliths from Ichinomegata volcano, NE Japan. *Bulletin of Volcanology* 48:313-324
- Kuno H. 1960. High alumina basalt. *Journal of Petrology* 1:121-145
- Kuno H. 1950. Petrology of Hakone volcano and adjacent area, Japan. *Geological Society of America Bulletin* 61:957-1020
- Kuntz MA, Rowley PD, MacLeod NS, Reynolds RL, McBroome LA, Kaplan AM, Lidke DJ. 1981. Petrography and particle-size distribution of pyroclastic-flow, ash cloud and surge deposits. *United States Geological Survey Professional Paper* 1250:525-539
- Kuo L-C, Essene EJ. 1986. Petrology of spinel hercynite xenoliths from the Kishb plateau, Saudi Arabia. *Contributions to Mineralogy and Petrology* 93:335-346
- Kuo LC, Kirkpatrick RJ. 1985a. Kinetics of crystal dissolution in the system, diopside-forsterite-silica. *American Journal of Science* 285:51-90
- Kuo LC, Kirkpatrick RJ. 1985b. Dissolution of mafic minerals and its implication for the ascent velocities of peridotite bearing basaltic magmas. *Journal of Geology* 93:691-700
- Kuroda N, Shiraki K, Urano H. 1988. Ferropigeonite quartz dacites from Chichi-jima, Bonin Islands: latest differentiates from boninite-bearing magma. *Contributions to Mineralogy and Petrology* 100:129-138
- Kushiro I. 1960. Si-Al relation in clinopyroxenes from igneous rocks. *American Journal of Science* 258:548-554
- Kushiro I. 1972. Determination of liquidus relations in synthetic silicate systems with electron probe analysis: the system forsterite-diopside-silica at 1 atmosphere. *American Mineralogist* 57:1260-1271
- Kutolin VA, Rolova VM. 1970. Petrology of ultramafic inclusions from basalts of Minusa and Transbaikalian regions (Siberia, USSR). *Contributions to Mineralogy and Petrology* 29:163-179
- Kyle PR. 1981. Mineralogy and geochemistry of a basanite to phonolite sequence at Hut Point peninsula, Antarctica, based on core from Dry Valley Drilling Project drillholes 1, 2 and 3. *Journal of Petrology* 22:451-500
- Lacroix A. 1893. Les enclaves des roches volcaniques. *Masson, Paris*.
- Larsen ES, Irving J, Gonyer FA, Larsen ES III. 1936. Petrologic results of a study of the minerals from the Tertiary volcanic rocks of San Juan, Colorado. 2. The silica minerals. *American Mineralogist* 21:679-701
- Larsen ES, Irving J, Gonyer FA, Larsen ES III. 1937a. Petrologic results of a study of the minerals from the Tertiary volcanic rocks of the San Juan region, Colorado. 5. The amphiboles. *American Mineralogist* 22:889-898
- Larsen ES, Irving J, Gonyer FA, Larsen ES III. 1937b. Petrologic results of a study of the minerals from the Tertiary volcanic rocks of the San Juan region, Colorado. 6. Biotite. *American Mineralogist* 22:898-905
- Larsen LM. 1976. Clinopyroxenes and coexisting mafic minerals from the alkaline Ilimaussaq intrusion, South Greenland. *Journal of Petrology* 17:258-290
- Lasaga AC. 1982. Towards a master equation in crystal growth. *American Journal of Science* 282:1264-1288
- Leat PT, Thompson RN, Morrison MA, Hendry GL, Dickin AP. 1988. Silicic magmas derived by fractional crystallization from Miocene minette, Elkhead Mountains, Colorado. *Mineralogical Magazine* 52:577-585
- Le Bas. 1962. The role of aluminum in igneous clinopyroxenes with relation to their parentage. *American Journal of Science* 260:267-288
- Le Maitre RW. 1962. Petrology of volcanic rocks, Gough Island, South Atlantic. *Geological Society of America Bulletin* 73:1309-1340
- Le Maitre RW. 1965. The significance of the gabbroic xenoliths from Gough Island, South Atlantic. *Mineralogical Magazine* 34:303-317
- Le Maitre RW. 1969. Kaersutite-bearing plutonic xenoliths from Tristan da Cunha; South Atlantic. *Mineralogical Magazine* 37:185-197
- Lewis JF. 1968. Tauhara volcano, Taupo Zone. Part 2 - mineralogy and petrology. *New Zealand Journal of Geology and Geophysics* 11:651-684
- Lindsley DH. 1983. Pyroxene thermometry. *American Mineralogist* 68:477-493
- Löffler, J. 1958. Diffusionsvorgänge um das Sandkorn II. (Diffusion phenomena around a sandgrain). *Glastechnisches Berichte* 31:268 - 269
- Lofgren GE. 1974. An experimental study of plagioclase crystal morphology: isothermal crystallization. *American Journal of Science* 274:243-273
- Lofgren GE. 1980. Experimental studies on the dynamic crystallization of silicate melts. In "Physics of magmatic processes", ed Hargraves RB. Princeton University Press, p487-551.
- Lofgren GE. 1983. Effect of heterogeneous nucleation on basaltic textures: a dynamic crystallization study. *Journal of Petrology* 24:229-255
- Lofgren GE, Norris. 1981. Experimental duplication of plagioclase sieve and overgrowth textures. *Geological Society of America Abstracts*

- Long PE, Wood BJ. 1986. Structure, textures and cooling histories of Columbia River basalt flows. *Geological Society of America Bulletin* 97:1144-1155
- Lorand JP, Cottin JY. 1987. Na-Ti-Zr-H<sub>2</sub>O-rich mineral inclusions indicating post cumulus chrome spinel dissolution and recrystallization in the Western Laouni mafic intrusion, Algeria. *Contributions to Mineralogy and Petrology* 97:251-263
- Lowder GG, Carmichael ISE. 1970. The volcanoes and caldera of Talasea, New Britain: geology and petrology. *Geological Society of America Bulletin* 81:17-38
- Luhr JF, Carmichael ISE. 1980. The Colima volcanic complex, Mexico, I. Post caldera andesites from Volcan Colima. *Contributions to Mineralogy and Petrology* 71:343-372
- Macdonald GA, Katsura T. 1965. Eruption of Lassen peak, Cascade Range, California, in 1915: example of mixed magmas. *Geological Society of America Bulletin* 76:475-482
- MacGregor AG. 1938. The Royal Society Expedition to Montserrat, B.W.I. The volcanic history and petrology of Montserrat, with observations on Mt. Pelé, in Martinique. *Philosophical Transactions of the Royal Society of London* B229:1-90
- MacKensie DE, Chappell BW. 1972. Shoshonitic and calc-alkaline lavas from the highlands of Papua New Guinea. *Contributions to Mineralogy and Petrology* 35:50-62
- Marsh BD. 1981. On the crystallinity, probability of occurrence and rheology of lava and magma. *Contributions to Mineralogy and Petrology* 78:85-98
- Marsh BD. 1988. Crystal size distribution (CSD) in rocks and the kinetics and dynamics of crystallization. I. Theory. *Contributions to Mineralogy and Petrology* 99:277-291
- Marsh BD, Leitz RE. 1978. Geology of Amak Island, Aleutian Islands, Alaska. *Journal of Geology* 87:715-723
- Martin D, Griffiths RW, Campbell IH. 1987. Compositional and thermal convection in magma chambers. *Contributions to Mineralogy and Petrology* 96:465-475
- Maury RC, Bizouard H. 1974. Melting of acid xenoliths into a basanite: an approach to the possible methods of contamination. *Contributions to Mineralogy and Petrology* 48:275-286
- Mazzone P, Stewart DC, Hughes JM. 1987. Subsolidus dehydration of amphiboles in an andesitic magma. *Contributions to Mineralogy and Petrology* 97:292-296
- McBirney AR. 1984. Igneous petrology. *Freeman, San Francisco.*
- McBirney AR, Aoki K-I. 1968. Petrology of the Island of Tahiti. *Geological Society of America Memoir* 116:523-556
- McBirney AR, Murase T. 1984. Rheological properties of magmas. *Annual Reviews in Earth and Planetary Sciences* 12:337-357
- McCormick GR, Heathcote RC. 1987. Mineral chemistry and petrogenesis of carbonatite intrusions, Perry and Conway counties, Arkansas. *American Mineralogist* 72:59-66
- McKenzie DP. 1984. The generation and compaction of partially molten rock. *Journal of Petrology* 25:713-765
- McKenzie DP. 1985. The extraction of magma from the crust and mantle. *Earth and Planetary Science Letters* 74:81-91
- McMillan NJ, Dungan MA. 1988. Open system magmatic evolution of the Taos Plateau Volcanic field, northern New Mexico: 3. Petrology and geochemistry of andesite and dacite. *Journal of Petrology* 29:527-557
- Mercier J-C C, Nicholas A. 1975. Textures and fabrics of upper mantle peridotites as illustrated by xenoliths from basalts. *Journal of Petrology* 16:454-487
- Mies JW, Glazner AF. 1987. Quartz xenocrysts with rhyolite glass inclusions as evidence of assimilated granite. *EOS* 68
- Mokhtari A, Velde D. 1988. Xenocrysts in Eocene camptonites from Taourirt, northern Morocco. *Mineralogical Magazine* 52:587-601
- Morimoto N, Chairman, Subcommittee on Pyroxenes, IMA. 1988. Nomenclature of pyroxenes. *American Mineralogist* 73:1233-1333, also *Mineralogical Magazine* 52:535-550
- Morioka M. 1981. Cation diffusion in olivine II. Ni-Mg, Mn-Mg, Mg and Ca. *Geochimica et Cosmochimica Acta* 45:1573-1580
- Morse SA. 1980. Basalts and phase diagrams. *Springer Verlag, New York.*
- Muir ID, Long JVP. 1965. Pyroxene relations in two hypersthene-bearing basalts. *Mineralogical Magazine* 34:358-369
- Muir ID. 1953. Quartzite xenoliths from the Ballachulish granodiorite. *Geological Magazine* 90:409-428
- Nabelek PI, Lindsley DH, Bohlen SR. 1987. Experimental examination of two-pyroxene graphical thermometers using natural pyroxenes with application to metaigneous pyroxenes from the Adirondack Mountains, New York. *Contributions to Mineralogy and Petrology* 97:66-71
- Nakamura Y, Coombs DS. 1973. Clinopyroxenes in the Tawhīroko tholeiitic dolerite at Moeraki, northeastern Otago, New Zealand. *Contributions to Mineralogy and Petrology* 42:213-228
- Naslund HR. 1984. Supersaturation and crystal growth in the roof zone of the Skaergaard magma chamber. *Contributions to Mineralogy and Petrology* 86:89-93
- Nelson SA, Carmichael ISE. 1979. Partial molar volumes of oxide components in silicate liquids. *Contributions to Mineralogy and Petrology* 71:117-124
- Nicholls IA. 1971. Petrology of Santorini volcano, Cyclades, Greece. *Journal of Petrology* 12:67-119

- Nicholls J, Carmichael ISE, Stormer JC Jr. 1971. Silica activity and  $P_{TOTAL}$  in igneous rocks. *Contributions to Mineralogy and Petrology* 33:1-20
- Nicholls J, Stout MZ, Fiesinger DW. 1982. Petrologic variations in the Quaternary volcanic rocks, British Columbia, and the nature of the underlying upper mantle. *Contributions to Mineralogy and Petrology* 79:201-218
- O'Brien HE, Irving AJ, McCallum IS. 1988. Complex zoning and resorption of phenocrysts in mixed potassic mafic magmas of the Highland Mountains, Montana. *American Mineralogist* 73:1007-1024
- O'Callaghan LJ, Francis PW. 1986. Volcanological and petrological evolution of San Pedro volcano, Provincia El Loa, North Chile. *Journal of the Geological Society of London* 143:275-286
- O'Hara MJ. 1968. The bearing of phase equilibria studies in synthetic and natural systems on the origin and evolution of basic and ultrabasic rocks. *Earth Science Reviews* 4:60-133
- Oishi Y, Cooper AR, Kingery WD. 1965. Dissolution in ceramic systems: III, layer concentration gradients. *Journal of the American Ceramic Society* 48:88-95
- Papike JJ, Cameron KL, Baldwin K. 1974. Amphiboles and pyroxenes: characterization of other than quadrilateral components and estimates of ferric iron from microprobe data. *Geological Society of America Abstracts* 6: 1053-1054
- Paterson BA, Stephens WE, Herd DA. 1989. Zoning in granitoid accessory minerals as revealed by backscattered electron imagery. *Mineralogical Magazine* 53:55-61
- Pe GG. 1973. Petrology and geochemistry of volcanic rocks of Aegina, Greece. *Bulletin Volcanologique* 37:491-514
- Pe GG. 1974. Volcanic rocks of Methana, South Aegean arc, Greece. *Bulletin Volcanologique* 38:270-290
- Pearce TH, Russell JK, Wolfson I. 1987. Laser interference and Nomarski interference imaging of zoning profiles in plagioclase phenocrysts from the May 18, 1980, eruption of Mt. St. Helens, Washington. *American Mineralogist* 72:1131-1143
- Powers HA. 1932. The lavas of the Modoc lava-bed quadrangle, California. *American Mineralogist* 17:253-294
- Rafferty WJ, Heming RF. 1979. Quaternary alkalic and sub-alkalic volcanism in South Auckland, New Zealand. *Contributions to Mineralogy and Petrology* 71:139-150
- Reid AM, Le Roex AP. 1988. Kaersutite-bearing xenoliths and megacrysts in volcanic rocks from the Funk Seamount in the southwest Indian Ocean. *Mineralogical Magazine* 52:359-370
- Reid FW, Cole JW. 1983. Origin of dacites of Taupo Volcanic Zone, New Zealand. *Journal of Volcanology and Geothermal Research* 18:191-241
- Rodgers KA, Brothers RN, Searle EJ. 1975. Ultramafic nodules and their host rocks from Auckland, New Zealand. *Geological Magazine* 112:163-174
- Roeder PL, Emslie RF. 1970. Olivine-liquid equilibrium. *Contributions to Mineralogy and Petrology* 29:275-281
- Sack RO, Carmichael ISE, Rivers M, Ghiorso MS. 1980. Ferric-ferrous equilibria in natural silicate liquids at 1 bar. *Contributions to Mineralogy and Petrology* 75:369-376
- Sack RO, Carmichael ISE. 1984.  $Fe^{2+}$ -Mg and  $TiAl_2$ - $HgSi_2$  exchange reactions between clinopyroxenes and silicate melts. *Contributions to Mineralogy and Petrology* 85:103-115
- Sakuyama M. 1978. Petrographic evidence of magma mixing in Shirouma-Oike volcano, Japan. *Bulletin Volcanologique* 41:501-512
- Sakuyama M. 1979. Evidence of magma mixing: petrological study of Shirouma-Oike calc-alkaline andesitic volcano, Japan. *Journal of Volcanology and Geothermal Research* 5:179-208
- Sakuyama M. 1981. Petrological study of the Myoko and Kurohime volcanoes, Japan: crystallization sequence and evidence for magma mixing. *Journal of Petrology* 22:553-583
- Sato H. 1975. Diffusion coronas around quartz xenocrysts in andesite and basalt from Tertiary volcanic region in northeastern Shikoku, Japan. *Contributions to Mineralogy and Petrology* 50:49-64
- Saxena SK, Sykes J, Eriksson G. 1986. Phase equilibria in the pyroxene quadrilateral. *Journal of Petrology* 27:843-852
- Saxena SK. 1983. Problems of two-pyroxene thermometry. *Earth and Planetary Science Letters* 65:382-388
- Scarfe CM. 1973. Viscosity of basic magmas at varying pressure. *Nature Physical Sciences* 241:101-102
- Scarfe CM, Takahashi E, Yoder HS Jr. 1980. Rates of dissolution of upper mantle minerals in an alkali olivine basalt at high pressures. *Carnegie Institute of Washington Year Book* 79:290-296
- Schiffman P, Lofgren GE. 1982. Dynamic crystallization studies on the Grande Ronde pillow basalts, central Washington. *Journal of Geology* 90:49-78
- Schwerdtfeger K. 1966. Dissolution of solid oxides in oxide melts. The rate of dissolution of solid silica in  $Na_2O$ - $SiO_2$  and  $K_2O$ - $SiO_2$  melts. *Journal of Physical Chemistry* 70:2131-2137
- Searle EJ. 1961. The petrology of the Auckland basalts. *New Zealand Journal of Geology and Geophysics* 4:165-204
- Searle EJ. 1962a. Quartzose xenoliths and pyroxene aggregates in the Auckland basalts. *New Zealand Journal of Geology and Geophysics* 5:130-140
- Searle EJ. 1962b. Xenoliths and metamorphic rocks associated with the Auckland basalts. *New Zealand Journal of Geology and Geophysics* 5:384-403
- Shaw HR. 1963. Obsidian- $H_2O$  viscosities at 1000 bars and 2000 bars in the temperature range 700° to 900°C. *Journal of Geophysical Research* 68:6337-6343

- Shaw HR. 1969. Rheology of basalt in the melting range. *Journal of Petrology* 10:510-535
- Shaw HR. 1972. Viscosities of magmatic silicate liquids; an empirical method of prediction. *American Journal of Science* 272:870-893
- Shaw HR. 1980. The fracture mechanisms of magma transport from the mantle to the surface. In "Physics of magmatic processes", ed. Hargraves RB. Princeton University Press.
- Shaw HR, Wright TL, Peck DL, Okamura R. 1968. The viscosity of basalt magma: an analysis of field measurements in Makaopuhi lava lake, Hawaii. *American Journal of Science* 266:225-264
- Sinton JM. 1979. Ultramafic inclusions and high pressure xenocrysts in submarine basanitoid, Equatorial Mid Atlantic Ridge. *Contributions to Mineralogy and Petrology* 70:49-57
- Smith IEM, White AJR, Chappell BW, Eggleton RA. 1988. Fractionation in a zoned monzonite pluton: Mount Dromedary, southeastern Australia. *Geological Magazine* 125:273-284
- Smith D, Lindsley DH. 1971. Stable and metastable augite crystallization trends in a single basalt flow. *American Mineralogist* 56:225-233
- Smith PPK. 1977. An electron microscope study of amphibole lamellae in augite. *Contributions to Mineralogy and Petrology* 59:317-322
- Sparks RSJ, Huppert HE. 1984. Density changes during the fractional crystallization of basaltic magmas: fluid dynamical implications. *Contributions to Mineralogy and Petrology* 85:300-309
- Sparks RSJ, Huppert HE, Turner JS. 1984. The fluid dynamics of evolving magma chambers. *Philosophical Transactions of the Royal Society of London* A310:511-534
- Sparks RSJ, Marshall LA. 1986. Thermal and mechanical constraints on mixing between mafic and silicic magmas. *Journal of Volcanology and Geothermal Research* 29:99-124
- Sparks RSJ, Meyer P, Sigurdsson H. 1980. Density variation amongst MORB: implications for magma mixing and the scarcity of primitive magmas. *Earth and Planetary Science Letters* 46:419-430
- Sparks RSJ, Pinkerton H, Macdonald R. 1977a. The transport of xenoliths in magmas. *Earth and Planetary Science Letters* 35:234-238
- Sparks RSJ, Sigurdsson H, Wilson L. 1977b. Magma mixing: a mechanism for triggering acid explosive eruptions. *Nature* 267:315-318
- Sparks RSJ, Tait SR, Huppert HE, McKenzie DP, Kerr RC. 1985. Postcumulus processes in layered intrusions. *Geological Magazine* 122:555-568
- Spera FJ. 1980. Aspects of magma transport. In "Physics of magmatic processes", ed. Hargraves RB. Princeton University Press.
- Steiner A. 1958. Petrogenetic implications of the 1954 Ngauruhoe lava and its xenoliths. *New Zealand Journal of Geology and Geophysics* 1:325-363
- Stevenson DJ. 1986. On the role of surface tension in the migration of melts and fluids. *Geophys Res Letters* 13:1149-1152
- Stormer JC Jr. 1972. Mineralogy and petrology of the Raton-Clayton volcanic field, NE New Mexico. *Geological Society of America Bulletin* 83:3299-3322
- Swanson SE, Fenn PM. 1986. Quartz crystallization in igneous rocks. *American Mineralogist* 71:331-342
- Tait SR, Huppert HE, Sparks RSJ. 1984. The role of compositional convection in the formation of adcumulus rocks. *Lithos* 17:139-146
- Takahashi E. 1980. Melting relations of an alkali-olivine basalt to 30kbar, and their bearing on the origin of alkali basalt magmas. *Carnegie Institute of Washington Year Book* 79:271-276
- Talbot JL, Hobbs BE, Wilshire HG, Sweetman TR. 1963. Xenoliths and xenocrysts from lavas of the Kerguelan archipelago. *American Mineralogist* 48:159-179
- Taylor TR, Vogel TA, Wilband JT. 1980. The composite dykes of Mount Desert Island, Maine: an example of coexisting acidic and basic magmas. *Journal of Geology* 88:433-444
- Thomas HH, Smith WC. 1932. Xenoliths of igneous origin in the Trégastrel-Ploumanac'h granite, Côtes du Nord, France. *Quarterly Journal of the Geological Society of London* 88:274-296
- Thompson RA, Dungan MA. 1985. The petrology and geochemistry of the Handkerchief Mesa mixed magma complex, San Juan Mountains, Colorado. *Journal of Volcanology and Geothermal Research* 26:251-274
- Thompson RN, Esson J, Dunham AC. 1972. Major element chemical variation in the Eocene lavas of the the Isle of Skye, Scotland. *Journal of Petrology* 13:219-253
- Thornber CR, Huebner JS. 1985. Dissolution of olivine in basaltic liquids: experimental observations and applications. *American Mineralogist* 70:934-945
- Tormey DR, Grove TL, Bryan WB. 1987. Experimental petrology of normal MORB near the Kane Fracture Zone: 22-25°N, mid-Atlantic Ridge. *Contributions to Mineralogy and Petrology* 96:121-139
- Tsuchiyama A. 1985. Dissolution kinetics of plagioclase in the melt of the system diopside-albite-anorthite, and the origin of dusty plagioclase in andesites. *Contributions to Mineralogy and Petrology* 89:1-16
- Tsuchiyama A. 1986a. Melting and dissolution kinetics: application to partial melting and dissolution of xenoliths. *Journal of Geophysical Research* 91:9395-9406
- Tsuchiyama A. 1986b. Experimental study of olivine-melt reaction and its petrological implications. *Journal of Volcanology and Geothermal Research* 29:245-264
- Tsuchiyama A, Takahashi E. 1983. Melting kinetics of a plagioclase feldspar. *Contributions to Mineralogy and Petrology* 84:345-354

- Turner JS, Campbell IH. 1986. Convection and mixing in magma chambers. *Earth Science Reviews* 23:255-352
- Turnock AC, Lindsley DH. 1981. Experimental determination of pyroxene solvi for  $P < 1$  kbar, 900 and 1000°C. *Canadian Mineralogist* 19:255-267
- Uchimizu M. 1966. Geology and petrology of alkali rocks from Dogo, Oki Islands. *Journal of the Faculty of Science of the University of Tokyo, Section II* 16:85-159
- Varne R. 1977. On the origin of spinel hercynites in basaltic rocks from Tasmania and elsewhere. *Journal of Petrology* 18:1-23
- Waff HS, Bulau JR. 1979. Equilibrium fluid distribution in an ultramafic partial melt under hydrostatic stress conditions. *Journal of Geophysical Research* 84:6109-6114
- Wager LR, Vincent EA, Brown GM, Bell JD. 1965. Marscoite and related rocks of the Western Redhills complex, Isle of Skye. *Philosophical Transactions of the Royal Society of London A257:273-306*
- Wager LR, Vincent EA. 1962. Ferrodiorite from the Isle of Skye. *Mineralogical Magazine* 33:26-36
- Walker D, Jurewicz SR, Watson EB. 1985. Experimental observation of an isothermal transition from orthocumulus to adcumulus texture. *EOS* 66(18): 362
- Walker D, Jurewicz S, Watson EB. 1988. Adcumulus dunite growth in a laboratory thermal gradient. *Contributions to Mineralogy and Petrology* 99:306-319
- Walker D, Kirkpatrick RJ, Longhi J, Hays JF. 1976. Crystallization history of lunar picritic basalt sample 12002: Phase equilibria and cooling rate studies. *Geological Society of America Bulletin* 87:646-656
- Waters AC. 1955. Volcanic rocks of the Southern Rocky Mountains. In "Volcanic rocks and the tectonic cycle" ed. Poldervaart, *Geological Society of America Special Paper* 62:703-722
- Watson EB. 1979. Calcium content of forsterite coexisting with silicate liquid in the system  $\text{Na}_2\text{O}-\text{CaO}-\text{MgO}-\text{Al}_2\text{O}_3-\text{SiO}_2$ . *American Mineralogist* 64:824-829
- Watson EB. 1982. Basalt contamination by continental crust: some experiments and models. *Contributions to Mineralogy and Petrology* 80:73-87
- Watson EB, Jurewicz SR. 1984. Behaviour of alkalis during diffusive interaction of granitic xenoliths with basaltic magma. *Journal of Geology* 92:121-131
- Webb RW. 1941. Quartz xenocrysts in olivine basalt from the southern Sierra Nevada of California. *American Mineralogist* 26:321-337
- Wells PRA. 1977. Pyroxene thermometry in simple and complex systems. *Contributions to Mineralogy and Petrology* 62:129-139
- White RW. 1966. Ultramafic inclusions in basaltic rocks from Hawaii. *Contributions to Mineralogy and Petrology* 12:245-314
- Wiebe RA. 1986. Lower crustal cumulate nodules in Proterozoic dykes of the Main Complex: evidence for the origin of Proterozoic anorthositic. *Journal of Petrology* 27: 1253-1276
- Wilcox RE. 1944. Rhyolite - basalt complex on Gardner River, Yellowstone Park, Wyoming. *Geological Society of America Bulletin* 55:1047-1080
- Wilcox WR. 1983. Influence of convection on the growth of crystals from solution. *Journal of Crystal Growth* 65:133-142
- Wilkinson JFG. 1962. Mineralogical, geochemical, and petrogenetic aspects of an analcite basalt from the New England district of New South Wales. *Journal of Petrology* 3:192-214
- Williams H. 1931. The dacites of Lassen Peak and vicinity, California, and their basic inclusions. *American Journal of Science* 22:385-403
- Williams RJ, Mullins O. 1976. A system using solid ceramic oxygen electrolyte cells to measure oxygen fugacities in gas-mixing systems. *NASA Technical Memorandum X-58167*
- Wilshire HG, Binns RA. 1961. Basic and ultrabasic xenoliths from volcanic rocks of New South Wales. *Journal of Petrology* 2:185-208
- Wilshire HG. 1961. Sedimentary xenoliths and dolerite patch pegmatites from an analcite basalt intrusion. *American Journal of Science* 259:260-279
- Wilson AH. 1982. The geology of the Great "Dyke", Zimbabwe: the ultramafic rocks. *Journal of Petrology* 23:240-292
- Wise WS. 1969. Geology and petrology of the Mt. Hood area: a study of High Cascade volcanism. *Geological Society of America Bulletin* 80:969-1006
- Wood BJ, Banno S. 1973. Garnet-orthopyroxene and orthopyroxene-clinopyroxene relationships in simple and complex systems. *Contributions to Mineralogy and Petrology* 42:109-124
- Wyllie PJ. 1984. Constraints imposed by experimental petrology on possible and impossible magma sources and products. *Philosophical Transactions of the Royal Society of London A310:439-456*
- Wyers GP, Barton M. 1986. Petrology and evolution of transitional alkaline-sub alkaline lavas from Patmos, Dodecanesos, Greece: evidence for fractional crystallization, magma mixing and assimilation. *Contributions to Mineralogy and Petrology* 93:297-311
- Wyers GP, Barton M. 1989. Polybaric evolution of calc-alkaline magmas from Nisyros, Southeastern Hellenic Arc, Greece. *Journal of Petrology* 30:1-37
- Yoder HS Jr. 1973. Contemporaneous basaltic and rhyolitic magmas. *American Mineralogist* 58:152-171
- Yoder HS Jr. 1976. Generation of basaltic magma. *National Academy of Sciences, Washington DC.* 265p.
- Yoder HS, Eugster HP. 1954. Phlogopite synthesis and stability range. *Geochimica et Cosmochimica Acta* 6:157-185
- Zhang Y, Walker D, Leshner CE. 1989. Diffusive crystal dissolution. *Contributions to Mineralogy and Petrology* 102:492-513